UNIVERSITÀ DEGLI STUDI DI PALERMO

Dottorato in Energia e Tecnologie dell'Informazione
Dipartimento di Energia, Ingegneria dell'Informazione e Modelli Matematici
Settore Scientifico Disciplinare ING-IND/11 – Fisica Tecnica Ambientale

INNOVATIVE APPLICATIONS OF EXERGY ANALYSIS AND THERMOECONOMICS IN CHEMICAL, THERMAL AND COOLING ENERGY CONVERSION SYSTEMS

IL DOTTORE
ING. PIETRO CATRINI

IL COORDINATORE
PROF. MAURIZIO CELLURA

IL TUTOR
PROF. MAURIZIO CELLURA

CO-TUTOR
PROF. ANTONIO PIACENTINO

CICLO XXXI
ANNO CONSEGUIMENTO TITOLO 2019

Acknowledgments

This thesis is the product of my 3-years research activity as PhD student in "*Energy and Information Technologies*" at the University of Palermo.

First of all, I want to acknowledge Prof. Maurizio Cellura and Prof. Antonio Piacentino for giving me this great opportunity which has introduced me to the research world. Especially, I want to acknowledge Prof. Antonio Piacentino for supporting me constantly and patiently, for teaching me a lot about research and for giving me all the tips on a proper behavior in professional life. All these things will be useful for my future career.

I would like to acknowledge Prof. Giorgio Domenico Maria Micale and Prof. Andrea Cipollina for involving me in the EU Project *RED-Heat to Power*. This great experience has introduced me to the concept of high innovation project and it allowed me for enlarging my knowledge about chemical processes. To this regard, I would like to thank Dr. Francesco Giacalone who spent a lot of time with me while working hardly on exergy analysis.

I would like to acknowledge Prof. James E. Braun at Purdue University, West Lafayette (Indiana, USA), who let me spend 6-months as an Exchange Visitor at Herrick Laboratories. Thanks to that great experience, I had the opportunity to improve my experimental skills, to join a different academic life and to know lot of people from

all around the world. I want to thank Dr. Akash Patil, Dr. Parveen Dhillon and Dr. Andrew Leroy Hjortland who supported me constantly during my research activities at Herrick Laboratories.

I would like to acknowledge Dr. Ana Picallo-Perez from University of Basque Countries, who spent 3-months here in Palermo, for sharing her point of view about Thermoeconomics and about life as well.

I would like to thank my colleagues Dr. Antonino D'Amico and Dr. Teresa Maria Gulotta for sharing with me lot of their free time during this year.

To All,

Thanks!

Contents

Chapter 6:
Thermoeconomic Diagnosis of Air Conditioning Systems

Chapter 7: Integrating Thermoeconomics and Life Cycle Assessment for the analysis of energy systems

Introduction

Since 70s, the world has been becoming more and more concerned about energy and environmental issues. The need of meeting the current energy demand by guaranteeing the ability of future generation to satisfy theirs have been pushing research not only to exploit alternative energy sources such as renewable energies, but also to improve the efficiency of energy conversion systems. To this regard, developing systems that use efficiently energy is of paramount importance especially in those countries which rely on non-renewable energy sources such as oil, natural gas, and coal. In fact, the reduction of energy consumption will lead not only to the saving of unrestorable and limited energy resources but also to some environmental benefits, such as the reduction of carbon dioxide emissions.

To this am, a lot of methods have been developed across scientific research. Among them, *Exergy Analysis* and *Thermoeconomics* are well-recognized for supporting the analysis and design of any energy conversion system. Over time, a plethora of papers have been published but both of them are still limited to the research fields.

This thesis has been focused on innovative applications of *Exergy Analysis* and *Thermoeconomics* in chemical, thermal and cooling energy conversion systems. It

aims at demonstrating the capabilities of both methods to provide insights into design alternatives and operation strategies of any energy system.

At this point, two questions could arise: "What is Exergy? Why adopting exergy for analyzing and improving the performance of energy systems?"

Exergy measures the maximum amount of work producible by a system when it evolves to thermodynamic equilibrium with the environment. Actually, part of this potential is "destroyed" due to *thermodynamic imperfections* that unavoidably occur in real processes such as flow friction, ohmic resistance, mixing and so on. Differently from energy, exergy is not *conservative*. The more exergy destroyed along the conversion process, the more exergy supplied (for instance via fossil fuels) for achieving a given productive purpose such as electric power generation, cooling and heating, separation of solutions and so on. By quantifying exergy destruction, it is possible to set actions aimed at improving the overall thermodynamic performance of an energy conversion process. To this regard, exergy analysis of the *Reverse Electrodialysis* process is carried out is in this thesis. Reverse Electrodialysis (RED) is a membrane-based technology which is able to harvest energy from salinity gradients and converts it to electricity. This renewable energy source is not currently exploited. However, a large potential is wasted when considering the continuous mixing of river water with the sea. Even though the principles of this technology dates back to 1950s, only recently industry and academia have been renewed their attention to this process, thanks to the improvements attained in the membrane manufacturing. As will be duly shown, two solutions at different concentration are placed in contact by means of Ionic Selective Membranes which allow for the "direct" conversion of the chemical energy into electricity. It is obvious that membranes play a key role in the efficiency of this process. For the first time, a detailed exergy analysis of the RED process is carried out. The analysis aims at providing insights into the effects on the exergy performance of the current membrane properties and of some design and

operating parameters such as flow arrangements, concentrations of the feed streams and so forth. Results will be useful for the future development of this energy system.

A further step involves the exergy analysis of the integrated process *Reverse Electrodialysis and Multi-Effect Distillation* (RED-MED). In this system, a Multi-Effect Distillation unit is coupled to the RED process in order to restore the initial salinity gradient of solutions exiting the RED unit by exploiting low-grade heat available from industrial processes or from renewable energy sources. Then, the overall process results in a conversion of heat to electric power in a closed-loop configuration. This concept is indicated as *RED-Heat Engine* (RED-HE) which is being investigated within the framework of the European Union project *RED-Heat-to-Power*. Due to the innovative features of this process, no exergy analysis has been carried out yet. The analysis aims at evaluating the effect of design parameters and/or operation strategies on the thermodynamic efficiency of the process.

During the decades, more refined exergy-based methods than Exergy Analysis have been proposed such as *Thermoeconomics*, *Advanced Exergy Analysis*, *Extended Exergy Analysis*, *Thermoecology*, *Exergy Input-Output Analysis* and so forth. These methods have tried to thoroughly account for economic and environmental aspects related to the operation of energy conversion systems.

For instance, Thermoeconomics is a well-recognized method for the analysis and optimization of energy systems, and it rests on the idea that exergy is a rational basis to allocate costs sustained in energy systems. At the very beginning this method was aimed at allocating cost in multi-purpose systems, but over time its application has been enlarged. Nowadays, Thermoeconomics aims at supporting: (i) cost accounting procedures, (ii) optimization of the design and operation of energy systems and (iii) analysis of the operating conditions in order to detect faults. This thesis is focused only on two of these three fields, i.e. *cost accounting* and *diagnosis*.

More specifically, two innovative applications of *thermoeconomic cost accounting* are carried out. In particular:

- An exergy cost accounting for an existing *Parallel-Feed Multi Effect Distillation-Thermal Vapor Compression* located in Trapani (SICILY) is carried out. The exergy analysis is based on real data and it allows for quantifying the exergy destruction occurring in each subprocess of the MED-TVC unit. Then, the exergy cost accounting allows for evaluating the effect of exergy destruction on the unit cost of the produced freshwater.
- An exergy analysis and exergoeconomic cost accounting of a *Combined Heat and Power (CHP) steam cycle integrated with Multi Effect Distillation-Thermal Vapor Compression (MED-TVC) plant* is performed. Multi-Effect Desalination systems are energy-intensive and this fact has limited their spread during the decades. However, the possibility to be fueled by low-grade heat makes them profitable when coupled with fossil-fueled plant or with renewable thermal energies. Among the main innovative aspects of this work, it is worth mentioning: (i) the formulation of a productive structure for the whole CHP-MED-TVC (iii) the analysis of electricity and freshwater unit costs by considering the effects of some design and operating parameters.

The other application field of Thermoeconomics investigated in this thesis is the *Diagnosis of Malfunction* in energy systems. At the very beginning, this *Fault and Detection Technique* was extensively applied to thermal power plants, but only recently it has been extended to heating, ventilation and air conditioning systems (HVAC). The quantitative information provided by this diagnostic technique allows for an optimal scheduling of maintenance strategies, which prioritizes those faults with the highest economic impact. As concern HVAC systems, most of results achieved so far have been based on a set of virtual-experiments thus not allowing for accounting

for real operation of these system. For the first time, the method is tested using experimental data obtained from a packaged rooftop air conditioning unit.

Last but not least, the applications of exergy-based methods to environmental analyses is considered. Generally, Exergy Analysis and Thermoeconomics optimize the performance of energy systems focusing only on the operational phase. Such an analysis, excludes the remaining phases of life cycle, as construction and disposal of energy facilities. As a consequence, if not duly accounted, some impacts may be only "moved" from the operational phases to the other phases of life cycle. However, to overcome these limits, some exergy-based methods have been developed but lots of them reduce the set of impact indicators only to one synthetic indicator, thus not allowing *decision makers* for understanding all the environmental issues arising from the construction/operation/disposal of energy systems.

In order to overcome this limit, an innovative approach based on integration of *Thermoeconomics* and *Life Cycle Assessment* (LCA) is here proposed. The procedure combines the capabilities of these two techniques to account simultaneously for aspects related to thermodynamics of energy conversion processes and to the overall impacts along the plant life cycle, i.e. from raw material extraction to the disposal of facilities. The capabilities of this approach are illustrated by applying it to a water-cooled vapor compression chiller.

Outline of this thesis

A brief outline of this thesis is here given. In ***Chapter 1***, some insights into Exergy Analysis and Thermoeconomics will be provided. In particular, the exergy content of a heat flow and of a stream of matter will be explained. Details on exergy and

exergoeconomic cost will be given and the main tools of *Symbolic Exergoeconomics* will be thoroughly presented.

In ***Chapter 2***, a brief outline on *Salinity Gradient Power* technology will be given. Then, among salinity gradient engine, the *Reverse Electrodialysis* will be presented. Exergy analysis of this system will be carried out by considering the effect of some design and operating parameters. In ***Chapter 3***, the *RED-MED Heat-Engine* concept will be introduced. A detailed exergy analysis of this integrated system will be carried out and the effect of some design and operating parameters will be investigated.

In ***Chapter 4***, exergy analysis and exergy cost accounting will be carried out for an existing Multi-Effect Desalination system. First, some general details about technical, economic and environmental aspects of the Multi-Effect Desalination process will be provided. In ***Chapter 5*** exergoeconomic cost accounting of a Combined Heat and Power Steam Cycle integrated with a Multi Effect Distillation-Thermal Vapor Compression (MED-TVC) will be presented.

In ***Chapter 6***, a general overview on thermoeconomic diagnosis will be given first. A description of the experimental set-up and of the testing procedures will be duly provided. Then, the performance of the diagnostic technique will be investigated in single and multiple faults scenarios.

In ***Chapter 7***, an overview on exergy-based environmental analyses proposed in literature will be provided. Then, the main features and capabilities of the integrated approach based on Thermoeconomics and Life Cycle Assessment will be described, and a selected case study will be analyzed.

Chapter 1

Overview on Exergy Analysis and Thermoeconomics of Energy Conversion Systems

This chapter addresses fundamental principles of Exergy Analysis and Thermoeconomics. These topics are covered in a broad manner in order to provide with information for understanding the following chapters of this thesis.

First, an historical background and a literature review of Exergy Analysis is provided. Limits and strengths of this method are pointed out and some insights into more refined exergy-based methods are briefly given. Then, Thermoeconomics is introduced and a description of its historical development is provided. An extensive literature review points out the variety of fields investigated during the decades. Both exergoeconomic and exergy costs are presented and principles of the Theory of Exergetic Cost are provided. Finally, *Symbolic Exergoeconomic* is presented.

1.1 Introduction on Exergy and Exergy Analysis

Exergy Analysis (ExA) is a well-established method which allows for evaluating the rational use of energy in thermal and chemical processes. A comprehensive and interesting review of exergy concept and its applications can be found in [1.1].

What is *Exergy*?

Lots of definitions about exergy can be found in books and scientific papers. The one presented by Kotas in 1985 [1.2] is here reported. Kotas defined the exergy of a system as:

"*the maximum amount of work obtainable when the system evolves from its thermodynamic state to the thermomechanical and chemical equilibrium with the environment through reversible processes involving mass, heat and work transfer between the system and the environment*".

Exergy measures how much a system

departs from thermodynamic equilibrium with the environment. It provides a quantitative information on the *maximum* amount of work that can be obtained when a given system reaches the thermodynamic equilibrium with the environment. Dually, it allows for quantifying the *minimum* amount of work required when a system is brought reversibly from equilibrium with the environment to a non-equilibrium state.

Some examples could clarify these concepts. For example, in the case of a steam turbine, steam flow rate is supplied in order to generate mechanical work. The maximum amount of work is produced only if no flow friction occurs. The difference between the maximum amount of work and the actual work is equal to the exergy destruction (or irreversibility) occurring within the turbine. The more irreversible the process occurring in the turbine, the higher the exergy destruction. Conversely, in the case of an air compressor, if a reversible compression process is considered (i.e. a compression without friction losses), the minimum amount of work is required. This quantity is equal to the increase in exergy content of compressed air.

From the previous examples, it is apparent that exergy is not a thermodynamic property of the system itself (like temperature or pressure), but it is a *co-property* of the system and the reference environment. This fact suggests that a proper definition of the reference environment in terms of temperature, pressure and compositions is due [1.3].

From an historical point of view, the concept of the *maximum amount of work* produced by a system dates back to the nineteenth century, when Gibbs, Maxwell and Clausius introduced the concept of *"availability of energy to be converted into work"*. Over the decades, lots of expressions were used to refer to this quantity such as *available energy*, *availability*, *available work*, *potential work*, *useful energy*, *potential entropy* [1.1], [1.2], [1.4] The term "exergy" was coined only in 1956 by the Slovenian Zoran Rant (1904–1972) who merged the Greek words ***ex*** and ***ergon*** which literally mean "*from work*" [1.2]. Over time, all expressions previously adopted have been abandoned.

Differently from energy, exergy is *not conservative*. In fact, exergy is usually destroyed due to irreversibility sources like flow friction, finite temperature differences, ohmic resistance and so forth. The more exergy destroyed within a process, the higher the consumption of exergy resources from the environment, such as coal, oil or natural gas. To this regard, the minimization of exergy destruction may lead to cost-effective energy saving in those systems where energy consumption highly influences operating costs. In fact, looking at the amount of exergy destroyed at subprocess level, it is possible to identify which ones greatly affect the overall exergy destruction and to develop design alternatives or operation strategies which may improve the performance of the investigated process.

Exergy has also been assumed as a *"metric"* for quantifying the consumption of natural resources such as energy, water, mineral ores and so forth [1.5]. For instance, energy quantity is commonly used when accounting for the consumption of energy resources. However, energy does not account for the quality of this resources. In fact, *high-quality* energy, as the one contained in fossil and nuclear fuels, is actually useful for human activities. In order to account for the consumption of these sources, *exergy* may be a more appropriate basis. In fact, energy is conservative, it is available

everywhere and in any time. From the perspective of sustainable development, since these sources are limited and not evenly distributed in the world, the current society is trying to set actions in order to avoid a future *exergy crisis*, rather than an energy crisis [1.6].

The capability of exergy to account for the consumption of natural resources has been applied not only to a *microeconomic level* such as energy conversion systems, but also to a *macroeconomic level* such as national economies. As concern the latter, exergy has been combined with the *Input-Output Analysis* [1.7], in order to evaluate the primary exergy cost of goods and services produced by a given country. Similarly to the concept of the embodied energy, *embodied exergy* of a product has been proposed. As will be shown in Chapter 7, other refined exergy based-approaches have been developed to assess the embodied exergy of services and products during these decades.

Exergy-based methods can be used to evaluate actions aimed at supporting a *sustainable development* [1.8]. To this aim, two parallel routes could be followed:

- *Increasing the exergy efficiency of processes*: an increase in the efficiency of the processes reduce the amount of exergy needed for their purposes. This will lead to short-term economic and environmental benefits, but also it allows for preserving limited resources as fossil fuels for future generations (long-term effects) and contains the effect of emissions.
- *Promoting the use of renewable exergy sources* as solar energy and so forth. The Earth is an open system subject to a net influx of exergy from the sun. It is the exergy (or order states) delivered with solar radiation, and other part is converted into other exergy forms like wind or biomass. The impacts of anthropogenic activities can be reduced by exploiting these limitless and nearly cost-zero energy sources. However, it is worth stressing that in order to achieve this should be done from a life cycle perspective.

As stated by Connelly and Koshland in [1.9] there is an intrinsic relationship among (i) sustainability (ii) environmental impact and (iii) the exergy efficiency of a process. More specifically, as the exergy efficiency of a process approaches 100%, the related environmental impact approaches zero, since exergy is totally converted from one form to another one without any loss. In this case, the sustainability of the process approaches infinity. Conversely, as the exergy efficiency approaches 0%, sustainability approaches zero because exergy resources are exploited without achieving useful results.

1.2 Exergy of a heat flow and a stream of matter

In this paragraph, exergy is introduced. Since this thesis considered only *flow systems* (i.e. those which exchange heat, work and mass across their physical boundaries), details about exergy of *non-flow systems* are omitted.

1.2.1 Exergy associated with heat flow and work

The exergy associated with a heat flow $\dot{Q}$ coming from a thermal reservoir at temperature T_r is indicated as "*thermal exergy flow*" and it is denoted by $\dot{B}_Q$ [1.2]. In Equation (1.1) the formula for calculating this quantity is shown.

$$\dot{B}_Q = \left|1 - \frac{T_0}{T_r}\right| \dot{Q} \tag{1.1}$$

The factor $\tau_C = \left|1 - \frac{T_0}{T_r}\right|$ is named *dimensionless exergetic temperature* [1.2]. Its values are plotted in Figure 1.1, where the temperature of the reference environment T_0 is equal to 298.15 K (25°C). In order to clarify the physical meaning of the dimensionless exergetic temperature, the two cases $T_r > T_0$ and $T_r < T_0$ are analyzed separately.

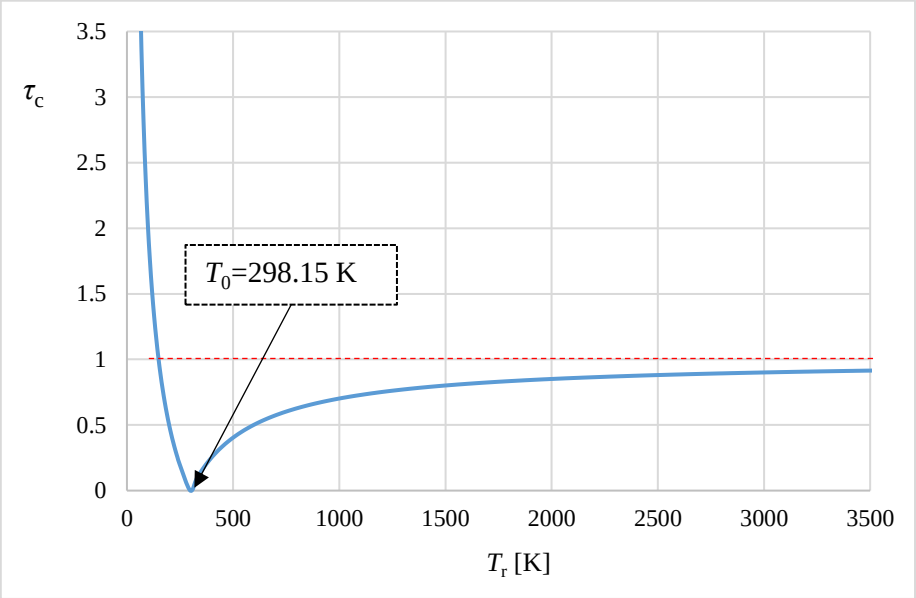

Figure 1.1 *Dimensionless Exergetic Temperature Plot*

When T_r is *greater* than T_0, τ_C represents the efficiency of a Carnot Engine operating between the thermal reservoir T_r and the reference environment T_0. From Equation (1.1), it follows that $\dot{B}_Q$ is the maximum amount work obtainable from the heat flow $\dot{Q}$. The remaining part, i.e. $\dot{Q} - \dot{B}_Q = \frac{T_0}{T_r}\dot{Q}$, cannot be transformed into work and it is usually indicated as "*Anergy*" [1.10], and it is indicated here as $\dot{A}_Q$. In Figure 1.2, the heat flow $\dot{Q}$ and the related exergy and anergy content are shown.

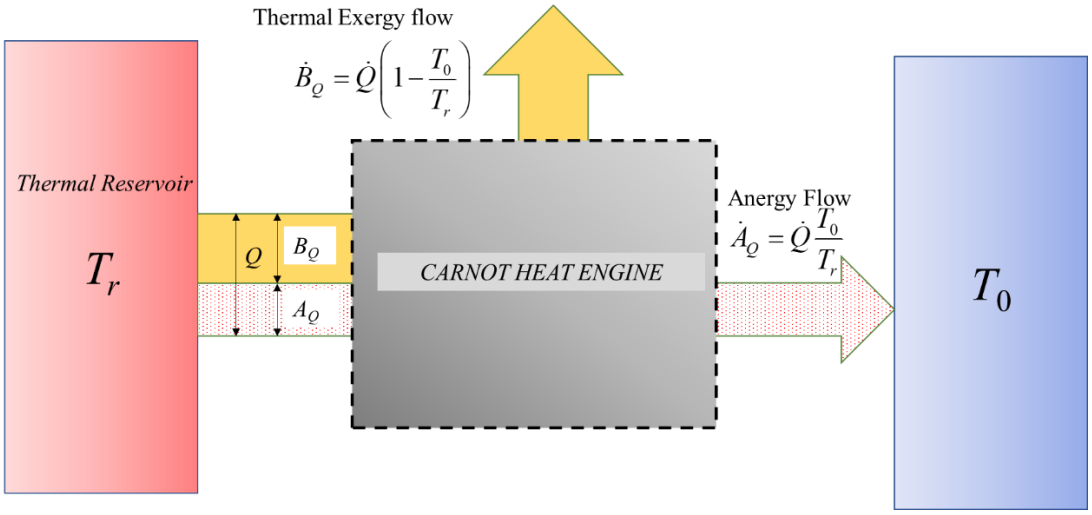

Figure 1.2 *Exergy and Anergy Flow for the case $T_r > T_0$*

As shown in Figure 1.1, the values of τ_C increases when increasing the temperature of the thermal reservoir T_r. The greater the temperature of the heat reservoir, the higher the exergy content of the heat flow. This explains why 1 MWh of heat rejected by the condenser of a thermal power plant does not have the same quality of 1 MWh of heat supplied by burning directly natural gas in a boiler, though from an "energy" point of view they are quantitively the same. When the temperature of the thermal reservoir approaches infinite, the factor τ_C approaches the unity. In this case, the exergy content of the heat flow is equal to its energy content and its anergy becomes negligible.

When T_r is *lower* than the T_0, the factor τ_C is the inverse of the Coefficient of Performance of a Carnot Reverse Cycle which has to maintain the temperature T_r by transferring a given quantity of heat $\dot{Q}$ (usually named *cooling duty*), from the temperature level T_r to the reference environment T_0. Equation (1.1) quantifies the *minimum amount work* to be supplied to the "refrigeration machine" in order to transfer the heat flow $\dot{Q}$ between the two temperature levels. In Figure 1.3 exergy and anergy flow are shown. It is important to note that in this case exergy and anergy have different directions. Also, the content of the heat discharged to the environment is

totally anergy, since it is available at the temperature of the reference environment. Conversely, it possible to observe that an exergy flow (yellow arrow in Figure 1.3) enters the cooled environment.

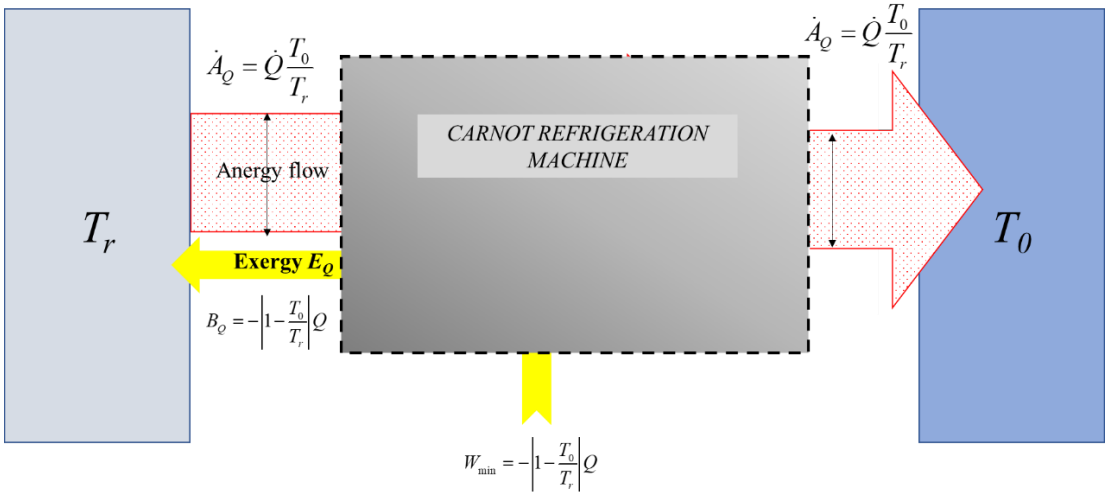

Figure 1.3 *Exergy and Anergy Flow for the case $T_r < T_0$*

As shown in Figure 1.1, the lower the temperature of the refrigerated environment, the greater the minimum power needed to maintain it. This trend suggests that since a lot of exergy is spent for "generating" 1 kWh of cooling, exergy destruction in low temperature applications, such as cryogenics, should be minimized as possible. For this reason, lower minimum temperature differences are generally allowed for heat exchange in cryogenic applications, in order to reduce the impact of exergy destruction due to finite temperature difference.

When T_r=T_0, the exergy content of the heat flow is equal to zero. This means that the environment could be considered as an *infinite zero-grade heat source*.

As concerns the exergy associated with work flow such as shaft work, electric work and so on, it is equal to the energy amount of each of these quantities.

1.2.2 Exergy of a stream of matter

According to Kotas [1.2], the exergy of a stream of matter is defined as:

"the maximum amount of work obtainable when the stream of matter evolves from its thermodynamic state to the thermodynamic equilibrium with the environment through reversible processes involving mass and heat transfer between the system and the environment".

In order to derive a general expression for the exergy content of a stream flow, the general approach presented in [1.11] is here adopted. To this aim, it is useful to consider the scheme shown in Figure 1.4. A stream flow in a given thermodynamic state, identified respectively by its altitude *z*, mean velocity $\bar{v}$ temperature *T*, pressure *p*, and composition (which is identified by the molar fraction x_i for each of the "i-th" species in the mixture), reaches thermodynamic equilibrium with the environment by exchanging "*reversibly*" mass, heat and work with the environment. The final thermodynamic state of the stream flow, which is commonly named "*dead state*", is characterized by: (i) a null velocity and altitude with respect to the earth, (ii) the same temperature T_0, pressure p_0, and composition (defined by the molar fraction of the "i-th" species, i.e. $x_{i,0}$, at equilibrium) of the environment.

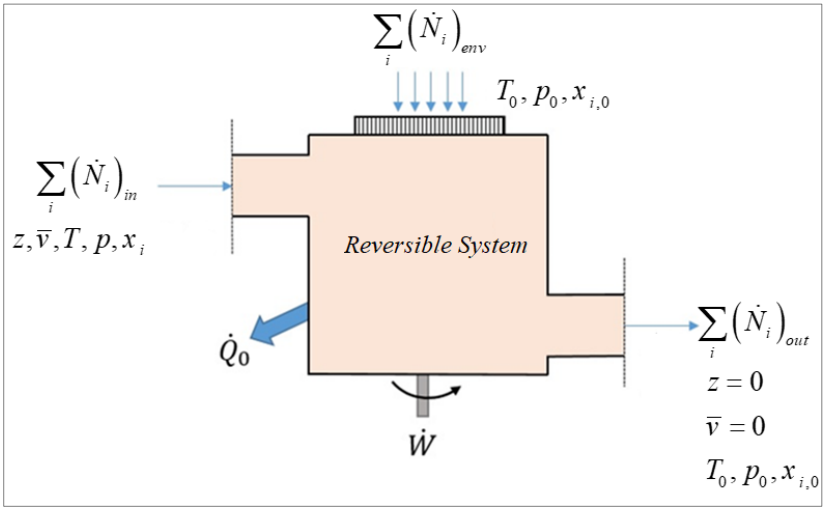

Figure 1.4 *Reversible Evolution of a stream of matter to thermodynamic equilibrium with the environment*

The general expression for the exergy content of the inlet stream is derived by applying to the open system represented in Figure 1.4, the mass and the energy conservation principles and the entropy balance (which is not initially formulated as a conservation equation, due to the possible contribution of entropy generation).

However, once introduced the hypothesis of process reversibility, no entropy is generated, thus obtaining the production of the maximum possible amount of work. According to the definition of exergy provided above, the work obtained in this ideal reversible case equals the exergy content of the inlet stream flow and provides the following analytical expression to be used to calculate it:

$$\dot{B} = \left(gz + \frac{\overline{v}}{2} \right) \sum_{i=1}^{n} MM_i \dot{N}_{i,in} + \\ + \sum_{i=1}^{n} \left[\left(\tilde{h}_i \left(T, p, x_i \right) - T_0 \tilde{s}_i \left(T, p, x_i \right) \right) - \left(\tilde{h}_i \left(T_0, p_0, x_{i,0} \right) - T_0 \tilde{s}_i \left(T_0, p_0, x_{i,0} \right) \right) \right] \cdot \dot{N}_{i,in} \tag{1.2}$$

In Equation (1.2) $\dot{N}_i$ is the molar flow of the "i-th" species constituting the inlet flow, $\tilde{h}_i$ and $\tilde{s}_i$ respectively indicate its partial molar enthalpy and entropy, MM_i is the molar mass of the "i-th" species and n is the number of species of the inlet flow.

Since velocity, altitude, temperature, pressure and composition of a stream flow changes during its evolution from its thermodynamic state to the equilibrium with the environment, it is opportune to account separately for the fractions of the produced work produced by change in chemical composition, those related to changes in temperature and pressure and those related to changes in velocity and altitude of the stream [1.2].

From this perspective, the exergy of a stream is usually divided into:

- *Kinetic and Potential exergy:* kinetic and potential energy are "ordered" form of energy thus fully convertible to work. It follows that they are entirely form of exergy. The potential component of exergy is important in exploitation of hydraulic energy, where it is converted in shaft work by hydraulic turbine. The

kinetic portion is of utmost important in compressor where it is usually converted into pressure-related exergy. In Equation (1.2), $\overline{v}$ is the bulk velocity of the fluid stream relative to the surface of the earth, and *z* is the altitude of the stream above the sea level. The environmental reference for these quantities is only important where there is direct interaction of the stream with the environment, for example when evaluating kinetic exergy of the exhaust gases of a jet engine. In most other cases, only changes in kinetic and potential exergies are considered and, therefore, any inertial reference frame may be used.

$$\dot{B}_p = gz \sum_{i=1}^{n} MM_i \dot{N}_{i,in} \tag{1.3}$$

$$\dot{B}_k = \frac{1}{2} \overline{v}^2 \sum_{i=1}^{n} MM_i \dot{N}_{i,in} \tag{1.4}$$

- *Thermo-mechanical exergy*: this quantity indicates the amount of work obtainable when the examined stream reaches only thermal and mechanical equilibrium with the environment, not observing any change in its chemical composition (i.e. not reaching a chemical equilibrium with the surrounding ambient). The final thermodynamic state of the stream flow is characterized by the same temperature and pressure of the environment, i.e. T_0, p_0, and it is commonly named "*restricted dead state*" [1.3]. In Equation (1.5), expression for a generic stream flow is shown.

$$\dot{B}_{ph} = \sum_{i=1}^{n} \left[\left(\tilde{h}_i(T, p, x_i) - T_0 \tilde{s}_i(T, p, x_i) \right) - \left(\tilde{h}_i(T_0, p_0, x_i) - T_0 \tilde{s}_i(T_0, p_0, x_i) \right) \right] \dot{N}_{i,in} \tag{1.5}$$

- *Chemical exergy*: this component is the maximum amount of work obtainable when the stream, supposed in physical equilibrium with the restricted dead state, modifies its chemical composition thus reaching also chemical equilibrium with the environment; the thermodynamic state parameters of the

stream flow in this case are equal to the ones of environment, i.e. T_0 , p_0 , $x_{i,0}$. In Equation (1.6) expression for the chemical exergy is presented.

$$\begin{aligned}\dot{B}_{ch} &= \sum_{i=1}^{n}\left[\left(\tilde{h}_i\left(T_0, p_0, x_i\right) - T_0\tilde{s}_i\left(T_0, p_0, x_i\right)\right) - \left(\tilde{h}_i\left(T_0, p_0, x_i\right) - T_0\tilde{s}_i\left(T_0, p_0, x_{i,0}\right)\right)\right]\dot{N}_{i,in} \\ &= \sum_{i=1}^{n}\left[\left(\mu_i\left(T_0, p_0, x_i\right) - \mu_i\left(T_0, p_0, x_{i,0}\right)\right)\right]\dot{N}_{i,in}\end{aligned} \tag{1.6}$$

Proper selection of dead state parameters, i.e. pressure, temperature and composition, is necessary. With reference to temperature and pressure values, common practice assumes them equal to the respective average values of the site where the system is going to operate. As regards chemical composition of the reference environment, it is common to refer, for each of the substances compounding the examined stream, to the most abundant natural element where it appears in the environment (either it be in the atmosphere, the seawater or the earth crust) [1.3].

As can be seen, from Equation (1.6), chemical potential calculation for each species in the mixture is implied. Clearly, this means that suitable *thermodynamic modelling* is necessary when assessing the chemical exergy component.

1.3 Exergy Balances, Exergy Destruction and Loss and Exergy Efficiency

As already mentioned, exergy is not a conservative quantity. Only if the process in the system evolved reversibly, exergy would be conserved. In real systems part of the supplied exergy is *destroyed* due to irreversibility sources like: heat transfer across finite temperature differences, mixing of flows at different concentrations, flow friction, ohmic resistance, throttling process, and so forth [1.2].

In order to calculate the amount of exergy destroyed (or the irreversibility generated), a balance equation is set. More specifically, referring to Figure 1.5 where a flow-system operates in a steady state condition, the exergy balance can be written as shown in Equation (1.7).

$$\sum_{net} \dot{B}_W - \sum_{l=1}^{p} \left(\dot{B}_Q \right)_l - \sum_{\substack{k=1 \\ inlet}}^{q} \dot{B}_k + \sum_{\substack{k=1 \\ outlet}}^{r} \dot{B}_k = \dot{B}_D \qquad (1.7)$$

In Eq. (1.7), $\sum_{net} \dot{B}_W$ is the net-work produced (i.e. the algebraic sum of the exiting work flow, assumed positive, and entering exergy flow, assumed negative), $\dot{B}_Q$ is the exergy of a heat flow, $\dot{B}_{t,k}$ $\dot{B}_{t,j}$ are the exergy of the streams of matters entering and exiting the component, which are calculated according to Eq. (1.2). $\dot{B}_D$ is the amount of exergy destroyed. According to *Gouy-Stodola Theorem* [1.2], the exergy destruction $\dot{B}_D$ equals the entropy generation rate $\dot{S}_{gen}$ in the system times the absolute temperature of the reference environment, i.e. $\dot{B}_D = T_0 \dot{S}_{gen}$.

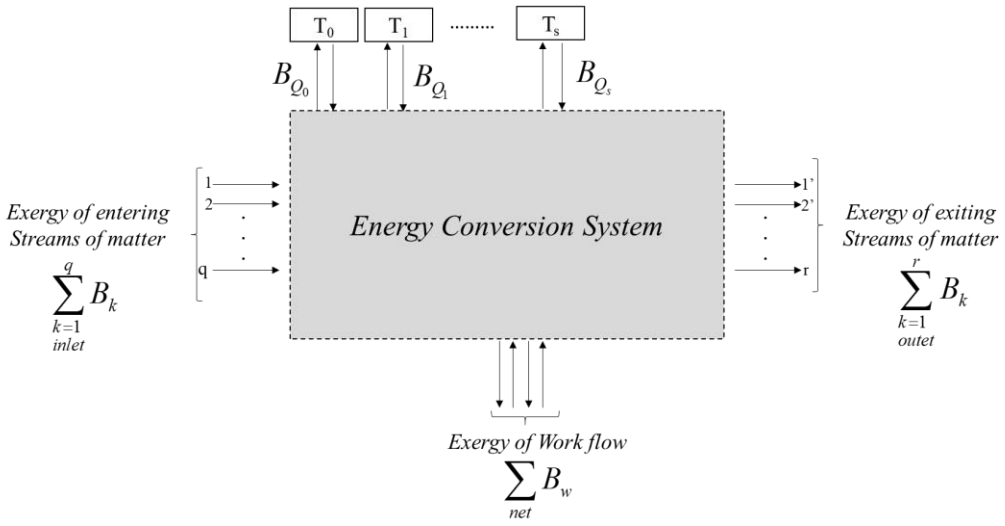

Figure 1.5 *Exergy Flows exchanged by a "flow-system" operating in steady state*

In Equation (1.8), the exergy performance of the system ε_k is calculated as the ratio of the exergy flow exiting the system and the amount of exergy supplied. This quantity

provides a measure of the relative incidence of exergy destruction, i.e. what percentage of the exergy flow entering the system is destroyed with no possibility of further reuse.

$$\varepsilon_k = \frac{\sum_{outlet} \dot{B}_o}{\sum_{inlet} \dot{B}_i} \tag{1.8}$$

1.3.1 On the "Productive" definition of the exergy performance of a process

The exergy efficiency defined in Equation (1.8) does not discriminate if the exiting exergy flows are used as resources to other components or if they are disposed back to the environment. To this regard, it is necessary to stress that exergy destructions are only a portion of the *thermodynamic inefficiencies* occurring in energy systems. In fact, two sources of thermodynamic inefficiencies are commonly identified: (i) ***exergy destructions*** and (ii) ***exergy losses***. Exergy destructions have been already defined. Conversely, exergy losses occur when exergy flows are released into the environment without exploiting their exergy content. Typical examples of exergy losses are: the concentrated brine stream exiting a desalination plant and disposed back to the environment, the high temperature gases released by the stack of a thermal power plant, the thermal exergy discharged by the condenser of a refrigeration system, and so on.

When defining the exergy efficiency of a process, it is important to distinguish which among the exiting exergy flows are "useful" and which ones are eventually "lost". To exemplify this concept, a desalination system is shown in Figure 1.6. In this case, two streams exiting the system can be identified: freshwater and a brine flow. The freshwater produced is the useful product of this system. Conversely, the exergy of the brine is not useful, since this flow is disposed back to the sea.

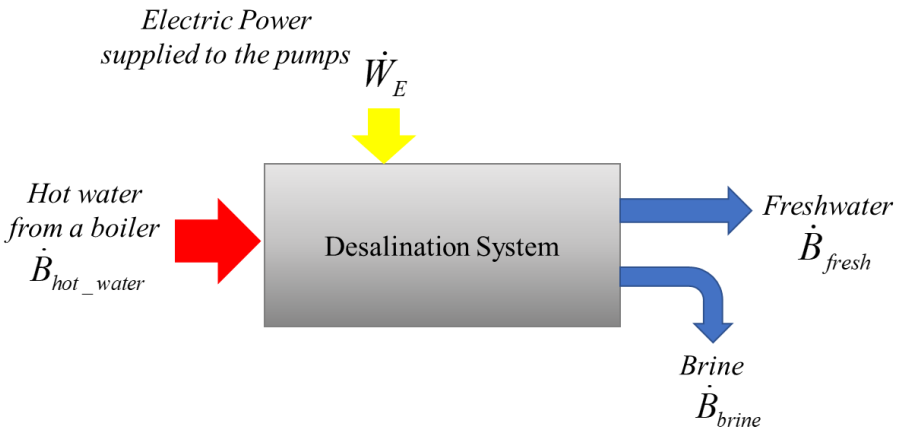

Figure 1.6 *Exergy Flows entering and exiting a desalination system*

In order to distinguish useful exergy flows from the ones that are eventually lost, the concept of *Fuel* and *Product* have been introduced by Tsatsaronis in [1.12]. The Product is composed by the "*subset of the exiting exergy flows*" which are supplied to other system components as fuels or to an external user as the final product. The *Fuel* is the amount of exergy supplied to the given component for producing the exergy product $\dot{B}_P$. Also, $\dot{B}_D$ is the amount of exergy destroyed in the process, and $\dot{B}_L$ is the exergy loss.

Based on these definitions, the exergy balance can be expressed by mean of fuels and products as in Equation (1.9), and graphically presented in Figure 1.7.

$$\dot{B}_F = \dot{B}_P + \dot{B}_D + \dot{B}_L \tag{1.9}$$

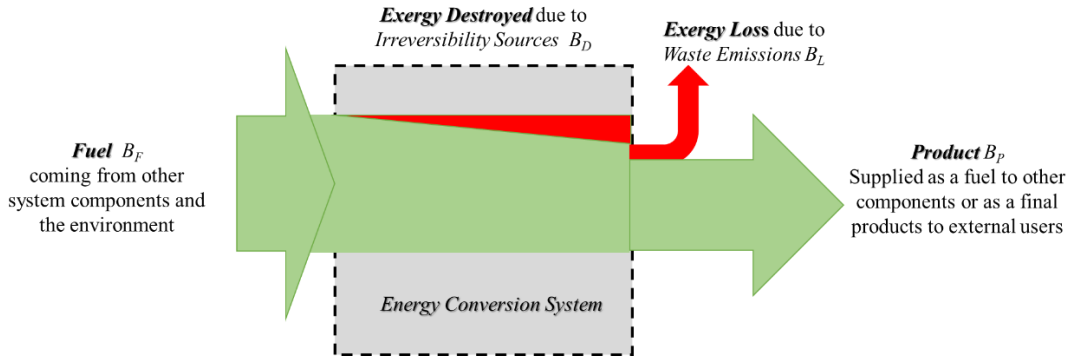

Figure 1.7 *Graphical Representation of Exergy Balance for an energy conversion system based on Fuel-Product definition*

On the basis of the exergy balance proposed in Equation (1.9), a *productive exergy efficiency* $\varepsilon_{k,prod}$ is defined as follows:

$$\varepsilon_{k,prod} = \frac{\dot{B}_P}{\dot{B}_F} = 1 - \frac{\dot{B}_D + \dot{B}_L}{\dot{B}_F} \tag{1.10}$$

Referring to the desalination system shown in Figure 1.6, it is possible to distinguish:

- ***Fuels****:* (i) the thermal exergy of the hot water or steam supplied in order to evaporate water from the incoming seawater, and (ii) the electrical power used to drive pumps.
- ***Product*****:** the chemical exergy of the freshwater produced.
- ***Exergy destruction:*** typical irreversibility sources in this system are heat transfer through finite temperature differences within each heat exchanger, pressure drop, etc.
- ***Exergy loss****:* the chemical exergy of the concentrated brine which is disposed back to the environment.

1.4 Brief literature review on Exergy Analysis

Exergy analysis has been extensively applied to energy systems and chemical processes. There is a plethora of publications and only some of them are here cited for a sake of brevity. However, the variety of fields investigated across scientific research suggests the well-recognized capabilities of this method.

Lots of published papers have concerned cryogenic applications. For instance, an interesting exergy analysis of an *air distillation plant* was carried out by Cornelissen et al. in [1.13]. First, the analysis quantified the exergy loss within each component in each plant section. From these results, the authors suggested some improvements aimed at reducing the main exergy loss in the system. In [1.14], an energy and exergy analysis of different systems for Liquified Natural Gas application were carried out. The analysis aimed at evaluating the theoretical performance of these systems, and it investigated the main sources of irreversibility in order to assess potential energy saving.

Another energy intensive process widely investigated by means of ExA has been the crude oil distillation. A detailed exergy analysis of this process was carried out by Al-Muslim et al. in [1.15]. In this paper, a thermodynamic analysis through energy and exergy analyses of crude oil distillation plants (composed by atmospheric distillation column (ADU) and vacuum distillation column (VDU)) were conducted. The effects of some operating parameters such as overhead pressure and temperature, on the exergy efficiencies of each component and on the overall system were investigated.

As regards Heating, Ventilation and Air Conditioning systems (HVAC), Marletta [1.16] showed that very poor exergy efficiency are achieved in these fields, as these systems are generally fuelled with high quality energy, such as fossil fuel or electricity, for producing low exergy content flows, such as hot/cold water required by heating and cooling processes. The author showed that the most rational way to supply energy in these systems consists of the use of low-quality energy sources as process waste heat or renewable energies such as solar or geothermal energy. Another very

interesting paper concerning the exergy performance of HVAC systems in building was carried out by [1.17]. In particular, the author investigated the so-called Low-Exergy HVAC technologies which provide heating and cooling energy at a temperature close to room temperature and which are fueled by sustainable energy sources.

Exergy analysis has been also extended to *desalination processes* [1.18][1.19]. It is widely recognized that desalination processes are capital and energy intensive. In fact, according to Semiat [1.20], the energy cost of an optimized desalination plant is approximately 30-44% of the total cost of water produced. Exergy analysis has been applied in order to provide routes for reducing the high energy consumption. A review of the second-law performance of the most common desalination systems was carried out in [1.21]. Cerci et al. carried out the exergy analysis of an existing Reverse Osmosis plant in California [1.22]. The analysis pinpointed that high exergy destructions occur in the membrane modules. Some improvements where proposed and analyzed from a second low perspective. Kahraman and Cengel [1.23] evaluated the exergy performance of a large-scale Multi-Stage Flash desalination plant (870000 m^3/day). An overall thermodynamic efficiency equal to 4.2% resulted and the majority of exergy destruction occurred in the MSF unit. Other studies concerning the exergy performance of MSF processes can be found here [1.24]. Another thermal desalination process widely investigated by means of exergy analysis is the Multi-Effect Desalination processes [1.25]. In these systems, great exergy destructions are related to temperature difference in evaporating process within each effect. Kahraman et al. [1.26] carried out exergy analysis of a combined RO, NF, and EDR desalination plant.

Exergy analysis has been applied to a variety of processes for producing chemicals and other products. For instance, De Souza et al. [1.27] studied the ethanol steam reforming to produce hydrogen. The exergy analysis of blast furnace in steel manufacturing was carried out by Ziebek and Stanek in [1.28]. A review of exergy

analysis of internal combustion engines is provided by Rakopoulos and Giakoumis [1.29]. In [1.30], application of exergy analysis to petroleum refining and the petrochemical industry was carried out. Exergy analysis of the production processes of methanol from synthesis gas was carried out in [1.31], [1.32]. Other processes analyzed via exergy analysis include pulp and paper plants [1.33] and metallurgical industries [1.34].

A comprehensive exergy analysis of combined cycle power plants can be found in [1.35]. Exergy analysis has been extensively applied to the analysis of renewable energy systems [1.36]. In that work, a comprehensive study dealing with solar energy, wind power and geothermal energy was carried out. Other studies have been focused on solar electricity production [1.37], solar thermal [1.38], biomass-based fuels [1.39].

In 1998, Feng and Zhu [1.40] proposed an innovative method aimed at recognizing the feasible exergy saving in complex energy system by combining Pinch Analysis and ExA. The method based on ad-hoc diagrams, named *H-Ω diagram* analogous to the composite curves graph, provides analysts with a graphical evaluation of the achievable exergy saving due modifications in the design of the system with respect to a base case. A combined-cycle power plant was selected in order to demonstrate the capabilities of this method.

1.5 On the limits of ExA and developments of refined exergy-based methods

When analyzing or designing energy conversion systems, the reduction of thermodynamic inefficiencies represents an opportunity to reduce the operating costs and the environmental impacts. As observed in [1.41], ExA provides information about the amount of exergy destroyed and lost in each component but the following limits can be recognized:

- ExA is not able to quantify at which extent the exergy destruction occurring within a system component affects the exergy consumption of other system components. For example, when analyzing a steam power plant, it is worth questioning

if 1 MW of exergy destruction in the low-pressure steam turbine and 1 MW of exergy destruction in one of the preheaters affect at the same extent the overall exergy consumption. ExA is not able to answer this question due to its incapability to evaluate the mutual interdependencies among components. In fact, each of them has a different impact on the use of external exergy resources. As will be show in Chapter 6, this fact is known as *Principle of not equivalence of irreversibilities* [1.42].

- ExA is not able to account for the maximum decrease of exergy destruction achieved by improving the thermodynamic performance of components while considering physical, technical and economic constraints.

These limits have paved the way to more refined exergy-based methods, such as *Thermoeconomics* and *Advanced Exergy Analysis* which nowadays are extensively applied when analyzing and optimizing energy conversion systems.

Details about Thermoeconomics will be provided in the paragraph 1.6. As concerns *Advanced Exergetic Analysis* (AExA), a brief description is worth due to the increasing interest shown across scientific literature. This method has been developed by Prof. G. Tsatsaronis around 15 years ago [1.43] . The basic idea of the AExA is to split the exergy destruction $B_{D,k}$ within the "k-th" component into the following fractions:

1. The ***Endogenous exergy destruction*** $B_{D,k}^{EN}$ which is the part of exergy destruction occurring in the "k-th" component obtained when other system components operate ideally and the "k-th" component operates with the same efficiency as in the real system.
2. The ***Exogenous exergy destruction*** $B_{D,k}^{EX}$ is the difference between the actual exergy destruction and the endogenous part.

By means of these two fractions, the mutual interactions among components are evaluated. Procedure for calculating both of them are provided in [1.44].

A further distinction has been introduced in order to quantify the *feasible exergy saving* obtained by improving the thermodynamic efficiencies while considering economic and technical constraints. In particular, the ***Unavoidable Exergy Destruction*** $B_{D,k}^{UN}$ represent the part of exergy destruction that cannot be further reduced due to technological limits such as availability, cost of materials and manufacturing methods. The difference between the total exergy destruction and the unavoidable part is indicated as ***Avoidable Exergy Destruction*** $B_{D,k}^{AV}$. Only this latter should be minimized when trying to maximize the thermodynamic performance of the system. The formal procedures for calculating these exergy fractions are proposed in [1.43].

Only the *avoidable* part of exergy destructions provides a quantitative evaluation about the *feasible exergy saving* for a given energy conversion system. To this aim, a modified exergy efficiency, i.e. ε_k^*, has been proposed in [1.42] and here reported in Equation (1.11). This formula is more realistic in evaluating the exergy performance of a component since it considers only "avoidable endogenous irreversibility sources".

$$\varepsilon_k^* = \frac{B_{P,k}}{B_{F,k} - B_{D,k}^{UN}} \tag{1.11}$$

However, some drawbacks are related to the AExA method as outlined in [1.46]: (i) the "*arbitrariness"* associated when selecting values aimed at evaluating the endogenous exergy destruction (for instance the minimum temperature difference for heat exchanger, or the values adopted for isoentropic efficiency of turbine and compressor), (ii) the "*large number of simulations"* required for splitting the exergy flows in all the aforementioned fractions, and (iii) a more refined approach is required for splitting exergy destruction in systems involving chemical reactions [1.46].

Further developments of AExA are the *Advanced Exergoeconomic and Exergoenvironmental Analyses*. These methods extend the concept of avoidable

exergy destruction to identify the *avoidable/unavoidable capital investment costs* and the *avoidable/unavoidable construction-of-component-related environmental impact* [1.47], [1.48].

An very interesting and exemplifying application of these refined methods can be found in [1.47]. In that paper, Morosuk and Tsatsaronis proved the capabilities of the method to provide insights into the feasible exergy saving in a vapor compression system. For instance, results showed that the exergy destruction occurring in the evaporator could be entirely classified as endogenous (being related to the minimum temperature difference between the fluids within this component). The avoidable part of the endogenous exergy destruction in the evaporator accounted nearly for the 50% of total exergy destruction. The compressor and condenser had comparable values of endogenous avoidable exergy destruction. The detailed values of the exogenous exergy destruction demonstrate that the exergy destruction in the evaporator had the largest effect on the exogenous avoidable exergy destruction in the compressor, condenser and throttling valve. These results clearly suggested the important role of the evaporator in improving the overall efficiency. An improvement in the evaporator had beneficial effects on the thermodynamic performance of all other components. A further step of the analysis involved the splitting of investment costs for each component of the system. The evaporator was again the component that mainly affects the exogenous investment cost for the compressor and the condenser.

Lots of papers have been published during these decades, and only some of them are here cited in order to demonstrate the variety of fields investigated. In [1.50], the authors investigated the effect of different working fluids of vapor-compression refrigeration machines. In [1.50], Wei et al. investigated the potential for energy and cost savings in distillation processes by using the concepts of avoidable/unavoidable exergy destruction and by advanced exergoeconomic evaluation. In [1.51], Mehdizadeh-Fard et al. combined pinch analysis and advanced exergy analysis in order to assess the unavoidable/avoidable exergy destruction in a heat exchange network for

a natural gas refinery. Hepbasli et al. [1.52] applied AExA to analyze geothermal district heating heat pump systems by using operation data from a real network in Turkey. In [1.53], Erbay et. applied AExA to a gas engine heat pump system for food drying. The analysis highlighted the condenser as the component with the highest feasible exergy saving since 90% of the exergy destruction in this component is avoidable. In [1.54] an advanced exergoeconomic cost accounting was applied to a combined power plant for electricity production. The analysis pointed out that the combustion chamber, the high-pressure steam turbine and the condenser had great economic improvement potential because of their high exergy destruction cost rates. Similarly, the heat recovery steam generator and the condenser had significant potential because of their high investment costs.

1.5.1 Limits of ExA results in context with high renewable energy exploitation

Another limit of ExA can be recognized when analyzing energy conversion processes in those contexts characterized by a high penetration of renewable energies. An example could help to clarify this concept. A domestic hot-water boiler fueled by electricity is characterized by a very low exergy efficiency, since high-quality energy as electricity (which is entirely exergy), is used to produce low-quality energy such as hot water. The electricity supplied to this system can be produced by exploiting a renewable or a non-renewable energy source, according to the context where the system is operated. To this regard, renewable energy sources are limitless and their economic cost is “approximately” zero (in fact, only the costs of facilities necessary to exploit them contribute to their costs). Conversely, non-renewable exergy is not limitless and its cost is not zero. Regardless the exergy sources supplied, the low exergy efficiency suggests that this process is not rational and should be avoided. For instance, replacing the existing boiler with a higher exergy performing system may be a profitable solution. However, in the first case, the low exergy performance could be

accepted by considering the "free-cost" nature of the exergy sources used. In the second case, conversely, this process should be avoided. This trivial example shows that exergy efficiency cannot be assumed as the "unique" indicator when evaluating an energy conversion process.

1.6 Thermoeconomics: historical developments

Thermoeconomics is a branch of thermal engineering which combines exergy to the economic concept of cost. The following questions may arise: "Why combining exergy with cost? Is not exergy sufficient to assess the value of a product?" "Why should *exergy costing* be more rational than *energy costing*?"

To answer the first two questions, there is a very explanatory example provided in "*The Thermodynamic process of cost formation*" [1.55] by Prof. Antonio Valero, one of the main contributor to the development of Thermoeconomics. He stated that when a glass is broken, no exergy is wasted since the glass is near equilibrium with the environment. What is actually wasted is the total amount of exergy resources consumed along the productive process of the glass itself. This example explains why energy analysts should pay attention not only to the exergy content of products, but also to the total amount of exergy resources burdening their production. This concept, as will be shown in next paragraph, is thoroughly described by the *exergy cost* of a product [1.42] which quantifies the amount of exergy consumed to obtain it according to a given productive process. Obviously, the higher the exergy cost, the highest its value.

As concern the last question, the idea of using exergy for costing purposes was already suggested in 1932 by J. H. Keenan [1.56]. At that time, the problem was to provide a rational basis for allocating costs on electric power and steam generated by a cogeneration system. Keenan pointed out that the economic value of steam and electricity generated is related to their exergy content and not to the energy one. In

order to clarify this concept, an example based on a steam and electricity produced by a cogeneration system was provided in Gaggioli and Wepfer [1.57]. The authors showed that misleading results would be obtained when trying to allocate cost on electric power and steam on an energy basis. In particular, a very high cost for the cogenerated steam was observed which resulted not competitive with values obtained by a separate production. Conversely, when using exergy costing, a lower and more competitive cost for the cogenerated steam was obtained. Also, a sensitivity analysis of the unit cost of the steam to pressure was carried out. In this case, if costing was carried out on energy basis, the unit cost of steam would be not highly sensitive to changes in the pressure level. Conversely, if exergy costing was adopted, the unit cost of steam would be highly sensitive to the pressure level and it would decrease down to zero for very low-pressure. These facts testified that exergy costing provides with more intuitive results than energy costing.

The term *Thermoeconomics* was introduced by Tribus and Evans in 1962 while carrying out exergy analysis in desalination processes [1.58]. They proposed again the idea to assign cost on the basis of the exergy content of the streams and cost equations for each component were formulated. In the late 1960s, El-Sayed, Evans and Tribus, during their research on desalination, published an important paper where the mathematical foundations for thermoeconomic optimization were given [1.59]

It is worth mentioning here that it is very common across scientific literature to use Thermoeconomics and Exergoeconomics interchangeably. The term *Exergoeconomics* was introduced by Tsatsaronis in 1984 [1.4] in order to indicate all procedures aimed at allocating cost on an exergy basis. The same author highlighted how the term Thermoeconomics should be used in a broader sense, in order to include all methods resulting from the combination of Thermodynamics and Economic Analysis. Under this hypothesis, Exergoeconomic should be considered as a part of Thermoeconomics.

After 70s, when the world has begun to be concerned about energy crisis, Thermoeconomics undergone a great development across scientific literature, and different thermoeconomic approaches were developed. All these methods were aimed not only at analyzing energy conversion systems but also at supporting the optimization of design and operation of these systems.

Generally, thermoeconomic methods can be divided in two categories:

- those aimed at supporting cost accounting procedures, e.g. *Exergy Cost Theory* (ECT)[1.42], *Last-In-First-Out Approach* (LIFOA)[1.60] and *Specific Exergy Costing Approach* (SPECO)[1.61].
- those aimed at supporting optimization as *Thermoeconomic Functional Analysis* (TFA) [1.62], *Engineering Functional Analysis* (EFA) [1.63].

The *Thermoeconomic Functional Analysis* (TFA) has been developed by Frangopoulos [1.66] since 1983. The method introduced the *Functional Diagram* concept, dual to the physical structure of the system, which describes interaction among system components on the basis of exergy exchanges. The method was aimed at optimizing design and operation of energy systems while satisfying constraints derived from both the physical and productive structure. Some years later, C. Frangopoulos formulated the *Intelligent Functional Approach* (IFA) in order to find the optimal solution for more complex systems with respect to TFA, which was a further development of the TFA. Another thermoeconomic method, similar to TFA which is also aimed at optimizing the design of energy systems is the *Engineering Functional Analysis* developed by von Spakovsky and Evans [1.63].

In 1986, Valero introduced the concept of the *exergetic cost* of a product [1.64] and in 1993, an interesting paper regarding the *Theory of Exergy Cost* (ECT) was published. The mathematical formalization underlying the thermoeconomic modeling

of the system was duly described. Also, the paper showed the main applications of this theory: (i) assessment of alternatives for energy savings, (ii) cost allocation, (iii) operation optimization, (iv) local optimization of subsystems, and (v) assessment of fuel impact of malfunctions.

An alternative exergoeconomic approach, i.e. the *Specific Exergy Costing* (SPECO), was proposed by Tsatsaronis et al. [1.61] to support cost accounting procedure. A brief description of this method will be provided in the next paragraph.

All previous thermoeconomic methods were developed by different scientists around the world. Only around 1990, the group of specialists composed by C. Frangopoulos, G. Tsatsaronis, A. Valero, and M. von Spakovsky decided to compare their methods in order to describe features and to provide the unification of all thermoeconomic methods. They considered a simple optimization problem, named CGAM after the first initials of all investigators [1.65].

The CGAM problem considers a cogeneration plant which provides 30 MW_e and 14 kg/s of saturated steam at 20 bar. Once defined the problem, a preliminary solution by mean of conventional optimization criteria was found and presented also in [1.65]. After that, the following thermoeconomic methods were applied separately, and results published in a special issue of Energy in 1994: the Theory of Exergetic Cost [1.66] - the Engineering Functional Approach [1.63]- Thermoeconomic Functional Analysis [1.67] - Exergoeconomic Approach [1.68].

Around 90s, Thermoeconomics has been extended to the diagnosis of malfunctions in energy systems [1.69], [1.70]. More insights about this application field will be given in Chapter 6.

In 1992 the *Structural Theory of Thermoeconomics* was presented by Valero et al. [1.71]. This theory was not intended to introduce any new procedure, but it attempts to provide a mathematical formalization for including whatever thermoeconomic methods proposed (i.e. from cost accounting to optimization and diagnosis). The

"*generalized fuel impact formula*" was derived as a tool which encompasses optimization or diagnosis procedures. Some comparisons between the results obtained using the original procedure and applying the structural theory to the same representation can be found in literature. To this regard, Erlach et al. [1.71] applied the Last In-First Out approach and the Structural Theory to a combined cycle plant and they showed that thermoeconomic modellings obtained from both methods for the investigated system were the same.

1.7 Literature review on Thermoeconomics

Since 1970s, there have been numerous published papers all around the world on Thermoeconomics, and only some of them are here cited in order to highlight contributions and application fields. As previously said, Thermoeconomics can support: (i) costing procedures, (ii) design improvement and optimization and (iii) the analysis of operating conditions of energy systems. In this chapter, no literature review about *Thermoeconomic Diagnosis* is presented, since it will be the object of Chapter 6.

Lots of papers concerning thermoeconomic analysis and optimization of *desalination processes* have been published. To this regard, thermoeconomic analysis can be used to evaluate the cost-effectiveness of design options and operating strategies for these systems. For instance, in [1.21] Mabrouk et al. carried out a critical thermoeconomic analysis for some existing desalination processes as Multi Stage Flash (MSF), Multi Effect Evaporation (MEE), Thermal Vapor Compression-MEE (MEE-TVC), Mechanical Vapor Compression (MEE-MVC) and Reverse Osmosis (RO). For each process, the analysis allowed to quantify the exergy destruction at subprocess level and the impact of these on operating costs. Also, the cost due to exergy destruction was compared with respect to equipment purchase costs. In [1.72], Fiorini and Sciubba carried out a thermoeconomic analysis in order to investigate the

optimal configuration of a MSF plant. The analysis was supported by a software developed by the same authors. In [1.73], Sayyaadi et Saffari carried out a thermoeconomic optimization for a MED-TVC desalination systems. A detailed thermodynamic, economic and exergetic modelling of the system was carried out. The analysis aimed at minimizing the unit cost of produced freshwater. In [1.25], Piacentino carried out a thermoeconomic and exergy cost accounting for a Forward-Feed Multi-Effect distillation plant. The analysis was carried out at single effect levels in order to shed light on the cost formation process of freshwater through each effect. In [1.74], Elsayed et al. carried out detailed exergy and exergoeconomic analysis of four different feed configurations of a MED-TVC system. The analyzed configurations were the backward feed (BF), the forward feed (FF), the parallel feed (PF) and the parallel cross feed (PCF). The analysis was carried out at each subprocess level and results showed that a great amount of exergy is destroyed in the TVC. Exergoeconomic indicators (i.e. exergoeconomic factors) highlighted the great influence of exergy destruction on the freshwater cost with respect to purchase costs. An exergoeconomic analysis for a seawater reverse osmosis plant (SRO) was carried out in [1.75] by Jamil. Various retrofit options aimed at improving the thermodynamic efficiency of the system were evaluated by means of Thermoeconomics.

Lots of paper on Thermoeconomics have been focused on the possibility of coupling desalination systems with non-renewable and renewable-fueled power plant. For instance, Uche et al in [1.76] carried out a thermoeconomic optimization of the design of dual-purpose power plant, composed by a steam power plant coupled with a MSF desalination unit. The minimization of total cost was achieved by the local optimization of each subprocess thus allowing for a reduction in the computing resources and for a simplification of the mathematical problem. In [1.77], a Thermoeconomic optimization of a hybrid pressurized water reactor (PWR) power plant coupled to a multi effect distillation desalination system with thermo-vapor compressor (MED-TVC) was carried out. In [1.78], a thermoeconomic-aided

optimization of a MSF desalination system coupled with PWR nuclear power plant was carried out. In [1.79], Wellmann et al. carried out an exergoeconomic evaluation of a CSP plant in combination with a desalination unit. The exergoeconomic costs of both products, i.e. electricity and freshwater, were investigated for two selected operating conditions of the system. Other exergoeconomic evaluations of innovative distillation system have been proposed in [1.80], [1.81].

Thermoeconomics has also been extended to refrigeration and heat pump systems. The following work have been published during these decades. In [1.82] thermoeconomic optimization of a single-stage heat-pump was carried out. The authors evaluated the marginal cost of exergy flows when varying the efficiencies of the compressor, condenser, evaporator, and electric motor. Dentice d'Accadia et al. [1.83] applied Exergoeconomics to determine the optimal configuration of the condenser of an heat pump by considering the effect of pressure drop and heat transfer area. The approach relied on *Coefficient of Structural Bonds* which allows to assess the impact of local exergy destruction in the condenser with respect to the overall exergy destruction. In [1.84], Dentice d'Accadia et al. carried out a thermoeconomic optimization of a conventional refrigeration plant. A simplified optimization based on the Theory of Exergetic Cost was used. The authors showed the capability of achieving a global optimal solution by locally optimizing the system, thus simplifying the optimization procedure. The results obtained showed acceptable accuracy when compared with those provided by a conventional and more complex optimization methods. In [1.85], Misra et al. optimized the design of a $LiBr/H_2O$ vapor absorption system fueled by pressurized hot water for air conditioning applications by means of the Theory of Exergy Cost. Some years later, a thermoeconomic optimization for a double effect $LiBr/H_2O$ vapor-absorption refrigeration system was carried out by the same authors [1.86]. Other interesting studies concerning Exergoeconomics of vapor compression system and cooling devices can be found here [1.87]–[1.89].

A great numbers of work have applied Exergoeconomic Analysis for comparing alternative and competitive technologies: for instance, in [1.90], Fiaschi et al. carried out an exergoeconomic analysis of Organic Rankine Cycle (ORC) and Kalina Cycle (KC), for generating power from low and medium temperature geothermal sources. The analysis allowed for selecting the technology characterized by the lowest electric power cost. In [1.91], an interesting comparative exergoeconomic evaluation of two commercial combined-cycle power plants was carried out. An iterative exergoeconomic optimization allowed for reducing the levelized cost of electricity. In [1.92], Hofmann et Tsatsaronis carried a comparative exergoeconomic assessment between a Binary Rankine cycle (based on water and potassium as working fluid) and a conventional steam cycle for coal-fired power plants. Results provided insights into exergy destructions and cost formation of electricity at a component-level. Similar and interesting studies can be found in the following [1.93]–[1.100].

Thermoeconomic analysis has be also carried out for the design of innovative combined power plants, as shown in [1.101]–[1.107], and of renewable fueled power plant as well [1.108]–[1.111].

Lots of paper have been published on Thermoeconomics for cogeneration and trigeneration systems. In [1.112], Guarinello et al. carried out cost accounting based on Theory of Exergetic Cost for a gas turbine-based cogeneration system for a district sited in Brazil. The production costs of electricity and steam were evaluated for two levels of electric power generation. In [1.113], a thermoeconomic cost accounting has been carried for a biogas engine-powered cogeneration system. Four different thermoeconomic methods were compared, the *Exergy Cost Theory*, the *Specific Exergy Cost*, The *Wonergy* and the *Modified Productive Structure Approach*) in order to highlight differences in results. Very different unit costs for the products were obtained.

Kim et al. [1.114] carried out an exergoeconomic cost accounting for a cogeneration system based on a 1000-kW gas turbine with a waste-heat boiler in this study. Results were used to analyze the operation of the system and to propose replacements in order to improve the overall performance. In [1.115], Yang et al. carried out an exergy and exergoeconomic analyses of a combined cooling, heating, and power (CCHP) system based on dual-fuel of biomass and natural gas. By means of preliminary exergy analysis the authors identified the main locations of exergy destruction. After that by means of the exergoeconomic analysis, they evaluated variation of products prices with the price of BG and biomass and also during the year.

Other works have been focused on the analysis and optimization of medium and small sizes of CHP and CHCP systems where the variable energy demands and the interaction with the electric grids highly influence the optimal design and operation of these systems. For instance, in [1.116], a thermoeconomic analysis of a trigeneration system was carried out to figure out the best operational strategy as a function of the demand for energy services and the prices of the resources consumed. In [1.117], Piacentino et al. thermoeconomic-aided algorithm for the integrated optimization of design and operation of energy systems was proposed. The algorithm relies on an analytical solution by the Lagrange multipliers method and on a multi-objective decision function, expressed either in terms of net cash flow or primary energy saving. The method is suitable for analyzing very complex systems where more units can participate for producing the same energy flows as CHCP systems connected to external grids. In order to show the capabilities of this method, the authors carried out this analysis for a grid connected trigeneration system to be installed in a large hotel. In [1.118], Diaz et al. proposed thermoeconomic model of a complex CHP and CCHP systems based on exergoeconomic and structural coefficients of internal bonds. The model was aimed at providing insights into the impact of each subsystem and control variables on the overall plant efficiency when considering variable energy demands.

In [1.119], Pina et al. focused on cost allocation in trigeneration systems including thermal energy storage (TES), for buildings of the residential-commercial sector. The paper addresses two issues not deeply studied in Thermoeconomics: (i) the joint production of energy services in dynamic energy systems; and (ii) the incorporation of TES. The authors proposed an innovative thermoeconomic model for accounting the inertial behavior of the storage. In [1.120], the same authors considered the exploitation of renewable energy sources within the same trigeneration system.

In [1.121], Picallo-Perez et al. carried out a symbolic exergoeconomic study of a retrofitted heating and DHW facility located in Bilbao. Results were used to evaluate exergy and exergoeconomic cost of heating and domestic hot water for the old and retrofitted cases. The analysis was supported by a dynamic simulation of the system. In [1.122], Symbolic Thermoeconomics has been rigorously applied for cost allocations for a system supplying heating and hot water to a building under variable load conditions.

Thermoeconomics has also been applied to the analysis of polygeneration systems. The cost formation process allows to identify for each product, which subsystems contributed most to the increase of their cost. In [1.123] an exergetic and exergoeconomic analysis of a renewable polygeneration system serving small isolated communities were carried out. In particular, the system includes a solar field based on parabolic trough photovoltaic/thermal collectors, a biomass heater, an absorption chiller and a Multiple Effect Distillation desalination unit. The polygeneration system was dynamically simulated by TRNSYS. Exergoeconomic analysis allowed to identify fluctuations on annual and seasonal basis. Also, it was shown that the unit cost of energy delivered to space heating uses is higher than that of energy for space cooling, due to the much lower irradiation levels observed during the winter period and the consequently higher incidence, per unit energy, of the capital investment. In [1.124], Leiva-Illanes et al. carried out an exergy cost analysis for solar multi-generation schemes for producing power, fresh water, cooling, and process heat. A concentrated

solar power as the prime mover, a multi-effect distillation plant, a refrigeration plant, and a process heat unit. A very large number of configurations for the proposed systems were investigated. The results of exergy cost analysis suggested: (i) the key equipment whose design should be improved in order to reduce the costs of products (for instance, solar collector, multi-effect distillation system, and other components) (ii) comparison among the different integration schemes. In [1.118], Calise et al. carried out an exergetic and exergoeconomic analyses of a novel solar–geothermal polygeneration system equipped with an Organic Rankine Cycle fueled by medium-enthalpy geothermal energy and by a Parabolic Trough Collector solar field. The system supplies electrical, thermal and cooling energy and freshwater for a small community, connected to a district heating and cooling network. Dynamic simulations were performed in order to design the system. The exergetic analysis allows to pinpoint how each subprocess affected the global exergy efficiency, thus suggesting possible system enhancements.

In [1.125], Verda et al. showed the capability of thermoeconomic analysis of providing criteria for cost assessment in district heating systems. The approach considered the effects of investment, operating costs and thermodynamic irreversibility on the cost formation of heat from its production in the plants to its use in the buildings. In [1.126] an exergoeconomic optimization of a district cooling network was carried out. The authors developed an exergoeconomic model of a district cooling network in order to optimize the diameters and insulation thicknesses. Another interesting study on exergoeconomic analysis of geothermal district heating systems can be found in [1.127].

Thermoeconomics has also been applied to the analysis of the performance of control system. For instance in [1.128], Verda and Borchiellini analyzed the performance of a gas-turbine control system when variations in the operating condition occur. Different control strategies were compared in order to quantify their effect on the performance of the component and on operating costs. An interesting

thermoeconomic analysis of an environmental-control system of an commercial aircraft was carried out in [1.129].

Thermoeconomics has been also extensively applied to the analysis of hydrogen production process [1.130]–[1.135] and to other chemical process as methanol and biodiesel production [1.136]–[1.138].

1.8 Thermoeconomic Cost Accounting: objectives and tools

It is possible to summarize the main objectives of any cost accounting procedure [1.139] as follows:

- determining the actual cost of products relying on a rational basis for cost apportioning;
- providing a means for controlling expenditures and for evaluating operating decisions.

First of all, the "cost of a product" is defined as the amount of resources (monetary, energetic, etc.) consumed to produce it along a given productive process. It follows that cost is not an intensive property (like temperature or pressure), but it is an "*emergent*" property, being strictly related to the productive process burdening its production [1.55]. Obviously, the more resources consumed, the higher the cost of the product. The objective of thermoeconomic cost accounting is to explain the cost formation process throughout the system from the energy resources to the final products, by assuming exergy as a *rational basis* for cost allocation [1.140].

In Thermoeconomics two kinds of cost can be adopted:

- the *exergoeconomic cost* which quantifies the monetary expenses sustained to produce an exergy flow and it accounts for operating costs (which are related to the exergy consumed for its production) and other costs as amortization, etc.

- the *exergetic cost* which represents the amount of external exergy resources consumed to obtain an exergy flow according to a selected energy conversion system [1.64].

Regardless the kind of cost adopted (i.e. exergoeconomic or exergetic), the thermoeconomic model of the system is composed by:

- *cost balances* for each unit in the system, where the sum of the costs of resources supplied equal the sum of the costs of products
- *auxiliary costing equations* aimed at defining the cost of external resources and providing information when more than one product result from a given unit.

As previously mentioned, according to the criteria adopted for defining Fuels, Products and auxiliary equations, different exergoeconomic cost accounting methods have been formulated during these years as the Exergy Cost Theory (ETC)[1.42] and the Specific Exergy Cost approach (SPECO) [1.61].

Before ending this section, it is worth mentioning that a further distinction on costs should be made when carrying out thermoeconomic analyses:

- *Average costs*: these costs are defined by dividing the resources consumed and the amount of product obtained. As a consequence, they are not predictive, since they are only known after the products have been obtained. Thermoeconomic cost accounting methods rely on the average cost concept.

- *Marginal Costs:* they quantify the variation in the resource consumption (both exergy and money) when a unit change in the production level occur. Marginal costs are predictive, and they are used in thermoeconomic optimization procedure.

1.8.1 Exergy Cost Theory

The first step in thermoeconomic analysis consists in the identification of the "*productive structure*" (or *functional diagram*) of the investigated system. In this scheme, the following information is provided for each component: (i) the amount of exergy consumed and the exergy products (ii) exergy exchanges among plant components according to their "*functional*" interaction.

The productive structure is developed starting from the physical scheme of the investigated system. However, it is worth stressing that each units of the physical scheme may not have a corresponding unit on the productive structure. For instance, for cost accounting purpose in HVAC systems, the evaporator coil and the fan of an air cooler could be treated as a unique component, which aims at cooling and dehumidifying an air stream by consuming electric power supplied to the fan and the refrigerant exergy. However, the deeper the disaggregation level adopted, the more insights into the cost formation process obtained. The productive structure is highly influenced by the expertise of the analysts thus, for a given process, multiple productive structures could be developed.

Once defined the productive structure of the system, the cost formation process of each product can be analyzed. In particular, analysts will be able to: (i) quantify how the inefficiencies of each subprocess affects the total exergy cost of each product, (ii) determine those subprocesses where the cost has a high increase, and (iii) verify the effect on the costs of improvements which may be realized in that points.

According to the productive model proposed for the "i-th" component, identified respectively by its Fuel F_i and its product P_i, the exergy balance in Equation (1.12) allows for quantifying the amount of irreversibility I_i generated (or exergy destroyed).

$$F_i - P_i = I_i \tag{1.12}$$

Also, the unit exergy consumption k_i can be calculated as Equation (1.13).

$$k_i = \frac{P_i}{F_i} \tag{1.13}$$

Looking at Figure 1.8, both the Fuel F_i and Product P_i of the "i-th" component can be further decomposed by considering interactions among other system components (Equations (1.13) and (1.14)).

$$P_i = B_{i0} + \sum_{j=1}^{N} B_{ij} \tag{1.14}$$

In Equation (1.14), B_{ij} is the portion of the "i-th" component product supplied as a fuel to the "j-th" component. B_{i0} is the part of the product P_i which is supplied to the external environment (the subscript "0" is used to indicate the outdoor environment).

$$F_i = B_{0i} + \sum_{j=1}^{N} B_{ji} \tag{1.15}$$

where B_{ji} is the portion of the "j-th" component product that fuels the "i-th" component. B_{0i} is the portion of the fuel of the "i-th" component supplied by the external environment.

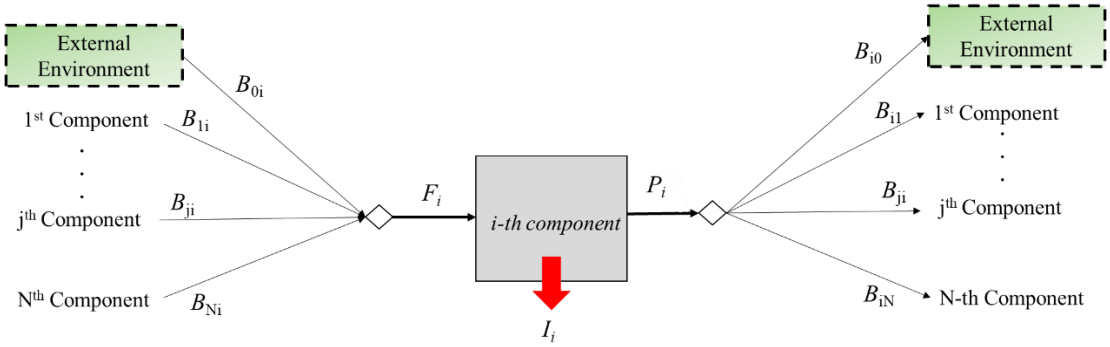

Figure 1.8 *Fuel-Product model for the "i-th" component*

Dividing both sides of Equation (1.15) for the product P_i, the exergy unit consumption of the "i-th" component can be decomposed as follow:

$$k_i = k_{0i} + \sum_{j=1}^{N} k_{ji} \tag{1.16}$$

The total fuel F_T and the total product P_T of the overall system can be calculated as shown in Equations (1.17) and (1.18).

$$F_T = \sum_{i=1}^{N} B_{0i} \tag{1.17}$$

$$P_T = \sum_{i=1}^{N} B_{i0} \tag{1.18}$$

In order to set cost equation for each component, four propositions were proposed for defining the thermoeconomic model and setting auxiliary equations in the Theory of Exergy Cost [1.42].

P1. The exergy cost of an energy/matter flow is the amount of exergy of external resources needed to produce it according to a given productive process. The exergy cost is *conservative* and for each unit, a cost conservation equation can be set (Eqs. 1.19)

$$F_i^* = P_i^* \tag{1.19}$$

As can be seen from Equation (1.19), the cost of the fuel F_i (i.e. F_i^*) is entirely charged on the product P_i. No cost is allocated on the irreversibility generated, since it is not a useful product. Also, if N units are identified in the investigated system, N cost equations can be set. An important indicator is the *unit exergy cost* of the product P_i defined in Equation (1.20)

$$k_{P,i}^* = \frac{P_i^*}{P_i} \tag{1.20}$$

Since no cost is allocated on the irreversibility generated in the process, the exergy unit of a product is greater than one.

P2. The exergy cost of the flows entering the system should be provided as an input data (*external assessment*). In absence of information, this is assumed equal to its exergy content (Equation (1.21)).

$$B_{0i}^{*} = B_{0i} \tag{1.21}$$

P3. If one or more outlet flows are considered as by-products, then their unit exergy cost is equal to the average unit exergy cost of the inlet flows

P4. If an output flow of a unit is a part of the fuel of the unit, then its unit exergy cost is the same as the input flow (*extraction method*). If a unit has more than one product, then the same unit exergetic cost will be assigned to all of them (*equality method*) (Equation (1.22)).

$$k_{ij}^{*} = k_{P,i}^{*} \tag{1.22}$$

Based on the **P1**-**P4** prepositions, the exergy cost of the fuel of the "i-th" component F_i^{*} can be formulated as follow:

$$F_i^{*} = B_{0i}^{*} + \sum_{j=1}^{N} B_{ji}^{*} \tag{1.23}$$

Since $B_{ji}^{*} = k_{P,j}^{*} B_{ji}$ and $F_i^{*} = P_i^{*}$, Equation (1.23) becomes:

$$P_i^{*} = B_{0i}^{*} + \sum_{j=1}^{N} k_{P,j}^{*} B_{ji} \tag{1.24}$$

Dividing both sides of the Equation (1.24) for the product P_i, it is possible to relate the unit exergy cost of the product $k_{P,i}^{*}$ with the unit exergy cost of the flows B_{ji} fueling the "i-th" component.

$$k^*_{P,i} = k^*_{0i} + \sum_{j=1}^{N} k^*_{P,j} \frac{B_{ji}}{P_i} = k^*_{0i} + \sum_{j=1}^{N} k^*_{P,j} k_{ji} \qquad (1.25)$$

The previous equation is defined for all N-components of the productive structure. This set of equations, along with external assessment for exergy flows supplied from the environment, constitutes a linear system which provides the unit exergy cost of each flow of the productive structures.

Before ending this section, some details on an alternative exergoeconomic method named Specific Exergy Costing (SPECO) [1.61] are here given. This approach aims at providing un unambiguous way for calculating fuel, product and auxiliary equations. In fact, the productive structure proposed for a given system may be susceptible of the expertise of the analysts (for instance, the disaggregation level adopted depend upon analyst's choices and expertise).

According to SPECO, fuels and products of each component are defined by systematically registering "additions to" and "removals from" each material/energy stream crossing the boundaries of the component (the so-called *F-rule* and *P-rule*). Exergy additions were considered as parts of Product, conversely, exergy removals were considered as parts of the Fuel. The component interacts by adding and removing exergy only through the mass and energy streams crossing its boundaries. As a consequence, the productive "function" of the component is independent of the presence of the other components in the system, and the interaction among systems components with the rest of the system remain the same as those in the "physical structure".

The first paper on SPECO [1.60] was based on the *Last In-First Out* accounting principle (LIFOA). In [1.61] the SPECO approach was extended to the calculation of average costs, and a computer code was developed to take an automatic record of all exergy additions and removals from mass and energy streams.

1.8.2 Overview on thermoeconomic approaches proposed for the analysis of "Dissipative Units"

In thermoeconomic analyses, Fuels and Products must be preliminary defined for each system component. To this regard, a critical aspect is represented by those components that lack of a clear "*productive scope*", which are essential for plant operation. These components are generally named "*dissipative units*" and they can be classified in three groups [1.2]:

- *Systems which exchange heat with the Environment:* the thermal exergy associated with such heat transfer is zero. Common examples are heat pump evaporators, refrigerator condensers, and cooling towers.
- *Systems aimed at accelerating otherwise spontaneous processes*, as drying plants and mechanical separation plant such as dust separators and moisture separators.
- *Devices which are dissipative by design*. These involve inherently irreversible processes such as throttling and stirring.

In these years, scientific literature has provided several allocation criteria for "*residues*" (i.e. for these exergy flows destroyed in dissipative components) but no unique indication on the best choice has been defined yet. Here only some of them are briefly described.

One approach, which is suitable for closed cycles such as Rankine cycles, allocates the cost of residues on other system components by means of "*negentropy*" [1.62]. Negentropy is defined as the negative of entropy multiplied by the temperature of the reference environment. In this case, the negentropy flow is considered the product of the dissipative component and its cost is allocated according to the entropy variations on other system components. This criterion has limitations when applied to open systems such as Brayton cycles [1.141].

Another approach proposed by Lazzaretto and Tsatsaronis allocates the cost of residues to the final product of the system under investigation [1.61]. In [1.142], a criterion based on combination of Thermoeconomics and cost-benefit analysis was used to allocate cost for those cases where wastes could be sold thus leading to revenue generation. A new approach proposed by Torres et al. in [1.143] allocates waste cost in system components proportionally to their contribution in the generation of the exergy that is finally destroyed in the dissipative component (i.e. identification of the process of formation of the cost of waste). This criterion is more objective since it is based on the productive structure proposed for the investigated system. In [1.144], the same authors based on the mathematical model proposed in [1.143] the authors suggested an improved definition of waste cost distribution ratios, which allocates waste cost proportionally to the cost of exergy flows which constitute the exergy flow dissipated. This improved approach was applied to a combined power plant and a cogeneration system.

1.9 Symbolic Exergoeconomics

Based on Exergy Cost Theory, *Symbolic Exergoeconomics* [1.145] was developed to generate formulas which relate the overall efficiency and other thermoeconomic variables (as fuel, product, exergy cost)of any energy system to the efficiency of each component of the investigated system.

Once identified the Fuels, Products and Residues for each component, two representations of the productive structure are proposed: the **FP** (*Fuel-Product*) and the **PF** (*Product-Fuel*) representation. In both of them, a matrix approach is used and a compact formulation of the thermoeconomic model of the system is obtained, which is easily solvable. However, both approaches are complementary and a complete picture of the productive process and cost formation is provided.

1.9.1 FP representation of the Productive Structure

In the **FP** (***Fuel-Product***) representation, Fuel and Product and costs are expressed as a function the exergy resources coming from the external environment. Here, the information flow has the direction of the productive process, i.e. from the fuels to products. This means that if the amount of external resources consumed is known, it is possible to evaluate the rest of the thermoeconomic variables and costs of each flows. The ***FP*** representation commonly supports cost accounting procedures.

As shown in Table 5.1, the vectors of Fuels **F**, Products **P**, Residue **R** and related costs, i.e. $\mathbf{F}^*$, $\mathbf{P}^*$ and $\mathbf{R}^*$ are expressed as a function of:

- the external exergy resources vector $\mathbf{F}_{e,}$ which collects the fuel of the "i-th" component $F_{e,i}$ supplied from the environment;
- the diagonal matrix $\mathbf{K}_D$, which contains the unit exergy consumption k_i of each component;
- the matrix of *distribution coefficients*: ⟨**FP**⟩ and ⟨**RP**⟩. The ⟨**FP**⟩ matrix contains the *product distribution ratios* y_{ij}. As shown in Equation (1.26), y_{ij} is the fraction of the product of the "j-th" component used as a fuel by the "i-th" component. The ⟨**RP**⟩ matrix contains the *residue distribution ratio* ψ_{ij} (Equation (1.27)) which is the fractions of the residue generated in "j-th" component which is allocated as an additional exergy resources to the "i-th" component. Both coefficients are derived from the inspection of the productive structure.

From Equation (1-29) to (1.32), Fuels, Products and Residues are shown as a function of the vector of external exergy resources $\mathbf{F}_{e,}$ by means of the distribution coefficients matrices. From Equation (1.33) to (1.35), cost equations are shown. This set of equations constitutes a system of linear equations which can be solved once known the unit exergy cost of external resources.

Table 1.1 *Main equations of the* ***FP*** *representation*

FP Representation

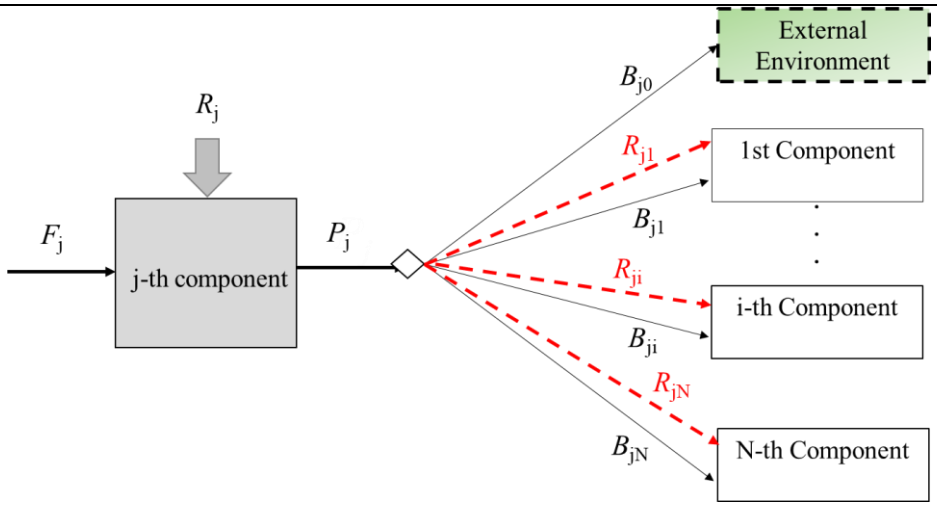

$y_{ij} = \frac{B_{ji}}{P_j}$		(1.26)
$\psi_{ij} = \frac{R_{ji}}{P_j}$		(1.27)
$\sum_{i=1}^{N}\left(y_{ij} + \psi_{ij}\right) = 1$		(1.28)
$\mathbf{P} = \langle \mathbf{P} \vert \mathbf{F}_e$	$\langle \mathbf{P} \vert = \left(\mathbf{K}_D - \langle \mathbf{FP} \rangle - \langle \mathbf{RP} \rangle\right)^{-1}$	(1.29)
$\mathbf{F} = \langle \mathbf{F} \vert \mathbf{F}_e$	$\langle \mathbf{F} \vert = \mathbf{K}_D \langle \mathbf{P} \vert$	(1.30)
$\mathbf{I} = \langle \mathbf{I} \vert \mathbf{F}_e$	$\langle \mathbf{I} \vert = \left(\mathbf{K}_D - \mathbf{U}_D\right) \langle \mathbf{P} \vert$	(1.31)
$\mathbf{R} = \langle \mathbf{R} \vert \mathbf{F}_e$	$\langle \mathbf{R} \vert = \langle \mathbf{RP} \rangle \left(\mathbf{K}_D - \langle \mathbf{FP} \rangle\right)^{-1}$	(1.32)
Cost Equations		
$\mathbf{P}^* = \langle \mathbf{P}^* \vert \mathbf{F}_e$	$\langle \mathbf{P}^* \vert = \left(\mathbf{U}_D - \langle \mathbf{FP} \rangle - \langle \mathbf{RP} \rangle\right)^{-1}$	(1.33)
$\mathbf{F}^* = \mathbf{F}_e + \langle \mathbf{FP} \rangle \mathbf{P}^* = \left(\mathbf{U}_D + \langle \mathbf{FP} \rangle \langle \mathbf{P}^* \vert\right) \mathbf{F}_e$		(1.34)
$\mathbf{R}^* = \langle \mathbf{RP} \rangle \mathbf{P}^* = \langle \mathbf{RP} \rangle \langle \mathbf{P}^* \vert \mathbf{F}_e$		(1.35)

In Equation (1.36), the final product P_T is shown. The vector $\boldsymbol{y}_0$ collects the y_{0i} value defined as the fraction of the product of the "i-th" component" supplied to the final users. Conversely, the total fuel consumption F_T can be calculated as shown in Equation (1.37), being $\boldsymbol{F}_e$ the vector of external exergy resources consumed by each component and ${}^T\mathbf{u}$ (1xn) vector of unit.

$$P_T = {}^t\mathbf{y}_0\mathbf{P} \tag{1.36}$$

$$F_T = {}^T\mathbf{u}\mathbf{F}_e \tag{1.37}$$

As shown in Equation (1.38), the exergy performance of the overall system ε_T is the ratio of the total exergy product P_T and total fuel consumption F_T. It is worth noting that the overall exergy performance is expressed as function of the distribution parameters contained inside the $\langle \mathbf{P} |$ matrix (defined in Equation (1.29)), and the vector of the external exergy resources $\boldsymbol{F}_e$.

$$\varepsilon_T = \frac{P_T}{F_T} = \frac{{}^t\mathbf{y}_0\mathbf{P}}{{}^T\mathbf{u}\mathbf{F}_e} = \frac{{}^t\mathbf{y}_0\langle \mathbf{P}|\mathbf{F}_e}{{}^T\mathbf{u}\mathbf{F}_e} \tag{1.38}$$

1.9.2 PF representation of the Productive Structure

The **PF** representation uses an equivalent logic structure of the **FP** representation, but the information flow has an opposite direction. In this case, if the plant product is known, it is possible to quantify the resources required for obtaining any internal product and its cost. For instance, the optimization and diagnosis analysis of a thermal system requires studying the behavior of the productive structure as a function of the total products. In these cases, the ***PF representation*** is more helpful. Thus, as shown in Table 1.2, the thermoeconomic variables of a system expressed as a function of:

- The final product vector $\mathbf{P}_s$ which contains the portion of the product of the i/th components supplied to external users;

- The unit exergy consumption of each component contained in the $\mathbf{K}_D$ matrix;
- The *recirculation coefficient* matrices ⟨**PF**⟩ and ⟨**PR**⟩ or the *technical coefficient matrices* ⟨**KP**⟩ and ⟨**KR**⟩.

The ⟨**PF**⟩ matrix collects the *junction coefficients* r_{ij}, which are defined as the fraction of the resources of the "j-th" component coming from the "i-th" component product (Eq. 1.39). The ⟨**PR**⟩ contains the ρ_{ij} coefficient, which are defined as the fraction of residue allocate on the "j-th" component which is generated by the "i-th" component (Eq. 1.40).

$$r_{ij} = \frac{B_{ij}}{F_j} \tag{1.39}$$

$$\rho_{ij} = \frac{R_{ij}}{R_j} \tag{1.40}$$

From the definition of the junction coefficients, it is easy to show that the vector of product **P** can be decomposed as follow:

$$\mathbf{P} = \mathbf{P}_s + \langle \mathbf{PF} \rangle \mathbf{F} + \langle \mathbf{PR} \rangle \mathbf{R} \tag{1.41}$$

An alternative representation of the product **P** relies on *technical coefficient*s κ_{ij} and θ_{ij} contained respectively in the ⟨**KP**⟩ and ⟨**KR**⟩ matrixes. The elements of the ⟨**KP**⟩ matrix, κ_{ij} are the defined by dividing the portion of the exergy flow produced by the "i-th" component and supplied as fuel to the "j-th" component to the product P_j as shown in Equation (1.42). The matrix ⟨**KR**⟩ collects the ratio θ_{ij}, which is defined as the ratio of the residue produced by the "i-th" component and allocated to the "j-th" component and the product of the "j-th" component Equation (1.43).

$$\kappa_{ij} = \frac{B_{ij}}{P_j} \tag{1.42}$$

$$\theta_{ij} = \frac{R_{ij}}{P_j} \tag{1.43}$$

From the definition of the technical coefficients, it is to show that the vector of product **P** can be decomposed as shown in Equation (1.44):

$$\mathbf{P} = \mathbf{P}_s + \langle \mathbf{KP} \rangle \mathbf{P} + \langle \mathbf{KR} \rangle \mathbf{P} \tag{1.44}$$

By introducing the vector $\boldsymbol{\kappa}_e$, which collect the values of κ_{0i} defined respectively as the of external exergy resource consumed by the "i-th" component per unit exergy of its product, the total fuel consumption F_T and the total plant product P_T can be calculated as follow:

$$F_T = {}^T\boldsymbol{\kappa}_e \left| \mathbf{P} \right\rangle \mathbf{P}_s \tag{1.45}$$

$$P_T = {}^t\mathbf{u}\mathbf{P}_s \tag{1.46}$$

In Equation (1.47) the unit exergy cost of the product P_i, $k^*_{P,i}$, is expressed as a function of: (i) the unit exergy cost of external resources consumed quantified by $\kappa^*_{0,i}$ and (ii) the unit exergy cost of fuel supplied by the "j-th" component and the residue generated by the "j-th" component and allocated on the "i-th" component, both quantified by $k^*_{P,j}$.

$$k^*_{P,i} = \kappa^*_{0,i} + \sum_{j=1}^{N} \left(\kappa_{ji} + \theta_{ji} \right) k^*_{P,j} \tag{1.47}$$

In Equation (1.48), the overall exergy performance ε_T is expressed as function of the technical coefficients κ_{ij} and θ_{ij} contained in the $\left| \mathbf{P} \right\rangle$ matrix (Equation (1.50)), and the vector of final product $\boldsymbol{P_s}$.

$$\varepsilon_T = \frac{P_T}{F_T} = \frac{{}^T\boldsymbol{\kappa}_e \left|\mathbf{P}\right\rangle \mathbf{P}_s}{{}^t\mathbf{u}\mathbf{P}_s} \tag{1.48}$$

.

Table 1.2 *Main equation of the* ***PF*** *representation*

PF Representation

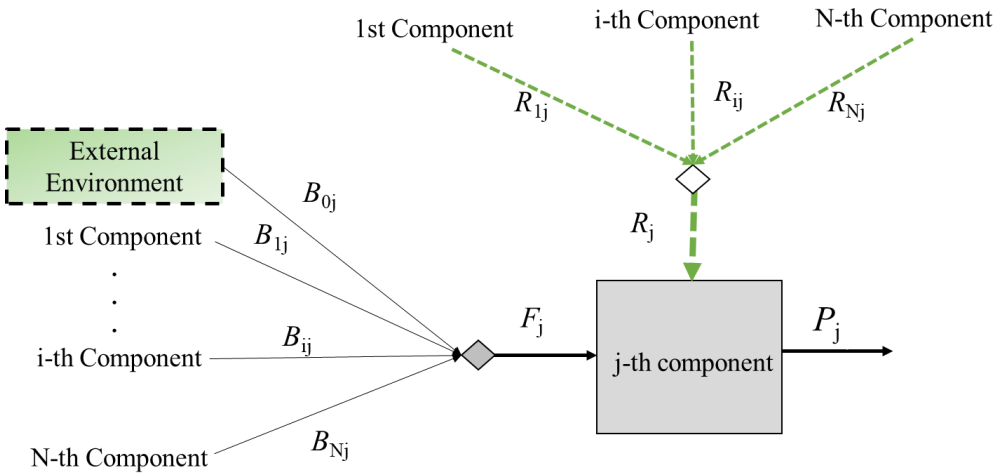

$$k_j = \sum_{\substack{i=1 \\ i \neq j}}^{N} \kappa_{ij} \tag{1.49}$$

$\mathbf{P} = \left\|\mathbf{P}\right\rangle \mathbf{P}_s$	$\left\|\mathbf{P}\right\rangle = \left(\mathbf{U}_D - \left\langle\mathbf{KP}\right\rangle - \left\langle\mathbf{KR}\right\rangle\right)^{-1}$	(1.50)
$\mathbf{F} = \left\|\mathbf{F}\right\rangle \mathbf{P}_s$	$\left\|\mathbf{F}\right\rangle = \mathbf{K}_D \left\|\mathbf{P}\right\rangle$	(1.51)
$\mathbf{I} = \left\|\mathbf{I}\right\rangle \mathbf{P}_s$	$\left\|\mathbf{I}\right\rangle = \left(\mathbf{K}_D - \mathbf{U}_D\right)\left\|\mathbf{P}\right\rangle$	(1.52)
$\mathbf{R} = \left\|\mathbf{R}\right\rangle \mathbf{P}_s$	$\left\|\mathbf{R}\right\rangle = \left\langle\mathbf{KR}\right\rangle \left\|\mathbf{P}\right\rangle$	(1.53)

Cost Equation

$$\mathbf{k}_P^* = \kappa_e + {}^t\left|\mathbf{P}\right\rangle \mathbf{k}_P^* \tag{1.54}$$

1.10 Exergoeconomic Costs

Another cost usually adopted in thermoeconomic analysis is the *exergoeconomic cost* C_i. It quantifies the monetary expenses sustained for obtaining the product P_i by considering not only the operating costs, but also the expenses for equipment purchase. The exergoeconomic cost referred to the exergy content of the product P_i (i.e. the *exergoeconomic unit cost*) is indicated as c_{Pi} (€/kWh$_{ex}$)

In order to calculate the exergoeconomic cost, cost equations have to be set for each component in the system. Considering the "i-th" plant component presented in Figure 1.9, cost equations for its fuel and its product are written as follow:

$$C_{P,i} = C_{F,i} + C_{R,i} + Z_i \tag{1.55}$$

$$C_{F,i} = C_{i,0} + \sum_{j=1}^{N} C_{ji} \tag{1.56}$$

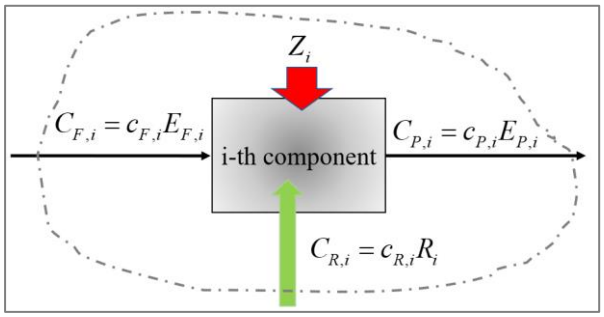

Figure 1.9 *Exergoeconomic Cost equation for the "i-th" component*

In Equation (1.55), the exergoeconomic cost of the product P_i, $C_{P,i}$, is imposed equal to the sum of the costs of fuels, $C_{F,i}$, allocated residues, $C_{R,i}$, and to the capital investment Z_i. Once introduced a notation C_{ji} for the cost of the product of the "j-th" component consumed by the "i-th" component, in Equation (1.56) the total cost of the fuel is trivially broken down into the cost $C_{i,0}$ of the "external" fuel coming from the surrounding environment (assumed as a virtual "component 0", where the physical

plant components are numbered from 1 to N) and the cost of the products of other components (j≠i) which are consumed by the "i-th" component.

As previously shown, *Symbolic Exergoeconomic* provides a compact formulation of the FPR model, based on the definition of "cost distribution ratios" of products and residues, i.e. y_{ij} and ψ_{ij} defined in Table 1.1. Then, the exergoeconomic cost of fuels and residues can be written as follows:

$$C_{F,i} = \sum_{j=1}^{N} y_{ij} \cdot C_{P,j} + C_{i,0} \tag{1.57}$$

$$C_{R,i} = \sum_{j=1}^{N} \psi_{ij} \cdot C_{P,j} \tag{1.58}$$

Combining Equations (1.55), (1.57) and (1.58), the cost balance equation of the "i-th" component can be rearranged as:

$$C_{P,i} - \sum_{j=1, j\neq i}^{N} y_{ij} \cdot C_{P,j} - \sum_{j=1, j\neq i}^{N} \psi_{ij} \cdot C_{P,j} = C_{i,0} + Z_i \tag{1.59}$$

where the product costs $C_{P,i}$ are the only unknown variables. Eq. (1.58) can be written using the **FP** matrix notation as:

$$(\boldsymbol{U}_D - \langle \boldsymbol{FP} \rangle - \langle \boldsymbol{RP} \rangle) \cdot \boldsymbol{C}_P = \boldsymbol{C}_e + \boldsymbol{Z} \tag{1.60}$$

In Equation (1.60) $\boldsymbol{C_P}$, $\boldsymbol{C_e}$ and $\boldsymbol{Z}$ are "N×1" vectors which respectively represent the costs of component products, external fuels and capital investments. The $\langle \boldsymbol{FP} \rangle$ and $\langle \boldsymbol{RP} \rangle$ matrices respectively contain the distribution factors y_{ij} and ψ_{ij}, while the elements of the vectors $\boldsymbol{C_e}$ and $\boldsymbol{Z}$ are respectively the cost of fuels coming from the external environment and the purchase cost of plant components. Equation (1.61) constitutes a set of linear equations, which can be easily solved. For systems operating

in steady state, $\boldsymbol{C_P}$, $\boldsymbol{C_e}$ and $\boldsymbol{Z}$ could be replaced with cost flow vectors, indicated respectively as $\boldsymbol{\dot{C}_P}$, $\boldsymbol{\dot{C}_e}$ and $\boldsymbol{\dot{Z}}$, which are measured in €/h.

References

[1.1] E. Sciubba and G. Wall, "A brief commented history of exergy from the beginnings to 2004," *Int. J. Thermodyn.*, vol. 10, no. 1, pp. 1–26, 2007.

[1.2] T. J. Kotas, *The exergy method of thermal plant analysis*, vol. 20. Butterworths, 1985.

[1.3] P. Szargut, J. (Silesian University of Technology, *Exergy Method: Technical and Ecological Applications*. WITPRESS, 2005.

[1.4] G. Tsatsaronis, "Thermoeconomic analysis and optimization of energy systems," *Prog. Energy Combust. Sci.*, vol. 19, no. 3, pp. 227–257, Jan. 1993.

[1.5] J. Szargut, A. Ziębik, and W. Stanek, "Depletion of the non-renewable natural exergy resources as a measure of the ecological cost," *Energy Convers. Manag.*, vol. 43, no. 9–12, pp. 1149–1163, Jun. 2002.

[1.6] M. A. Rosen, "Energy crisis or exergy crisis?," *Exergy, An Int. J.*, vol. 2, no. 3, pp. 125–127, Jan. 2002.

[1.7] M. V. Rocco, "Exergy based Input-Output analysis," in *Primary Exergy Cost of Goods and Services: An Input -- Output Approach*, Cham: Springer International Publishing, 2016, pp. 61–90.

[1.8] I. Dincer and M. A. Rosen, *Exergy Energy, Environment and Sustainable Development*, Second. Elsevier Science, 2012.

[1.9] L. Connelly and C. P. Koshland, "Two aspects of consumption: using an exergy-based measure of degradation to advance the theory and implementation of industrial ecology," *Resour. Conserv. Recycl.*, vol. 19, no. 3, pp. 199–217, Mar. 1997.

[1.10] Z. Rant, "Exergie and Anergie." Wissenschaftliche Zeitschrift der TU Dresden, pp. 1145–1149, 1964.

[1.11] A. Bejan, *Advanced Engineering Thermodynamics*, Fourth Edi. WILEY, 2016.

[1.12] G. Tsatsaronis and M. Winhold, "Exergoeconomic analysis and evaluation of energy-conversion plants—I. A new general methodology," *Energy*, vol. 10, no. 1, pp. 69–80, Jan. 1985.

[1.13] R. L. Cornelissen and G. G. Hirs, "Exergy analysis of cryogenic air separation," *Energy Convers. Manag.*, vol. 39, no. 16–18, pp. 1821–1826, Nov. 1998.

[1.14] S. Mokhatab, J. Y. Mak, J. V Valappil, and D. A. Wood, Eds., "Chapter 4 - Energy and Exergy Analyses of Natural Gas Liquefaction Cycles," in *Handbook of Liquefied Natural Gas*, Boston: Gulf Professional Publishing, 2014, pp. 185–228.

[1.15] H. Al-Muslim and I. Dincer, "Thermodynamic analysis of crude oil distillation systems," *Int. J. Energy Res.*, vol. 29, no. 7, pp. 637–655.

[1.16] L. Marletta, Marletta, and Luigi, "Air Conditioning Systems from a 2nd Law Perspective," *Entropy*, vol. 12, no. 4, pp. 859–877, Apr. 2010.

[1.17] A. Hepbasli, "Low exergy (LowEx) heating and cooling systems for sustainable buildings and societies," *Renew. Sustain. Energy Rev.*, vol. 16, no. 1, pp. 73–104, Jan. 2012.

[1.18] V. G. Gude, "Exergy Evaluation of Desalination Processes," *ChemEngineering*, vol. 2, no. 2, 2018.

[1.19] K. S. Spiegler and Y. M. El-Sayed, "The energetics of desalination processes," *Desalination*, vol. 134, no. 1–3, pp. 109–128, Apr. 2001.

[1.20] R. Semiat, "Energy Issues in Desalination Processes," *Environ. Sci. Technol.*, vol. 42,

no. 22, pp. 8193–8201, Nov. 2008.
[1.21] A. A. Mabrouk, A. S. Nafey, and H. E. S. Fath, "Thermoeconomic analysis of some existing desalination processes," *Desalination,* vol. 205, no. 1–3, pp. 354–373, Feb. 2007.
[1.22] Y. Cerci, "Exergy analysis of a reverse osmosis desalination plant in California," *Desalination*, vol. 142, no. 3, pp. 257–266, Mar. 2002.
[1.23] N. Kahraman and Y. A. Cengel, "Exergy analysis of a MSF distillation plant," *Energy Convers. Manag.*, vol. 46, no. 15–16, pp. 2625–2636, Sep. 2005.
[1.24] A. S. Nafey, H. E. S. Fath, and A. A. Mabrouk, "Exergy and thermoeconomic evaluation of MSF process using a new visual package," *Desalination,* vol. 201, no. 1–3, pp. 224–240, Nov. 2006.
[1.25] A. Piacentino, "Application of advanced thermodynamics, thermoeconomics and exergy costing to a Multiple Effect Distillation plant: In-depth analysis of cost formation process," *Desalination*, vol. 371, pp. 88–103, Sep. 2015.
[1.26] N. Kahraman, Y. A. Cengel, B. Wood, and Y. Cerci, "Exergy analysis of a combined RO, NF, andEDR desalination plant," *Desalination,* vol. 171, no. 3, pp. 217–232, Jan. 2005.
[1.27] A. C. Caetano de Souza, J. Luz-Silveira, and M. I. Sosa, "Physical-Chemical and Thermodynamic Analyses of Ethanol Steam Reforming for Hydrogen Production," *J. Fuel Cell Sci. Technol.*, vol. 3, no. 3, pp. 346–350, Jan. 2006.
[1.28] A. Ziębik and W. Stanek, "Energy and exergy system analysis of thermal improvements of blast-furnace plants," *Int. J. Energy Res.*, vol. 30, no. 2, pp. 101–114, Jun. 2005.
[1.29] C. D. Rakopoulos and E. G. Giakoumis, "Second-law analyses applied to internal combustion engines operation," *Prog. Energy Combust. Sci.*, vol. 32, no. 1, pp. 2–47, Jan. 2006.
[1.30] R. Rivero, "Application of the exergy concept in the petroleum refining and petrochemical industry," *Energy Convers. Manag.*, vol. 43, no. 9–12, pp. 1199–1220, Jun. 2002.
[1.31] K. J. Ptasinski, C. Hamelinck, and P. J. A. M. Kerkhof, "Exergy analysis of methanol from the sewage sludge process," *Energy Convers. Manag.*, vol. 43, no. 9–12, pp. 1445–1457, Jun. 2002.
[1.32] K. Okazaki, T. Kishida, K. Ogawa, and T. Nozaki, "Direct conversion from methane to methanol for high efficiency energy system with exergy regeneration," *Energy Convers. Manag.*, vol. 43, no. 9–12, pp. 1459–1468, Jun. 2002.
[1.33] M. Gong, "Exergy analysis of a pulp and paper mill," *Int. J. Energy Res.*, vol. 29, no. 1, pp. 79–93, Dec. 2004.
[1.34] D. R. Morris and F. R. Steward, "Exergy analysis of a chemical metallurgical process," *Metall. Trans. B*, vol. 15, no. 4, pp. 645–654, 1984.
[1.35] T. K. Ibrahim *et al.*, "A comprehensive review on the exergy analysis of combined cycle power plants," *Renew. Sustain. Energy Rev.*, vol. 90, pp. 835–850, Jul. 2018.
[1.36] A. Hepbasli, "A key review on exergetic analysis and assessment of renewable energy resources for a sustainable future," *Renew. Sustain. Energy Rev.*, vol. 12, no. 3, pp. 593–661, Apr. 2008.
[1.37] F. Bayrak, N. Abu-Hamdeh, K. A. Alnefaie, and H. F. Öztop, "A review on exergy analysis of solar electricity production," *Renew. Sustain. Energy Rev.*, vol. 74, pp. 755–

770, Jul. 2017.
[1.38] S. A. Kalogirou, S. Karellas, V. Badescu, and K. Braimakis, "Exergy analysis on solar thermal systems: A better understanding of their sustainability," *Renew. Energy*, vol. 85, pp. 1328–1333, Jan. 2016.
[1.39] R. Saidur, G. BoroumandJazi, S. Mekhilef, and H. A. Mohammed, "A review on exergy analysis of biomass based fuels," *Renew. Sustain. Energy Rev.*, vol. 16, no. 2, pp. 1217–1222, Feb. 2012.
[1.40] X. Feng and X. X. Zhu, "Combining pinch and exergy analysis for process modifications," *Appl. Therm. Eng.*, vol. 17, no. 3, pp. 249–261, Mar. 1997.
[1.41] G. Tsatsaronis, "Strengths and Limitations of Exergy Analysis," in *Thermodynamic Optimization of Complex Energy Systems*, A. Bejan and E. Mamut, Eds. Dordrecht: Springer Netherlands, 1999, pp. 93–100.
[1.42] M. A. Lozano and A. Valero, "Theory of the exergetic cost," *Energy*, vol. 18, no. 9, pp. 939–960, Sep. 1993.
[1.43] G. Tsatsaronis and M.-H. Park, "On avoidable and unavoidable exergy destructions and investment costs in thermal systems," *Energy Convers. Manag.*, vol. 43, no. 9–12, pp. 1259–1270, Jun. 2002.
[1.44] S. Kelly, G. Tsatsaronis, and T. Morosuk, "Advanced exergetic analysis: Approaches for splitting the exergy destruction into endogenous and exogenous parts," *Energy*, vol. 34, no. 3, pp. 384–391, Mar. 2009.
[1.45] T. Morosuk and G. Tsatsaronis, "Strengths and Limitations of Advanced Exergetic Analyses," no. 56291. p. V06BT07A026, 2013.
[1.46] G. T. T. Morosuk, "Advanced exergy analysis for chemically reacting systems – application to a simple open gas-turbine system," *Int. J. Thermodyn.*, vol. 12, no. 3, pp. 105–111, 2009.
[1.47] G. Tsatsaronis and T. Morosuk, "Advanced Exergoeconomic Evaluation and Its Application to Compression Refrigeration Machines," no. 43009. pp. 859–868, 2007.
[1.48] G. Tsatsaronis and T. Morosuk, "A General Exergy-Based Method for Combining a Cost Analysis With an Environmental Impact Analysis: Part I — Theoretical Development," no. 48692. pp. 453–462, 2008.
[1.49] T. Morosuk and G. Tsatsaronis, "Advanced exergetic evaluation of refrigeration machines using different working fluids," *Energy*, vol. 34, no. 12, pp. 2248–2258, Dec. 2009.
[1.50] Z. Wei, B. Zhang, S. Wu, Q. Chen, and G. Tsatsaronis, "Energy-use analysis and evaluation of distillation systems through avoidable exergy destruction and investment costs," *Energy*, vol. 42, no. 1, pp. 424–433, Jun. 2012.
[1.51] M. Mehdizadeh-Fard, F. Pourfayaz, M. Mehrpooya, and A. Kasaeian, "Improving energy efficiency in a complex natural gas refinery using combined pinch and advanced exergy analyses," *Appl. Therm. Eng.*, vol. 137, pp. 341–355, Jun. 2018.
[1.52] A. Hepbasli and A. Keçebaş, "A comparative study on conventional and advanced exergetic analyses of geothermal district heating systems based on actual operational data," *Energy Build.*, vol. 61, pp. 193–201, Jun. 2013.
[1.53] Z. Erbay and A. Hepbasli, "Application of conventional and advanced exergy analyses to evaluate the performance of a ground-source heat pump (GSHP) dryer used in food drying," *Energy Convers. Manag.*, vol. 78, pp. 499–507, Feb. 2014.
[1.54] E. Açıkkalp, H. Aras, and A. Hepbasli, "Advanced exergoeconomic analysis of an

electricity-generating facility that operates with natural gas," *Energy Convers. Manag.*, vol. 78, pp. 452–460, Feb. 2014.
[1.55] A. Valero, "THE THERMODYNAMIC PROCESS OF COST FORMATION," in *EXERGY, ENERGY SYSTEM ANALYSIS AND OPTIMIZATION*, C. A. Frangopoulos, Ed. Encyclopedia Life Support Systems, 2009.
[1.56] J. H. Keenan, "A Steam Chart for Second Law Analysis," *Mech. Eng.*, vol. 54, pp. 195–204, 1932.
[1.57] R. A. Gaggioli and W. J. Wepfer, "Exergy economics: I. Cost accounting applications," *Energy*, vol. 5, no. 8–9, pp. 823–837, Aug. 1980.
[1.58] R. B. Evans and M. Tribus, "Thermo-Economics of Saline Water Conversion," *Ind. Eng. Chem. Process Des. Dev.*, vol. 4, no. 2, pp. 195–206, Apr. 1965.
[1.59] Y. M. El-Sayed and R. B. Evans, "Thermoeconomics and the Design of Heat Systems," *J. Eng. Power*, vol. 92, no. 1, pp. 27–35, Jan. 1970.
[1.60] G. Tsatsaronis, L. Lin, and J. Pisa, "Exergy Costing in Exergoeconomics," *J. Energy Resour. Technol.*, vol. 115, no. 1, pp. 9–16, Mar. 1993.
[1.61] A. Lazzaretto and G. Tsatsaronis, "SPECO: A systematic and general methodology for calculating efficiencies and costs in thermal systems," *Energy*, vol. 31, no. 8–9, pp. 1257–1289, Jul. 2006.
[1.62] C. A. Frangopoulos, "Thermo-economic functional analysis and optimization," *Energy*, vol. 12, no. 7, pp. 563–571, Jul. 1987.
[1.63] M. R. von Spakovsky, "Application of engineering functional analysis to the analysis and optimization of the CGAM problem," *Energy*, vol. 19, no. 3, pp. 343–364, Mar. 1994.
[1.64] A. Valero, M. A. Lozano, and M. Munoz, "No A general theory of exergy saving I. On the exergetic cost," pp. 1–8.
[1.65] A. Valero *et al.*, "CGAM problem: Definition and conventional solution," *Energy*, vol. 19, no. 3, pp. 279–286, Mar. 1994.
[1.66] A. Valero, M. A. Lozano, L. Serra, and C. Torres, "Application of the exergetic cost theory to the CGAM problem," *Energy*, vol. 19, no. 3, pp. 365–381, Mar. 1994.
[1.67] C. A. Frangopoulos, "Application of the thermoeconomic functional approach to the CGAM problem," *Energy*, vol. 19, no. 3, pp. 323–342, Mar. 1994.
[1.68] G. Tsatsaronis and J. Pisa, "Exergoeconomic evaluation and optimization of energy systems — application to the CGAM problem," *Energy*, vol. 19, no. 3, pp. 287–321, Mar. 1994.
[1.69] C. Torres, A. Valero, L. Serra, and J. Royo, "Structural theory and thermoeconomic diagnosis: Part I. On malfunction and dysfunction analysis," *Energy Convers. Manag.*, vol. 43, no. 9–12, pp. 1503–1518, Jun. 2002.
[1.70] A. Valero, F. Lerch, L. Serra, and J. Royo, "Structural theory and thermoeconomic diagnosis: Part II: Application to an actual power plant," *Energy Convers. Manag.*, vol. 43, no. 9–12, pp. 1519–1535, Jun. 2002.
[1.71] B. Erlach, L. Serra, and A. Valero, "Structural theory as standard for thermoeconomics," *Energy Convers. Manag.*, vol. 40, no. 15–16, pp. 1627–1649, Oct. 1999.
[1.72] T. D. Čož, A. Kitanovski, and A. Poredoš, "Exergoeconomic optimization of a district cooling network," *Energy*, vol. 135, pp. 342–351, Sep. 2017.
[1.73] H. Sayyaadi and A. Saffari, "Thermoeconomic optimization of multi effect distillation

desalination systems," *Appl. Energy*, vol. 87, no. 4, pp. 1122–1133, Apr. 2010.
[1.74] M. L. Elsayed, O. Mesalhy, R. H. Mohammed, and L. C. Chow, "Exergy and thermo-economic analysis for MED-TVC desalination systems," *Desalination*, vol. 447, pp. 29–42, Dec. 2018.
[1.75] M. A. Jamil, B. A. Qureshi, and S. M. Zubair, "Exergo-economic analysis of a seawater reverse osmosis desalination plant with various retrofit options," *Desalination*, vol. 401, pp. 88–98, Jan. 2017.
[1.76] J. Uche, L. Serra, and A. Valero, "Thermoeconomic optimization of a dual-purpose power and desalination plant," *Desalination*, vol. 136, no. 1–3, pp. 147–158, May 2001.
[1.77] K. Ansari, H. Sayyaadi, and M. Amidpour, "Thermoeconomic optimization of a hybrid pressurized water reactor (PWR) power plant coupled to a multi effect distillation desalination system with thermo-vapor compressor (MED-TVC)," *Energy*, vol. 35, no. 5, pp. 1981–1996, May 2010.
[1.78] M. H. Khoshgoftar Manesh and M. Amidpour, "Multi-objective thermoeconomic optimization of coupling MSF desalination with PWR nuclear power plant through evolutionary algorithms," *Desalination*, vol. 249, no. 3, pp. 1332–1344, Dec. 2009.
[1.79] J. Wellmann and B. Meyer-Kahlen, "Exergoeconomic evaluation of a CSP plant in combination with a desalination unit," *Renew. Energy*, vol. 128, pp. 586–602, Dec. 2018.
[1.80] D. B. Singh and G. N. Tiwari, "Exergoeconomic, enviroeconomic and productivity analyses of basin type solar stills by incorporating N identical PVT compound parabolic concentrator collectors: A comparative study," *Energy Convers. Manag.*, vol. 135, pp. 129–147, Mar. 2017.
[1.81] A. G. M. Ibrahim, A. M. Rashad, and I. Dincer, "Exergoeconomic analysis for cost optimization of a solar distillation system," *Sol. Energy*, vol. 151, pp. 22–32, Jul. 2017.
[1.82] G. Wall, "Thermoeconomic optimization of a heat pump system," *Energy*, vol. 11, no. 10, pp. 957–967, Oct. 1986.
[1.83] M. Dentice d'Accadia, A. Fichera, M. Sasso, and M. Vidiri, "Determining the optimal configuration of a heat exchanger (with a two-phase refrigerant) using exergoeconomics," *Appl. Energy*, vol. 71, no. 3, pp. 191–203, Mar. 2002.
[1.84] A. Achilli *et al.*, "List of contributors," in *Sustainable Energy from Salinity Gradients*, 2016, pp. ix–x.
[1.85] R. D. Misra, P. K. Sahoo, and A. Gupta, "Application of the exergetic cost theory to the LiBr/H2O vapour absorption system," *Energy*, vol. 27, no. 11, pp. 1009–1025, Nov. 2002.
[1.86] R. D. Misra, P. K. Sahoo, and A. Gupta, "Thermoeconomic evaluation and optimization of a double-effect H2O/LiBr vapour-absorption refrigeration system," *Int. J. Refrig.*, vol. 28, no. 3, pp. 331–343, May 2005.
[1.87] A. Piacentino and E. Cardona, "Scope Oriented Thermoeconomic analysis of energy systems. Part II: Formation Structure of Optimality for robust design," *Appl. Energy*, vol. 87, no. 3, pp. 957–970, Mar. 2010.
[1.88] E. Hürdoğan, O. Büyükalaca, M. Tolga Balta, A. Hepbasli, and T. Yılmaz, "Experimental exergoeconomic assessment of a desiccant cooling system," *Energy Convers. Manag.*, vol. 69, pp. 9–16, May 2013.
[1.89] A. Piacentino and F. Cardona, "Scope-Oriented Thermoeconomic analysis of energy

systems. Part I: Looking for a non-postulated cost accounting for the dissipative devices of a vapour compression chiller. Is it feasible?," *Appl. Energy*, vol. 87, no. 3, pp. 943–956, Mar. 2010.

[1.90] D. Fiaschi, G. Manfrida, E. Rogai, and L. Talluri, "Exergoeconomic analysis and comparison between ORC and Kalina cycles to exploit low and medium-high temperature heat from two different geothermal sites," *Energy Convers. Manag.*, vol. 154, pp. 503–516, Dec. 2017.

[1.91] T. Blumberg, M. Assar, T. Morosuk, and G. Tsatsaronis, "Comparative exergoeconomic evaluation of the latest generation of combined-cycle power plants," *Energy Convers. Manag.*, vol. 153, pp. 616–626, Dec. 2017.

[1.92] M. Hofmann and G. Tsatsaronis, "Comparative exergoeconomic assessment of coal-fired power plants – Binary Rankine cycle versus conventional steam cycle," *Energy*, vol. 142, pp. 168–179, Jan. 2018.

[1.93] V. Zare, "A comparative exergoeconomic analysis of different ORC configurations for binary geothermal power plants," *Energy Convers. Manag.*, vol. 105, pp. 127–138, Nov. 2015.

[1.94] M. K. Sahu and Sanjay, "Comparative exergoeconomics of power utilities: Air-cooled gas turbine cycle and combined cycle configurations," *Energy*, vol. 139, pp. 42–51, Nov. 2017.

[1.95] A. Nemati, H. Nami, and M. Yari, "Assessment of different configurations of solar energy driven organic flash cycles (OFCs) via exergy and exergoeconomic methodologies," *Renew. Energy*, vol. 115, pp. 1231–1248, Jan. 2018.

[1.96] H. Athari, S. Soltani, A. Bölükbaşi, M. A. Rosen, and T. Morosuk, "Comparative exergoeconomic analyses of the integration of biomass gasification and a gas turbine power plant with and without fogging inlet cooling," *Renew. Energy*, vol. 76, pp. 394–400, Apr. 2015.

[1.97] S. Wang, C. Wu, and J. Li, "Exergoeconomic analysis and optimization of single-pressure single-stage and multi-stage CO2 transcritical power cycles for engine waste heat recovery: A comparative study," *Energy*, vol. 142, pp. 559–577, Jan. 2018.

[1.98] F. Mohammadkhani, F. Ranjbar, and M. Yari, "A comparative study on the ammonia–water based bottoming power cycles: The exergoeconomic viewpoint," *Energy*, vol. 87, pp. 425–434, Jul. 2015.

[1.99] S. Soltani, S. M. S. Mahmoudi, M. Yari, T. Morosuk, M. A. Rosen, and V. Zare, "A comparative exergoeconomic analysis of two biomass and co-firing combined power plants," *Energy Convers. Manag.*, vol. 76, pp. 83–91, Dec. 2013.

[1.100] F. A. Boyaghchi and S. Asgari, "A comparative study on exergetic, exergoeconomic and exergoenvironmental assessments of two internal auto-cascade refrigeration cycles," *Appl. Therm. Eng.*, vol. 122, pp. 723–737, Jul. 2017.

[1.101] F. Petrakopoulou, A. Boyano, M. Cabrera, and G. Tsatsaronis, "Exergoeconomic and exergoenvironmental analyses of a combined cycle power plant with chemical looping technology," *Int. J. Greenh. Gas Control*, vol. 5, no. 3, pp. 475–482, May 2011.

[1.102] F. Mohammadkhani, N. Shokati, S. M. S. Mahmoudi, M. Yari, and M. A. Rosen, "Exergoeconomic assessment and parametric study of a Gas Turbine-Modular Helium Reactor combined with two Organic Rankine Cycles," *Energy*, vol. 65, pp. 533–543, Feb. 2014.

[1.103] G. Bonforte, J. Buchgeister, G. Manfrida, and K. Petela, "Exergoeconomic and

exergoenvironmental analysis of an integrated solar gas turbine/combined cycle power plant," *Energy*, vol. 156, pp. 352–359, Aug. 2018.
[1.104] C. Wu, S. Wang, and J. Li, "Exergoeconomic analysis and optimization of a combined supercritical carbon dioxide recompression Brayton/organic flash cycle for nuclear power plants," *Energy Convers. Manag.*, vol. 171, pp. 936–952, Sep. 2018.
[1.105] S. Katulić, M. Čehil, and D. R. Schneider, "Exergoeconomic optimization of a combined cycle power plant's bottoming cycle using organic working fluids," *Energy Convers. Manag.*, vol. 171, pp. 1721–1736, Sep. 2018.
[1.106] S. M. Seyyedi, M. Hashemi-Tilehnoee, and M. A. Rosen, "Exergy and exergoeconomic analyses of a novel integration of a 1000 MW pressurized water reactor power plant and a gas turbine cycle through a superheater," *Ann. Nucl. Energy*, vol. 115, pp. 161–172, May 2018.
[1.107] H. Ghaebi, T. Parikhani, and H. Rostamzadeh, "Energy, exergy and thermoeconomic analysis of a novel combined cooling and power system using low-temperature heat source and LNG cold energy recovery," *Energy Convers. Manag.*, vol. 150, pp. 678–692, Oct. 2017.
[1.108] S. Anvari, S. Khalilarya, and V. Zare, "Exergoeconomic and environmental analysis of a novel configuration of solar-biomass hybrid power generation system," *Energy*, vol. 165, pp. 776–789, Dec. 2018.
[1.109] E. J. C. Cavalcanti and H. P. Motta, "Exergoeconomic analysis of a solar-powered/fuel assisted Rankine cycle for power generation," *Energy*, vol. 88, pp. 555–562, Aug. 2015.
[1.110] J. Gómez-Hernández, P. A. González-Gómez, J. V. Briongos, and D. Santana, "Influence of the steam generator on the exergetic and exergoeconomic analysis of solar tower plants," *Energy*, vol. 145, pp. 313–328, Feb. 2018.
[1.111] J.-Y. Jung, H. S. Lee, H.-J. Kim, Y. Yoo, W.-Y. Choi, and H.-Y. Kwak, "Thermoeconomic analysis of an ocean thermal energy conversion plant," *Renew. Energy*, vol. 86, pp. 1086–1094, Feb. 2016.
[1.112] F. Guarinello, S. A. A. G. Cerqueira, and S. A. Nebra, "Thermoeconomic evaluation of a gas turbine cogeneration system," *Energy Convers. Manag.*, vol. 41, no. 11, pp. 1191–1200, Jul. 2000.
[1.113] D. Haydargil and A. Abuşoğlu, "A comparative thermoeconomic cost accounting analysis and evaluation of biogas engine-powered cogeneration," *Energy*, vol. 159, pp. 97–114, Sep. 2018.
[1.114] S.-M. Kim, S.-D. Oh†, Y.-H. Kwon, and H.-Y. Kwak, "Exergoeconomic analysis of thermal systems," *Energy*, vol. 23, no. 5, pp. 393–406, May 1998.
[1.115] K. Yang, N. Zhu, Y. Ding, C. Chang, D. Wang, and T. Yuan, "Exergy and exergoeconomic analyses of a combined cooling, heating, and power (CCHP) system based on dual-fuel of biomass and natural gas," *J. Clean. Prod.*, vol. 206, pp. 893–906, Jan. 2019.
[1.116] M. A. Lozano, M. Carvalho, and L. M. Serra, "Operational strategy and marginal costs in simple trigeneration systems," *Energy*, vol. 34, no. 11, pp. 2001–2008, Nov. 2009.
[1.117] A. Piacentino and F. Cardona, "On thermoeconomics of energy systems at variable load conditions: Integrated optimization of plant design and operation," *Energy Convers. Manag.*, vol. 48, no. 8, pp. 2341–2355, Aug. 2007.
[1.118] F. Calise, M. D. d'Accadia, A. Macaluso, A. Piacentino, and L. Vanoli, "Exergetic

and exergoeconomic analysis of a novel hybrid solar–geothermal polygeneration system producing energy and water," *Energy Convers. Manag.*, vol. 115, pp. 200–220, May 2016.

[1.119] E. A. Pina, M. A. Lozano, and L. M. Serra, "Thermoeconomic cost allocation in simple trigeneration systems including thermal energy storage," *Energy*, vol. 153, pp. 170–184, Jun. 2018.

[1.120] E. A. Pina, M. A. Lozano, and L. M. Serra, "Allocation of economic costs in trigeneration systems at variable load conditions including renewable energy sources and thermal energy storage," *Energy*, vol. 151, pp. 633–646, May 2018.

[1.121] A. Picallo-Perez, J. M. Sala-Lizarraga, E. Iribar-Solabarrieta, and J. M. Hidalgo-Betanzos, "A symbolic exergoeconomic study of a retrofitted heating and DHW facility," *Sustain. Energy Technol. Assessments*, vol. 27, pp. 119–133, Jun. 2018.

[1.122] A. Picallo, C. Escudero, I. Flores, and J. M. Sala, "Symbolic thermoeconomics in building energy supply systems," *Energy Build.*, vol. 127, pp. 561–570, Sep. 2016.

[1.123] F. Calise, M. Dentice d'Accadia, and A. Piacentino, "Exergetic and exergoeconomic analysis of a renewable polygeneration system and viability study for small isolated communities," *Energy*, vol. 92, pp. 290–307, Dec. 2015.

[1.124] R. Leiva-Illanes, R. Escobar, J. M. Cardemil, D.-C. Alarcón-Padilla, J. Uche, and A. Martínez, "Exergy cost assessment of CSP driven multi-generation schemes: Integrating seawater desalination, refrigeration, and process heat plants," *Energy Convers. Manag.*, vol. 179, pp. 249–269, Jan. 2019.

[1.125] V. Verda, M. Caccin, and A. Kona, "Thermoeconomic cost assessment in future district heating networks," *Energy*, vol. 117, pp. 485–491, Dec. 2016.

[1.126] T. D. Čož, A. Kitanovski, and A. Poredoš, "Exergoeconomic optimization of a district cooling network," *Energy*, vol. 135, pp. 342–351, Sep. 2017.

[1.127] L. Ozgener, A. Hepbasli, I. Dincer, and M. A. Rosen, "Exergoeconomic analysis of geothermal district heating systems: A case study," *Appl. Therm. Eng.*, vol. 27, no. 8–9, pp. 1303–1310, Jun. 2007.

[1.128] V. Verda and R. Borchiellini, "Exergetic and economic evaluation of control strategies for a gas turbine plant," *Energy*, vol. 29, no. 12–15, pp. 2253–2271, Oct. 2004.

[1.129] T. J. Leo and I. Pérez-Grande, "A thermoeconomic analysis of a commercial aircraft environmental control system," *Appl. Therm. Eng.*, vol. 25, no. 2–3, pp. 309–325, Feb. 2005.

[1.130] Y. Kalinci, A. Hepbasli, and I. Dincer, "Exergoeconomic analysis of hydrogen production from biomass gasification," *Int. J. Hydrogen Energy*, vol. 37, no. 21, pp. 16402–16411, Nov. 2012.

[1.131] E. Akrami, A. Nemati, H. Nami, and F. Ranjbar, "Exergy and exergoeconomic assessment of hydrogen and cooling production from concentrated PVT equipped with PEM electrolyzer and LiBr-H2O absorption chiller," *Int. J. Hydrogen Energy*, vol. 43, no. 2, pp. 622–633, Jan. 2018.

[1.132] M. N. Khan and T. Shamim, "Exergoeconomic analysis of a chemical looping reforming plant for hydrogen production," *Int. J. Hydrogen Energy*, vol. 42, no. 8, pp. 4951–4965, Feb. 2017.

[1.133] H. Kianfard, S. Khalilarya, and S. Jafarmadar, "Exergy and exergoeconomic evaluation of hydrogen and distilled water production via combination of PEM electrolyzer, RO desalination unit and geothermal driven dual fluid ORC," *Energy*

Convers. Manag., vol. 177, pp. 339–349, Dec. 2018.
[1.134] H. Caliskan, I. Dincer, and A. Hepbasli, "Exergoeconomic and environmental impact analyses of a renewable energy based hydrogen production system," *Int. J. Hydrogen Energy*, vol. 38, no. 14, pp. 6104–6111, May 2013.
[1.135] M. F. Orhan, I. Dincer, and M. A. Rosen, "Exergoeconomic analysis of a thermochemical copper–chlorine cycle for hydrogen production using specific exergy cost (SPECO) method," *Thermochim. Acta*, vol. 497, no. 1–2, pp. 60–66, Jan. 2010.
[1.136] M. Aghbashlo, M. Tabatabaei, H. Rastegari, and H. S. Ghaziaskar, "Optimization of continuous glycerol esterification with acetic acid based on exergoeconomic and exergoenvironmental approaches," *Sustain. Prod. Consum.*, vol. 17, pp. 62–73, Jan. 2019.
[1.137] F. Joda and F. Ahmadi, "Exergoeconomic analysis of conventional and using reactive distillation biodiesel production scenarios thermally integrated with a combined power plant," *Renew. Energy*, vol. 132, pp. 898–910, Mar. 2019.
[1.138] S. C. Nimkar, R. K. Mewada, and M. A. Rosen, "Exergy and exergoeconomic analyses of thermally coupled reactors for methanol synthesis," *Int. J. Hydrogen Energy*, vol. 42, no. 47, pp. 28113–28127, Nov. 2017.
[1.139] G. J. (Georgia I. of T. Thuesen and W. J. (Virginia P. I. Fabrycky, *Engineering Economy*, Ninth Edit. PEARSON, 2000.
[1.140] R. A. GAGGIOLI, "Second Law Analysis for Process and Energy Engineering," in *Efficiency and Costing*, vol. 235, AMERICAN CHEMICAL SOCIETY, 1983, pp. 1–3.
[1.141] Santos J, N. M, L. E, and M. M, "On the productive structure for the residues cost allocation in a gas turbine cogeneration system," in *Proceedings of ECOS 2008*, 2008, pp. 641–648.
[1.142] A. Banerjee, M. J. Tierney, and R. N. Thorpe, "Thermoeconomics, cost benefit analysis, and a novel way of dealing with revenue generating dissipative units applied to candidate decentralised energy systems for Indian rural villages," *Energy*, vol. 43, no. 1, pp. 477–488, Jul. 2012.
[1.143] C. Torres, A. Valero, V. Rangel, and A. Zaleta, "On the cost formation process of the residues," *Energy*, vol. 33, no. 2, pp. 144–152, Feb. 2008.
[1.144] A. Agudelo, A. Valero, and C. Torres, "Allocation of waste cost in thermoeconomic analysis," *Energy*, vol. 45, no. 1, pp. 634–643, Sep. 2012.
[1.145] C. T. Cuadra, "SYMBOLIC THERMOECONOMIC ANALYSIS OF ENERGY SYSTEMS," in *EXERGY, ENERGY SYSTEM ANALYSIS AND OPTIMIZATION – Vol. II*, C. A. Frangopoulos, Ed. Encyclopedia of Life Support Systems (EOLSS), 2009.

Chapter 2

Exergy Analysis of Reverse Electrodialysis Process

In this chapter, Exergy Analysis of the Reverse Electrodialysis process (RED) is presented. In the first part, a brief outline of RED process is provided, and some insights into design and operating aspects of this process are given.

The analysis is supported by 1-D model for the description of all the transport phenomena within the RED unit, and a detailed description of the modelling approach is provided.

The effects of each Ion Exchange Membranes (IEMs) property (i.e. permselectivity, water and salt permeability, and resistance) on the exergy performance and power yield are quantitatively investigated. Relevant information for orienting future development of better performing IEMs are provided. Finally, a sensitivity analysis is carried out for evaluating the effects of the main operating parameters on the exergy performance of the RED pile.

2.1 Introduction on Salinity Gradient Power technologies

Energy from salinity gradients, commonly indicated as *Salinity Gradient Power* (SGP), is a clean and sustainable form of energy which arises from the "controlled" mixing of solutions at different concentrations [2.1],[2.2]. A natural salinity gradient source is represented by the continuous flowing of rivers into the seas. To this regard, according to [2.3], the world theoretical potential of SGP which may result by

exploiting this source, may range between 1.4 and 2.7 TW. Also, other advantages of this energy source are: (i) no discontinuities in the availability are observed like solar or wind energies and (ii) no CO2 emission occurs during its operational phase.

This energy source was described for the first time in the 1954 by Pattle [2.4], who proposed to extract it by employing *Ionic Exchange Membranes* (IEMs). However, this renewable energy source was not extensively investigated due to limitations in membrane technologies. After the energy crisis in 1970s, the interest in SGP was renewed and many research efforts in industry and academia have been devoted to the development of these technologies. As a result, a large number of SGP technologies have been proposed [2.1], but among them, *Pressure Retarded Osmosis* (PRO) and *Reverse Electrodialysis* (RED) have been the most widely investigated.

- In *Pressure Retarded Osmosis* [2.5]-[2.6], osmotic membranes are interposed between two solutions at different concentration. A conceptual scheme is shown in Figure 2.1. The difference of the *chemical potential* between the two solutions produces an osmotic flux from the dilute solution channel to the concentrate one. As a difference from Forward Osmosis (FO), in PRO a hydrostatic pressure lower than the osmotic pressure difference between the two channels is applied to the concentrate solution. The resulting water flux occurring from the dilute to the concentrate compartment is thus “retarded” yet pressurized. This pressure energy gained by the permeating water is subsequently converted into electrical energy by means of a hydro-turbine coupled with a generator.

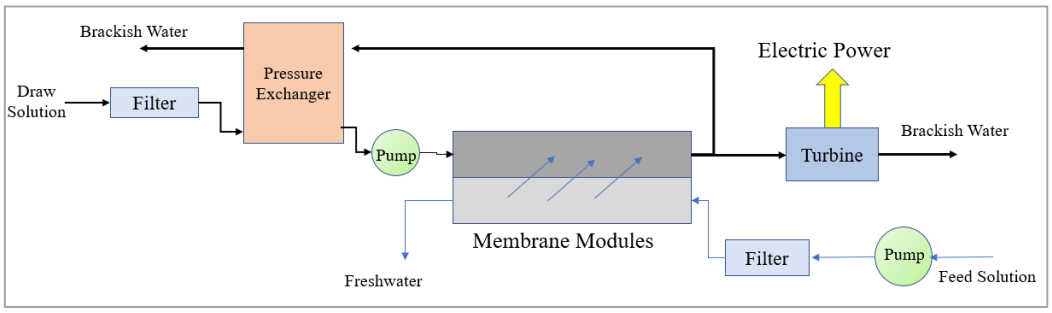

***Figure 2.1**. Conceptual scheme of PRO process*

- *Reverse Electrodialysis* allows for the direct conversion of salinity gradients into electricity. A schematic representation of a RED pile is shown in Figure 2.2. RED units consist of several repetitive unit called “cell pair”. A cell pair consist of two ionic exchange membranes, an anion and a cation exchange membrane interposed between two channels where the solutions at different saline concentrations flow. The chemical potential difference between the two solutions generates a selective transport of cations and anions through the membranes resulting in an ionic current and an electric potential difference over each membrane. Then, this ionic current is converted into electricity by redox reactions, which occur at two electrodes placed at the end of the pile.

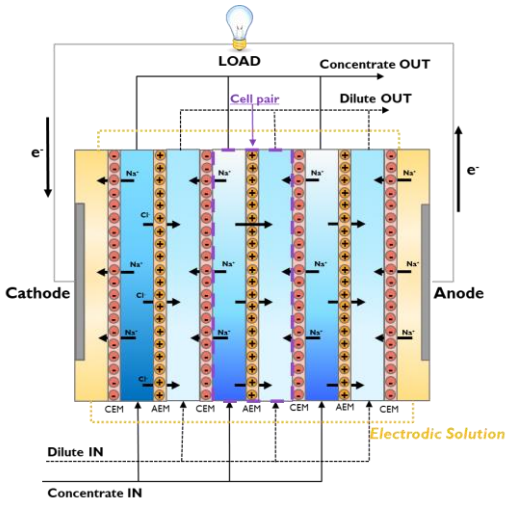

***Figure 2.2**. Conceptual schematic of a RED process*

Although both processes are very promising and currently investigated, the RED process has a remarkable advantage with respect to PRO: in fact, in PRO process the salinity gradient is converted first into pressure/mechanical energy and, then, into electrical energy by means of turbines. Conversely, thanks to the electrochemical nature of the RED process, a direct conversion of the salinity gradient into electric energy is achieved. Moreover, the use of concentrated brines would lead in a PRO system to very high osmotic pressure differences, which would be difficult to handle with available osmotic membranes.

In order to gain more insights into the PRO process (which is not investigated in this thesis), the reader is invited to refer to [2.1] .

2.2 Reverse Electrodialysis: fundamentals and historical outlines

Reverse ElectroDialysis (RED) relies on *Ion Exchange Membranes* (IEMs) to exploit the chemical potential difference between water solutions with a concentration difference. Generally, a membrane is a *selective* barrier which allows for the passage of selected components of a mixture, while retaining the others. IEMs are a particular case of membranes, consisting of polymeric films where charged groups are attached. On the basis of the functionality of these charged groups (i.e. fixed basic or acidic dissociating groups), the membrane may result charged positive or negative when it is immerged in water. A *Cation Exchange Membrane* (CEM) contains negative fixed charges, thus allowing positive ions (*counter-ions*) for passing through it while rejecting negative ions (*co-ions*). Conversely, an *Anion Exchange Membrane* (AEM) allows for the passage of anions and rejects cations. These facts are also known as *Donnan's exclusion* phenomena.

Since IEMs allow only one type of ion (positively or negatively charged) to cross, a concentration difference over the membrane generates a voltage difference over the membrane itself. For instance, if a CEM is placed between two NaCl solutions with different concentrations, an electrical potential difference is generated by the diffusion of Na^+ ions through the membrane. The resulting electrical potential across the CEM is calculated by means of Equation (2.1), which is formally equal to *Nernst Equation*.

$$E_{CEM} = \frac{RT}{zF} \ln\left(\frac{a^+_{conc}}{a^+_{dil}}\right) \tag{2.1}$$

In Equation (2.1), R the ideal gas constant (8.314 J/(mol K)), F the Faraday constant (96 485 C/mol), T is the *operating temperature*, *z* is the valence of ions, and a_{conc} and a_{dil} are the activities of the sodium ions in the concentrate ad dilute solutions respectively.

As previously said, a *reverse electrodialysis pile* (or stack) consists of repetitive *cell pair* (Figure 2.2). A schematic representation of a cell pair is provided in Figure 2.3. Each cell pair consists of two membranes, i.e. a CEM and an AEM, and two compartments, i.e. a dilute (or low) and a concentrate (or high) compartment.

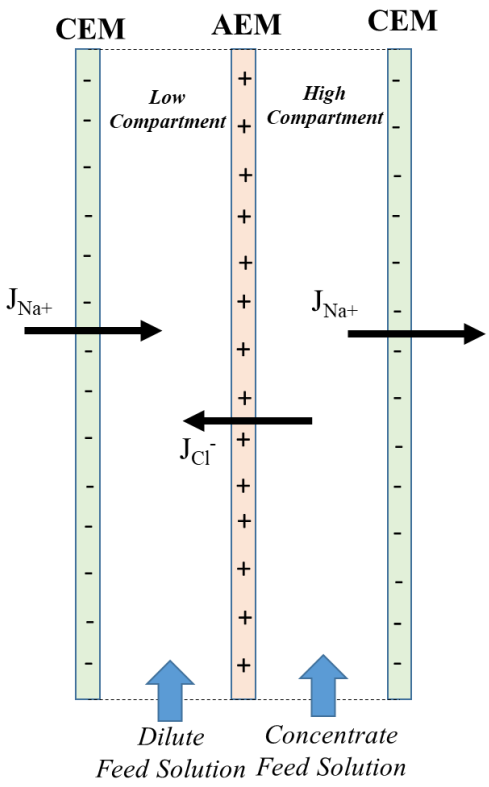

Figure 2.3 *Scheme of a RED cell pair*

All the compartments are alternately fed with the two feed streams, i.e. the concentrate and the dilute, thus generating a concentration gradient across all the membranes. Basically, within each cell pairs the concentrated solution encounters a dilution, conversely, the dilute solution is concentrated. Once the RED system is connected to an external load, an ionic current is produced within the pile. Then, the *ionic current* is converted into an *electronic current* within the electrode compartments

by mean of an "electrode rinse solution", composed by ad-hoc redox couple (e.g. $K_3Fe(CN)_6$ / $K_4Fe(CN)_6 \cdot 3H_2O$) which is continuously recirculated.

In particular, under the hypothesis of ideal performing IEMs, the voltage generated from each cell pair, i.e. E_{cell}, is calculated by summing up the contribution of electrical potential generated respectively across the CEM and the AEM as shown in Equation (2.2).

$$E_{cell} = E_{CEM} + E_{AEM} = 2\frac{RT}{zF}\ln\left(\frac{a_{conc}}{a_{dil}}\right) \tag{2.2}$$

When multiple cell pairs are stacked, the overall voltage is proportional to the number of cell pairs installed.

As shown in Figure 2.4 (a), the standard geometry adopted in the design of RED unit is the *plate-and-frame*: membranes and spacers are piled up between two end plates. The sealing between each compartment is provided by means of rubbery gaskets. The electrodic compartments, including electrodes and electrolyte rinse solution channels, are generally located in the end-plate. Conventional RED unit adopts *net spacers* interposed between the membranes in order to generate the feed channels, maintain a fixed channel dimension and promote fluid dynamic. Common spacers are made by two arrays of polymeric wires either extruded (overlapped, Figure 2.4(d)) or woven (Figure 2.4 (e)), with circular cross section, though other geometries have been devised too [2.7]-[2.8]. In novel stack configurations, profiled membranes are adopted Figure 2.4 (c). One advantage of using profiled membranes is the possibility to avoid the net spacers: in fact, the surface contains the so called "*membrane's reliefs*" which act as the traditional spacers.

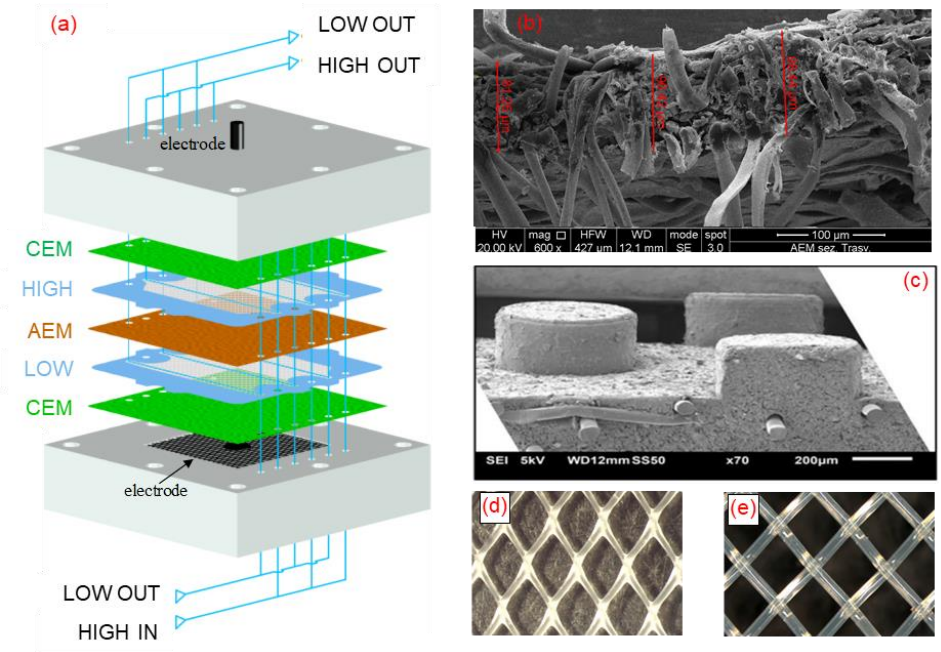

Figure 2.4 *Schematic representation of a RED stack elements (a); Standard IEM membrane (FujiFilm® type III) (b) profiled membrane (c) Overlapped spacers (d); Woven (e) [2.9].*

Three flow arrangements can be adopted within a RED pile: (i) a co-current, (ii) a counter-current and (ii) a cross-flow. Differently from the co-current, counter-current flow arrangement gives a higher driving force and yield (i.e. the energy generated per cubic meter of feed solutions**)** but it causes larger pressure difference between the two feed solutions. As a consequence, leakages and membrane deformations may result. In the cross-flow arrangement, the largest driving force is generated but a low yield results.

2.2.1 Ion Exchange Membranes: definition of main properties

As previously shown, IEMs constitute the heart of the *RED* process. The performance of an IEM is characterized by several properties related to physical and chemical aspects. The main properties used for characterizing the performance of

IEMs are: (i) the *permselectivity*, (ii) the *membrane resistance* and (iii) *water and salt permeability*. For a sake of brevity, no details concerning the physics underlying membrane properties are here provided. However, a thorough description of it can be found in [2.1].

Membrane Permselectivity

In an ideal-performing IEM, only counter-ions would cross them, while co-ions would be rejected. It has been understood that the IEMs are not perfectly selective to one ion, but it allows more ions to pass. These co-ions fluxes generally contribute to lower the electromotive force generated by the process. In order to account for this phenomenon, a factor named "*permselectivity*" (usually indicated by α) has been introduced. This factor can range among 0 and 1 and it represents a measure of *Donnan's* exclusion phenomena. For instance, a value of permselectivity equal to one indicates that only counter-ions would cross the membrane. The resulting electric potential generated across each cell pair is shown in Equation (2.3).

$$E_{cell} = E_{CEM} + E_{AEM} = \alpha_{AEM} \frac{RT}{zF} \ln\left(\frac{a^{-}_{conc}}{a^{-}_{dil}}\right) + \alpha_{CEM} \frac{RT}{zF} \ln\left(\frac{a^{+}_{conc}}{a^{+}_{dil}}\right) \qquad (2.3)$$

The membrane permselectivity depend on concentration of the fixed ion of the membrane matrix and on the concentration of the concentrated solution. More specifically, it has been found that when the concentrate is around 0.5M NaCl, typical α_{IEM} values of commercial membrane range among 80-99% [2.10]. Conversely, in applications with larger high solution concentrations permselectivity values decrease significantly reaching values between 50-70% [2.11].

Commonly, IEM permselectivity is evaluated through static membrane potential measurement [2.12]. This method consists in to measure the electrical potential arising in the two side when an IEM is placed between a concentrated and a diluted solution.

The permselectivity is then evaluated by comparing the "*measured*" potential (ΔV_{meas}) with the "*theoretical*" value (ΔV_{theo}).

Membrane Electrical Resistance

The electrical membrane resistance quantifies the "opposition" of the membrane to the flux of counter-ions across it. It is usually expressed in the form of areal resistance ($\Omega \cdot cm^2$) and it is referred to the active surface of the membranes.

Power output and efficiency of the RED unit are highly sensitive to the membrane resistance. For instance, in applications where low concentrations for both feed solutions are involved, i.e. $\underline{C_{Conc}}$=0.6M an C_{dil}=0.02M, membrane resistance account for as much as 30% of total stack resistance (in this latter, ohmic resistances of both solutions are accounted) while it becomes the highest contribution in applications where high solution concentrations are considered (C_{Conc}=4-5M) [2.13].

Membrane resistance is influenced by a number of factors related to (i) *membrane structure*, as charge density and ions mobility, (ii) *solutions properties*, as composition and concentrations, and (iii) the *operating temperature*.

From experimental activities [2.13]-[2.14], it was found that the membrane resistance highly increases when the solution concentration is decreased from the values of 0.1-0.3M. Conversely, it remains approximatively constant for higher concentration values.

Temperature has a large influence on the membrane resistance value. In particular, an increase in the operating temperature leads to a large decrease on the membrane resistance as demonstrated by Benneker et al. [2.15]. Some relevant data for IEMs commercially available are reported in Ref. [2.10]

Salt and Water Diffusion across IEMs

As previously said, for ideal-performing IEMs, only counter-ions can move through them, while co-ions are rejected. In real IEMs small flux of co-ions exists and

the effect on the reduction of electrical potential generated is accounted for by introducing permselectivity. At, the same time, the sum of a co- and a counter-ion results in a diffusive flux of neutral salt, from the concentrate to the dilute solution across the membranes. This effect is responsible for a loss of salinity gradient between the channels and it is more evident when highly concentrated solutions are considered. The diffusive salt flux across each membrane can be modelled using an equation formally equal to the Fick's law as shown in Equation (2.4).

$$J_{diff} = \frac{P_s}{\delta_m}\left[C_{Conc} - C_{Dil}\right] \tag{2.4}$$

where C_{Conc} and C_{Dil} are the concentrations of the two solutions at the membrane interface, δ_m is membrane thickness and P_s is the salt permeability .Using the same approach adopted in [2.16], the permeability (P_s) is the product of salt diffusion and sorption coefficient in membrane.

Another diffusion phenomenon which highly affects the performance of a RED pile, is the water flux across the membranes. This flux is due to two different contributions: (i) the *osmotic flux* and (ii) the *electro-osmotic flux*.

The *osmotic flux* is originated by the osmotic pressure difference across the *IEMs.* The concentration difference between the membrane results in a difference of chemical potential of the water molecules in the two solutions, generating a flux of water directed from the dilute (higher water activity) to the concentrate (lower water activity), which is modelled according to the diffusion theory as shown in Equation (2.5).

$$J_w = -\nu RTP_w\left(\phi_{conc} m_{conc} - \phi_{dil} m_{dil}\right) \tag{2.5}$$

P_w is the average water permeability of the *IEM*s, ϕ the osmotic coefficient, m the molal concentration, and *v* is the number of ions.

The *electro-osmotic flux* is due to the water molecules transported by the ions as first hydration shell. Assuming a certain number of water molecules in the first hydration shell (*n*) of the ions, the electro-osmotic flux (J_{eosm}) is given by:

$$J_{eosm} = n \cdot J_s \tag{2.6}$$

2.2.2 Operational Aspects of a RED pile

The main *operating parameters* of the RED stack are: (i) the *stack voltage* E_{stack} and (ii) the *power density* (P_d) (i.e. the power produced by the unit divided by the total membrane area (W/m^2_m) or by the cell pair area (W/m^2_{cp})). Typical curves obtained for E_{stack} and P_d as a function of the stack current (I_{stack}) are shown in Figure 2.5 (a) and (b).

The electrical current and the electrical potential produced by the *RED* unit are related by the Ohm's law:

$$I_{stack} = \frac{E_{stack}}{R_{stack}} \tag{2.7}$$

where E_{stack} is the electrical potential measured on the electrodes of the *RED* unit, I_{stack} is the electrical current generated by the *RED* unit and R_L is the external resistance of the load connected to the *RED* electrodes.

The electrical potential of the *RED* unit may be evaluated as:

$$E_{stack} = OCV - R_{stack} \cdot I_{stack} \tag{2.8}$$

Where OCV is the electrical voltage in open circuit condition (i.e. Open Circuit Voltage) and R_{STACK} is the internal resistance of the stack which accounts for the resistance of channels, membranes and electrodic compartments. The stack resistance

is the slope of the curve electrical potential vs current. Worth noting that for small residence times (i.e. high solution flow rates), the relation between voltage and current is represented by a straight line, meaning that the resistance is approximatively constant in the unit, varying R_{ext} value. In the case of large residence times, the concentration of the inlet/outlet solutions varies a lot with R_{ext} producing a variation of the solution and membrane resistances, and then of R_{stack}. Therefore, the relationship voltage/current deviated from the linear behaviour.

The electrical power generated by the *RED* unit (P_{RED}) is given by:

$$P_{RED} = E_{stack} \cdot I_{stack} \tag{2.9}$$

while the power density for unit of membrane area ($P_{d,m}$) and cell pair area ($P_{d,cp}$) are equal to:

$$P_{d,m} = \frac{P_{RED}}{2N_{cp} \cdot A_{cp}} \tag{2.10}$$

$$P_{d,cp} = \frac{P_{RED}}{N_{cp} \cdot A_{cp}} \tag{2.11}$$

where N_{cp} and A_{cp} are the number of cell pairs and the active area of one cell pair. The factor 2 in the denominator of the $P_{d,m}$ denotes that each cell pair consists of two membranes.

In order to evaluate the *stack voltage* (E_{stack}) and the *power density* (P_d), ad-hoc experimental procedure is set, which generally consist of a *RED* unit powered by the feed solutions at fixed flow rates and connected to a variable external load (R_L). Starting from Open Circuit condition (*O.C.* or $R_L \rightarrow \infty$), the resistance of the external load is gradually decreased until short-circuit condition (*S.C.* or $R_L \rightarrow 0$) is reached.

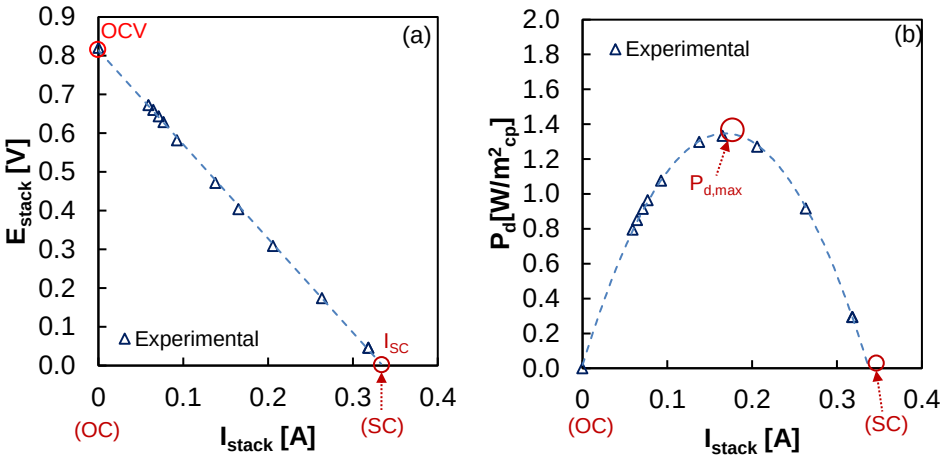

Figure 2.5 *Typical Electrical potential vs electrical current* ***(a)*** *and power density vs electrical current diagrams* ***(b)*** *for a RED unit*

When no external load is connected, the E_{stack} is equal to the Open Circuit Voltage. As shown Figure 2.5 (a) when the stack operates in *O.C.* condition the maximum electrical potential is generated. Conversely, the electrical current is zero and no electrical power is produced.

When the stack operates in *S.C.* the electrical current reaches the maximum values (this is usually named short-cut current I_{SC}). Conversely, both the stack voltage and the power output are equal to zero.

As shown in Figure 2.5 (b) the maximum power density is obtained when the external resistance is approximatively equals to the internal resistance of the *RED* unit or for electrical current closes to the half of the short-cut current (I_{SC}).

2.2.3 A brief historical outline and applications of Reverse Electrodialysis process

Several laboratory investigations have been performed and presented in literature during these decades, all focusing on influence of operating conditions and membrane properties on the main process performance parameters such as the power density and

the process yield (i.e. energy generated per cubic meter of feed solutions). The first experiments related to RED process were carried out by Pattle in 1954, who reported a power density of 0.05 W/m^2 [2.4]. Along the decades a substantial increase in the power density value was observed. In particular, in 1976, 0.17 W/m^2 was found by Weinstein and Leitz [2.17]. In 1986, Audinos [2.18] and Jagur-Grodzinski and Kramer [2.19] obtained a power density equal to 0.4 W/m^2. A further doubling, about 0.93 W/m^2, was achieved in 2008 by Veerman et al. [2.20].

During the last years, the process performance has been greatly enhanced thanks to the developments in membrane properties which have allowed for reaching power density equal to 2.2 W/m^2 [2.21]. Scientific efforts were focused on the overall system design [2.22]-[2.23], on the fluid-dynamics within the channels [2.8] or on the electrode material investigation [2.24]. Several studies are also focused on the development of Ionic Exchange Membranes (*IEM*s) with low electrical resistance and high perm-selectivity [2.25], on the investigation of membrane materials [2.11]-[2.26] and on the interactions between membrane and ions in the solution [2.27] -[2.28].

A further development of the *RED* process has been focused on the exploitation of high salinity streams, like saline waters or brine. Laboratory investigations performed by means of artificial brackish water and brine have shown the possibility to reach a power density up to 6.7 W/m^2 [2.29]. Furthermore, in 2014, the first demonstration plant operating with real brines and saline waters was built in Trapani (Italy) [2.23]-[2.30].

At the very beginning, applications of the RED process started for the case of *open-loop configuration systems,* where natural salinity gradients generated by mixing river water, seawater, brine, or brackish water were exploited to produce electricity and after released into the environment. However, the applications for the case of natural salinity gradients are limited in those areas where these sources are available. A possibility to overcome this natural limit is the use of artificial salinity gradients in a *closed-loop configuration,* named *RED* Heat Engine (*RED-HE*). The innovative *Reverse*

Electrodialysis-Heat Engine (RED-HE) [2.31] consists of a traditional RED unit coupled with a Thermal Regeneration Unit (TRU). The TRU is provided with waste heat, which is used in a purposely-selected thermally-driven process to restore the initial concentrations of the solutions exiting from the RED unit. In this way the regenerated solutions can be fed again to the RED unit, thus closing the cycle. These systems could be profitably coupled to several industrial processes, like manufacturing or metallurgical industries, where low-grade waste heat is discarded into the environment. In this way, a reduction of fossil fuel consumptions could be achieved with economic and environmental benefits.

One of the most significant features of the RED-HE process is that there is no need for natural salinity gradients sources, thus overcoming the main restriction of implementation of the RED process which is obviously limited only to those sites where natural sources of SGP are available. The RED-HE can be in fact implemented in principle anywhere, thanks to the use of a limited quantity of artificial saline solutions suitably-selected for optimal process performance [2.32]-[2.33].

Another interesting application of closed-loop reverse electrodialysis systems is the development of a "salinity gradient based battery". Some examples of this application have been proposed so far both in scientific papers [2.34]-[2.35] and high-risk cooperation projects [2.36]. Both in open- and closed-loop configuration the enhancement of energy performance of *RED* units is a matter of crucial importance. Further investigations are needed in order to make this green power production system competitive with the most common power generation processes.

2.2.4 Literature review on thermodynamic analyses of RED process

Few research efforts have been devoted so far to the thermodynamic analysis of RED units. Veerman et al. pointed out [2.37] the crucial role played by membrane properties on energy performance. On the basis of an ideal model for thermodynamic properties estimation, they experimentally analysed the thermodynamic efficiency and

power densities of a RED unit equipped with six commercial membranes, reporting thermodynamic efficiency between 14% and 35%. They also demonstrate that the non-ideal behaviour of the membranes is due to osmosis and co-ion transport and that loss in efficiency due to osmosis is small compared to co-ion. The same authors in [2.38] developed a 1-D model for the RED unit, which introduced the exergy concept. The model was calibrated with experimental data and used to study response parameters, suitable for optimization purposes. It was found that performance of co-current and counter-current operation is almost identical and that segmentation of the electrodes can increase the power density with about 15%. Yip et al. [2.39] proposed a model to assess the production of work respectively in a reversible and real RED process. The model defines suitable dimensionless parameters, which have to be properly assessed according to the type of membrane and operating conditions considered. By thoughtful selection of the operating parameters they achieved a thermodynamic efficiency of 37% and an overall gross power density of 3.5 W/m^2 with seawater-river water RED system with low-resistance ion exchange membranes (0.5 cm^2) at very small channels thickness (50 μm). Vermaas et al. in [2.40] investigated the effects of different flow arrangements, single and multi-electrodes configurations on the energy efficiency of RED unit equipped with perfect membranes. They reported a maximum energy efficiency of 95% when using seawater and river water flowing in counter-current arrangement.

Most of the works reported in literature limited their investigation to the case of seawater and river water as it is the most common natural salinity gradient. Conversely, a variety of artificial solutions could be in principle used in closed-loop applications, leaving large room for further studies. Moreover, literature works typically refer to thermodynamic efficiency (or energy efficiency) as performance indicator, while exergy efficiency is not mentioned or not properly quantified in any study.

2.3 Description of the modelling approach

In order to support the analysis, the RED model, implemented in the software *Engineer Equation Solver* (EES) [2.41], is divided in three sub-sections:

(i) *Thermodynamics* section, which reports the model and equations used to describe the properties of electrolyte solutions (e.g. osmotic and activity coefficients, density and conductivity of NaCl solutions).

(ii) *1-D RED model* section, which describes the main phenomena involved in the process (e.g. electrical phenomena, mass balances, salt and water fluxes, etc.). Also, model validation is reported in this section.

(iii) *Exergy analysis* section, which predicts all the exergy flows on the basis of the 1-D RED model inputs and outputs.

2.3.1 Thermodynamic of electrolyte solutions

Modelling RED and exergy analysis require an accurate evaluation of thermodynamic properties of the solutions involved in the process. Due to the wide range of concentration investigated, the simplifying hypothesis of *ideal solution* could be no more valid to describe the behaviour of solutions. In particular, only NaCl solutions are here considered but similar considerations can be easily applied for different electrolyte solutions.

As it is well known, the chemical potential of the generic solute *MX* of an electrolyte solution is defined in Equation (2.12) [2.42].

$$\mu_{MX} = \mu^0_{MX} + \nu RT ln(m_{\pm}\gamma_{\pm}) \quad (2.12)$$

In which μ°_{MX} is the chemical potential of the solute in the standard state (i.e., ideal 1 molal solution at 25°C and 1 atm), obtained as combination of the standard chemical potentials of the single ions, ν is the sum of ions in one molecule of solute ($\nu = \nu_+ + \nu_-$), $m_{\pm}$ the mean molality and $\gamma_{\pm}$ the mean activity coefficient. The mean molality and activity

coefficient are defined as geometric mean of the ions properties [2.42].

Similarly, the chemical potential of the solvent (i.e. water) is defined in Equation (2.13).

$$\mu_s = \mu_s^0 + RTln(a_s) \tag{2.13}$$

in which a_s is the solvent activity and $\mu_i°$ is the solvent chemical potential in the standard state. The activity of the solvent is related to the osmotic coefficient ϕ, defined in Equation (2.14).

$$\phi = -\frac{1000\ln(a_s)}{M_w \sum_i \nu_i m_i} \tag{2.14}$$

where M_W is the molecular weight of the solvent (g/mol), m_i is the i-ion molality in the solution (mol/kg), v_i the dissolution stoichiometric coefficients of i-ion.

Osmotic and mean activity coefficients

Pitzer's ion interaction model [2.42] is widely used to describe the behaviour of electrolyte solutions. In Pitzer's model, the osmotic and salt activity coefficients are described by semi-empirical equations in which the interactions of all ions in solution is considered by means of concentration-independent interaction coefficients. Thus, for an arbitrary composition of an aqueous electrolyte mixture, when the interaction coefficients are known, activities and osmotic coefficients of all ions can be estimated using Pitzer's model. For the case of a generic electrolyte *MX*, the Pitzer's equations for osmotic and activity coefficients are reported in Equations (2.15) and (2.16).

$$\phi = 1 - \left|z_M z_X\right| A_\phi \frac{I^{0.5}}{1 + b I^{0.5}} + 2m \frac{\nu_M \nu_X}{\nu} B_{MX}^{\phi} + 2m^2 \frac{(\nu_M \nu_X)^{3/2}}{\nu} C_{MX}^{\phi} \tag{2.15}$$

$$\ln(\gamma_\pm) = -\left|z_M z_X\right| A_\phi \left(\frac{I^{0.5}}{1 + b I^{0.5}} + \frac{2}{b}\ln(1 + b I^{0.5}) \right) + 2m \frac{\nu_M \nu_X}{\nu} B_{MX}^{\gamma} + 3m^2 \frac{(\nu_M \nu_X)^{3/2}}{\nu} C_{MX}^{\phi} \tag{2.16}$$

With

$$B^{\phi}_{MX} = B^{(o)}_{MX} + B^{(1)}_{MX} \exp(-\alpha I^{0.5}) \tag{2.17.a}$$

$$B^{\gamma}_{MX} = 2B^{(o)}_{MX} + \frac{2B^{(1)}_{MX}}{\alpha^2 I}\left[1-(1+\alpha I^{0.5} - \frac{\alpha^2 I}{2})\exp(-\alpha I^{0.5})\right] \tag{2.17.b}$$

in which $m_0 = 1$ mol · kg^{-1} is the standard molality, $b = 1.2$ kg$^{1/2}$· mol$^{-1/2}$ is a universal parameter; α is a numerical constant equal to 2 for univalent ions; I is the ionic strength A_ϕ , is the Debye-Huckel parameter for the osmotic coefficient; $B^{(0)}_{MX}$, $B^{(1)}_{MX}$, and C_{MX} are adjustable parameters, called *ion-interaction parameters or virial coefficients*, related to short-range interaction between the ions, thus particularly important when salt concentration is high. The virial coefficients are function of the electrolyte type, temperature and pressure. For some salts, like *NaCl* and *KCl* [2.43]-[2.44] some correlations to evaluate the interactions parameters were found in literature as function of temperature and pressure. Figure 2.6 shows the dependence of osmotic and salt activity coefficients on concentration at 298 K.

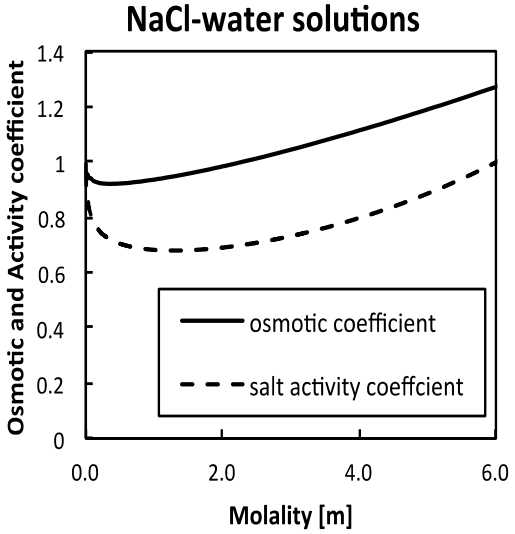

Figure 2.6 *Osmotic and salt Activity Coefficient for NaCl solution at 298.15 K as function of* molality.

As shown in Figure 2.6, both the osmotic coefficient and the salt activity coefficient depart from the unity. These results suggest the need to use a more complex thermodynamic model of solution in order to achieve more realistic results.

Density

The solutions density is also affected by salt concentration. For NaCl-water solutions, density was estimated as a linear function of the molar concentration according to Equation (2.18).

$$\rho = \rho_0 + \left(\frac{\Delta \rho}{\Delta C} \right) C \tag{2.18}$$

where ρ_0 is density of pure water at 298.15 K, which is equal to 997 kg/m^3. The slope of the function ($\Delta\rho/\Delta C$) was evaluated by fitting experimental data from literature [2.45]. For NaCl $\Delta\rho/\Delta C$ is equal to 37.4 kg/mol. Figure 2.7 (a) reports the density of NaCl aqueous solution as function of the molar concentration.

Conductivity

Solutions conductivity is another important property to be estimated, as it affects the electrical resistance of the solutions within the stack. Solutions with very low electrolyte concentration exhibit very low conductivity and high electrical resistance. The dependence of solution equivalent electrical conductivity on concentration was estimated according to Equation (2.19).

$$\Lambda = \Lambda_0 - \frac{A_\Lambda \, C^{1/2}}{1 + B_\Lambda \, C^{1/2}} - C_\Lambda C \tag{2.19}$$

where Λ_0 is the equivalent conductivity of salt at infinite dilution, A_Λ, B_Λ and C_Λ are fitting parameters, and C is the molar concentration. The parameters for NaCl solutions were obtained fitting literature experimental results [2.45]. At 298 K, A_Λ=*91.02*,

B_A=1.66 and C_A=6.80. Figure 2.7 (b) reports the conductivity of NaCl solution as function of the solution molar concentration.

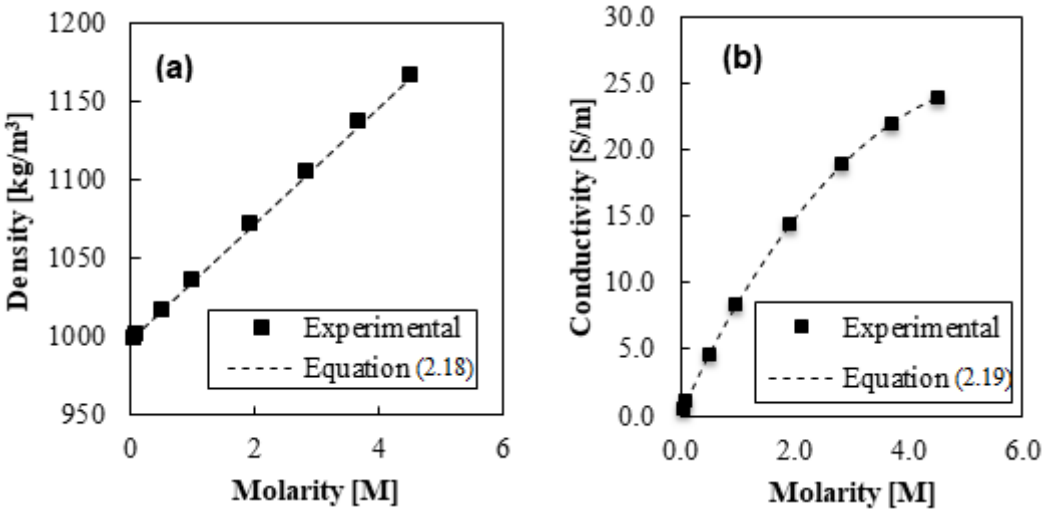

Figure 2.7 *Comparison between experimental* [2.45] *and fitting results of density (a) and conductivity (b) of NaCl solutions versus molarity at 298.15 K.*

2.3.2 RED process modelling

A schematic representation of a generic RED unit is reported in Figure 2.8 along with the indication of the repetitive unit, i.e. the *cell pair*. In agreement with previous studies available in the literature [2.38], [2.46], the present model is based on a few simplifying assumptions:

- a mono-dimensional approach was used to describe the system, considering the variation of the main variables (concentrations, electrical current, fluxes, resistances etc.) along the channel length (L) coinciding with the flow direction (both in co- and counter-current arrangement);
- salt concentration profiles (along the direction perpendicular to the IEMs) are assumed to be flat in both compartments, i.e. concentration polarisation phenomena are neglected;

- all cell pairs operate in the same way, assuming an ideal flow distribution with no parasitic currents [2.46].

In addition, given the preliminary nature of the present analysis, no pressure drop along the channel was considered and gross power values only are reported. In fact, pressure drops are strongly related to stack geometry and configuration, and the present analysis does not consider these aspects of the unit design. However, several works reported in literature provide useful information on how pressure drops are affected by stack geometry by means of theoretical [2.47]-[2.48] or experimental investigations [2.49]-[2.50].

The equivalent circuit scheme of the RED unit is reported in Figure 2.8 (a). The stack can be imagined as consisting of N_k parallel branches where N_k is the number of intervals adopted for the numerical discretization of the domain along the flow direction (channel length). Each of them supplies part of the current I circulating in the external circuit and consists of N_{cp} (cell pair number) identical repetitive units connected in series. As shown in Figure 2.8 (b) each cell pair is divided in N_k elements of length Δx along the main flow direction ($\Delta x = L / N_k$). The generic k-th element is constituted of two electric voltage generators, one for each IEM (E_{CEM} and E_{AEM}), and four resistances, relevant to the solutions (R_{conc} and R_{dil}) and the IEMs (R_{CEM} and R_{AEM}) resistances. It is worth noting that the sketch in Figure 2.8 (b) is only a schematic representation of the phenomena involved in the cell pair. Finally, RED equivalent circuit of Figure 2.8 (b) is serially connected to a branch indicating the resistance of the electrodic compartments R_{blank} and, eventually, closed by the external load resistance R_L. All the variables presented in this scheme will be described in details in the following paragraphs.

-

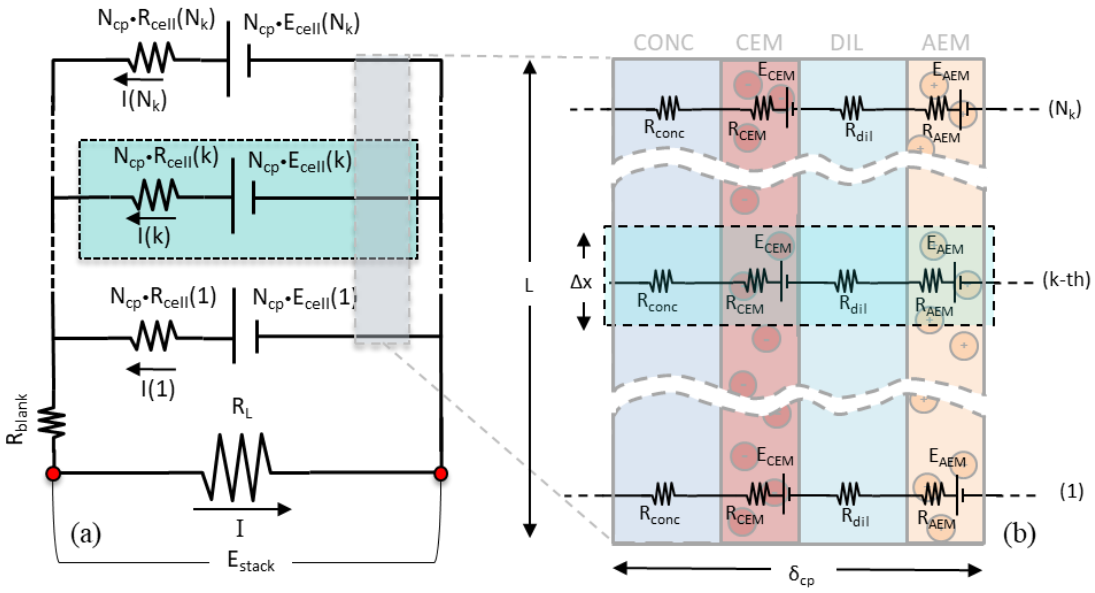

Figure 2.8 *Equivalent electrical circuit scheme of the RED unit (a) and of an individual cell pair (b).*

The voltage generated from each kth element of cell pair (E_{cell}), is calculated by an equation formally similar to the Nernst equation (Equation (2.20)).

$$E_{cell}(k) = E_{CEM}(k) + E_{AEM}(k) = 2\alpha_{av}(k)\frac{RT}{zF}\ln\left(\frac{m_{conc}(k)\cdot\gamma_{conc}(k)}{m_{dil}(k)\cdot\gamma_{dil}(k)}\right) \qquad (2.20)$$

in which α_{av} is the average permselectivity of the two IEMs. The kth internal resistance is made of 4 series resistances as reported in Equation (2.21).

$$R_{cell}(k) = \left[R_{CONC}(k) + R_{DIL}(k) + R_{CEM}(k) + R_{AEM}(k)\right]\cdot\frac{1}{\Delta x\cdot b} \qquad (2.21)$$

where $R_{conc}(k)$ and $R_{dil}(k)$ are the electrical resistances of feed compartments, while $R_{CEM}(k)$ and $R_{AEM}(k)$ are the IEMs resistances. The feed compartments resistance is calculated according to Equation (2.22).

$$R_{sol}(k) = f\,\frac{\delta_{sol}}{\Lambda_{sol}(i)\cdot C_{sol}(k)} \tag{2.22}$$

where *f* is called obstruction factor and represents a correction term which takes into account the increase of electrical resistance caused by the presence of the spacer (e.g. due to tortuosity of ion path or shadow effect on membranes). Its values are shown in Table 2.1. The subscript sol indicates either the concentrate or dilute compartment.

The electric current (*i*) generated in each ith branch of the circuit is calculated from Equation (2.23a):

$$E_{cell}(k) = i(k)R_{cell}(k) + E_{stack} + R_{blank}I \tag{2.23.a}$$

which can be rearranged into Equation (2.23b):

$$i(k) = \frac{E_{cell}(k) - (E_{stack} + R_{blank}I)}{R_{cell}(k)} \tag{2.23.b}$$

where E_{stack} is the stack voltage, the electric potential measurable from the outside of the RED unit and R_{blank} is the resistance of the electrodic compartments. The electric current circulating on the external load is the sum of each one produced in the "k-th" branch (*Kirchhoff's junction rule*).

$$I = \sum_{k} i(k) \tag{2.24}$$

The closing equation is obtained by the ohm-law on the external load as shown in Equation (2.25).

$$E_{stack} = R_L \cdot I \tag{2.25}$$

The Gross power (P_{RED}) and gross power density (P_d) of the RED unit are calculated according to Equations (2.26a) and Eq. (2.26b)

$$P_{RED} = N_{cp} \cdot E_{stack} \cdot I \tag{2.26.a}$$

$$P_d = \frac{P}{N_{cp} \cdot A_{cp}} \tag{2.26.b}$$

where A_{cp} is the membrane area of a cell pair.

The ohmic loss due to the internal resistance of the RED unit is calculated according to Equation (2.27)

$$P_{loss} = \sum_k R_{cell}(k) \cdot I(k)^2 + r_{blank} I^2 \tag{2.27}$$

Water and salt flux through the IEMs

As previously mentioned, the salinity gradient across each membrane is responsible for some detrimental effects producing *uncontrolled mixing phenomena*, which reduce the driving force of the process, generally identified with (i) water flux (J_w) and salt flux (J_s). In Figure 2.9 schematic representation of fluxes across the IEMs is provided.

Due to non-ideal performance of the membranes ($\alpha_{av} \neq 1$) few co-ions pass through the IEMs resulting in a diffusive flux of salt. The total salt flux from the two contiguous concentrate channels to the dilute one is described by Equation (2.28).

$$J_s(k) = J_{mig}(k) + J_{diff}(k) = \frac{i(k)}{zF} + 2\frac{P_s}{\delta_m}\left[C_{CONC}(k) - C_{DIL}(k)\right] \tag{2.28}$$

where i is the current density or the current for unit of membrane area, δ_m is membrane thickness (assumed equal for both IEMs and value reported in Table 2.1) and P_s is the salt permeability (value reported in Table 2.1). Using the same approach adopted in [2.16], the permeability (P_s) is the product of salt diffusion and sorption coefficient in membrane.

In Equation (2.28), the first term, the *migrative flux (J_{mig})*, gives the salt transferred with the counter-ions migration through the AEM and the CEM, while, the second term, the *diffusive flux (J_s)*, refers to the salt flux due to the co-ions diffusion. Factor 2

multiplying the second term considers the presence of two IEMs in contact with the dilute channel.

Also, the water flux consists of two terms (Equation (2.28)): (i) the first named *osmotic flux*, generated by the osmotic pressure difference between the two solutions and directed from the dilute to the concentrate chamber; (ii) the second named *electro-osmotic flux*, due to the water molecules transported in the solvation shells of the ions and directed in opposite direction.

$$J_w(k) = J_{osm}(k) + J_{eosm}(k) = -2\nu RTP_w\left[C_{CONC}(k)\varphi_{CONC}(k) - C_{DIL}(k)\varphi_{DIL}(k)\right] + n \cdot J_s(k) \qquad (2.29)$$

where P_w is the average water permeability of the IEMs (value reported in Table 2.1), ϕ the osmotic coefficient and n the hydration number for Na^+ and Cl^-. The hydration number was fixed equal to 7 according to [2.46]. From Equation (2.29) a volumetric water flux is calculated (m/s).

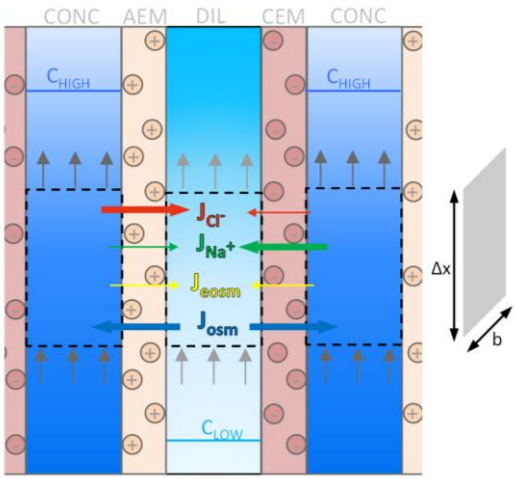

Figure 2.9 *Schematic representation of the modelled fluxes across the IEMs.*

Salt Mass Balances

For each computational domain element, considering a co-current flow arrangement, salt mass balance and global mass balance equations in each compartment (dilute and concentrate) are applied to calculate the exiting concentration and flow rate. These are adopted as inlet conditions of the following element, thus solving the system of equations and characterizing concentration and flow-rate profiles along the entire channel length.

Concentrate channel:

$$C_{conc}(k+1)Q_{conc}(k+1) = C_{conc}(k)\cdot Q_{conc}(k) - J_s(k)b\Delta x \tag{2.30}$$

$$\rho_{conc}(k+1)\cdot Q_{conc}(k+1) = \rho_{conc}(k)\cdot Q_{conc}(k) - J_w(k)\cdot b\Delta x\frac{\rho_w}{M_w} - J_s(k)\cdot b\Delta x M_s \tag{2.31}$$

where $C_{conc}(k+1)\cdot Q_{conc}(k+1) = C_{conc,out}(k)\cdot Q_{conc,out}(k)$ is the product of concentrate outlet concentration and concentrate outlet flow-rate (i.e. the salt molar flow rate).

Dilute channel:

$$C_{dil}(k+1)Q_{dil}(k+1) = C_{dil}(k)\cdot Q_{dil}(k) + J_s(k)b\Delta x \tag{2.32}$$

$$\rho_{dil}(k+1)\cdot Q_{dil}(k+1) = \rho_{dil}(k)\cdot Q_{dil}(k) + J_w(k)\cdot b\Delta x\rho_w + J_s(k)\cdot b\Delta x M_s \tag{2.33}$$

where $C_{dil}(k+1)\cdot Q_{dil}(k+1) = C_{dil,out}(k)\cdot Q_{dil,out}(k)$ is the product of dilute outlet concentration and dilute outlet flow-rate (i.e. the salt molar flow rate).

When a counter-current arrangement is considered, the mass balances are formally the same, though the inlet-outlet flow-rate terms in the dilute channel mass balance have the opposite sign, as shown in Equations (2.34a) and (2.34b)

$$C_{dil}(k)Q_{dil}(k) = C_{dil}(k+1)\cdot Q_{dil}(k+1) + J_s(k)b\Delta x \tag{2.34.a}$$

$$\rho_{dil}(k)\cdot Q_{dil}(k) = \rho_{dil}(k+1)\cdot Q_{dil}(k+1) + J_w(k)\cdot b\Delta x\rho_w + J_s(k)\cdot b\Delta x M_s \tag{2.34.b}$$

where $C_{dil}(k+1)\cdot Q_{dil}(k+1) = C_{dil,in}(k)\cdot Q_{dil,in}(k)$ is the product of dilute inlet concentration and dilute inlet flow-rate (i.e. the salt molar flow rate). The solution

flow-rates feed to the pile were selected imposing an inlet velocity of 1 cm/s within the channel, typical values adopted in RED systems [2.51].

Membranes properties for NaCl solutions

The IEMs behaviour is characterized by means of several properties already presented in the previous sections. The most relevant properties are the *permselectivity* (α_{AEM} or α_{CEM}), which identifies the selectivity of membrane to the passage of counter ions and rejections of co-ions, and *electrical resistance* (R_{AEM} or R_{CEM}). Other important features are the *water* and *salt permeability (*P_w and P_s*)* generate the osmotic water flux and diffusive salt flux, respectively. Manufacturers usually provide the values of these properties in reference conditions. In this study, Fujifilm's membranes were considered. Constant values of water and salt permeability, were fixed (see Table 2.1) while concentration dependent correlations were evaluated both permselectivity and electric resistance.

Numerical details and model validation

The integrated model was implemented in *Engineer Equation Solver* (EES) using the Euler's method to solve the mass balance equations. In this method, the numerical accuracy of the solution depends on the discretization length (Δx), which is a function of N_k and L. In order to identify the N_k value which gives a good compromise in accuracy and time calculation, a grid dependence analysis was performed, considering the longest RED unit presented in this study (L=1.0 m, b=0.1 m). As shown in Figure 2.10, the grid dependence analysis indicates that a discretization length of 2.5cm (40 steps) is small enough to get stable and accurate solutions. Further, passing from 40 to 50 discretization intervals the power output varies less than 1% and concentration profiles are practically overlapped

Table 2.1 *Physical and geometrical parameters assigned for simulations*

Parameter		Value
P_w[(1)]	[m/(Pa·s)]	$2.22 \cdot 10^{-14}$
δ_m	[m]	$1.25 \cdot 10^{-4}$
P_s	[m^2/s]	$1 \cdot 10^{-12}$
α_{av}[(2)]	[%]	95-98
$R_{AEM}=R_{CEM}$[(3)]	[ohm cm^2]	1.5
f	[-]	1.5625

[(1)]experimental values measured @ ref. conditions: T=25°C, C_{conc}=3 M C_{dil}=0.05M.
[(2)]experimental values measured @ ref. conditions: T=25°C, C_{conc}=0.5M C_{dil}=0.05M.
[(3)]experimental values measured @ ref. conditions: T=25°C, C_{sol}=2 M.

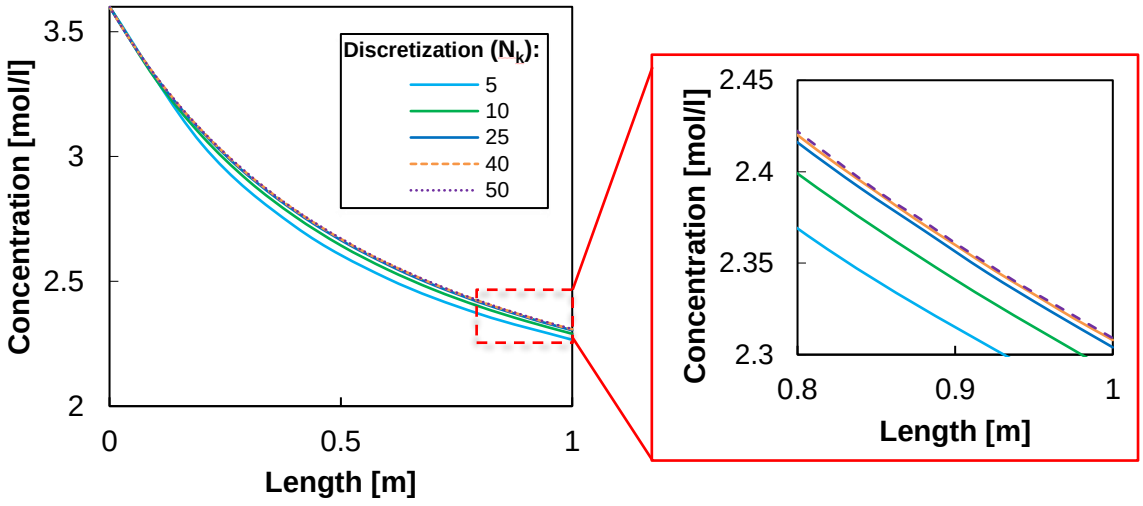

Figure 2.10 *Grid dependence analysis: Concentration profiles along the channel and b) Power output calculated varying the number of grid elements (N_k). RED stack of 1000 cell pairs 0.1 m x 1.0 m, $v_{conc}=v_{dil}$ =1 cm·s^{-1}, C_{conc}=3.6 M C_{dil}=0.05M.*

The mono-dimensional RED model was validated by comparison with experimental results reported in the literature [2.52]. Figure 2.11 (a) and 2.11 (b) show the trend of experimental stack voltages and power densities for three different

concentrate concentrations (i.e. 0.5, 2 and 5 M) as function of the current and the stack voltage, respectively.

Model predictions fit very well experimental trends, thus indicating the reliability of the model in the investigated concentration range. Model was further validated with different flow velocities and stack dimensions, resulting always in a good agreement between predictions and experiments. However, relevant graphs are omitted for the sake of brevity.

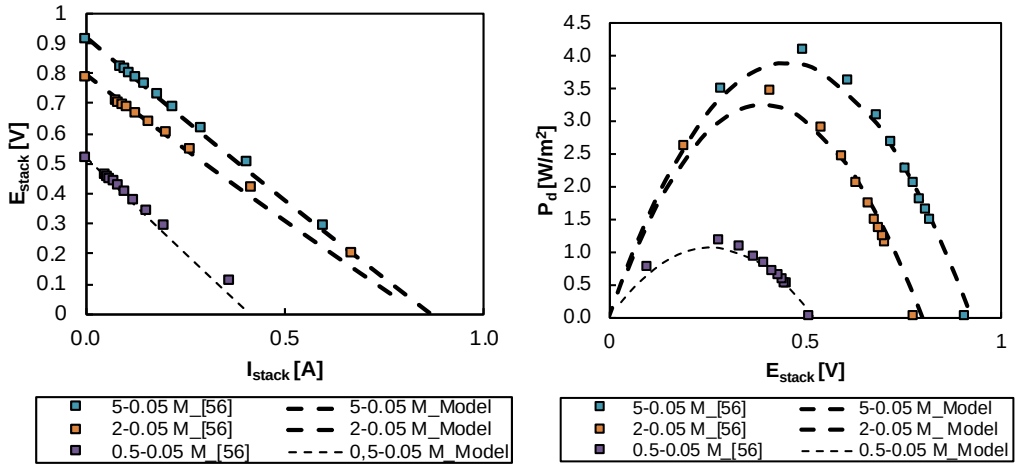

Figure 2.11 *Comparison between experimental trends and model predictions for (a) stack potential and (b) power density* [2.52] *. Operating conditions: 5 cell pairs-stack, A=0.1×0.1m^2; C_{dil}=0.05 M; C_{conc}=0.5M, 2M, 5M; v_{dil}=v_{conc}=2 cm/s, T=25°C.*

2.3.3 Description of the irreversibility sources and exergy modelling of the RED process

In a RED process, variations in the exergy content of the feed streams occur due to the variation in solutions composition within the unit. Only if the process was operated reversibly, exergy would be entirely converted into electric power. In real cases, some detrimental phenomena inevitably occur, which reduce the exergy performance of RED units. Irreversibility sources involved in the RED process are summarized in Table 2.2.

The non-ideal behaviour of ionic exchange membranes (IEMs) is responsible for uncontrolled mixing effects (i.e. water and salt diffusion), which consume part of the exergy content of the inlet streams without producing electrical power. Non-ideal IEMs permselectivity also affects the generated electromotive force, which is reduced when non-unitary permselectivity. Furthermore, membrane and solution resistances are also significant causes of exergy destruction (i.e. internal ohmic losses). Others sources of irreversibility are the friction losses inside the channels, the activation losses in the electrodic compartments and the parasitic currents in the distribution manifolds. However, frictions losses are dramatically dependent on channels configuration (not considered in this study) and the latter two losses have a minor role in the overall process exergy performance and have been thus neglected in the present analysis.

Table 2.2 *Description of the irreversibility sources involved in the RED process.*

Irreversibility source	**Description**
Permselectivity	Exergy destruction due to the non-ideal behaviour of the IEMs, which affects interface equilibria, thus also reducing the electro-motive force and the overall generated stack voltage.
Ohmic losses	Exergy destruction due to the power dissipated due to the internal stack resistance
Water flux	Exergy destruction associated to the water flux across the IEMs which reduces the available salinity gradient for power production.
Salt flux	Exergy destruction associated to the salt flux across the IEMs which reduces the available salinity gradient for power production.
Friction losses & pumping power	Exergy dissipated for flowing of the solutions within the channels.
Parasitic currents	Exergy destruction due to the generation of parasitic currents through the stack which dissipating part of the electrical energy generated inside the system

Activation losses	Exergy destruction due to the electrical potential drops often related to redox reactions in the electrodic compartments (smaller with reversible redox couples, as in the present case).

In order to assess the magnitude of exergy destruction occurring within RED unit, an exergy balance is set out as shown in Equation (2.35). The variation of the chemical exergy of dilute and concentrate solutions is described on the LHS, while the electrical power produced P_{RED} and the exergy destroyed due to irreversibility $Ir_{,RED}$ appear on the RHS.

$$\left(\dot{B}_{conc,in}-\dot{B}_{conc,out}\right)+\left(\dot{B}_{dil,in}-\dot{B}_{dil,out}\right)=\dot{P}_{RED}+\dot{I}r_{RED} \tag{2.35}$$

Since a RED unit often operates at environmental temperature (i.e. approximately T_0= 298 K) and pressure (i.e. approximately p_0=100 kPa), only chemical exergy was considered throughout the analysis, neglecting physical exergy variations within the unit. As already mentioned, no pressure drops were considered in the model, thus pressure was considered constant along the channels. Seawater composition of 38000 ppm NaCl was considered as reference state to evaluate the chemical exergy of each stream.

Equations (2.36) and (2.37) provide the chemical exergy variation of concentrate and dilute solutions respectively. Both equations were derived from general equation of chemical exergy presented in Chapter 1, where the chemical potential are explicitly expressed in terms of activities of salt and water.

$$\dot{B}_{conc,in}-\dot{B}_{conc,out}=RT_0\left[\begin{array}{l}\dot{N}_{conc,in}\left(x_{s,conc}^{in}\,v\ln\left(\frac{a_{s,conc}^{in}}{a_{s,0}}\right)+x_{w,conc}^{in}\ln\left(\frac{a_{w,conc}^{in}}{a_{w,0}}\right)\right)-\\-\dot{N}_{conc,out}\left(x_{s,conc}^{out}\,v\ln\left(\frac{a_{s,conc}^{out}}{a_{s,0}}\right)+x_{w,conc}^{out}\ln\left(\frac{a_{w,conc}^{out}}{a_{w,0}}\right)\right)\end{array}\right] \tag{2.36}$$

$$\dot{B}_{dil,in} - \dot{B}_{dil,out} = RT_0 \left[\begin{array}{l} \dot{N}_{dil,in} \left(x_{s,dil}^{in} \nu \ln\left(\frac{a_{s,dil}^{in}}{a_{s,0}} \right) + x_{w,dil}^{in} \ln\left(\frac{a_{w,dil}^{in}}{a_{w,0}} \right) \right) - \\ -\dot{N}_{dil,out} \left(x_{s,dil}^{out} \nu \ln\left(\frac{a_{s,dil}^{out}}{a_{s,0}} \right) + x_{w,dil}^{out} \ln\left(\frac{a_{w,dil}^{out}}{a_{w,0}} \right) \right) \end{array} \right] \tag{2.37}$$

Exergy efficiency can be defined as the ratio of electric power produced to the variation of chemical exergy of dilute and concentrate solutions.

$$\eta_{ex} = \frac{\dot{P}_{RED}}{\left(\dot{B}_{conc,in} - \dot{B}_{conc,out}\right) + \left(\dot{B}_{dil,in} - \dot{B}_{dil,out}\right)} \tag{2.38}$$

Exergy efficiency indicates the percentage of the chemical exergy consumed within RED stack which is usefully converted into electrical power. As it will be shown in the next section, it represents a thermodynamic indicator and its numerical values provide insights into the effect of irreversibility for alternative design and operating scenarios of RED process.

2.4 Exergy Analysis: Results

The integrated model was used to perform several sensitivity analyses in order to investigate the effects of irreversibility (permselectivity, water and salt fluxes), membrane properties, flow arrangements (co and counter current) and residence times on the exergy efficiency of the process. A stack of 1000 cell pairs was considered in order to neglect the effect of the electrodic compartment resistance (R_{blank}) on RED performance.

2.4.1Effect of the irreversibility sources

Exergy analysis of RED unit was carried out considering a stack equipped with square membranes of 0.1 m x 0.1 m. As regards concentrate and dilute feeds, *NaCl* solutions with a concentration respectively of 3.6 M and 0.05 M were supplied to the RED unit; the inlet velocity of both streams was set equal to 1 cm/s. As previously

shown, the main sources of irreversibility involved in RED process are: (i) *internal ohmic losses* (P_{loss}), which identify the power dissipated by the internal resistance; (ii) *membrane permselectivity* (α), which affects the electro-motive force of the pile; (iii) *diffusive salt flux* (J_s), which identifies the co-ions transport across the IEM; *water flux* (J_w), which identifies the flux of water across the IEM.

In order to assess at which extent each irreversibility source affects the exergy performance of the unit, four different scenarios were considered:

- *Scenario A:* the pile is equipped with ideal membranes (P_w=0 m/ (Pa·s), P_s=0 m^2/s and α=1) and internal resistance of the pile is considered as unique source of irreversibility;
- *Scenario B*: the effect of non-ideal permselectivity on the Donnan potential generation at the IEMs-solutions interface (and consequentially, on the electro-motive force) is considered still neglecting diffusive water and salt fluxes in the transport equations (P_w=0 m/ (Pa·s), P_s=0 m^2/s and $\alpha \neq 1$);
- *Scenario C:* non-ideal permselectivity and diffusive salt flux ($P_s=10^{-12}$ m^2/s and $\alpha \neq 1$), conversely, diffusive water flux is neglected (P_w=0 m/ (Pa·s));
- *Scenario D:* the pile is equipped with real membranes all the irreversibility sources are considered ($P_w=2.22 \cdot 10^{-14}$ m/ (Pa·s), $P_s=10^{-12}$ m^2/s and $\alpha \neq 1$).

In Figure 2.12 (a) and 2.12 (b), the exergy efficiency and power density are shown for each simulated scenario as a function of the ratio between external load and internal stack resistance (R_L/R_{int}). More specifically, when considering R_L/R_{int} equal to 0, the stack operates in short-circuit condition (SC): in this case the maximum electrical current through the pile is observed and no electrical power is produced. Conversely, when R_L/R_{int} tend to ∞, the pile works in open circuit condition (OC): in this case, the stack voltage is equal to the electro-motive force and no electric current circulates in the system. As shown in Figure 2.12 (b), the maximum power density is obtained when the ratio

R_L/R_{int} is approximately 1, with stack voltage equal to half of the Open Circuit Voltage [2.53].

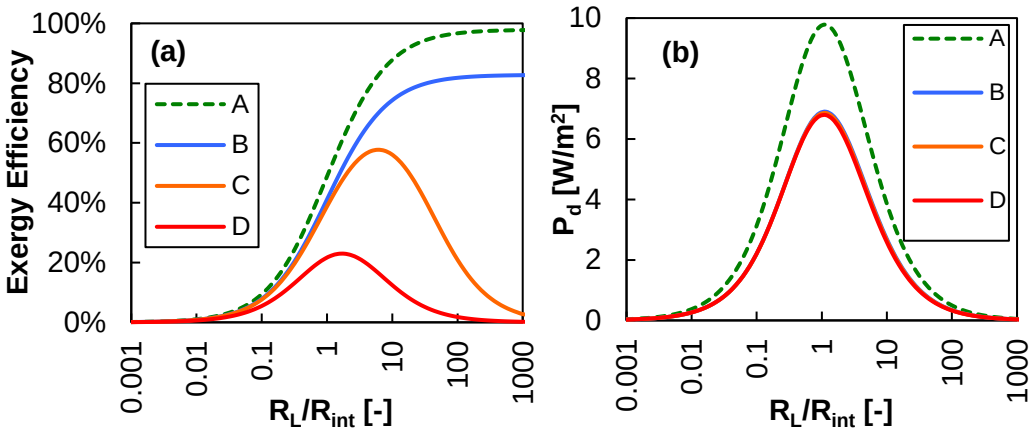

Figure 2.12 *Exergy Efficiency (a) and Power density (b) as a function of external/internal resistance ratio for each examined scenario. RED stack 0.1 m x 0.1 m, v_{conc}=v_{dil}=1 cm·s^{-1}, C_{conc}=3.6 M C_{dil}=0.05M.*

As shown in Figure 2.12 (a), when considering SC condition in all simulated scenarios, exergy efficiency is equal to zero; indicating that the exergy consumed is entirely destroyed by the pile internal resistance without producing electric power.

In *Scenario A*, RED exergy efficiency increases with the R_L/R_{int} ratio. It is worth noting that exergy efficiency is nearly equal to unity when approaching OC condition; this result indicates that under this circumstance, reversible transformation occurs within the pile, all the irreversibility approach to zero. When R_L/R_{int}=1, the exergy efficiency is equal to 0.5: half of the exergy consumption is converted into electric power by the pile, being the other fraction dissipated due to internal stack resistance.

In *Scenario B* the effect of non-ideal membrane permselectivity on the electrical voltage is considered. Comparing to case A, a similar trend for exergy efficiency is observed but lower values are obtained due to the decrease in the electro-motive force and power output.

In both A and B scenarios maximum exergy efficiency is obtained in OC condition though the power output from the stack tends to zero. In this ideal condition, solutions are virtually mixed through reversible steps with an infinitesimal current thus reducing to zero ohmic dissipations.

As previously mentioned, in case C salt diffusion and permselectivity were considered as sources of irreversibility; conversely, for case D, also osmosis was included. In these scenarios the exergy efficiency curve increases with the R_L/R_{int} ratio up to reach the maximum value slightly after the maximum power density (R_L/R_{int} between 1 and 10), while decreasing for higher values of R_L/R_{int}. In fact, a larger external load lowers the current (and the power output), while uncontrolled mixing phenomena keep the same absolute influence on mixing dissipation (as shown in Figure 2.13 (a)) as they only depend on salinity gradient and salt/water permeability of *IEMs*. This leads to a dramatic increase of the relative effect of irreversible phenomena on exergy efficiency, so that, in OC conditions, exergy efficiency approaches zero: even with zero electric current exergy can be totally destroyed within the stack due to uncontrolled mixing phenomena.

For the case of a pile equipped with real membranes, Figure 2.13 (a) and (b) show a breakdown of the exergy consumption (Ex_{cons}) into exergy destruction due to uncontrolled mixing phenomena ($E_{mix,}$), exergy destruction due to ohmic dissipation (P_{cons}), and electric power produced. It is interesting to observe that irreversibility magnitude due to uncontrolled mixing phenomena is almost equal for all operating conditions. Under these conditions, E_{mix} is dominated by the osmotic water transport, with migrative salt flux playing only a minor role in enhancing it when current is increased, contrarily to the effect of electro-osmosis (directly promoted by the current increase). Indeed, osmosis and salt diffusion phenomena themselves are indirectly reduced when current increase due to the reduction of concentration gradients. All these complex and counteracting phenomena lead to only a slight reduction (less than

5%) of $E_{mix,}$ observed when increasing stack current. Conversely, exergy destruction due to internal ohmic resistance strongly affects exergy performance when load resistance lower than internal stack resistance is considered, whereas being negligible when approaching OC condition.

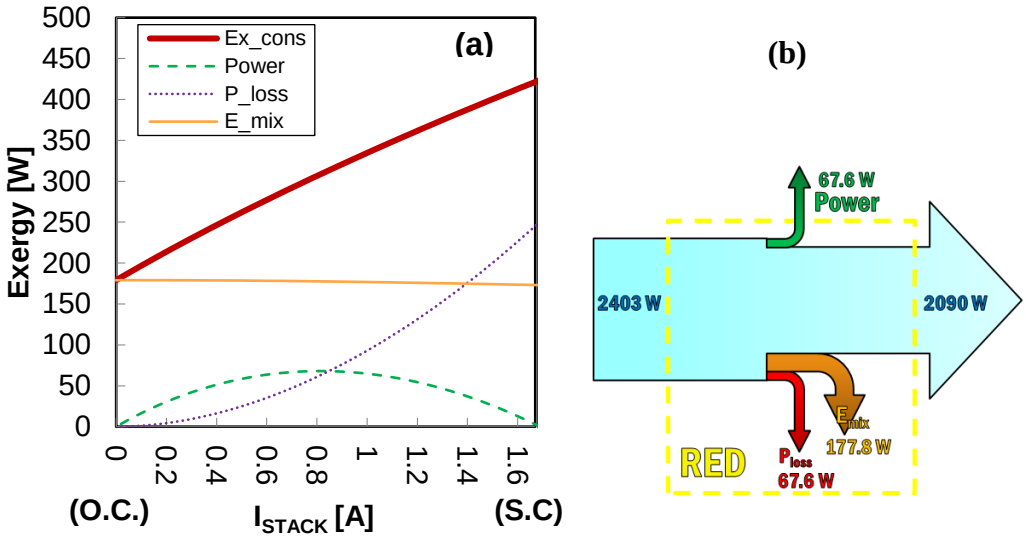

***Figure 2.13**. (a) Variation of exergy consumption/conversion terms as a function of the electrical current (I) showing total consumed exergy (Ex_cons), power output (Power), ohmic losses (P_loss) and uncontrolled mixing phenomena (E_mix); (b) Graphical* breakdown of exergy consumption/conversion terms for a real RED process in maximum power conditions. RED stack 0.1 m x 0.1 m, v_{conc}=v_{dil}=1 cm·s^{-1}, C_{conc}=3.6 M C_{dil}=0.05M, scenario D.

2.4.2 Effect of membrane properties

In the previous analysis, fixed values of membrane salt and water permeability were considered. It is worth assessing at which extent the RED exergy performance may change when membrane parameters change. To this aim, a sensitivity analysis changing salt and water permeability was carried out. Results are shown in Figure 2.14 (a) and (b); particularly:

- In Figure 2.14 (a) salt permeability P_s was fixed equal to P_s=10^{-12} m^2/s, while water permeability P_w was varied in the range of 2.22·10^{-14} to 0 m/(Pa·s). It can

be observed how exergy efficiency improves from 23% to 58%, when water flux is null: this proves a strong impact of water flux on the unit performance.

- In Figure 2.14 (b), a similar analysis was carried out by considering a reduced salt permeability from 10^{-12} m^2/s to 10^{-11} m^2/s. Results show a strong reduction of exergy efficiency due to the increase of salt flux effect. In particular, when no osmosis is considered (i.e. P_w = 0), the exergy efficiency is reduced from 58% to 27%.

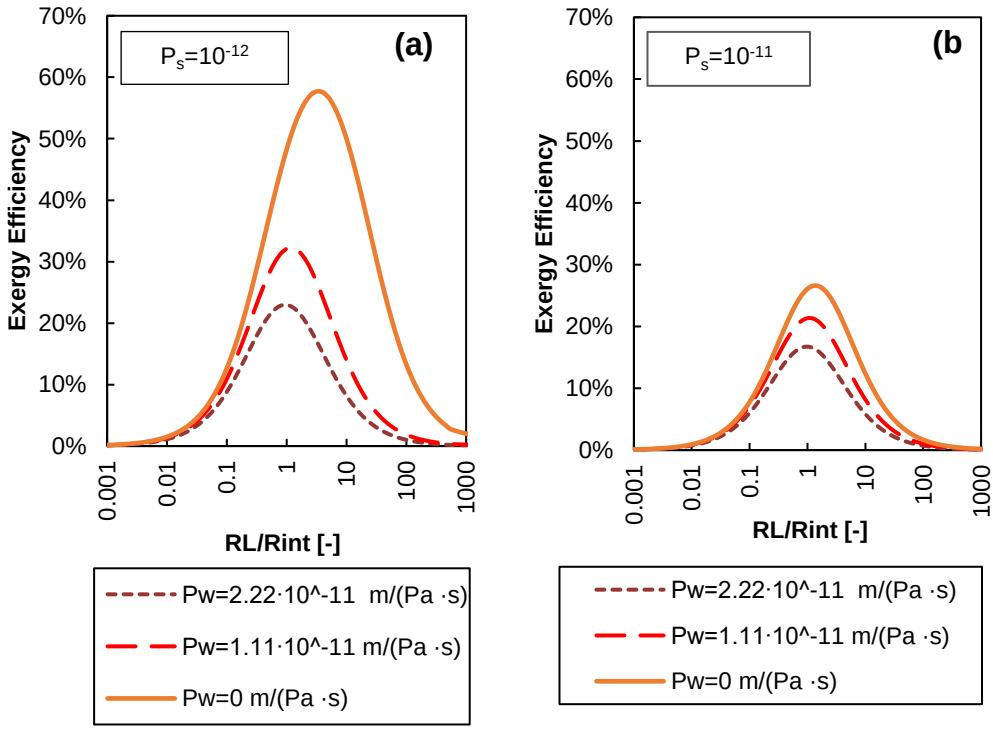

Figure 2.14 *Effect of diffusive water and salt flux on RED exergy efficiency varying the resistance ratio and assuming three different values for P_w ($2.22 \cdot 10^{-14}$, $1.11 \cdot 10^{-14}$ and 0 m/(Pa·s)) fixing P_s equal to 10^{-11} m^2/s in fig. (a) and 10^{-12} m^2/s in fig. (b). RED stack 0.1 m x 0.1 m, $v_{conc}=v_{dil}=1$ $cm \cdot s^{-1}$, $C_{conc}=3.6$ M $C_{dil}=0.05$M.*

2.4.3 Effect of concentrate and dilute concentrations

In this section, the influence of inlet concentrations of the feed solutions on the exergy efficiency and power density is analysed. As already mentioned, one of the main advantages of RED-HE is the possibility of selecting suitable feed concentrations which could lead to a more performing process. For the analysis, the same stack configuration previously proposed was considered.

First, the effect of the concentrate was evaluated by gradually decreasing its concentration from 5.0 to 0.5 M while keeping a dilute fixed to 0.05 M. Conversely, in the second analysis, the dilute concentration was increased from 0.05 to 1 M while keeping a concentrate at 3.6 M. Exergy efficiency and Power densities for all simulated cases are shown in Figure 2.15 (a)-(b) and Figure 2.16 (a)-(b).

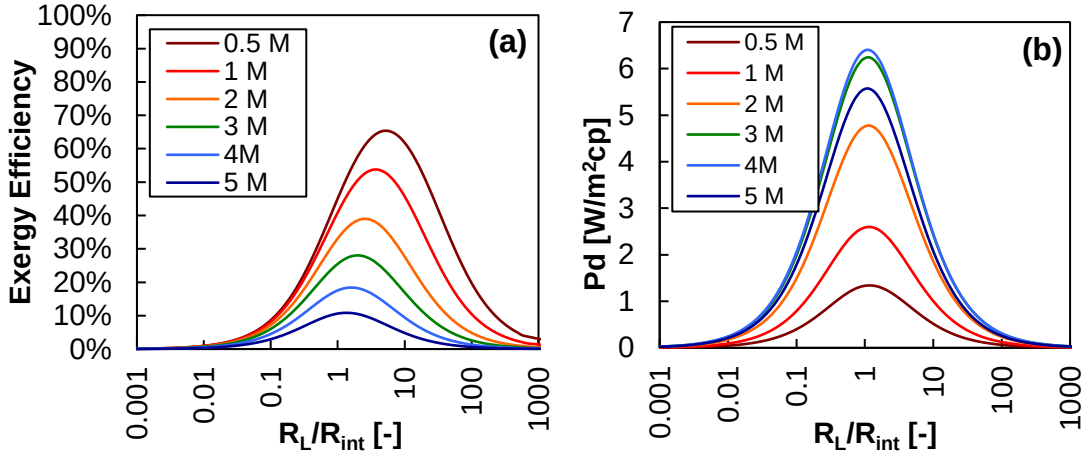

Figure 2.15 *Exergy efficiency (a) and Power density (b) as function of the R_L/R_{int} ratio and the concentrate solution concentration, setting the dilute concentration at 0.05 M. RED stack 0.1 m x 0.1 m, $v_{conc}=v_{dil}=1$ cm·s^{-1}, scenario D.*

Results shown in Figure 2.15 (a) and (b) indicate that a decrease in concentrate from 5.0 to 0.5 M produces a substantial improvement of exergy efficiency from 11% at 5.0 M to 65% for 0.05 M. Conversely, as regards power density, results show a decrease from 5.6 W/m^2 at 5 M to 1.3 W/m^2 at 0.5 M. The highest power density, equal

to 6.4 W/m^2, is observed for 3.6 M. This result is related to the membranes resistance, which approaches a minimum value near 3.6 M.

A reduction of salinity gradient reduces both electrical power produced and also osmosis and salt diffusion across the membranes.

The improvements of exergy efficiency when reducing concentrated solution indicate that even though less electrical power is produced, a better exploitation of exergy occurs due to a reduction of the exergy destroyed by uncontrolled mixing phenomena.

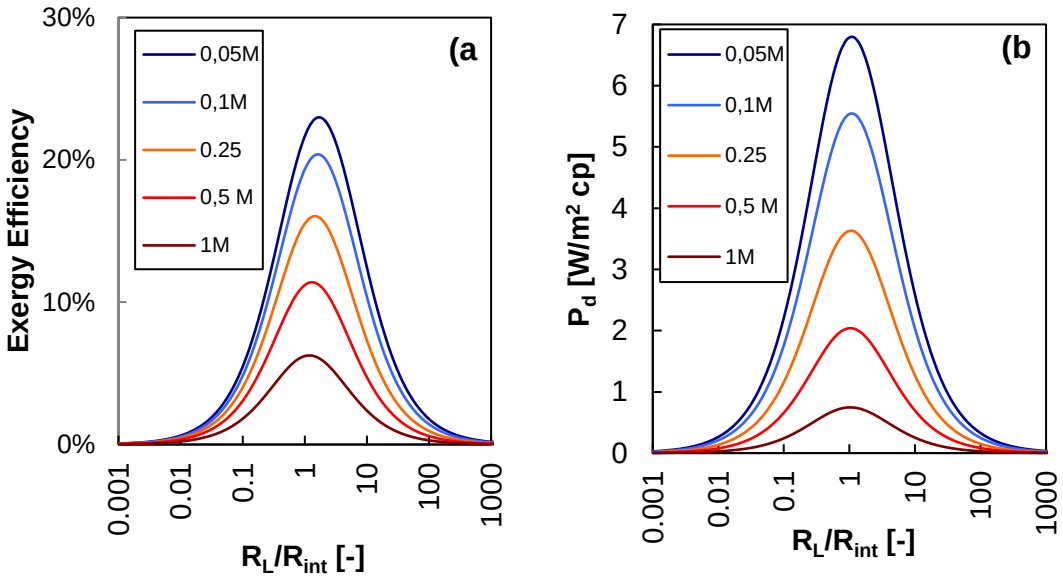

***Figure 2.16**. Exergy efficiency (a) and Power density (b) as function of the R_L/R_{int} ratio and the dilute solution concentration, setting the concentrate concentration at 3.6 M. RED stack 0.1 m x 0.1 m, $v_{conc}=v_{dil}=1$ cm·s^{-1}, scenario D.*

As shown in Figure 2.16 (a) and (b), different results were obtained when the dilute concentration was increased from 0.05 M to 1.00 M, while keeping the concentrate solution at 3.6 M (value maximizing the power). Also, in this case, the reduction in concentration difference produces a decrease of the uncontrolled mixing phenomena, however, the increase of the dilute solution concentration strongly affects OCV values. The OCV is dependent from the logarithm of the ratio between concentrate and dilute

solution. Thus, an increase of dilute solution concentration while keeping constant the concentrate solution, affect OCV much more a decrease in concentrate while keeping constant the dilute concentration.

As a consequence, the heavy reduction in OCV drastically reduces the electric power produced by the unit which is not compensated by the decrease of irreversibility generated by osmosis and salt diffusion.

2.4.4 Effect of flow arrangement and cell pair length

This section presents a sensitivity analysis to highlight the influence of flow arrangement and cell pair length (L) on RED performance.

The analysis was performed considering counter-current and co-current flow arrangement; also, stack length was varied between 0.1 m and 1.0 m; as it regards stream inlet velocity, a value equal to 1 $cm \cdot s^{-1}$ was set. Concentration values equal to 3.6 M and 0.05 M were considered for concentrate and dilute, respectively.

When changing channel length from 0.1 m to 1.0 m, residence time of solutions within the stack increases. Then, more electrical power is produced by the pile as well more water and salt are exchanged between solutions due to osmosis and salt fluxes.

Considering a stack length less or equal to 0.4 m (i.e. short stack), though for the two flow arrangements a different profile concentration is observed, the value of electrical outputs is practically the same due to low residence time of both stream within the stack. In these cases, flow arrangement does not influence RED exergy performance, which equals to 23 % for both cases. Conversely, when channel length is greater than 0.5 m, concentration profiles along stack length differ for the two cases. In both configurations, the exergy efficiency decreases when increasing the channel length. This trend can be easily explained by means of the following consideration: due to higher residence time within the stack, more electric power is produced as well more irreversibility is generated by uncontrolled mixing phenomena. In these cases, the exergy destruction

occuring due to osmosis and salt diffusion is not offset by the increase in electric power generation, thus a decrease of RED performance occurs.

Still, it is possible to observe how the counter-current stack is more performing than the co-current when incresing stack length. As shown in Figure 2.17 (a)-(b) moving from 0.1 m to 1 m, exergy destruction is nearly equal for both cases, conversely, power production is greater in counter-current arrangement.

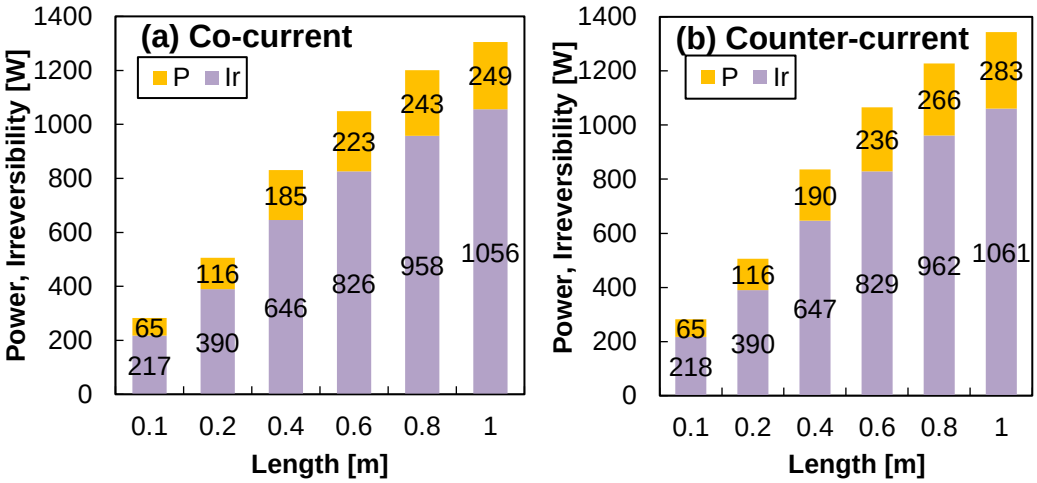

***Figure 2.17**. Power generation and Irreversibility losses in Co-current (a) and Counter-current (b) arrangements; (c) comparison of exergy efficiency with the two arrangements. RED stack L m x 0.1 m, C_{conc}=3.6 M C_{dil}=0.05M, v_{conc}= v_{dil}=1 cm·s^{-1}, scenario D.*

2.4.5 Effect of feed velocity

In this section, the effect of the different residence times on exergy efficiency and gross power is analysed. In the first scenario, the dilute velocity was set at 2 cm/s, while the concentrate velocity is increased from 0.4 cm/s to 2 cm/s. Conversely, in the second scenario, the concentrate velocity was set at 2 cm/s while dilute velocity was varied from 0.4 cm/s to 2 cm/s.

As shown in Figure 2.18 (a)-(b), when increasing dilute velocity from 0.4 to 2.0 cm/s, an increase of both power and exergy efficiency is observed. In particular, the

exergy efficiency improves from 8.6 % to 22%, while the power increases from 76 W to 440 W. The low residence time of dilute solution within the stack results in a low average dilute concentration; thus, a significant increase of the electric voltage is observed, with negligible variation of the uncontrolled mixing phenomena.

Conversely, the increase of the concentrate velocity results in a slight increase of power output and a decrease of the exergy efficiency as shown in Figure 2.18b. In particular, increasing concentrate velocity from 0.4 to 2 cm/s, the exergy efficiency decreases from 31% to 22%, while the power increases from 360 W to 440 W. In this case, the higher average concentration of concentrate along the channels results, in a slight increase in pile electric voltage. However, exergy destruction due to uncontrolled mixing phenomena is not balanced by the increase of electric power, leading to a less performing unit results. Interestingly, at very low v_{conc}, η_{ex} reaches the highest value indicating that the reduction of uncontrolled mixing phenomena (due to the much lower average concentration in the channel) dominates the overall efficiency being more important than the reduction of power output also caused by the lower average concentration.

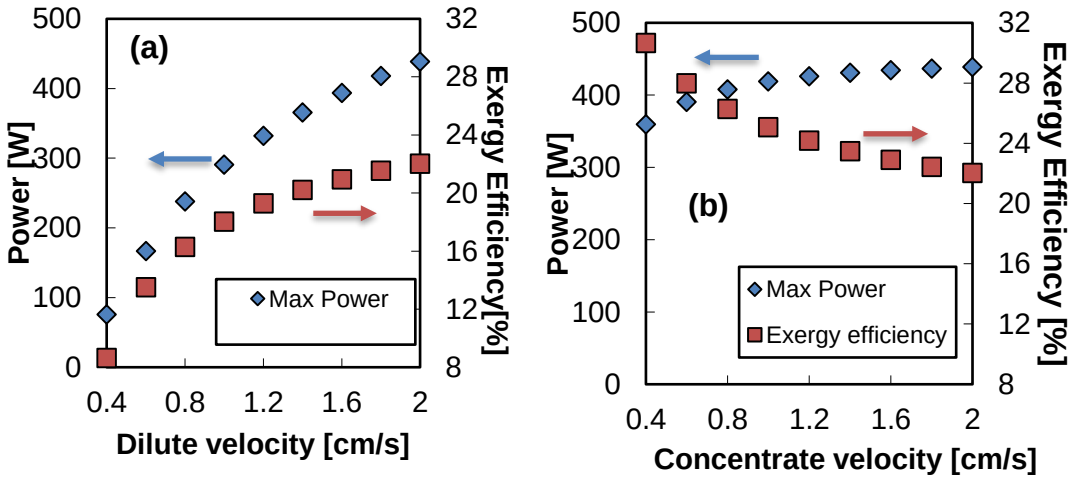

***Figure 2.18**. Maximum power and corresponding Exergy efficiency as function of: (a) dilute velocity, setting concentrate velocity at 2 cm·s^{-1}; (b) concentrate velocity, setting dilute velocity at 2 cm·s^{-1}. RED stack 1 m x 0.1 m Counter-Current arrangement, C_{conc}=3.6 M C_{dil}=0.05M, scenario D.*

The effect of varying saline solution concentrations (0.5-5 M for concentrate and 0.01-1M for dilute) were investigated including high concentrated cases which required a more complex formulation of the model than those reported so far in the literature [2.54]. Also, the effect of operating conditions (e.g. external load, residence time and flow-arrangements) on exergy efficiency was investigated, to support stack design and to identify optimal operating conditions to be used in RED process in closed loop applications aiming at reducing exergy consumption and increasing global process efficiency. In fact, in closed-loop applications exergy consumption related to the RED unit has to be restored by a thermal regeneration unit using low-grade waste heat. The higher the exergy destruction in the RED unit, the higher the thermal power required in the regeneration unit.

2.5 On the main outcomes of the analysis

The exergy analysis of the RED process has allowed for investigating RED performance in terms of exergy efficiency and power yield in a wide range of system operations.

The analysis has been supported by a robust 1-D model for the description of all the transport phenomena within the RED unit assuming real membrane properties. The effect of each IEM property (i.e. permselectivity, water and salt permeability, and resistance) is quantitatively identified, providing relevant information for orienting future development of better performing IEMs.

As concern the non-ideal behaviour of IEMs, the water flux due to osmosis has been found to have the most detrimental effect on exergy efficiency when salinity gradient above 2M was adopted, with exergy losses (at maximum Power output conditions) accounting for 60-80% of total losses in the worst scenarios. A less dramatic, yet important effect is associated with diffusive salt flux.

The influence of the following operating parameters has been assessed by means of a sensitivity analysis:

(i) *Concentration of Feed Solutions*: the analysis showed that exergy efficiency heavily increases when decreasing dilute concentration, while it increases when decreasing the salinity of concentrate feed reaching values up to 25% and 60% in the two cases. Power density decreases from values around 6.5 W/m^2_{cp} to slightly above 1 W/m^2_{cp} respectively, due to the salinity gradient reduction across the membranes.

(ii) Finally, different *residence times for dilute and concentrate* have been considered in each simulated scenario. Results indicate that exergy efficiency increases for longer residence time in the concentrate channel, while it decreases for shorter residence time in the dilute.

Finally, the effect of *counter-current* and *co-current flow arrangement* on the process performance has been assessed. Results indicate how the counter-current could lead to better performance only for long-length stack design. Conversely, for short-length design, no differences among them have been observed.

References

[2.1] A.C.G. Micale, ed., Sustainable Energy from Salinity Gradients, Woodhead Publishing, 2016.

[2.2] B.E. Logan, M. Elimelech, Membrane-based processes for sustainable power generation using water, Nature. 488 (2012) 313.

[2.3] F. Helfer, C. Lemckert, Y.G. Anissimov, Osmotic power with Pressure Retarded Osmosis: Theory, performance and trends – A review, J. Memb. Sci. 453 (2014) 337–358. doi:10.1016/J.MEMSCI.2013.10.053.

[2.4] R.E. Pattle, Production of Electric Power by mixing Fresh and Salt Water in the Hydroelectric Pile, Nature. 174 (1954) 660–660.

[2.5] A. Achilli, T.Y. Cath, A.E. Childress, Power generation with pressure retarded osmosis: An experimental and theoretical investigation, J. Memb. Sci. 343 (2009) 42–52.

[2.6] F. Giacalone, A. Cipollina, F. Grisafi, A. Tamburini, G. Vella, G. Micale, Characterization of pressure retarded osmosis lab-scale systems, Desalin. Water Treat. 57 (2016) 22994–23006.

[2.7] M. Tedesco, C. Scalici, D. Vaccari, A. Cipollina, A. Tamburini, G. Micale, Performance of the first reverse electrodialysis pilot plant for power production from saline waters and concentrated brines, J. Memb. Sci. 500 (2016) 33–45.

[2.8] L. Gurreri, A. Tamburini, A. Cipollina, G. Micale, CFD analysis of the fluid flow behavior in a reverse electrodialysis stack, 48 (2012) 390–403.

[2.9] A. Campione, L. Gurreri, M. Ciofalo, G. Micale, A. Tamburini, A. Cipollina, Electrodialysis for water desalination: A critical assessment of recent developments on process fundamentals, models and applications, Desalination. 434 (2018) 121–160.

[2.10] R. Ashu, S. Pawlowski, J. Veerman, K. Bouzek, E. Fontananova, S. Velizarov, J. Goulão, K. Nijmeijer, E. Curcio, Progress and prospects in reverse electrodialysis for salinity gradient energy conversion and storage, 225 (2018) 290–331.

[2.11] A.B. Yaroslavtsev, V. V. Nikonenko, Ion-exchange membrane materials: Properties, modification, and practical application, Nanotechnologies Russ. 4 (2009) 137–159.

[2.12] T. Xu, K. Hu, A simple determination of counter-ionic permselectivity in an ion exchange membrane from bi-ionic membrane potential measurements: Permselectivity of anionic species in a novel anion exchange membrane, Sep. Purif. Technol. 40 (2004) 231–236.

[2.13] S. Zhu, R.S. Kingsbury, D.F. Call, O. Coronell, Impact of solution composition on the resistance of ion exchange membranes, J. Memb. Sci. 554 (2018) 39–47.

[2.14] A.H. Galama, D.A. Vermaas, J. Veerman, M. Saakes, H.H.M. Rijnaarts, J.W. Post, K. Nijmeijer, Membrane resistance: The effect of salinity gradients over a cation exchange

membrane, J. Memb. Sci. 467 (2014) 279–291.
[2.15] A.M. Benneker, T. Rijnaarts, R.G.H. Lammertink, J.A. Wood, Effect of temperature gradients in (reverse) electrodialysis in the Ohmic regime, J. Memb. Sci. 548 (2018) 421–428.
[2.16] R.W. Baker, 2 Membrane Transport Theory, in: Membr. Technol. Appl., 2004: pp. 15–87.
[2.17] J.N. Weinstein, F.B. Leitz, Electric Power from Differences in Salinity: The Dialytic Battery, Science (80-.). 191 (1976) 557–559..
[2.18] R. Audinos, Electrodialyse inverse. Etude de l'energie electrique obtenue a partir de deux solutions de salinites differentes, J. Power Sources. 10 (1983).
[2.19] J. Jagur-Grodzinski, R. Kramer, Novel process for direct conversion of free energy of mixing into electric power, Ind. Eng. Chem. Process Des. Dev. 25 (1986) 443–449.
[2.20] J. Veerman, M. Saakes, S.J. Metz, G.J. Harmsen, Reverse electrodialysis: Performance of a stack with 50 cells on the mixing of sea and river water, J. Memb. Sci. 327 (2009) 136–144.
[2.21] D.A. Vermaas, M. Saakes, K. Nijmeijer, Doubled power density from salinity gradients at reduced intermembrane distance, Environ. Sci. Technol. 45 (2011) 7089–7095.
[2.22] P. Długołecki, A. Gambier, K. Nijmeijr, M. Wessling, Practical Potential of Reverse Electrodialysis As Process for Sustainable Energy Generation, Environ. Sci. Technol. 43 (2009) 6888–6894.
[2.23] M. Tedesco, C. Scalici, D. Vaccari, A. Cipollina, A. Tamburini, G. Micale, Performance of the first reverse electrodialysis pilot plant for power production from saline waters and concentrated brines, J. Memb. Sci. 500 (2016) 33–45.
[2.24] O. Scialdone, C. Guarisco, S. Grispo, A.D. Angelo, A. Galia, Investigation of electrode material – Redox couple systems for reverse electrodialysis processes. Part I: Iron redox couples, J. Electroanal. Chem. 681 (2012) 66–75.
[2.25] P. Długołecki, P. Ogonowski, S.J. Metz, M. Saakes, K. Nijmeijer, M. Wessling, On the resistances of membrane, diffusion boundary layer and double layer in ion exchange membrane transport, J. Memb. Sci. 349 (2010) 369–379.
[2.26] N.P. Berezina, N.A. Kononenko, O.A. Dyomina, N.P. Gnusin, Characterization of ion-exchange membrane materials : Properties vs structure, 139 (2008) 3–28.
[2.27] H.J. Cassady, E.C. Cimino, M. Kumar, M.A. Hickner, Specific ion effects on the permselectivity of sulfonated poly(ether sulfone) cation exchange membranes, J. Memb. Sci. 508 (2016) 146–152.
[2.28] G.M. Geise, H.J. Cassady, D.R. Paul, B.E. Logan, M.A. Hickner, E. Logan, M.A. Hickner, Specific ion effects on membrane potential and the permselectivity of ion exchange membranes, Phys. Chem. Chem. Phys. 16 (2014) 21673–21681.
[2.29] A. Daniilidis, D.A. Vermaas, R. Herber, K. Nijmeijer, Experimentally obtainable energy from mixing river water, seawater or brines with reverse electrodialysis, Renew. Energy. 64 (2014) 123–131.
[2.30] M. Tedesco, A. Cipollina, A. Tamburini, G. Micale, Towards 1 kW power production in a reverse electrodialysis pilot plant with saline waters and concentrated brines, J. Memb. Sci. 522 (2017) 226–236.
[2.31] A. Tamburini, A. Cipollina, M. Papapetrou, A. Piacentino, G. Micale, 7 – Salinity gradient engines, in: Sustain. Energy from Salin. Gradients, 2016: pp. 219–256.
[2.32] A. Tamburini, M. Tedesco, A. Cipollina, G. Micale, M. Ciofalo, M. Papapetrou, W.

Van Baak, A. Piacentino, Reverse electrodialysis heat engine for sustainable power production, Appl. Energy. 206 (2017) 1334–1353.
[2.33] M. Bevacqua, A. Tamburini, M. Papapetrou, A. Cipollina, G. Micale, A. Piacentino, Reverse electrodialysis with NH4HCO3-water systems for heat-to-power conversion, Energy. (2017).
[2.34] R.S. Kingsbury, K. Chu, O. Coronell, Energy storage by reversible electrodialysis: The concentration battery, J. Memb. Sci. 495 (2015) 502–516.
[2.35] W.J. van Egmond, U.K. Starke, M. Saakes, C.J.N. Buisman, H.V.M. Hamelers, Energy efficiency of a concentration gradient flow battery at elevated temperatures, J. Power Sources. 340 (2017) 71–79.
[2.36] Baobab Project: Blue Acid/Base Battery: Storage and recovery of renewable electrical energy by reversible salt water dissociation. European H200 project. Contract n° 73118, (n.d.).
[2.37] J. Veerman, R.M. de Jong, M. Saakes, S.J. Metz, G.J. Harmsen, Reverse electrodialysis: Comparison of six commercial membrane pairs on the thermodynamic efficiency and power density, J. Memb. Sci. 343 (2009) 7–15.
[2.38] J. Veerman, M. Saakes, S.J. Metz, G.J. Harmsen, Reverse electrodialysis: A validated process model for design and optimization, Chem. Eng. J. 166 (2011) 256–268.
[2.39] N.Y. Yip, D.A. Vermaas, K. Nijmeijer, M. Elimelech, Thermodynamic, Energy Efficiency, and Power Density Analysis of Reverse Electrodialysis Power Generation with Natural Salinity Gradients, Environ. Sci. Technol. 48 (2014) 4925–4936.
[2.40] D.A. Vermaas, J. Veerman, N.Y. Yip, M. Elimelech, M. Saakes, K. Nijmeijer, High efficiency in energy generation from salinity gradients with reverse electrodialysis, ACS Sustain. Chem. Eng. 1 (2013) 1295–1302.
[2.41] K. S.A., Engineering equation solver, (2010).
[2.42] T.Z. Fahidy, Activity coefficients in electrolyte solutions (second edition), edited by Kenneth S. Pitzer, 1991, 542 + vi pages, CRC Press, Boca Raton, FL; ISBN 0-8493-5415-3. Price: US$ 195.00, Can. J. Chem. Eng. 71 (1993) 494–494. doi:10.1002/cjce.5450710328.
[2.43] K.S. Pitzer, J.C. Peiper, R.H. Busey, Thermodynamic Properties of Aqueous Sodium Chloride Solutions, J. Phys. Chem. Ref. Data. 13 (1984) 1–102. doi:10.1063/1.555709.
[2.44] D.G. Archer, Thermodynamic propertis of the KCl + H2O system, J. Phys. Chem. Ref. Data. 28 (1999) 1–16.
[2.45] T. Isono, MEASUREMENTS OF DENSITY, VISCOSITY, AND ELECTROLYTIC CONDUCTIVITY OF CONCENTRATED AQUEOUS ELECTROLYTE SOLUTIONS - 1. LiCl, NaCl, KCl, RbCl, CsCl, MgSO//4, ZnSO//4 AND NiSO//4., Rika Gaku Kenkyujo Hokoku. 56 (1980).
[2.46] M. Tedesco, A. Cipollina, A. Tamburini, I.D.L. Bogle, G. Micale, A simulation tool for analysis and design of reverse electrodialysis using concentrated brines, Chem. Eng. Res. Des. 93 (2015) 441–456.
[2.47] L. Gurreri, M. Ciofalo, A. Cipollina, A. Tamburini, W. Van Baak, CFD modelling of profiled-membrane channels for Reverse Electrodialysis, (2014).
[2.48] L. Gurreri, A. Tamburini, A. Cipollina, G. Micale, M. Ciofalo, Flow and mass transfer in spacer-filled channels for reverse electrodialysis: a CFD parametrical study, J. Memb. Sci. 497 (2016) 300–317.
[2.49] L. Gurreri, A. Tamburini, A. Cipollina, G. Micale, M. Ciofalo, Pressure drop at low

Reynolds numbers in woven-spacer-filled channels for membrane processes : CFD prediction and experimental validation, 61 (2017) 170–182.
[2.50] S. Pawlowski, J.G. Crespo, S. Velizarov, Pressure drop in reverse electrodialysis : Experimental and modeling studies for stacks with variable number of cell pairs, J. Memb. Sci. 462 (2014) 96–111.
[2.51] M. Tedesco, E. Brauns, A. Cipollina, G. Micale, P. Modica, G. Russo, J. Helsen, Reverse electrodialysis with saline waters and concentrated brines: A laboratory investigation towards technology scale-up, J. Memb. Sci. 492 (2015) 9–20.
[2.52] M. Micari, M. Bevacqua, A. Cipollina, A. Tamburini, W. Van Baak, T. Putts, G.M. Micale, Effect of different aqueous solutions of pure salts and salt mixtures in reverse electrodialysis systems for closed-loop applications, J. Memb. Sci. in press (2018).
[2.53] J. Veerman, D.A. Vermaas, 4 – Reverse electrodialysis: Fundamentals, in: Sustain. Energy from Salin. Gradients, 2016: pp. 77–133.
[2.54] N.Y. Yip, M. Elimelech, Thermodynamic and Energy Efficiency Analysis of Power Generation from Natural Salinity Gradients by Pressure Retarded Osmosis, (2012).

Chapter 3

Exergy Analysis of Reverse Electrodialysis Heat Engine with Multi-Effect Distillation Regeneration Stage

In this chapter, exergy analysis is applied to a Reverse ElectroDialysis Heat Engine integrated with a Multi-Effect Distillation Regeneration Stage in order to provide insights into the performance potential of this innovative technology.

First, a brief introduction to the concept and purposes of *Salinity Gradient Power Heat-Engine* is provided with a description of the main regeneration strategies proposed. After that, a detailed description of the modelling of the integrated system is provided, with particular attention devoted to the Multi-Effect Distillation unit.

A base case scenario is selected, from which the main performance indicators (exergy and thermal efficiency, power density, specific thermal energy consumption, etc.) have been determined in Chapter 2. Later, the main sources of irreversibility are analysed as function of the external to internal resistance ratio in the RED unit. Also, sensitivity analyses of the exergy efficiency, at both global and component level, are carried out. In particular, the inlet concentration and velocity of the concentrate and dilute solutions to the RED stack are investigated, together with the stack geometry (length, width and thickness of the membranes). Finally, the exergy efficiency with future high-performing membranes is evaluated and compared with results obtained for current membranes.

3.1 Introduction on Salinity Gradient Power Heat-Engines (SGP-HEs)

In Chapter 2, the *Salinity Gradient Power* technology was introduced. It was pinpointed the capability of this technology to exploit natural salinity gradients in order to produce electricity [3.1]-[3.2]. The major drawback of the SGP technologies when operated in an *open-loop configuration*, is the unavailability of natural salinity gradients in areas of power demand. This limit can be overcome by introducing the concept of *Salinity Gradient Power-Heat Engine* (SGP-HE). In Figure 3.1, a simplified scheme is shown in order to get an idea about this technology. An SGP-HE consist of two main components: the SGP unit and the Thermal Regeneration Unit (TRU). The TRU aims at restoring the concentrations of the solution exiting the SGP unit at the values they exhibit at the SGP inlet. This process is achieved by fueling the TRU with low-temperature heat (usually among 40°C and 100°C).

This aspect is the main innovation of this technology since it can be operated in a temperature range where not many alternatives exist. To this regard, a cascading approach could be adopted in those applications where heat at higher temperatures is first used for industrial processes, and then the resulting waste heat is supplied to the salinity gradient engines. In Fact, according to [3.3] and [3.4], a large amount of heat from industrial processes is rejected to the atmosphere without further use, and this amount accounts up to 70% of the input energy. This valuable heat (usually termed *waste heat*), may be used to generate electricity by ad-hoc heat-to-power technologies. To this regard, there are several techniques available [3.4] other than SPG-HE, such as organic Rankine cycle, Kalina cycle, along with other novel methods under investigation [3.5], [3.6]. Other advantages are related to the use of the SGP-Heat Engine (RED-HE): (i) *ad-hoc* artificial saline solutions can be adopted, in order to increase the salinity gradient (i.e. the driving force of the process) and to significantly improve the performance of the RED unit, (ii) problems related with the fouling of the membranes when using natural water sources are solved, (iii) the RED-HE does not

have any environmental risk associated with the operation at high temperature with hazardous substances, and (iv) it is not constrained by the water resource location.

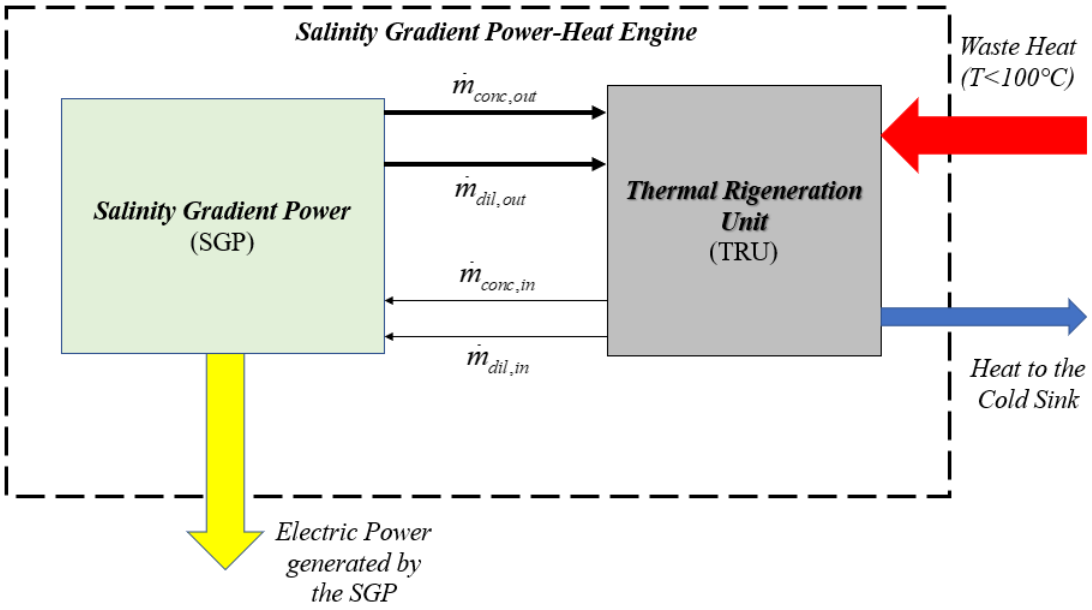

Figure 3.1 *Schematic of SGP-HE technology (adapted from* [3.7]*)*

The concept of SGP-HE dates back to 1975 when Loeb S. [3.8] proposed the idea of producing electric power from waste heat via SGP. At the very beginning, he proposed an SGP-HE based on Pressure Retarded Osmosis [3.8], and some years later in 1979, he introduced the RED heat engine concept [3.9]. However, only in 2012 research renewed the interest to this technology [3.1].

SGP Heat-Engines can be devised by using one of the three SGP technologies, i.e. *pressure retarded osmosis* (PRO), *reverse electrodialysis* (RED), and *accumulator mixing* (AccMix). Among them, the Reverse ElectroDialysis-HE is being investigated within the framework of the EU project RED-Heat-to-Power [3.10]. In this project, two different strategies are currently investigated for the regeneration unit: (i) "*solute extraction*" strategy, which can adopt Thermolytic Salts (such as ammonium bicarbonate) or Salt Precipitation Processes and (ii) the "*solvent extraction*" strategy, which can use Multi-Effect Distillation (MED) or Membrane Distillation (MD)

processes. Two simplified schemes of these two strategies are presented respectively in Figures 3.2 and 3.3. However, a brief description is worth and it is presented in the following subparagraphs.

3.1.1 Brief outline on "Solute Extraction" regeneration strategy

In Figure 3.2 a scheme of the solute extraction strategy is shown. Here, the solvent content passed from the dilute to the concentrate compartment due to osmotic phenomena, is restored by mixing the outlet-dilute solution with a suitable quantity of outlet-concentrate solution, indicated by m_1 in Figure 3.2. Obviously, this mixing lead to a further increase in the salt content of the outlet-dilute solution, which must be recovered by the regeneration unit. Then, with reference to Figure 3.2, the salt content of the concentrate solution is restored by extracting it from the dilute solution within the regeneration unit (RU), by means of a salt extraction process. This results in two exiting streams: m_5 which contains only the solute and $m_{dil,in}$, a solvent rich stream. Both of them regenerate the two input streams necessary for the SGP system operation.

The available regeneration methods based on the salt extraction strategy concern the use of ***thermolytic salts*** and ***salt precipitation processes***. For a sake of brevity, no details are here given about these processes. A thorough description can be found in [3.7].

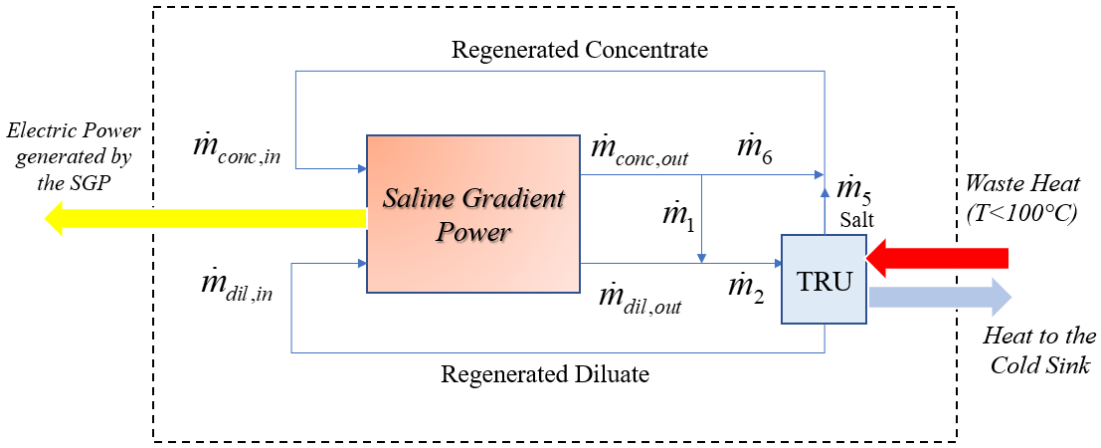

Figure 3.2 *Scheme of the Solute Extraction Strategy for SGP-HE (adapted from* [3.7]*)*

The RED-HE scheme with solute extraction has been analysed in literature by several authors. In 2012 Luo et al. [3.11] proposed a thermal-driven electrochemical generator for waste heat conversion to electricity, using a distillation column and ammonium bicarbonate as working fluid. The authors proved the feasibility of this integration and obtained a power density of 0.33 W/m^2 and an energy efficiency of 31%. In the same year Cusick et al. [3.12] presented a RED-HE using microbial cells and ammonium bicarbonate, with a continuous salinity regeneration of the solutions. They obtained a maximum power density of 5.6 W/m^2 using acetate, with an energy recovery of 30%, and 3 W/m^2 using domestic wastewater. Hatzell et al. [3.13] compared the power and hydrogen production in a closed-loop ammonium bicarbonate RED system. More recently, Bevacqua et al. [3.14] experimentally assessed the performance of a RED-HE using ammonium bicarbonate, and they obtained a maximum power density of 2.42 W/m^2 of cell pair at the lower feed flow velocity investigated (0.5 cm/s). They concluded that, although this technology can be comparable with the RED-HE with sodium chloride as working fluid, further improvement in the membrane's features should be accomplished. The same authors presented a model for the previous described cycle, which was validated by experimental data. In addition, they performed a sensitivity analysis of the performance as function of the inlet solutions concentration and velocity. The results obtained indicated that a power density of 9 W/m^2 and a global exergy efficiency of 22% could be reached with the best performing conditions and enhanced membranes.

3.1.2 Brief outline on "Solvent Extraction" regeneration strategies

As shown in Figure 3.3, the salt content is restored by mixing the outlet-concentrate solution with a suitable quantity of outlet-dilute solution, indicated by $m_{1,}$ which leads to a further unbalance of the solvent content in the outlet-concentrate solution. Then, the solvent content of the dilute solution is restored by extracting it from concentrate

solution within the regeneration unit. With reference to Figure 3.3, the amount of salt transferred in the SGP unit from the concentrate solution to the dilute one is rebalanced by the preliminary addition of stream m_1 to $m_{conc,out}$. The resulting stream m_2 is subjected to the necessary solvent excess extraction within the regeneration unit, which results into two exiting streams (i.e. one solute rich $m_5$and one solute free m_4), which regenerate the two input streams necessary for SGP system operation.

To this aim, two separation processes are suitable: ***evaporative processes*** such as Multi-Effect Distillation and ***temperature-driven membrane processes*** such as Membrane Distillation.

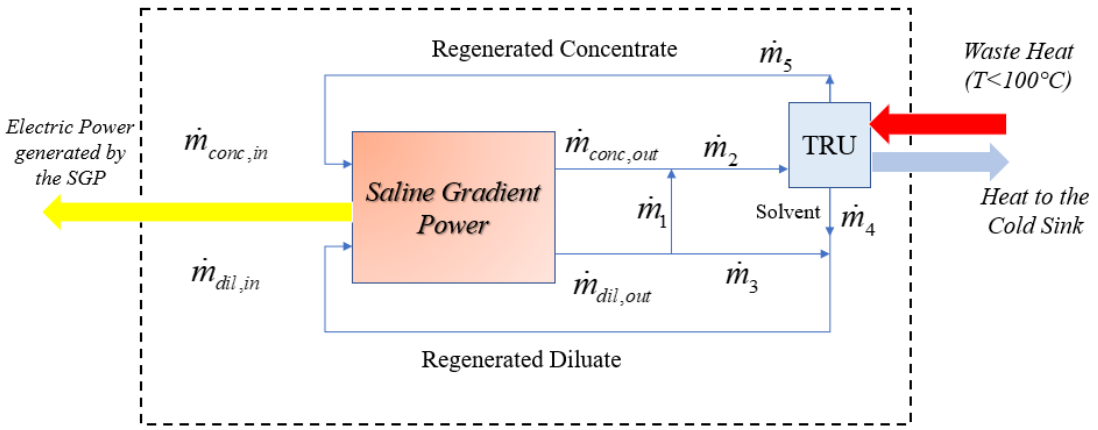

Figure 3.3 *Scheme of the Solvent Extraction Strategy for SGP-HE (adapted from [3.7])*

Regarding RED-HE with solvent extraction scheme, only few works can be found in the literature. In particular, Long et al. [3.15] analysed a RED unit coupled to a membrane distillation regeneration stage. They performed simulations by varying the heat source temperature and NaCl feed concentration, and obtained a maximum thermal efficiency value of 1.15% for the highest NaCl inlet concentration (5 mol/kg). Also, Tamburini et al. [3.16] presented a performance evaluation of the RED-HE system considering different salt solutions and regeneration methods. In particular, the MED process was considered using a simplified model and efficiency indicators

(specific thermal energy consumption) obtained from literature data. Preliminary results showed that the closed-loop heat engine can reach thermal and exergetic efficiencies up to 15% and 85%, respectively, using enhanced membranes. Therefore, the potential of the RED-MED scheme as electric power production process using waste heat as fuel, was highlighted. More recently, Hu et al. [3.17] presented an energetic analysis of the RED-MED integrated system. They found that the global energy efficiency could reach 1.01% with inlet brackish solution at 95°C and 3.75 mol/kg, using 10 MED effects.

3.2 Description and modelling of the integrated system RED-MED

Among *Solvent Extraction* processes, the Multi-Effect Distillation represents a possible solution for restoring the initial concentration of solution exiting the RED stack. The description of the integrated system is thus organized in this paragraph: (i) *Multi-effect distillation* plant (ii) *Reverse-Electrodialysis* unit and (iii) the integrated RED-MED.

3.2.1 Multi-effect distillation plant

The multi-effect distillation technique consists essentially in a sequence of evaporation and condensation processes taking place inside vessels (effects), each one at lower pressure and temperature than the previous. This thermal separation technology, high energy-intensive, has been widely used in the food and chemical industry since the beginning of the twentieth century, and after the 1950's, has been applied for seawater desalination as well. One of the first MED mathematical models was proposed by El-Sayed and Silver [3.18], based on simplifying assumptions such as constant properties of solutions during the process. El-Dessouky et al. [3.19] presented a detailed MED steady-state model, based on mass and energy balances, including the dependence of the water thermophysical properties on the temperature

and concentration. Also, they considered the non-condensable gases effect on heat transfer, the thermodynamic losses of the vapor across the effects, and assumed constant heat transfer areas both for evaporators and preheaters. The model was used to analyse the effect of the main design and operation variables of the system. Results obtained showed that the performance of the MED is almost independent of the top brine temperature, while is greatly affected by the number of effects. Another interesting work was presented by Mistry et al. [3.20], where they developed a detailed model for MED process, providing more results, such as the temperature profiles along the unit. The model was implemented in Engineering Equation Solver (EES) [3.21], relying on fewer assumptions than that one of El-Dessouky. Recently, Ortega-Delgado et al. [3.22] presented an advanced forward-feed MED model able to simulate a wide range of design and operating conditions (high number of effects, top brine temperature, and salinity), particularly adequate for the analysis of the RED-MED integrated system. The multi-effect distillation process is a thermally driven separation process, generally applied in the desalination field to evaporate water from seawater. In the MED process the solvent vaporization is obtained in several equilibrium effects. In this case study, a *Forward-Feed MED* (FF-MED) arrangement has been selected, which is depicted in Figure 3.4. This configuration is preferred when dealing with high salinity feedwater and high heating steam temperatures, due to the thermal losses caused by the boiling point elevation (BPE) are lower (the maximum concentration is reached in the effect of lower temperature). Each effect is basically composed of a falling-film heat exchanger, a demister to remove the droplets from the vapour, and a preheater of the feedwater. The only external energy introduced in the process takes place in the evaporator of the first effect, generally with saturated steam at a certain temperature. In this case, waste heat coming from any industrial process is used as the input energy to the MED plant. The feedwater is sprayed over the tubes of the evaporator where part of the solvent is evaporated increasing the concentration of the remaining solution collected on the bottom of the effect. Part of the generated vapour

is used to preheat the feedwater, while the rest is directed to the second evaporator, where the same process is repeated, at lower pressure and temperature. Starting from the second effect, the incoming brine flashes generating additional flash vapour. The condensate is collected in the flashing boxes, where extra vapour is produced as well. The vapour generated in the last effect condenses in the end condenser, which is cooled by an external source, such as river water. Finally, the concentrated solution is extracted from the last effect and the distillate stream from the last flashing box.

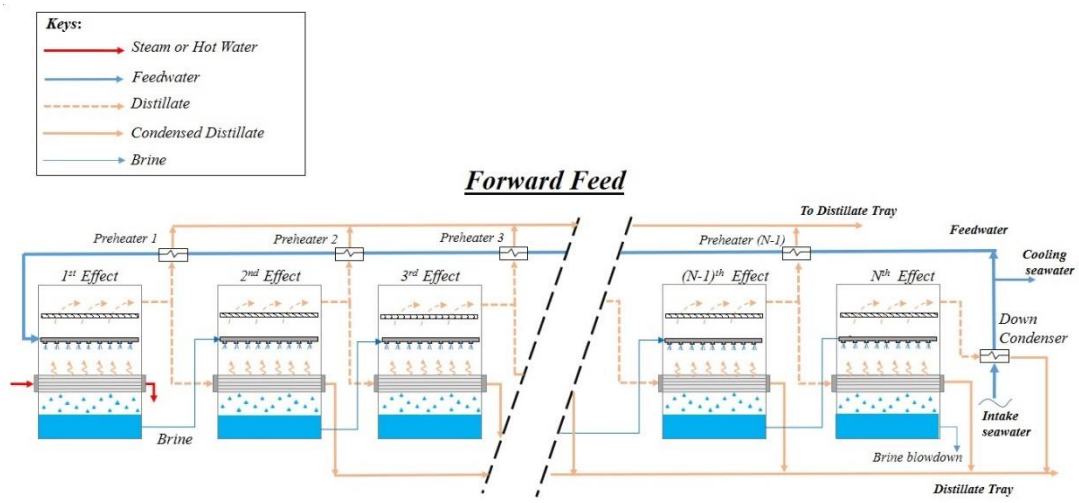

Figure 3.4 *Scheme of the multi-effect distillation unit.*

In this case study, the model from Ortega-Delgado et al. [3.22] has been adopted because it is very flexible, detailed and permits the simulation of high number of effects (>30) and high salinity feedwater. The model is based mainly on mass and energy balances applied on each component of the plant, along with the heat transfer equations for the heat exchangers (evaporators, preheaters and end condenser). Given a low number of inputs (which can be easily exchanged with the outputs), the model determines the main thermodynamic (temperatures, pressures, concentrations, flow rates, enthalpies, etc.) and design variables (heat exchanger areas, number of evaporator tubes, vapour velocities, pressure losses, etc.). A summary of the main

equations of the model are detailed in Table 3.1. The model establish several simplifying assumptions such as neglecting the thermal losses to the environment and the presence of non-condensable gases, assuming saturation conditions at the inlet and outlet of the evaporators, salt-free distillate, and also uses temperature-based correlations for the determination of the overall heat transfer coefficients of the heat exchangers [3.23]. More details about the model are provided in the selected reference [3.22].

Table 3.1 *Representative equations of the MED model.*

Equation		**Comment**
$\dot{m}_F = \dot{m}_B + \dot{m}_D$	(3.1)	Global mass balance
$\dot{m}_F X_F = \dot{m}_B X_B$	(3.2)	Global salt balance
$\dot{m}_D = \sum_{i=1}^{N} \dot{m}_{Di} + \sum_{i=2}^{N} \dot{m}_{FEi}$	(3.3)	Total distillate production
$\dot{m}_{Bi} = \dot{m}_{B,i-1} - \dot{m}_{Di} - \dot{m}_{FEi}$	(3.4)	Mass balance in effect i
$(1-\alpha_{i-1})\dot{m}_{T,i-1}\lambda_{c,i-1} + \dot{m}_{FBi}h''_{Vi} + \dot{m}_{B,i-1}h_{B,i-1} = (1-\alpha_i)\dot{m}_{T1}h'_{Vi} + \alpha_i\dot{m}_{Ti}h'_{ci} + \dot{m}_F\bar{c}_{p,preh,i}(t_{preh,i} - t_{preh,i+1}) + \dot{m}_{Bi}h_{Bi}$	(3.4)	Energy balance in effect i
$(1-\alpha_{i-1})\dot{m}_{T,i-1}\lambda_{c,i-1} = A_i U_{e,i}(T_{c,i-1} - T_i)$	(3.6)	Heat transfer equation evaporator i
$\dot{m}_F\bar{c}_{p,preh,i}(t_{preh,i} - t_{preh,i+1}) = \alpha_i\dot{m}_{Ti}\lambda'_{Vi} + \alpha_i\dot{m}_{Ti}\bar{c}_{p,BPE,i}(T'_{Vi} - T'_{Vsat,i})$	(3.7)	Energy balance on preheater i
$P_{Q,preh,i} = A_{preh,i}U_{preh,i}LMTD_{preh,i} = A_{preh,i}U_{preh,i}\frac{t_{preh,i} - t_{preh,i+1}}{ln\left(\frac{T'_{Vi} - t_{preh,i+1}}{T'_{Vi} - t_{preh,i}}\right)}$	(3.8)	Heat transfer equation evaporator i

The MED model also accounts for the pressure drop within the unit, it has been considered the total height to be overcome ($\Delta p_{MED,H}$), the restoration of the

atmospheric pressure at the exit ($\Delta p_{MED,out}$), and the pressure drop in the cooling process ($\Delta p_{MED,cooling}$) [3.24]. They have been calculated as follows:

$$\Delta p_{MED,H} = \rho \cdot g \cdot H \cdot N_{eff} \tag{3.9}$$

$$\Delta p_{MED,out} = p_{atm} - p_N \tag{1.10}$$

$$\Delta p_{MED,cooling} = \left(4 \cdot j_f \cdot \left(\frac{L}{d_i}\right) \cdot N_p + 4 \cdot N_p\right) \cdot \frac{1}{2} \rho v^2 \tag{3.11}$$

where H is assumed to be 1 m per effect, N_{eff} is the number of effects, p_N is the pressure in the last effect, j_f is the friction factor of the tube side, d_i is the internal diameter of the tubes, and N_p is the number of tube passes of the shell and tube condenser.

The thermal performance of the MED process can be obtained with using the *specific thermal energy consumption* (sE, kWh/m$^3_{distillate}$), defined as follows:

$$sE = \frac{\dot{m}_s \lambda_s}{\dot{m}_D / \rho_D} \cdot \frac{1}{3600} \tag{3.12}$$

3.2.2 Reverse ElectroDialysis Unit

For the RED unit, the model presented in Chapter 2 is adopted. A resume of the main representative equations is presented in Table 3.2. The model includes some simplifying assumptions such as considering a mono-dimensional system where the concentrations, fluxes, currents, etc. vary only along the channel length (L), which is discretized in N_k=40 calculation elements. Also, the parasitic currents have been neglected. Conversely, the effects of concentration polarization phenomena in the membranes and pressure drop along the channels have been here considered. Thermodynamic properties of the solutions, membrane properties, and polarization coefficients are reported in Appendix A of this chapter.

Table 3.2 *Main equations of the RED model.*

Equation		Description
$E_{cell}(k) = E_{CEM}(k) + E_{AEM}(k) = 2\alpha_{av}(k)\frac{R_g T}{F}\ln\left(\theta_H(k)\theta_L(k)\frac{m_H(k)\cdot\gamma_H(k)}{m_L(k)\cdot\gamma_L(k)}\right)$	(3.13)	Voltage generated in each k-element of the cell pair
$R_{cell}(k) = [R_H(k) + R_L(k) + R_{CEM}(k) + R_{AEM}(k)]\cdot\frac{1}{b\Delta x}$	(3.14)	Cell pair resistance of each k-element
$N_{cp}E_{cell}(k) = N_{cp}R_{cell}(k)\cdot i(k) + R_{blank}I + E_{stack}$	(3.15)	Kirchhoff's voltage law
$P_{gross} = I^2\cdot R_u$	(3.16)	Gross power
$P_{pump,RED} = \frac{\Delta p_H Q_H}{\eta_{p,H}} + \frac{\Delta p_L Q_L}{\eta_{p,L}}$	(3.17)	Pumping power
$P_{loss} = \sum_k R_{cell}(k)\cdot i^2(k) + R_{blank}\cdot I^2$	(3.18)	Ohmic losses
$J_s(k) = J_{mig}(k) + J_{diff}(k) = \frac{i(k)}{z\cdot F} + \frac{2P_s}{\delta_m}[C_H(k) - C_L(k)]$	(3.19)	Total salt flux
$J_w(k) = J_{osm}(k) + J_{eosm}(k) = -2\nu R_g T P_w[C_H(k)\phi_H(k) - C_L(k)\phi_L(k)] + n_H J_s(k)$	(3.20)	Water flux
$C_H(k+1)\cdot Q_H(k+1) = C_H(k)\cdot Q_H(k) - J_s(k)\cdot b\Delta x$	(3.21)	Salt balance concentrate channel
$\rho_H(k+1)\cdot Q_H(k+1) = \rho_H(k)\cdot Q_H(k) - J_w(k)\cdot b\Delta x\rho_w/M_w$	(3.22)	Global mass balance concentrate channel
$C_L(k)\cdot Q_L(k) = C_L(k+1)\cdot Q_L(k+1) + J_s(k)\cdot b\Delta x$	(3.23)	Salt balance dilute channel
$\rho_L(k)\cdot Q_L(k) = \rho_L(k+1)\cdot Q_L(k+1) + J_w(k)\cdot b\Delta x\rho_w + J_s(k)\cdot b\Delta x M_s$	(3.24)	Global mass balance dilute channel

As concern, the pressure drops (Δp) of the solutions within the RED concentrate and dilute channels have been calculated using the following expression:

$$f = \frac{\Delta p}{L}\cdot\frac{d_H}{\frac{1}{2}\rho v^2} \tag{3.25}$$

where d_h (m) is the hydraulic diameter (=$2\delta_{channel}$), L (m) the length of the channel, ρ (kg/m^3) the density of the solution, v (m/s) the velocity of the solution, and

f (-) the Fanning friction factor, which can be calculated as function of the Reynolds number [3.25].

3.2.3 Integration of RED unit with MED process

The RED unit and the MED plant are integrated as presented in Figure 3.5. Also, the RED-MED heat engine scheme proposed uses sodium chloride aqueous solutions.

At the outlet of the RED unit, the high concentrated solution has lost mass of salt, which passes to the dilute stream through the membranes. Conversely, the low concentrated solution has gained mass of salt. Therefore, two mixers (Mixer 1 and Mixer 2) are proposed to restore the salinity content of the solutions, although they consume part of the chemical exergy content of the two streams, reducing the efficiency of the process. In the Mixer 1 part of the outlet dilute (Q_{bypass}) is mixed with the outlet concentrate ($Q_{H,out}$), restoring the salt lost through the membranes. In Mixer 2, the distillate produced in the MED unit (Q_D) is mixed with the rest of the dilute solution ($Q_{L,Mixer2,in}$) re-establishing the initial dilute concentration ($Q_{L,in}$). The MED plant is used as a regeneration stage, rebuilding the initial concentrations of the solutions by evaporating the amount of solvent needed. By applying mass balances to the mixers and MED unit, the required bypass of dilute flow rate, distillate flow rate and the conversion ratio of the MED process are determined:

$$C_{H,out}Q_{H,out} + C_{L,out}Q_{bypass} = C_{H,in}Q_{H,in} \quad (3.26)$$

$$Q_{H,out} + Q_{bypass} = Q_{MED,in} \quad (3.27)$$

$$C_{MED,in}Q_{MED,in} = C_{H,in}Q_{H,in} \quad (3.28)$$

$$Q_{L,Mixer2,in} + Q_D = Q_{L,in} \quad (3.29)$$

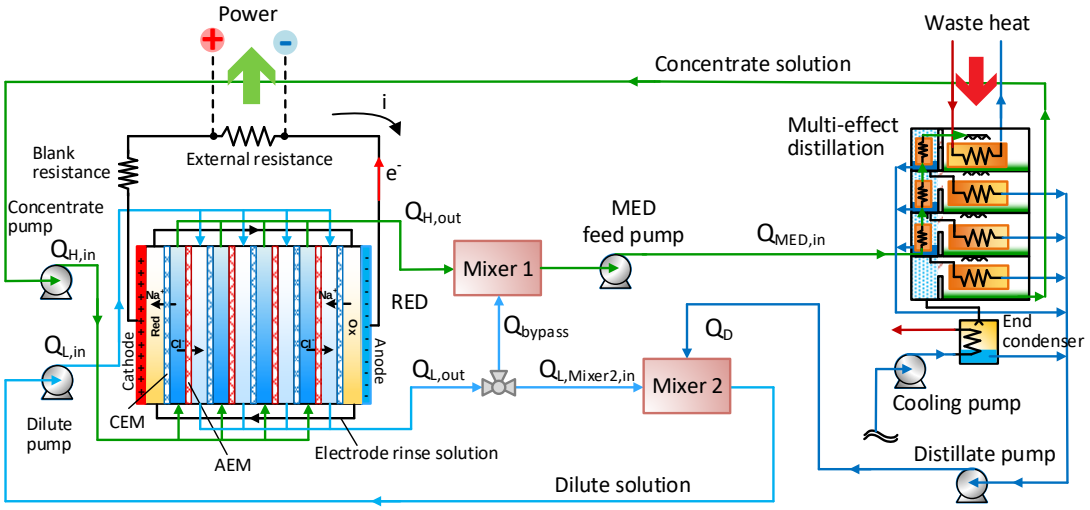

Figure 3.5 *Scheme of the closed-loop RED-MED Heat Engine*

The whole model has been implemented in *Engineering Equation Solver* (EES) software [3.21] and it is constituted by four sections:

(i) ***Reverse electrodialysis process model***, which is a mono-dimensional model describing all the main phenomena involved in the power generation process;

(ii) ***Multi-effect distillation process model*** based on the resolution of mass and energy balances applied on each component;

(iii) ***Model integration***, where the RED model and the MED model are coupled including also two mixing processes of the solutions;

(iv) ***Exergy analysis***, which provides the equations to evaluate the exergy flux and the exergy efficiency definition in each component of the system.

3.3 Exergy analysis of the RED-MED Heat Engine

Exergy analysis of the RED-MED Heat Engine allows for evaluating the exergy destroyed and lost in each sub-system. For each stream of matter in the system, the approach presented in Chapter 1 was used for evaluating thermal and chemical exergy.

3.3.1 Exergy efficiency definition

The exergetic (or exergy) efficiency definition of each component of the system follows the guidelines presented already in Chapter 1 [3.26]. For the RED-MED HE, the exergetic efficiency is calculated as the ratio of the exergy rate of the product ($\dot{B}_P$) and the exergy rate of the fuel ($\dot{B}_F$) as well.

$$\eta_X = \frac{\dot{B}_P}{\dot{B}_{Fuel}} = 1 - \frac{\dot{B}_L + \dot{B}_D}{\dot{B}_F} \tag{3.30}$$

where $\dot{B}_L$ represents the exergy of the loss streams (rejected to the environment without further use) and $\dot{B}_D$ is the exergy destruction due to irreversibility sources of the system. To this regard, the purpose of a RED unit is to generate electric power; therefore, the exergy product is defined as the net electric power produced (obtained by subtracting the pumping power consumption to the gross electric power). On the other hand, the fuel is the rate of exergy decrease of the inlet solutions (concentrate and dilute solutions):

$$\eta_{X,RED} = \frac{\dot{P}_{e,net}}{\left(\dot{B}_{Conc,in} - \dot{B}_{Conc,out}\right) + \left(\dot{B}_{Dil,in} - \dot{B}_{Dil,out}\right)} \tag{3.31}$$

The Mixer 1 restores the salt mass of the concentrate solution, lost within the RED unit, but decreases the concentration, as it involves the mixing of the outlet concentrate and part of the outlet dilute solution. Therefore, this component is needed but at the same time it reduces the performance of the system. For the Mixer 2, the mixing of the distillate from the MED unit and the remaining outlet dilute restores the concentration of the inlet dilute solution to the RED unit. The exergetic efficiency of the mixers is determined according to Equations. (3.32) and (3.33).

$$\eta_{X,mixer1} = \frac{\dot{B}_{Conc,mixer1,out}}{\dot{B}_{Conc,mixer1,in} + \dot{B}_{Dil,mixer1,in}} \quad (3.32)$$

$$\eta_{X,mixer2} = \frac{\dot{B}_{Dil,mixer2,out}}{\dot{B}_{dist,mixer2,in} + \dot{B}_{Dil,mixer2,in}} \quad (3.33)$$

The MED unit is used to restore the initial concentrations of the concentrate and dilute solutions, before entering in the RED unit. This component uses external heat for the thermal separation of the solute and the solvent, both with higher exergy than the feed stream. Therefore, the product of this subsystem can be defined as the increase of the exergy content of the outlet material streams (concentrate and distillate), with respect the inlet stream. The fuel is defined as the exergy content of the heat added to the MED (net value) plus the exergy of the pumping power consumed. Then overall exergy efficiency of the MED process is calculated as shown in Equation (3.34).

$$\eta_{X,MED} = \frac{\dot{B}_{Conc,MED,out} + \dot{B}_{dist,MED,out} - \dot{B}_{Conc,MED,in}}{\dot{B}_{Q,wh,in} - \dot{B}_{Q,wh,out} + \dot{B}_{W,pump,MED}} \quad (3.34)$$

The global exergy efficiency ($\eta_{X,g}$) is determined as the ratio between the exergy content of the net electric power produced by the RED unit and the exergy content of the heat supplied to the MED unit. It is worth stressing that the exergy produced by the RED unit is equal to the gross power produced minus the pumping power required by the RED unit and the MED unit. Due to the higher requirements of the MED pumping, this term will particularly affect the global performance of the system. Besides, the exergy rate of the waste heat can be expressed as function of the Carnot factor.

$$\eta_{X,g} = \frac{\dot{P}_{e,net}}{\dot{B}_{Q,wh,in} - \dot{B}_{Q,wh,out}} \quad (3.35)$$

The thermal efficiency of the overall system ($\eta_{th,g}$) is calculated as shown in Equation (3.36):

$$\eta_{th,g} = \frac{\dot{W}_{net}}{\dot{Q}_{wh}} \tag{3.36}$$

3.4 Analysis of results

In this section sensitivity analyses of the exergy efficiency of the overall RED-MED system and each component (RED stack, MED unit, Mixer 1 and Mixer 2) have been carried out, as function of the main operational and design variables. The effect of the inlet concentration and velocity of the solutions has been analysed, starting from a base case. In addition, the main sources of irreversibility have been investigated, i.e., internal resistance of the stack, permselectivity of the membranes, salt and water diffusivity fluxes, polarization phenomena, and pumping power consumption from the RED and MED units. Also, the influence on the performance of the stack geometry has been analysed. Finally, a case with improved membranes features is presented, in order to provide insight on the real exergy potential of the technology.

3.4.1 Definition of the "Base case"

As a first step, a base case is chosen to quantify the exergy potential of the system under common design and operational conditions. This scenario will be compared later on with the one obtained after the different sensitivity analyses, selecting the best obtained performing conditions for each case. The base case is selected from results obtained in Chapter 2, and the most representative input variables for the RED stack and MED unit are presented in Table 3. Note that the number of MED effects selected is limited by the inlet solutions concentration and velocity (high boiling point elevation).

Table 3.3 *Main inputs for the base case.*

Concept	**Value**
RED UNIT	
Cell pair	
Flow pattern, (-)	Counter-current
Number of cell pairs, (-)	1000
Width, b (m)	0.25
Length, L (m)	1
Blank resistance, R_{blank} ($\Omega \cdot m^2$)	$3.27 \cdot 10^{-3}$
Operation temperature, T (°C)	25
Solutions	
Concentrate inlet concentration, C_H (mol/L)	4.5
Dilute inlet concentration, C_L (mol/L)	0.05
Inlet concentrate velocity, v_H (cm/s)	1
Inlet dilute velocity, v_L (cm/s)	1
Membranes (Fujifilm Type 10)	
Thickness, δ_m (m)	$1.25 \cdot 10^{-4}$
Water permeability, L_p ($m^3/(m^2 \cdot s \cdot Pa)$)	$2.222 \cdot 10^{-14}$
Salt permeability coefficient, D_{salt} (m^2/s)	$4.52 \cdot 10^{-12}$
Spacer (Deukum)	
Concentrate spacer thickness, δ_H(m)	$1.5 \cdot 10^{-4}$
Dilute spacer thickness, δ_L(m)	$1.5 \cdot 10^{-4}$
Relative concentrate spacer volume, ϵ_H (-)	0.175
Relative dilute spacer volume, ϵ_L (-)	0.175
Shadow factor, sf (-)	1.563
MED UNIT	
Number of effects, (-)	22
Heating steam temperature, (°C)	100
Last effect temperature, (°C)	27
Terminal temp. difference preheater 1, (°C)	3
Terminal temp. difference end condenser, (°C)	3
Intake cooling water temperature, (°C)	15
Evaporators tube bundle	L: 1 m; ∅: 22 mm
End condenser tube bundle	L: 2 m; ∅: 25 mm
PUMPS	
Pumps efficiency, η_p (-)	0.8

Table 3.4 shows the results obtained after simulating the base case scenario. The low values of the exergy and thermal efficiencies (2.90% and 0.58%, respectively) are mainly due to the irreversibility sources and membrane properties, as it will be discussed in next sections. It is interesting to observe the low exergy efficiency of the RED stack, about 10%, while the MED unit reaches a relatively high performance, around 73%. Therefore, the exergy destruction in the RED stack is significant. The mixers 1 and 2 have also comparatively high exergy efficiencies, respectively equal to 91% and 76%, thus suggesting that the exergy destruction in these components is low under the considered conditions.

Table 3.4 *Results for the base case.*

Concept	**Value**
Global exergy efficiency, %	2.90
Global thermal efficiency, %	0.58
RED exergy efficiency, %	10.2
MED exergy efficiency, %	73.4
Mixer 1 exergy efficiency, %	91.1
Mixer 2 exergy efficiency, %	75.9
Net power, (W)	206.7
Heat rate, (W)	35,401

3.4.2 Effect of irreversibly sources

In Chapter 2, the effect of the main sources of irreversibility in a RED unit were analysed: the ohmic losses due to the internal resistance of the stack, the membrane permselectivity, the diffusive salt flux and the water flux across the IEMs. Here, the same analysis is proposed in order to obtain the exergy efficiency of the global system and components under the four scenarios proposed in Chapter 2, which quantifies the effect of each irreversibility source as function of the ratio between the external and internal resistance (R_L/R_{int}). Three additional scenarios (namely E, F and G) have

been considered in order to analyse the effect of the polarization phenomena, and RED and MED pumping power, respectively. For this analysis, same inputs as the base case have been taken (0.25 m × 1 m, 4.5 – 0.05 M, 1 cm/s – 1 cm/s), and the number of effects selected for each resistance ratio have been changed in order to adapt to the concentration factor (or recovery ratio) required. The seven scenarios selected are described as follows:

- *Scenario A.* Only the internal ohmic losses are considered (ideal membrane properties): $P_w = 0\ \mathrm{m/(Pa{\cdot}s)}$, $P_s = 0\ \mathrm{m/s^2}$, $\theta_H = 1$, $\theta_L = 1$, and $\alpha = 1$.
- *Scenario B.* The effect of the non-ideal permselectivity of the membranes is taken into account: $P_w = 0\ \mathrm{m/(Pa{\cdot}s)}$, $P_s = 0\ \mathrm{m/s^2}$, $\theta_H = 1$, $\theta_L = 1$, and $\alpha \neq 1$.
- *Scenario C.* In this case both the non-ideal permselectivity and diffusive salt flux are added, while neglecting the water flux: $P_w = 0\ \mathrm{m/(Pa{\cdot}s)}$, $P_s = 10^{-12}\ \mathrm{m/s^2}$, $\theta_H = 1$, $\theta_L = 1$, and $\alpha \neq 1$.
- *Scenario D.* This case adds the water diffusive flux: $P_w = 2.22 \cdot 10^{-14}\ \mathrm{m/(Pa{\cdot}s)}$, $P_s = 10^{-12}\ \mathrm{m/s^2}$, $\theta_H = 1$, $\theta_L = 1$, and $\alpha \neq 1$.
- *Scenario E.* The polarization effect is included in this scenario: $P_w = 2.22 \cdot 10^{-14}\ \mathrm{m/(Pa{\cdot}s)}$, $P_s = 10^{-12}\ \mathrm{m/s^2}$, $\alpha \neq 1$, $\theta_H \neq 1$, and $\theta_L \neq 1$
- *Scenario F.* In this case the pumping power consumption of the RED stack (concentrate and dilute solution pumps) is considered.
- *Scenario G.* The pumping power consumption of the MED unit (feedwater, concentrate, distillate and cooling pumps) is accounted.

Results of the RED exergy efficiency are shown on Figure 3.6 (a). It can be seen how for short-current conditions (external resistance approaching to zero) the global exergy efficiency is null as no voltage has been induced from the pile. Considering only the ohmic losses due to the internal resistance, when the resistance ratio increases the exergy efficiency increases as well, reaching a value of 99.5% for R_{ratio}=1000, in open circuit conditions (the stack voltage is equal to the electro-motive force). This is explained by the fact that when the internal resistance is reduced to zero, the process approximates to the reversibility. When the permselectivity is taken into account, the

same trend is followed and the higher performance is achieved for R_{ratio}=1000 but the exergy efficiency is lower than in the previous case (77.6%). The diffusive salt flux and water flux changes the trend of the exergy efficiency reaching a maximum (26.4% and 11%, respectively) for R_{ratio} between 1 – 10. After that, the uncontrolled mixing phenomena and electric current depletion are responsible for the subsequent decrease when the resistance ratio increases. Finally, the polarization effect slightly reduces the RED exergy efficiency, which results about 10.7%. As expected, the MED pumping irreversibility does not have any effect on the RED exergy efficiency.

The exergy efficiency of the MED is depicted in Figure 3.6 (b). From R_{ratio}=0.001 up to 10, its efficiency is almost constant (~76% for scenarios A-E), while in the scenario F, where the pumping power consumption of the MED pumps is accounted, the exergy efficiency decreases to 73%, approximately. When R_{ratio}> 10 is considered, a fast drop in the MED efficiency is observed. The higher the R_{ratio} the lower the electrical current and then, the controlled mixing process in the RED unit. Therefore, the MED unit produces only a small chemical exergy variation of the inlet stream, increasing the specific external heat consumption.

Figure 4.6 (c) shows the exergy efficiency of the Mixer 1. This efficiency is given by the sum of two different contributions. On one hand, when R_{ratio} approach to zero the ionic salt flux in the RED unit is the highest producing highest dilute concentration and lowest concentrate concentration, and therefore reducing the exergy dissipation by the mixing of the two solutions. On the other hand, when the R_{ratio} is increased the ionic salt flux is reduced (up to zero when R_{ratio} approach to infinite). In the ideal cases A and B no other dissipations are involved (i.e. diffusive water and salt flux) then the exergy of the mixer is reduced with the increase of the R_{ratio}, up to 10. After, the exergy efficiency begins to increase up to approximately 100% when R_{ratio} approaches to infinite. This latter effect is explained by the fact that the two solutions maintain approximatively its original concentrations, and the mixing of the solutions

to restore the initial salt content becomes less important with the increase of R_{ratio}. In the other cases (C-G) the impact of the uncontrolled mixing phenomena consumes part of the available salinity gradient also when infinite R_{ratio} is considered, therefore in those cases the mixing process is needed. The exergy efficiency shifting from case C to D is due to the effect of the water flux, which increases the dilute concentration, reducing the exergy destruction in the mixer.

The exergy efficiency of Mixer 2 is reported in Figure 3.6 (d). For all the cases, it is increased with the R_{ratio} because in this case the equivalent electric circuit approximates to open circuit conditions, and the lower the ionic current the lower the concentration variation within the RED unit, which reduces distillate flow rate required from the MED unit. Finally, the global exergy efficiency is presented in Figure 3.6 (e), where a maximum is found for resistance ratios between 1 and 10, derived from the combined effect of the RED and MED performances.

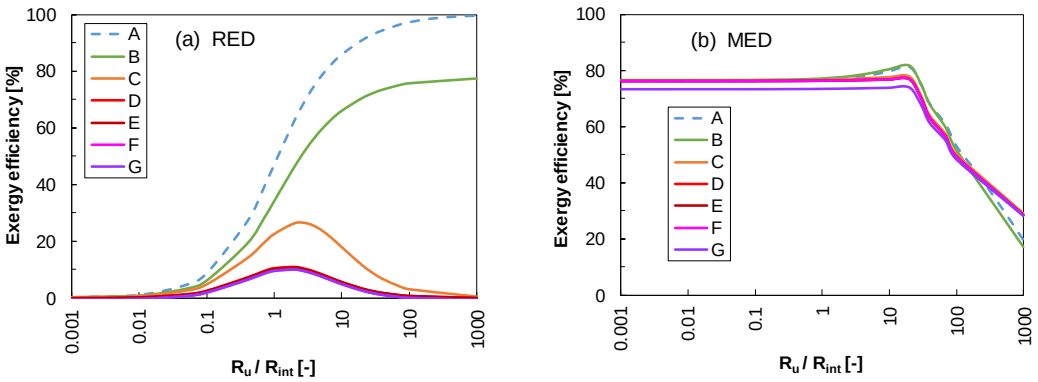

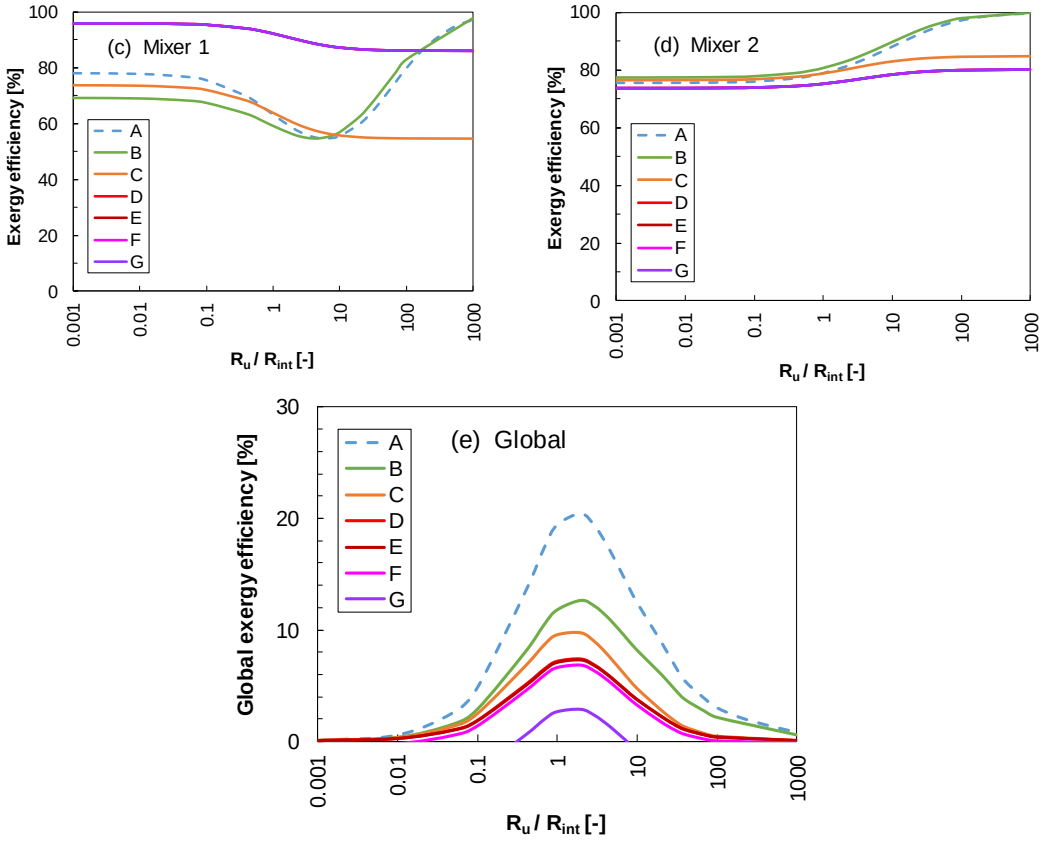

Figure 3.6 *Exergy efficiency as function of the external-to-internal stack resistance ratio and the irreversibility sources, in the base case: (a) RED, (b) MED, (c) Mixer 1, (d) Mixer 2, and (e) Global.*

3.4.3 Effect of inlet concentrations

In this section, the effects of the inlet solution concentrations to the RED unit, on the exergy efficiency for each subsystem are assessed. In particular, the component and global exergy efficiencies are analysed when the inlet concentrations vary between 2 – 5 M (concentrate) and 0.01 – 0.1 M (dilute), keeping constant the rest of parameters as in the base case. Figure 3.7 shows the results of the parametric evaluation for each component (RED stack, MED unit, Mixer 1 and Mixer 2) and for the overall RED-MED system.

The exergy efficiency of the RED stack (Figure 3.7 (a)) increases for lower values of the concentrate solution salinity, reaching almost 25%, while it is not affected by the dilute solution salinity in the range analysed. This behaviour is explained by the lower exergy destruction associated to the uncontrolled mixing phenomena, when the concentration difference is reduced. For the MED unit, the exergy efficiency increases up to 85% with the salinity of the concentrate solution (Figure 3.7(b)). That is directly related to the lower exergy destruction in the MED unit when the concentration increases. The exergetic performance of the Mixer 1 (Figure 3.7(c)) is also favoured by the salinity increase of the inlet concentrate solution, leading to values near 95% at 5 M. On the contrary, the exergy efficiency of the Mixer 2 increases up to about 95% with the decrease of the inlet dilute solution concentration (Figure 3.7 (d)), at 0.01 M. Finally, due to the opposite behaviour of the RED and MED exergy efficiencies, a maximum global exergy efficiency (3.44%) is reached at an intermediate inlet concentrate solution salinity, in particular for 3.87 – 0.01 M.

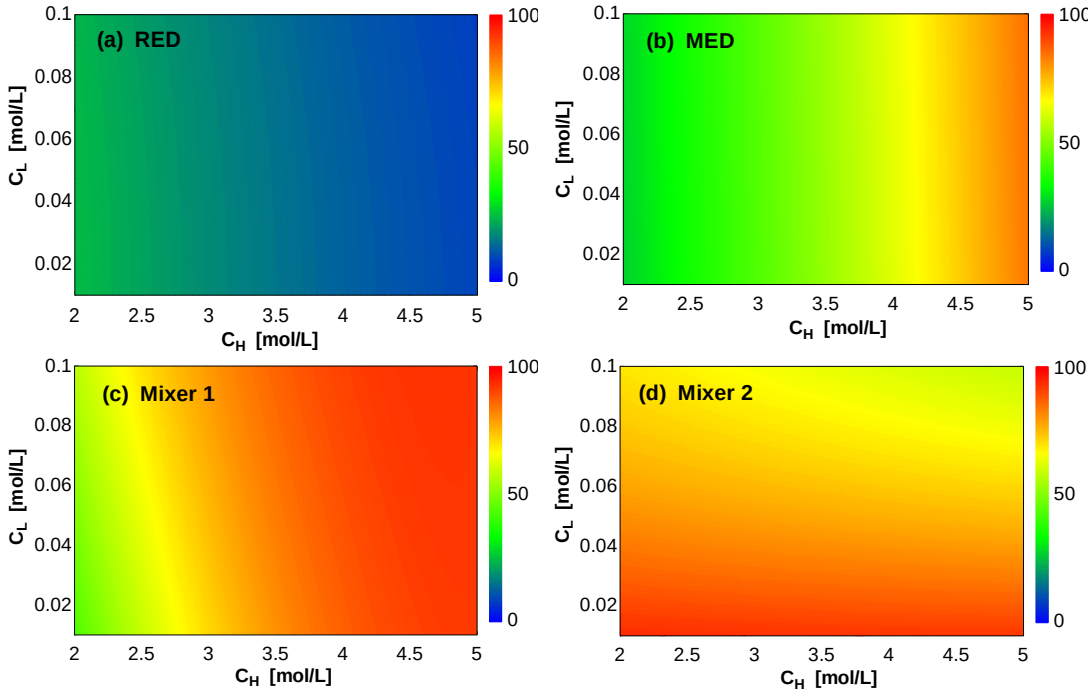

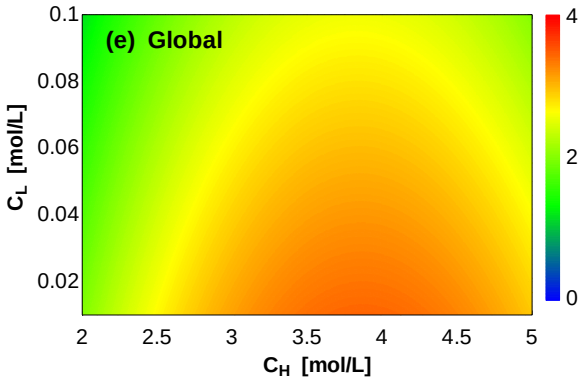

Figure 3.7 *Exergy efficiency as function of the concentrate and dilute inlet concentrations to the RED stack: (a) RED unit, (b) MED unit, (c) Mixer 1, (d) Mixer 2, (e) Global.*

3.4.4 Effect of inlet velocities

In this section, the effect of the inlet velocities of the concentrate and dilute solutions to the RED stack on the exergy efficiency is evaluated. In particular, the inlet concentration values leading to the maximum exergy efficiency obtained in the previous section have been considered (3.87 – 0.01 M), being the rest of parameters constant. Results are presented in Figure 3.8 (a)-(e).

The exergy efficiency of the RED stack (Figure 3.8 (a)) is increased for lower values of the inlet concentrate solution velocity and higher values of the dilute solution velocity. The first result is due to the reduction of the uncontrolled mixing phenomena (caused by a decrease in the concentration when the residence time is enlarged). On the contrary, the second effect can be attributed to the lower concentration of the dilute solution when its residence time increases, which enhances the induced voltage. Regarding the MED, the exergy efficiency (Figure 3.8 (b)) increases with the concentrate velocity and decreases with the dilute velocity, due to the higher concentration and flow rate of the feedwater obtained in those conditions. The inlet specific exergy is increased more than the heat rate, while the outlet flow exergy of the

concentrate and distillate streams remains equal. The exergy efficiency of the Mixer 1 (Figure 3.8 (c)) follows the same trend than that of the MED, as the higher the concentration and flow rate of the inlet streams are, the higher the exergy efficiency. On the contrary, the Mixer 2 (Figure 3.8 (d)) is not affected by the velocity of the concentrate solution, and only the dilute solution velocity has a slight influence on the exergy efficiency. Therefore, it is maintained almost constant for all the range of velocities analysed. Finally, the global exergy efficiency is depicted in (Figure 3.8 (e)). The trend results as a combination of the exergy efficiency of the RED and MED components. The maximum global exergy efficiency (5.15%) is reached for 0.25 – 0.82 cm/s concentrate and dilute solution velocities.

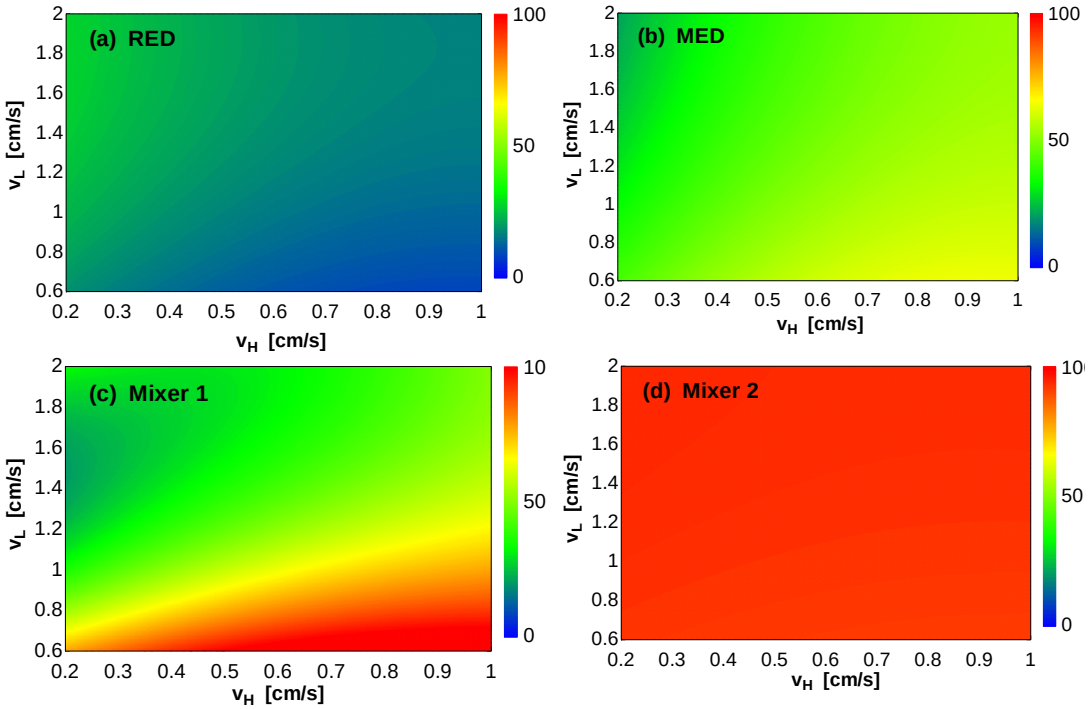

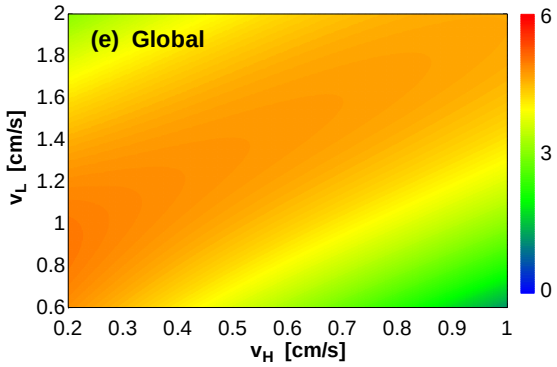

Figure 3.8 *Exergy efficiency as function of the concentrate and dilute inlet velocities to the RED stack: (a) RED unit, (b) MED unit, (c) Mixer 1, (d) Mixer 2, (e) Global.*

3.4.5 Effect of the stack geometry

Here, the effect of the RED stack geometry on the exergy performance is analysed. Specifically, the length-to-width ratio (i.e. the stack aspect ratio) and thickness of the membrane have been considered as geometrical parameters. For this analysis, the inlet concentration and velocity values of the concentrate and dilute solutions leading to the maximum exergy efficiency have been selected (3.87 – 0.01 M and 0.25 – 0.82 cm/s, respectively). Besides, a constant membrane's area of 0.25 m^2 is assumed. Figure 3.9 shows the evolution of the exergy efficiency. As it can be seen, the higher the membranes thickness, the higher the exergy efficiency, as the diffusive salt flux is reduced. Regarding the geometry ratio, intermediate values provide higher performance. This may be explained considering that the increase of the channel length (L) extends the residence time of the solutions, which leads to opposed effects: higher power is produced within the cell pair, and more water and salts are exchanged between the concentrate and dilute channel, losing driving force. The maximum exergy efficiency (6.24%) is reached with R_{geom}=4.23 (b=0.24 m, L=1.03 m) and δ_m =5·10^{-4} m.

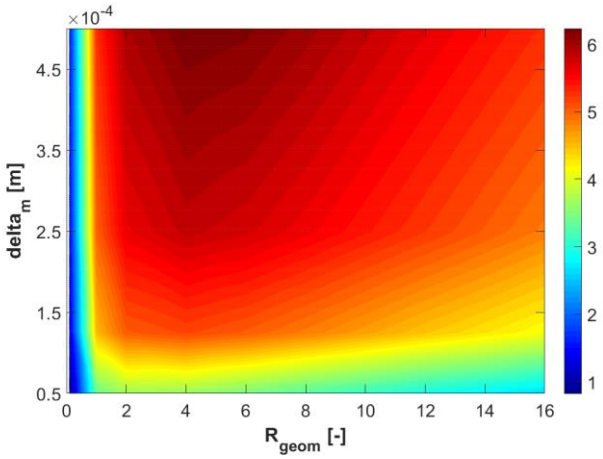

Figure 3.9 *Global exergy efficiency as function of the length-to-width (R_{geom}) ratio and membrane's thickness (δ_m).*

The membrane properties significantly affect to the performance of the RED-HE system, as phenomena such as permselectivity, salt diffusive flux, water diffusive flux, and membrane's resistance are sources of irreversibility, which degrade the total energy available. Therefore, in order to improve the overall exergy efficiency of the system, membranes with improved features are required. In addition, by increasing the number of effects in the MED unit (linked to the feedwater concentration level) the thermal energy consumption can be further reduced. In this section, it is analysed the exergy efficiency of the system if membranes with enhanced properties and higher number of MED effects are used. In particular, the permselectivity is fixed to 0.95, and the membrane's resistance, salt diffusive flux, and water diffusive flux, are decreased to one fourth of the base case values. The number of effects, previously limited because of the higher MED inlet concentration (which increases the BPE), can be increased in this case up to 26 effects.

Table 3.4 summarizes the main results obtained. The global exergy efficiency is about 26.5%, which represents a significant improvement with respect the one of the base case, 2.9% (using current membrane properties). In the same manner, the global thermal efficiency greatly increases from 0.6% to 5.3%. Regarding the RED exergy

efficiency, it reaches 62.6%, while initially was only of 10.2%, i.e., a six-fold increment. Therefore, the sensitivity analyses and the use of high-performing membranes allowed to decrease the exergy destruction within the RED stack. Conversely, the MED exergy efficiency decreases from 73.4% to 47.8%, mainly due to the decrease of the salinity and flow rate of the inlet and outlet concentrate solutions, i.e., less regeneration is needed. Comparing the Mixer 1 exergy efficiency, is slightly decreased from 91.1% to 87.2%, while in the case of the Mixer 2 it is increased from 75.9% to 93.3% (the reduction of the outlet dilute concentration enhances the exergy efficiency of the Mixer 2). Besides, more power is generated, 1322 W against the initial 522 W, while the heat rate input decreases from 35,410 to 21,677 W, that is, a reduction of 38.8%. The MED STEC is also decreased due to the higher number of effects.

Table 3.4 *Best case with high-performing membranes*.

Concept	**Value**
Global exergy efficiency, %	26.5
Global thermal efficiency, %	5.3
RED exergy efficiency, %	62.6
MED exergy efficiency, %	47.3
Mixer 1 exergy efficiency, %	87.2
Mixer 2 exergy efficiency, %	93.3
Gross power, (W)	1322
Pumping power, (W)	168.8
Heat rate, (W)	21,677
MED STEC, (kWh/m^3)	24.9

3.5 Comparative analysis

A summary of the overall improvement of the RED-MED exergy efficiency, after the different parametric analyses carried out on the inlet concentrations, velocities, stack geometry, and using high-performing membranes together with increased number of

MED effects, is presented in Table 3.5. Results show the great improvement achieved with respect to the base case. In particular, after the inlet solutions concentration, velocity and membrane geometry analysis the overall exergy efficiency has doubled from 2.9% to 6.2%, showing that the behaviour of the global system efficiency is largely affected by the RED process where larger exergy destructions are located. The highest efficiency is observed reducing the dilute solution concentration and the concentrate solution residence times. Concerning the stack geometry, asymmetric stack with aspect ratio between 4 and 5 results the most performing under the investigated conditions.

Further, the adoption of high performing membranes in the RED unit and the addition of more effects in the MED unit lead to a huge increase in the system efficiency, passing from 6.2% to 26.5%. This large efficiency increase is mainly due to the improvement of the membrane properties, which are the main limiting factor of this technology.

***Table 3.5**. Comparison of the RED-MED performance between the base case and the different cases analysed.*

Concept	**Base case**	**Inlet conc.**	**Inlet veloc.**	**Stack geom.**	**Memb. props. and N_{eff}**
Input variables					
Inlet concentrations, (mol/L)	4.5 – 0.05	3.87 – 0.01	3.87 – 0.01	3.87 – 0.01	3.87 – 0.01
Inlet velocities, (cm/s)	1 – 1	1 – 1	0.25 – 0.82	0.25 – 0.82	0.25 – 0.82
Membrane geometry, (m × m)	0.25 × 1	0.25 × 1	0.25 × 1	0.24 × 1.03	0.24 × 1.03
Membrane thickness, (m)	$1.25 \cdot 10^{-4}$	$1.25 \cdot 10^{-4}$	$1.25 \cdot 10^{-4}$	$5 \cdot 10^{-4}$	$5 \cdot 10^{-4}$
Membrane's properties	Current	Current	Current	Current	Enhanced
Number of MED effects	22	22	22	22	26
Results					
Global exergy efficiency, %	2.90	3.44	5.15	6.24	26.5
Global thermal efficiency, %	0.58	0.69	1.04	1.25	5.3
RED exergy efficiency, %	10.2	13.2	20.1	23.2	62.6

MED exergy efficiency, %	73.4	59.9	40.3	40.3	47.3
Mixer 1 exergy efficiency, %	91.1	84.8	58.7	44.1	87.2
Mixer 2 exergy efficiency, %	75.9	93.2	93.5	93.7	93.3
Gross power, (W)	522.6	563.2	439.6	477.9	1322
Pumping power, (W)	315.9	309.4	159.9	153.4	168.8
Heat rate, (W)	35,410	36,585	27,014	25,880	21,677
MED STEC, (kWh/m^3)	33.1	33.1	29.8	29.8	24.9

The exergy balance of the most performing case found, i.e., using membranes with enhanced properties and high number of MED effects, is depicted in Figure 3.10, which is the Grassmann diagram of this process. All the inlet and outlet exergy flow in the system are presented. In the RED unit, the exergy flow sum of the concentrate and dilute solutions is partly used to generate electric power, while an important amount of exergy is destroyed because of the irreversibility sources of the pile. A small part of the generated power is used to feed the RED pumps, while a larger share is consumed by the MED pumps. The remaining exergy flow is further degraded in the Mixer 1, before entering in the regeneration stage. At the MED unit, the exergy rate introduced in the cooling process is particularly high due to the large quantity of water flow rate needed at the end condenser. Also, it can be seen the great amount of waste heat exergy rate required by the system, hence the low value of the thermal efficiency. Conversely to the case where conventional membranes are used, the most limiting component is the MED unit, where the exergy destroyed is particularly high, playing an important role in the system performance. Finally, the exergy rate of the distillate produced in the MED unit is further decreased at the Mixer 2, where a small part is destroyed, before closing the loop.

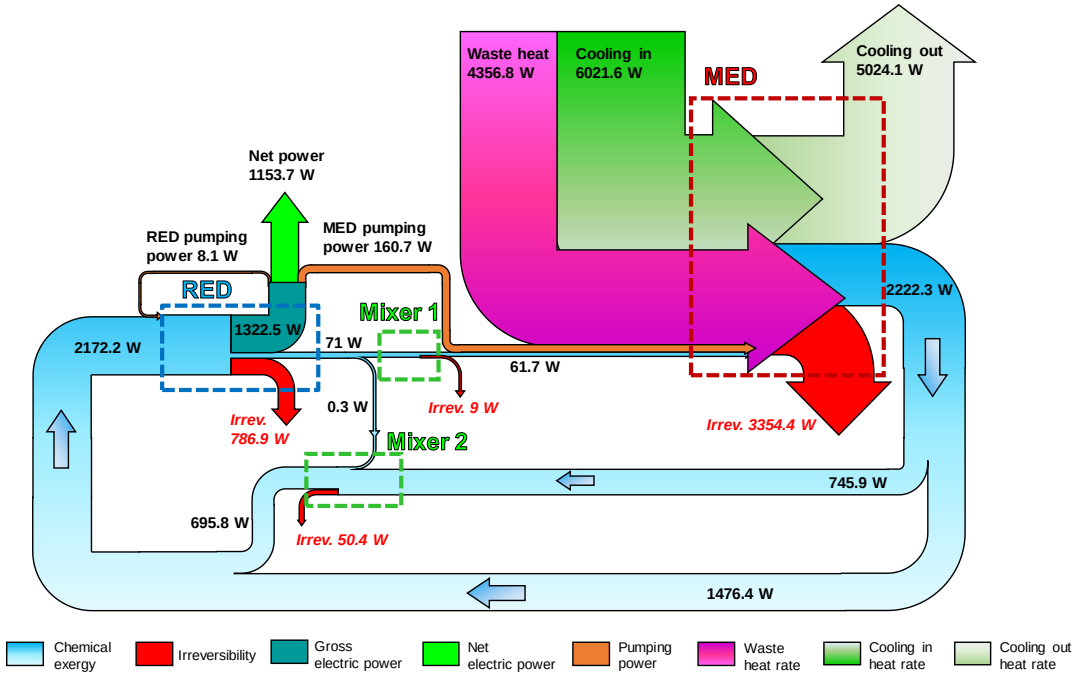

Figure 3.10 *Grassmann diagram of the most performing scheme found for the RED-MED system.*

3.6 On the main outcomes of this analysis

In this chapter, a detailed exergy analysis of a RED-MED heat engine has been carried out. *Ad-hoc* mathematical models of the RED and MED units have been used, which allowed to perform sensitivity analyses with the main operational and design variables of the system: inlet solutions concentration, velocity, and stack geometry.

Particularly, the effect of the inlet concentrations of the solutions to the RED stack on the exergy efficiency has been analysed. For the case considered, there are a pair of values (3.87 – 0.01 M) that maximizes the global exergy efficiency (passing from 2.90% in the base scenario to 3.44%), while keeping the rest of variables constant. In the same manner, the effect of the inlet velocities is significant, reaching the exergy efficiency a maximum (5.15%) with values 0.25 – 0.82 cm/s of the inlet concentrate and dilute solutions, respectively. A sensibility analysis on the stack geometry has

revealed that the exergy efficiency can be further increased by selecting the appropriate length-to-width ratio and thickness. In particular, an efficiency of 6.24% has been obtained for b = 0.24 m and L = 1.03 m.

In addition, the exergy destruction caused by the main sources of irreversibility of the system has been analysed as a function of the resistance ratio of the stack. The results obtained have shown that the permselectivity of the membranes, salt and water diffusivity fluxes greatly decreases the performance. On the contrary, the polarization phenomena only produce a slight reduction, as well as the RED pumping power. The influence of the MED pumping power has been found to be more significant, leading to an important decrease of the global exergy efficiency.

Finally, the exergy potential of the technology has been assessed using high-performing membranes and higher number of MED effects, reaching global exergy efficiency of 26.5%, showing the significant potential of the RED-MED HE for the conversion of waste heat into electricity.

Appendix A

Osmotic and activity coefficients

The model from Pitzer et al. [3.27] has been selected for the calculation of the osmotic coefficient of the water and the mean activity coefficient of the sodium chloride:

$$\phi - 1 = -|z_M z_X| A_\phi \frac{I^{0.5}}{1 + bI^{0.5}} + m\frac{2\nu_M\nu_X}{\nu}\left[\beta_{MX}^{(0)} + \beta_{MX}^{(1)}\exp(-\alpha I^{0.5})\right] + 2m^2\frac{(\nu_M\nu_X)^{3/2}}{\nu}C_{MX}^{\phi} \quad \text{(A.1)}$$

$$ln\gamma = -|z_M z_X| A_\phi\left(\frac{I^{0.5}}{1 + bI^{0.5}} + \frac{2}{b}\ln\left(1 + bI^{0.5}\right)\right) + 2m\frac{\nu_M\nu_X}{\nu}\cdot \cdot\left\{2\beta_{MX}^{(0)} + \frac{2\beta_{MX}^{(1)}}{\alpha^2 I}\left[1 - \left(1 + \alpha I^{0.5} - \frac{\alpha^2 I}{2}\right)\cdot\exp(-\alpha I^{0.5})\right]\right\} + 3m^2\frac{(\nu_M\nu_X)^{3/2}}{\nu}C_{MX}^{\phi} \quad \text{(A.2)}$$

Where z_M and z_X are the charge of the cation and anion, respectively, A_ϕ is the Debye-Huckel parameter for the osmotic coefficient, I is the ionic strengh, m is the molality, ν_M and ν_X are the number of cations and anions of the salt, $\beta_{MX}^{(0)}$, $\beta_{MX}^{(1)}$, and C_{MX}^{ϕ} are adjustable parameters, α is a constant (2 for univalent ions), and b is a constant (1.2 $kg^{1/2}mol^{-1/2}$).

Density

The density (kg/m^3) of the aqueous sodium chloride solution has been determined using a correlation obtained from the work of Rogers & Pitzer [3.28], as function of the molarity C (mol/L) and temperature T (°C) of the solution.

$$\rho = A + B \quad \text{(A.3)}$$

$$A = 1.003\cdot 10^3 - 1.373\cdot 10^{-2}\cdot T - 6.671\cdot 10^{-3}\cdot T^2 + 3.840\cdot 10^{-5}\cdot T^3 - 1.616\cdot 10^{-7}\cdot T^4 \quad \text{(A.4)}$$

$$B = 3.905\cdot 10^1\cdot C - 7.903\cdot 10^{-2}\cdot C\cdot T + 1.171\cdot 10^{-3}\cdot C\cdot T^2 - 8.444\cdot 10^{-7}\cdot C\cdot T^3 - 9.374\cdot 10^{-5}\cdot C^2\cdot T^2 \quad \text{(A.5)}$$

Conductivity

In order to determine the equivalent conductivity of the solutions, the following expression has been used as function of the molar concentration:

$$\Lambda_{sol}(x) = \Lambda_0 - \frac{A_\Lambda\sqrt{C_{sol}(x)}}{1 + B_\Lambda\sqrt{C_{sol}(x)}} - C_\Lambda C_{sol}(x) \quad \text{(A.6)}$$

where Λ_0 is the equivalent conductivity of the salt (infinite dilution), and A_Λ, B_Λ and C_Λ are specific parameters.

Electrical resistance of the membranes

The electrical resistance has been determined using quadratic empirical correlations obtained for FujiFilm® Type 10 membranes [3.29], as function of the molar concentration of the solutions:

$$\boldsymbol{R_{AEM}(x) = 0.487\, C_H^2(x) - 2.81\, C_H(x) + 7.21 - 0.14\, C_L(x)} \quad \text{(A.7)}$$

$$\boldsymbol{R_{CEM}(x) = 0.487\, C_H^2(x) - 2.81\, C_H(x) + 7.22 - 0.27\, C_L(x)} \quad \text{(A.8)}$$

Permselectivity of the membranes

The membrane permselectivity was determined by means of empirical correlations, obtained for FujiFilm® Type 10 membranes:

$$\boldsymbol{\alpha_{AEM}(x) = 0.987 - 0.0441\, C_H(x) - 0.183 C_L(x)} \quad \text{(A.9)}$$

$$\boldsymbol{\alpha_{CEM}(x) = 0.991 - 0.0441 C_H(x) - 0.253 C_L(x)} \quad \text{(A.10)}$$

Polarisation coefficients

The polarisation coefficients were calculated implementing suitable correlations, obtained through CFD simulations for the case of flat membranes and Deukum GmbH spacers [3.30].

$$\boldsymbol{\theta_L(x) = \left(1 + \left(\frac{2\, J_{migr}(x)\, \delta_L}{Sh_L(x)\, D_L\, C_L(x)}\right)\right)^{-1}} \quad \text{(A.11)}$$

$$\boldsymbol{\theta_H(x) = 1 - \left(\frac{2\, J_{migr}(x)\, \delta_H}{Sh_H(x)\, D_H\, C_H(x)}\right)} \quad \text{(A.12)}$$

where:

δ_H and δ_L are the thicknesses of the spacers used in the concentrate and in the dilute channel respectively; D_H and D_L are the salt diffusivity values in the concentrate and in the dilute channel respectively, considered constant and equal to 1.5×10^{-9} m^2/s; Sh_H and Sh_L are the Sherwood numbers, relevant to the concentrate and the dilute solutions, which are calculated as functions of the Reynolds numbers Re_H and Re_L, respectively [3.25].

$$\boldsymbol{Sh(x) = -2\cdot10^{-9}\cdot Re(x)^6 + 4\cdot10^{-7}\cdot Re(x)^5 - 2\cdot10^{-5}\cdot Re(x)^4 - 0.0005\, Re(x)^3 + 0.0509\, Re(x)^2 + 0.6125\, Re(x) + 6.2591} \quad \text{(A.13)}$$

References

[3.1] B. E. Logan and M. Elimelech, "Membrane-based processes for sustainable power generation using water," *Nature*, vol. 488, p. 313, Aug. 2012.

[3.2] G. Micale, A. Cipollina, and A. Tamburini, "1 – Salinity gradient energy," in *Sustainable Energy from Salinity Gradients*, 2016, pp. 1–17.

[3.3] A. C. G. Micale, Ed., *Sustainable Energy from Salinity Gradients*. Woodhead Publishing, 2016.

[3.4] T. Q. Nguyen, J. D. Slawnwhite, and K. G. Boulama, "Power generation from residual industrial heat," *Energy Convers. Manag.*, vol. 51, no. 11, pp. 2220–2229, 2010.

[3.5] W. He, S. Wang, and L. Yue, "High net power output analysis with changes in exhaust temperature in a thermoelectric generator system," *Appl. Energy*, vol. 196, pp. 259–267, Jun. 2017.

[3.6] A. R. Tavakolpour-Saleh, S. Zare, and H. Bahreman, "A novel active free piston Stirling engine: Modeling, development, and experiment," *Appl. Energy*, vol. 199, pp. 400–415, Aug. 2017.

[3.7] A. Tamburini, A. Cipollina, M. Papapetrou, A. Piacentino, and G. Micale, "7 – Salinity gradient engines," in *Sustainable Energy from Salinity Gradients*, 2016, pp. 219–256.

[3.8] S. Loeb, "A method and apparatus for generating power utilizing pressure-retarded osmosis," US 3906250, 1975.

[3.9] S. Loeb, "Method and apparatus for generating power utilizing reverse electrodialysis," US 4171109, 1979.

[3.10] "Conversion of Low Grade Heat to Power through closed loop Reverse ElectroDialysis—Horizon 2020 programme, Project Number: 640667: www.red-heat-to-power.eu."

[3.11] X. Luo *et al.*, "Power generation by coupling reverse electrodialysis and ammonium bicarbonate : Implication for recovery of waste heat," *Electrochem. commun.*, vol. 19, pp. 25–28, 2012.

[3.12] R. D. Cusick, Y. Kim, and B. E. Logan, "Energy capture from thermolytic solutions in microbial reverse-electrodialysis cells.," *Science*, vol. 335, no. 6075, pp. 1474–7, Mar. 2012.

[3.13] M. C. Hatzell, I. Ivanov, R. D. Cusick, X. Zhu, and B. E. Logan, "Comparison of hydrogen production and electrical power generation for energy capture in closed-loop ammonium bicarbonate reverse electrodialysis systems," vol. 16, no. 4, pp. 1632–1638, Jan. 2014.

[3.14] M. Bevacqua, A. Carubia, A. Cipollina, A. Tamburini, M. Tedesco, and G. Micale, "Performance of a RED system with ammonium hydrogen carbonate solutions," *Desalin. Water Treat.*, vol. 3994, no. February, pp. 1–12, 2016.

[3.15] R. Long, B. Li, Z. Liu, and W. Liu, "Hybrid membrane distillation-reverse electrodialysis electricity generation system to harvest low-grade thermal energy," *J. Memb. Sci.*, vol. 525, pp. 107–115, 2017.

[3.16] A. Tamburini *et al.*, "Reverse electrodialysis heat engine for sustainable power production," *Appl. Energy*, vol. 206, no. August, pp. 1334–1353, 2017.

[3.17] J. Hu *et al.*, "Theoretical simulation and evaluation for the performance of the hybrid multi-effect distillation—reverse electrodialysis power generation system," *Desalination*, vol. 443, pp. 172–183, Oct. 2018.

[3.18] Y. M. El-Sayed and R. S. Silver, "Chapter 2 – Fundamentals of Distillation," in *Principles of Desalination*, K. S. Spiegler and A. D. K. Laird, Eds. Academic Press, 1980, pp. 55–109.
[3.19] H. El-Dessouky, I. Alatiqi, S. Bingulac, and H. Ettouney, "Steady-state analysis of the multiple effect evaporation desalination process," *Chem. Eng. Technol.*, vol. 21, no. 5, pp. 437–451, 1998.
[3.20] K. H. Mistry, M. A. Antar, and J. H. Lienhard, "An improved model for multiple effect distillation," *Desalin. Water Treat.*, vol. 51, no. 4–6, pp. 807–821, 2013.
[3.21] S. A. Klein, *Engineering Equation Solver Software (EES)*. 2013.
[3.22] B. Ortega-Delgado, L. García-Rodríguez, and D.-C. Alarcón-Padilla, "Opportunities of improvement of the MED seawater desalination process by pretreatments allowing high-temperature operation," *Desalin. Water Treat.*, vol. 97, 2017.
[3.23] H. T. El-Dessouky and H. M. Ettouney, *Fundamentals of Salt Water Desalination*. Elsevier, 2002.
[3.24] S. Kakaç, H. Liu, and A. Pramuanjaroenkij, *Heat Exchangers: Selection, Rating, and Thermal Design*. Boca Raton, FL: CRC Press, 2002.
[3.25] L. Gurreri, A. Tamburini, A. Cipollina, G. Micale, and M. Ciofalo, "CFD prediction of concentration polarization phenomena in spacer-filled channels for reverse electrodialysis," *J. Memb. Sci.*, vol. 468, pp. 133–148, Oct. 2014.
[3.26] G. Tsatsaronis, "Thermoeconomic analysis and optimization of energy systems," *Prog. Energy Combust. Sci.*, vol. 19, no. 3, pp. 227–257, Jan. 1993.
[3.27] K. S. Pitzer, J. C. Peiper, and R. H. Busey, "Thermodynamic Properties of Aqueous Sodium Chloride Solutions," *J. Phys. Chem. Ref. Data*, vol. 13, no. 1, pp. 1–102, 1984.
[3.28] P. S. Z. Rogers and K. S. Pitzer, "Volumetric Properties of Aqueous Sodium Chloride Solutions," *J. Phys. Chem. Ref. Data*, vol. 11, no. 1, pp. 15–81, Jan. 1982.
[3.29] M. Micari *et al.*, "Effect of different aqueous solutions of pure salts and salt mixtures in reverse electrodialysis systems for closed-loop applications," *J. Memb. Sci.*, vol. in press, 2018.
[3.30] M. La Cerva *et al.*, "Coupling CFD with a one-dimensional model to predict the performance of reverse electrodialysis stacks," *J. Memb. Sci.*, vol. 541, pp. 595–610, Nov. 2017.

Chapter 4

Exergy Analysis and Thermoeconomics of Multi-Effect Desalination Processes

In this chapter, Exergy Analysis and Thermoeconomic Cost Accounting for a Multi-Effect Desalination Thermo-Vapor Compression system (MED-TVC) located in Sicily (Italy) is presented.

In the first part of this chapter, a brief overview on the Multi-Effect Desalination process is provided along with a description of technical, economic and environmental aspects of this process.

Details about the reference MED-TVC plant are given and a preliminary exergy analysis is carried out in order to calculate exergy flows and exergy efficiencies for each system component. Then, by means of exergy cost accounting, the cost formation process of freshwater within this process is analyzed. A thorough description of thermoeconomic model adopted is provided.

4.1 Overview on Thermal Desalination Processes

Population growth, economic developments and improving of living standards has involved increase in water usage during last decades. In this sense, water shortage is a pressing concern in many countries around in the world, above all in arid zones as Middle East and North Africa (MENA). According to the World Health Organization Statistics (WHO) [4.[4.1]], about 20 per cent of the world's population

lives in countries where water is scarce. This problem is expected to worsen during the next decades.

The desalination industry plays a key role in addressing water scarcity, by supplying freshwater from natural sources as seawater, brackish and brines. According to Worldwide Desalting Inventory, published by [4.[4.2]] the total capacity of commissioned desalination plant in the world at 2015 is around 86.8 million m^3/d and 300 million is the number of people around the world who rely on desalinated water for some or all their daily needs. Currently, according to data provided by [4.[4.2]] desalination processes largely rely on Reverse Osmosis (RO), Multi Stage Flash (MSF) and Multi Effect Distillation (MED). More specifically as shown in Figure 4.1, among these technologies, RO has achieved a dominant role during last decades due to improvements in membranes properties, accounting for nearly 65% of the total worldwide installed capacity [4.[4.2]]. Thermal desalination process account for nearly 28% of global installed capacity, which is shared for 21% by MSF and for 7% by MED. The remaining fraction of global desalination capacity is covered by Nano Filtration (NF), Electrodialysis (ED) and other processes.

Even though the RO process is leading worldwide desalination market [4.3, 4.4, 4.5], thermal desalination processes are still predominant in *Gulf cooperation council countries* (GCC), i.e. Bahrain, Kuwait, Oman, Qatar, Saudi Arabia and the United Arab Emirates [4.4, 4.5]. Indeed, in GCC, thermal processes account for about 56% of installed desalination capacity, being the remaining fraction, i.e. the 44%, covered by RO process. The usage of thermal technologies in these countries is mainly due to (i) the poor quality of water sources to be desalted (ii) the high availability of cogenerative steam from local thermoelectric plant. Firstly, feedwater supplied from Arabian Gulf is characterized by high temperature, high salinity and high impurity thus increasing operating cost for RO process due to membrane replacement and pre-treatment processes. In addition, in those countries, the large amount of low-grade

thermal energy from thermal power plants allows for a cogeneration operating mode which leads to a more cost-effective and energy-saving desalination process.

From the previous data, it is clear that MED technology is not extensively used from a worldwide point of view. Although MED process is more efficient from a thermodynamic point of view than MSF [4.6], its initial spread was arrested due to serious scaling and corrosion problems occurring on the external surface of evaporator bundle. However, during the last decades, improvement in MED technology contributes to solve the initial technical issues, thus becoming more competitive with respect to MSF technology. Nowadays, according to [4.7, 4.8], MED unit capacity usually ranges from 600 to 36,000 m^3/day

MED processes are highly capital intensive and energy consuming process. For instance, in [4.6, 4.9, 4.10], energy consumption of MED process is nearly 2-3 times higher than the energy consumption of RO process. It is clear that lowering energy requirements for MED process is the current challenge for research in order to achieve a more competitive, cost-effective and sustainable process.

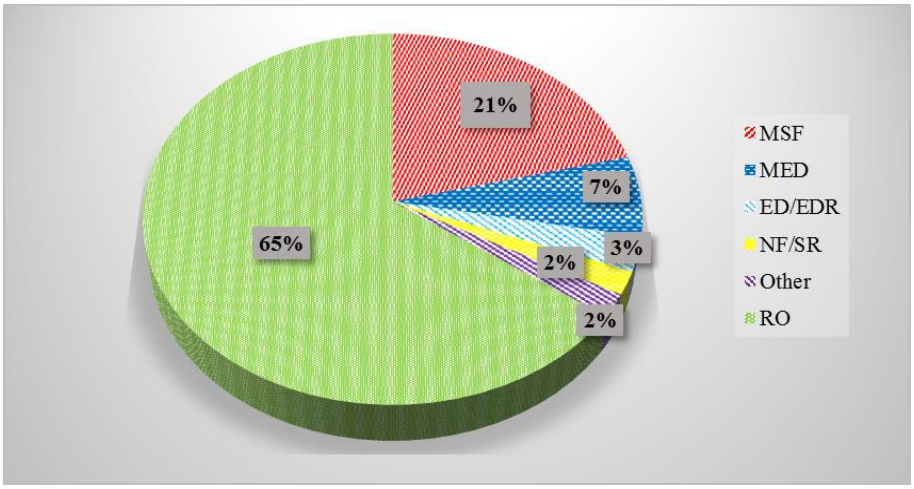

Figure 4.1 *Global desalination capacity by process [4.2]*

In Table 4.1, some recent MED installations around the world during the decade 2006-2016 are shown. One of the largest MED plants, is installed in Marafiq (Saudi Arabia) with a total capacity of 800,000 m^3/day (27 units of 30,000 m^3 /day each) [4.7, 4.8]. It is worth stressing how the majority of MED units are installed in GCC.

Table 4.1 *Examples of recent MED installations around the world [4.7, 4.8]*

Country	*Location*	*Commissioning Year*	*Number of Units*	*Unit Capacity* (m^3/day)	*Manufacturer*
UAE	Layyah	2006	1	36,368	SIDEM
India	Gujarat	2006	4	8,450	IDE
Bahrain	Al Hidd	2007	10	27,300	SIDEM
India	Jamnagar	2008	4	24,000	IDE
Saudi Arabia	Al Jubail	2009	27	30,000	SIDEM
UAE	Fujairah II	2009	12	37,900	SIDEM
Lybia	Zawia	2009	4	20,000	SIDEM
Qatar	Ras Laffan C	2010	10	28,640	SIDEM
China	Tianjin	2010	4	25,000	IDE
India	Gujarat	2012	2	24,000	IDE
Saudi Arabia	Yanbu	2013	2	31,674	SIDEM
India	Gujarat	2013	4	25,000	IDE
India	Jamnagar	2015	3	24,000	IDE
Kuwait	Az Zour	2016	10	49,279	SIDEM

4.2 Fundamentals on Multi-Effect Desalination process

Multiple-effect distillation is prevalently used for seawater desalination, but it is often applied for treatment of process water in industries as i.e. sugar, paper and pulp, dairy, textiles, acids and desalination. It represents a well consolidated technology, which has observed a large spread since the late 1950s.

The MED process consists of a sequence of effects, whose number usually ranges up to 16, where pure water is separated from the feed by means of evaporation. The necessity of operating with a multiple effects configuration is due to the poor performance of a single effect system [4.11]. In fact, the possibility to recover the thermal energy content of the generate vapor into the successive effect avoid the waste of large amount of energy which is otherwise rejected when a single effect configuration is considered.

In most of MED process, the *falling film evaporator* is used for heat transfer between the feed seawater to be evaporated and the heat source. In this configuration, seawater is sprayed over the outer surface of heated tubes. Steam produced within each effect is then transferred to the next effect for boiling seawater or the brine coming from the previous effect. Other evaporator configuration as vertical falling film or submerged tube have been investigated during these years [4.6, 4.12].

In order to order to avoid scaling and reduce corrosion on the outside of tube bundle, the top temperature brine (TBT) has been limited to 70°C [4.6, 4.11]. This temperature limit allows for the exploitation of low-grade heat, or the integration of vapor compression within the process. Another advantage is the use of alternative construction materials which leads to a decrease of capital cost. More specifically, aluminum alloys are used for the heat transfer tubes, as well as carbon steel epoxy coated shells for the evaporator shells.

Temperature gradually decreases when passing through one effect to the next one, reaching about 30°C-40°C in the last effect.

Due to temperature lowering along MED process, each effect operates at a decreasing level of pressure in order to allow for water evaporation. Also, the amount of distillate generated in each effect is less than the distillate generated in the previous effect due to the increase in the specific latent heat of vaporization when decreasing the effect temperature.

The intake seawater is preheated within the down condenser by condensing a fraction of distillate generated from the last effect. After that, a fraction of the intake seawater, which is usually named *cooling seawater*, is disposed back to the sea. Cooling seawater aims at removing the excess heat added into the system in the first effect [4.11]. Conversely, the remaining fraction is further preheated by distillate generated before being supplied to the effects for producing freshwater.

Regarding pumping unit, MED process is usually equipped with large pump for seawater intake, distillate product, brine blow down, and chemical dosing. The feedwater stream is chemically treated and de-aerated, before being sprayed into the effects [4.6, 4.11].

4.2.1 MED process configurations

MED plants can be classified according to the direction of the feedwater flow and heat flow respectively as: *forward feed plants* (FF-MED), *parallel feed plants* (PF-MED) and *backward feed plants* (BF-MED) [4.6, 4.11, 4.13]. Schemes for each MED configuration are shown in Figures 4.2 (a), (b) and (c). Some details on each configuration plant are here provided:

- *Forward feed plants*: as shown in Fig. 4.2 (a), feedwater after being preheated into the down condenser and the series of preheaters, is introduced into the first effect where it is separated into pure water and brine. Then, the brine flow is transferred to the next effect where pure water is further separated

by means of the heat released from the distillate generated into the previous effect. Obviously, brine concentration increases when passing from the first effect to the last. Also, the highest concentrated brine is found into the effect at the lowest temperature, thus avoiding scale formation. The FF-MED system is not found on industrial scale for desalination industry, due to its complex layout with respect to the parallel feed configuration. Conversely, it is widely used in the sugar and paper industries.

- *Parallel feed plants*: as shown in Fig. 4.2 (b), the feedwater, after being preheated into the down condenser, is equally distributed among effects. In each effect, pure water is separated from feedwater by means of heat released from the condensing distillate formed in the previous effect. The main advantages of this configuration are its simple layout and the lower risk of scale formation. For these reasons, it is largely used as base technology for seawater desalination.

- *Backward feed plants:* as shown in Fig. 4.2 (c) the feedwater is introduced into the last effect, which operates at the lowest pressure and temperature of the system. Then, the brine flows from the last to the first effect, for further distillate generation. The main advantage of this configuration is that no feedwater preheaters are required, thus lowering the amount of capital investment necessary. Conversely, the increase in the operating pressure across the effects requires the use of pumps, thus increasing operating costs. Also, the highest brine concentration occurs in the first effect, which operates at the highest temperature of the system, thus increasing the risk of scale formation. For this reason, this configuration is not applied to seawater desalination.

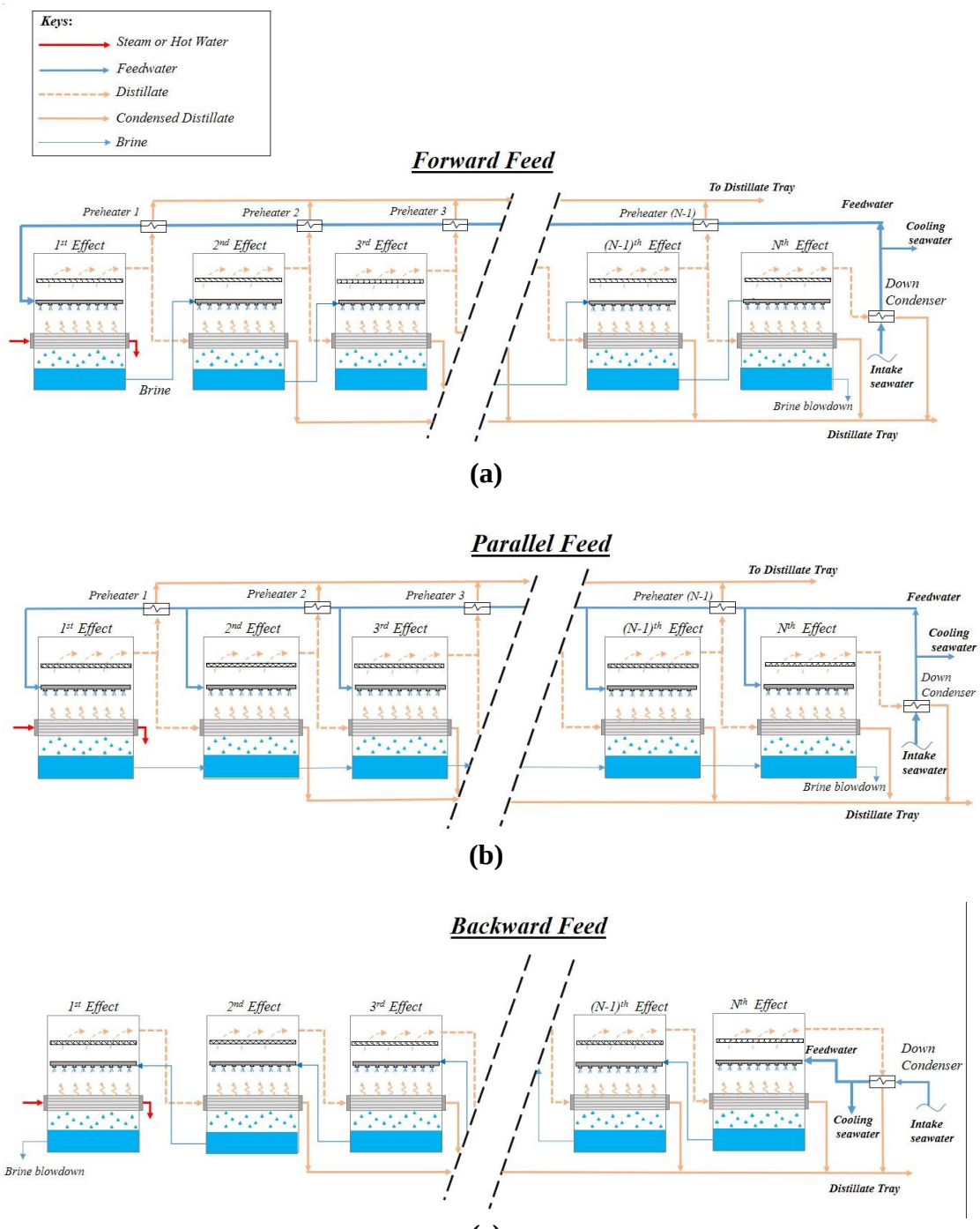

Figure 4.2 *MED process configurations: (a) Forward Feed, (b) Parallel Feed and (c) Backward Feed*

4.3 Energy consumption of MED process

MED processes are usually driven by external heat flow supplied by means of a dedicated combustion of fossil fuel within a boiler or by waste heat available from an industrial process. Typical values of 40-80 kWh_t/m^3 are found in literature [4.6, 4.8, 4.11]. Electricity consumed for pumping and auxiliaries ranges among 1.5-2.5 kWh_e/m^3.

Following El-Dessouky approach [4.11], the following indicators are adopted for assessing the MED process performance.

- ***Gain Output Ratio*** (GOR): which expresses the amount of thermal energy consumed in the desalination process, and is defined as the ratio of the mass of distillate to the mass of the input steam. As shown [4.11], GOR values up to 10 may be obtained for a standard MED process. This indicator heavily depends from the number of effects compounding the MED system, and in particular, an increase in the numbers of effects allows for an additional distillate generation.

- The ***Specific heat transfer surface area*** expresses the area required for heat transfer process for unit distillate product. As shown in [4.11], a typical value of 250 $m^2/(kg_{dist}/s)$ is obtained for a MED process constituted by 12^{th} effects and a TBT equal to 60°C. This indicator is highly sensitive to the number of effect and to the TBT values. More specifically, its values decrease when operating with high values TBT, due to the higher driving force available for heat transfer process.

- The ***specific cooling water flow rate*** indicate the amount of cooling water supplied to the down condenser for condensing the unit mass of

distillate generated. This indicator is a measure of electricity consumed for pumping and treatments. Its values decrease from 9 to 2.7 (kg_{CW}/s)/(kg_{dist}/s) while increasing the number of effects respectively from 6 to 12 [4.11]. This trend can be explained by considering that an increase in the number of effects allows for an additional distillate generation thus reducing the amount of cooling water required for condensation,

Both the *GOR* and the *specific flow rate of cooling* are a measure of MED operating costs, since they are related respectively to the supplied motive steam and to electricity consumed for pumping the intake seawater. Conversely, *specific heat transfer surface area* is a measure of capital investment required for process realization.

4.3.1 Enhancement of MED process performance by means of "Vapor Compression"

In order to enhance the process energy efficiency, MED units are often equipped with vapor compression system, which compresses part of the distillate vapor generated within the last effect before supplying it to the first effect. The following systems are used for vapor compression: (i) Thermal Vapor Compression (MED-TVC), (ii) Mechanical Vapor Compression (MED-MVC).

In MED-TVC configuration, a fraction of the steam from the last effect is entrained and compressed to the pressure of the first effect in a steam jet ejector by means of a middle pressure steam. A scheme of MED-TVC plant is provided in Figure 4.4. Once compressed, the steam flow is supply to the first effect where it releases its energy content to the feedwater [4.6, 4.11, 4.13]. By means of this configuration, the GOR of the plant increases for about the 30–40% with respect to the standard MED process, thus producing 15–16 kg of distillate per kg of motive steam supplied to TVC. Also, the specific electricity consumption is lowered for this configuration with respect to a standard MED process. Indeed, due to steam

extraction from the last effect, less cooling seawater is required to reject heat from distillate coming from the last effect, thus reducing the electricity consumption for pumping intake seawater. Typical specific electricity consumption value ranges from 1.5 to 2 kWh_e/m^3. As concerns specific heat transfer surface not sensible variation are observed for a MED-TVC configuration with respect to a standard MED [4.11]. It is worth stressing that all the recent MED installation showed in Table 4.1 are of the MED-TVC type.

In MED-MVC system, only electric power is supplied to the process. The MVC process was developed in the early 1980s. A scheme of this system is shown in Fig. 4.3. The necessity to develop this technology was motivated by the need to have an alternative thermal desalination system which uses electric power as unique energy source. The electrical consumption of such system ranges among of 8 to 15 kWh_e/m^3 [4.8, 4.14]. Due to current limitation in compressors technology, the maximum capacity of MED-MVC units is limited to 5000 m^3/day per unit. [4.14]

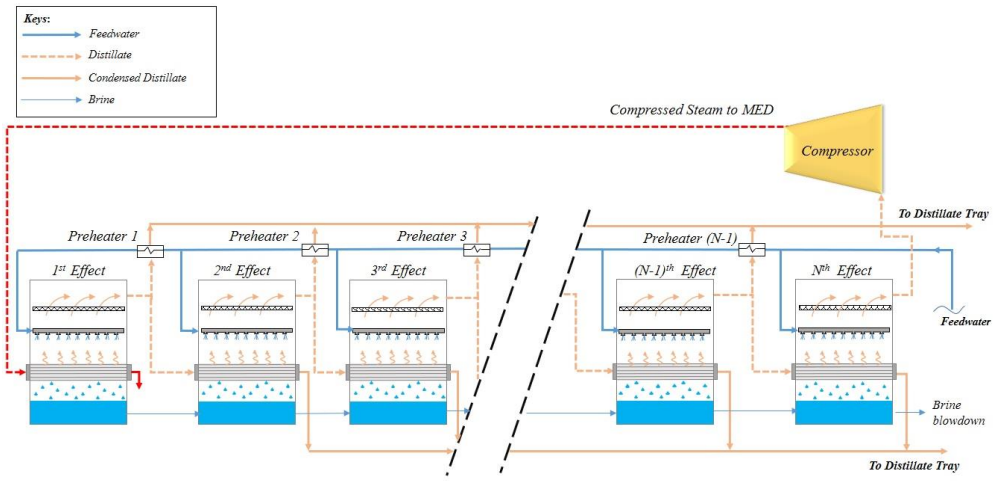

Figure 4.3 *Typical MED-MVC system layout*

4.4 Environmental impacts of MED process

As explained in [4.6, 4.22, 4.27], the main environmental burdens of desalination process can be grouped as follows: (i) greenhouse gases (GHG) and air pollutants emissions due to energy consumptions, (ii) brine disposal back the sea, (iii) the use of large quantities of seawater for cooling purposes and as feed water and (iv) construction-related impacts on coastal and nearshore habitats

As concerns GHG emissions, it is clear that since most of the MED process still rely on fossil fuel powered generation system, a large amount of CO_2 is produced for supplying steam to MED process. In [4.16] CO_2 emissions for a stand-alone process account for 18–24 kg_{CO2}/m^3 according to the type of fossil fuel used for steam generation.

With respect to brine disposal, it important to consider the effect of scale inhibitor, antifoam chemicals and metals (usually nickel and copper are released from corrosion of evaporator bundle) which could be harm for the receiving environment [4.22]. Brine temperature is usually 15°C higher than that of the seawater before blending with cooling water. In order to avoid "thermal pollution", rigorous guidelines provided by national authorities must be followed in order to avoid local increase on seawater temperature. With respect to brine concentration, a pre-dilution of this flow is usually carried out by means of waste water before brine disposal to the seawater. [4.6, 4.22, 4.23].

4.5 Economic aspects of MED process

Many studies have been carried out during these years on economics of desalination processes [4.25-4.30]. From a keen analysis of scientific literature, it could be noted that freshwater unit cost from MED process differs from case to case. As explained in [4.6, 4.25, 4.30], differences in cost values can be attributed to several factors which may be summarized as follow: (i) plant capacity and design (ii) site condition (iii) feed water properties, in particular salinity and turbidity, (iv)

energy cost, (v) plant life and amortization. In Alardin et al. [4.30] provided a typical breakdown of freshwater unit cost from thermal desalination process. More specifically, the authors stressed how the overall energy consumption (i.e. both thermal and electrical) account for 60-80% of operating cost, thus stressing the criticism of energy consumption in this process. Nowadays, typical specific capital cost values for MED process range among 900 and 2000 US$/($m^3$/day) [4.5]. Regarding unit fresh water cost, Soldatos et al. [4.25] classified values according to MED plants capacity. In particular, for plant capacity of more than 90,000 m^3/day, the reported cost ranged between 0.52 and 1.01 US$/$m^3$. Conversely, for medium MED capacities of 12,000 to 55,000 m^3/day, the cost varies between 0.95 and 1.95 US$/$m^3$. For plant capacity less than 100 m^3/day, unit cost ranges among 2 and 8 US$/$m^3$.

Freshwater unit cost higher than 2 US$/$m^3$ are typical of MED process powered by renewable energy sources as solar thermal (for instance, solar pond/MED or concentrating solar plant (CSP)/MED) and geothermal energy [4.30-4.39], whose costs are heavily affected by the high capital cost of the renewable energy technology and the low capacity of MED system.

4.6 Exergy and Thermoeconomic Analysis of MED process: literature review

Very few studies focusing on exergy evaluation of the MED process have been carried out so far. In [4.40], Nafey et al. carried out an exergy analysis for a 15,000 m^3/day capacity MED desalination plant. In that paper, the author showed that the number of effects influences the exergy efficiency of the desalination process. More specifically, an increase in the number of effects, from 1 effect to 6 effects, increases the exergy efficiency from 3.8% to 8.4%. In [4.41], a comparative study of three different configurations of MED-TVC systems highlighted the thermocompressor and effects as the units most contributing to the exergy losses. Other works focused

on the ExA of the MED-TVC process can be found in [4.42-4.44]. As concern thermoeconomic application to multiple effect distillation desalination systems, many research works have been focused on the exergoeconomic optimization. For instance, in in a recent paper by Sayyaadi and Saffari [4.45], a multi-objective evolutionary algorithm was used to minimize the unit cost of product calculated by a thermoeconomic expression. The analysis identifies relevant margins for improvement by reduction of exergy destruction and product cost compared to a reference base case. Manesh et al. [4.46] proposed an exergoeconomic multi-objective optimization of an integrated MED-RO desalination plant, identifying a Pareto optimal frontier for the two objective functions "Gained Output Ratio" and "cost of desalinated water production". In [4.47], Piacentino studied an 8-effect forward feed MED plant's thermodynamic performance and thermoeconomics by using a high disaggregation level which allowed for analyzing in depth the exergy (physical and chemical) costs variation throughout the plant.

4.7 Description of the reference MED-TVC plant

The examined TVC–MED is an existing plant located in Trapani (Sicily), constructed and started up in 1995. The plant is composed of four identical MED–TVC units with a specific capacity of 9000 m^3/day each, for a total plant capacity of 36,000m3/day [4.6, 4.48, 4.49, 4.50]. A schematic layout is presented in Figure 4.4. The MED–TVC unit configuration is parallel-feed type with 12 effects each. Each effect is a falling-film evaporator with the feed water sprayed on the external part of the tube-bundle. The produced distillate within each effect is condensed into the next one, by releasing its latent energy content for generating further distillate from seawater. Each effect is equipped with a tube bundle counting about 11,000 tubes, 7 m long and with an external diameter of 22 mm. In each unit steam is extracted from the 12^{th} effect at a 6 kPa absolute pressure and compressed up to the pressure

reigning in the first effect, i.e. 22 kPa, by means of thermal vapor compression. The steam re-compressed and de-superheated into the TVC is supplied to the first effect at a temperature around 63°C, in order to minimize scaling problems in the tube bundle. A temperature drops between two consecutive stages of 2–3 C is maintained, and the temperature of the brine exiting from the last effect ranges between 35°C and 38°C. As concerns details for each effect, experimental data are provided in Table 4.2. For a sake of clearness, the subscript "D" is referred to distillate, whereas "B" is referred to brine.

The feedwater is preheated into the down condenser by condensing a fraction of distillate generated into the 12^{th} effect; then, along its way to the first effect, feed pre-heaters are located every two effects. The *GOR* of the plant ranges between 14 and 16 kg distillate per kg of motive vapor. At the moment, the motive steam, whose total flowrate is equal from 36 up to 60 t/h, is produced by two boilers at 260°C and 45 bar, with a methane consumption estimated at 5.56 Nm^3 per m^3 distillate. Electrical energy consumption is estimated at 2 kWh/m^3, including pumps and utilities from the intake to the post-treatment section.

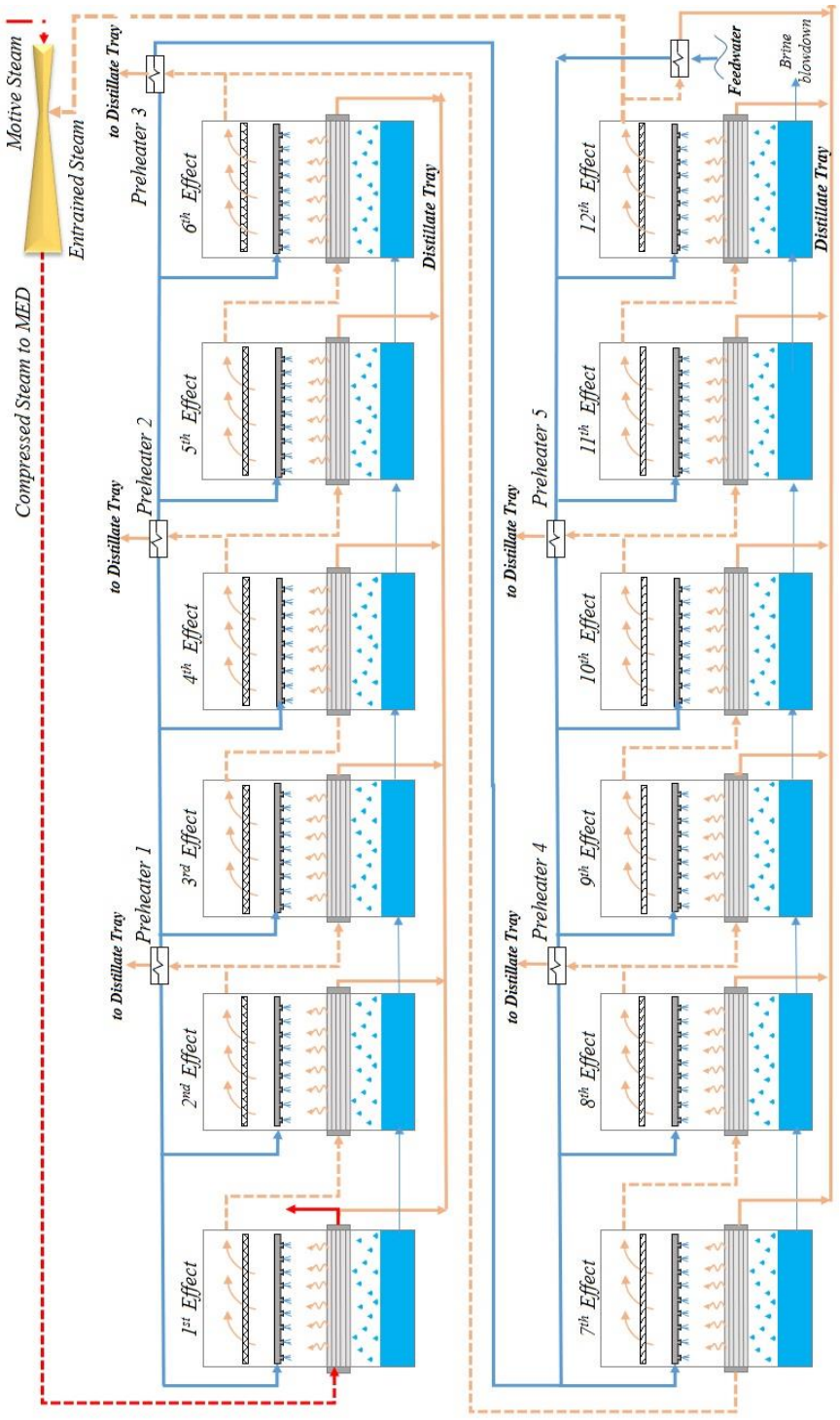

Figure 4.4 *Layout of the reference MED-TVC.*

Table 4.2 *Thermodynamic data for the reference MED-TVC plant [4.6, 4.48-4.50]*

		Effect 1	***Effect 2***	***Effect 3***	***Effect 4***	***Effect 5***	***Effect 6***
t_{feed}	(°C)	55.0	55.0	53.3	53.3	48.8	48.8
C_{feed}	(mol/l)	0.63	0.63	0.63	0.63	0.63	0.63
$\dot{m}_{feed}$	(kg/s)	26.2	26.2	26.2	26.2	26.2	26.2
t_D	(°C)	61.7	60.3	58	55.8	53.5	51.3
$\dot{m}_D$	(kg/s)	10	9.94	9.8	9.74	9.84	9.08
t_B	(°C)	62.5	61.5	59.4	57.3	55.0	52.9
C_B	(mol/l)	1.021	1.016	1.015	1.014	1.004	1.000
$\dot{m}_B$	(kg/s)	16.2	32.6	49.0	65.3	82.4	99.2

		Effect 7	***Effect 8***	***Effect 9***	***Effect 10***	***Effect 11***	***Effect 12***
t_{feed}	(°C)	44.2	44.2	39.6	39.6	29.6	29.6
C_{feed}	(mol/l)	0.63	0.63	0.63	0.63	0.63	0.63
$\dot{m}_{feed}$	(kg/s)	26.2	26.2	26.2	26.2	26.2	26.2
t_D	(°C)	49	46.7	44.4	42.1	39.8	37.2
$\dot{m}_D$	(kg/s)	9.29	8.20	8.54	7.16	7.63	5.63
t_B	(°C)	50.6	48.4	46.1	43.9	41.5	39.1
C_B	(mol/l)	0.989	0.982	0.968	0.962	0.945	0.934
$\dot{m}_B$	(kg/s)	117.2	134.8	153.8	172.3	192.8	212.7

4.8 Exergy Analysis of MED processes

In this paragraph, insights into the exergy analysis of MED processes are provided. First, the exergy analysis for the whole MED process is presented, then the analysis is carried out at subprocess level.

4.8.1 Exergy Analysis for the whole MED process

Exergy analysis can be applied to MED desalination processes at a whole system level, by referring to Figure 4.5. As shown in the scheme, according to the disaggregation level adopted, the entire process is treated as a “black box”, where only the exergy of energy/matter flows entering and exiting the whole plant are considered.

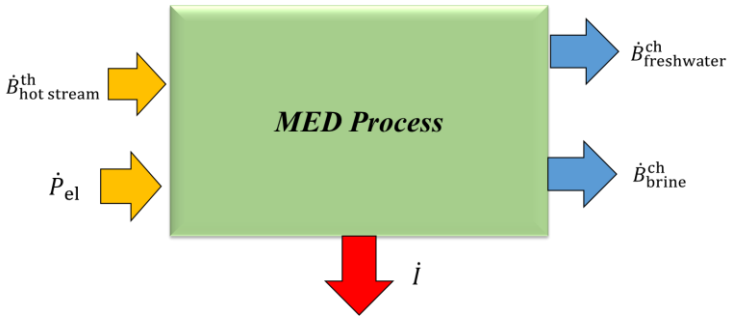

Figure 4.5 *Exergy Balance for the whole MED process*

As previously shown, energy input for a MED process is constituted by the following contributions: (i) heat supplied by means of a *"hot stream"*, commonly in the form of low-pressure steam or, more rarely, hot water produced by a boiler or supplied by an industrial process and (ii) electricity used to drive pumps and auxiliaries. In terms of exergy inputs to the MED process, it must be considered that: (i) the amount of thermal exergy released by the *"hot stream"* is lower than the heat content of the stream, and it may be calculated by the expression given in Equation (4.1) and (ii) the electricity used to drive pumps and other auxiliaries may be considered as pure exergy.

$$\dot{B}_{hot\ stream} = \dot{m}_{hot\ stream} \cdot \left[\left(h_{hot\ stream} - h_0 \right) - T_0 \cdot \left(s_{hot\ stream} - s_0 \right) \right] \tag{4.1}$$

As can be seen in the previous equation, the chemical exergy of the supplied steam or hot water (i.e. hot stream) is not considered, since no variation in its chemical composition is observed.

The exergy output is constituted by the chemical exergy of the brine and freshwater flows exiting the MED process, whose expressions are respectively provided in Equations (4.2) and (4.3). Both these expressions are derived from the chemical exergy of a stream of matter equations presented in Chapter 1, where chemical potentials are explicitly expressed in terms of salt and water activities in each solution and in the reference state. The thermal exergy content of these flows is

not considered since they are assumed to leave the whole system approximately in thermal equilibrium with the environment.

$$\dot{B}_{ch,\,fresh} = RT_0 \left[\dot{N}_{fresh} \ln\left(\frac{1}{a_{w,0}} \right) \right] \tag{4.2}$$

$$\dot{B}_{ch,brine} = RT_0 \left[\dot{N}_B \left(x_{s,B} \ln\left(\frac{a_{s,B}}{a_{s,0}} \right) + x_{w,B} \ln\left(\frac{a_{w,B}}{a_{w,0}} \right) \right) \right] \tag{4.3}$$

It is worth underlining that no exergy flow enters the MED system with the feedwater stream, since it is assumed in thermo-mechanical and chemical equilibrium with the environment. By setting the exergy balance to the overall process as shown in Eq. (4.4), exergy destruction due to all the irreversibility occurring within the plant is easily assessed by the following equation:

$$\dot{B}_{hot\ \ stream} + \dot{P}_{el} - \left(\dot{B}^{ch}_{brine} + \dot{B}^{ch}_{freshwater} \right) = \dot{I} \tag{4.4}$$

If the unit operated reversibly, no irreversibility would be generated and the minimum amount of exergy input to the system would be required for a specified freshwater production rate. It is trivial that under this ideal condition all the supplied exergy, i.e. $\left(\dot{B}^{th}_{hot\ \ stream} + P_{el} \right)$, would be entirely converted into the exergy content of concentrated brine and freshwater.

In order to formulate a synthetic indicator for the thermodynamic performance of the MED process, exergy efficiency for this unit may be defined as shown in Equation (4.5). In particular, this 2nd law-based efficiency is calculated as the ratio between the chemical exergy of the freshwater product and the thermal exergy of the supplied hot stream driving the unit [4.51].

$$\eta_{ex,MED-TVC} = \frac{\dot{B}^{ch}_{freshwater}}{\dot{B}_{hot\ \ stream} + P_{el}} \tag{4.5}$$

It is worth observing that chemical exergy of the exiting brine is not accounted for in the exergy efficiency of the MED process as shown in Equation (4.5). This choice is justified by the productive scope of MED plants which consists in producing freshwater, without further exploiting the chemical exergy of brine which is usually discarded back to sea. Only when the exiting brine is supplied to further units (such as a Salinity Gradient Power system that recovers it to produce electricity [4.52]), its exergy content would represent a useful product of the MED-TVC plant.

The examined MED-TVC plant is constituted by four identical units. For the sake of simplicity, below in this section the analysis is carried out for only one of the installed units.

Based on their chemical composition, both seawater and brine streams were properly modelled as water-NaCl solutions. In order to calculate activity coefficients, the Pitzer's model was adopted, which has been outlined in details in Chapter 2.

With reference to the environmental conditions to be used when calculating specific exergy of the material streams involved in the MED process, an average ambient temperature T_0= 298.15 K and pressure p_0=101.3 kPa were considered. Also, a salt concentration of seawater equal to 37000 ppm was considered as reference for chemical exergy calculations.

As clarified in the previous sections, the reference MED-TVC is fueled with motive steam produced by pressurized boilers at 260°C and 45 bar. The thermal exergy flow $\left(\dot{B}_{motive,in} - \dot{B}_{cond\ to\ boiler}\right)$, difference between the exergy of the superheated steam and the exergy of condensate water recirculated back to the boilers, represents the total exergy consumption of the whole MED-TVC process.

The exergy efficiency at a whole plant-level is calculated according to Eq. (4.6):

$$\eta_{ex,MED-TVC} = \frac{\dot{B}^{ch}_{freshwater}}{\left(\dot{B}_{motive,in} - \dot{B}_{cond\ to\ boiler}\right) + \dot{P}_{el}} = \frac{299.8}{\left(6348 - 64.42\right) + 750} \approx 0.043 \tag{4.6}$$

The low value of exergy efficiency at a whole plant level pinpoints the high incidence of thermodynamic irreversibility occurring along the MED system, when attempting to convert the thermal exergy content of motive steam into chemical exergy of freshwater product.

4.8.2 Exergy Analysis of the MED system at single-subprocesses level

In order to understand the origin of the low exergy efficiency of the MED-TVC system, exergy analysis may be carried out at a higher disaggregation level, i.e. by examining separately the elementary subprocesses involved in the MED plant. In this way, a complete and detailed picture of exergy flows, irreversibility and exergy efficiencies of each specific conversion process could be obtained. Looking at the MED-TVC process, the following main subprocesses could be distinguished:

4.8.2.1 Thermal Vapor Compression of the entrained steam

As previously mentioned, in the MED-TVC process a fraction of distillate generated within the last effect is entrained and compressed from the pressure level of the last effect to the pressure reigning in the first effect by means of a steam ejector. As clearly explained in [4.53], the ejector is a static component where low pressure steam is compressed by means of a mid or high-pressure steam, usually named "*motive steam*".

Once indicated with $b_{steam\ to\ MED}$ the specific exergy of the compressed steam exiting the TVC (corresponding to the inlet condition to the 1st effect of MED) and with $b_{entrained}$ the specific exergy of the steam exiting the 12th effect and entrained by the TVC, it follows that:

1) the exergy consumed by the TVC unit is equal to the exergy variation of the motive steam when expanding from its high pressure p_{motive} to the pressure of the

compressed steam supplied to the 1st effect, i.e. $p_{steam\ to\ MED}$. Then, the amount of exergy consumed is expressed by $\dot{m}_{motive}(b_{motive} - b_{steam\ to\ MED})$ as shown in Figure 4.6;

2) the increase of exergy content of entrained steam, due to compression from $p_{entrained}$ to $p_{steam\ to\ MED}$, is equal to $\dot{m}_{entrained} \cdot (b_{steam\ to\ MED} - b_{entrained})$ as shown in Figure 4.6 .

In Equations (4.7) and (4.8) exergy balance and exergy performance for the thermal vapor compressor are respectively given.

$$\dot{m}_{motive} \cdot (b_{motive} - b_{steam\ to\ MED}) - \dot{m}_{entrained} \cdot (b_{steam\ to\ MED} - b_{entrained}) = \dot{I}_{TVC} \tag{4.7}$$

$$\eta_{ex,TVC} = \frac{\dot{m}_{entrained}(b_{steam\ to\ MED} - b_{entrained})}{\dot{m}_{motive}(b_{motive} - b_{steam\ to\ MED})} \tag{4.8}$$

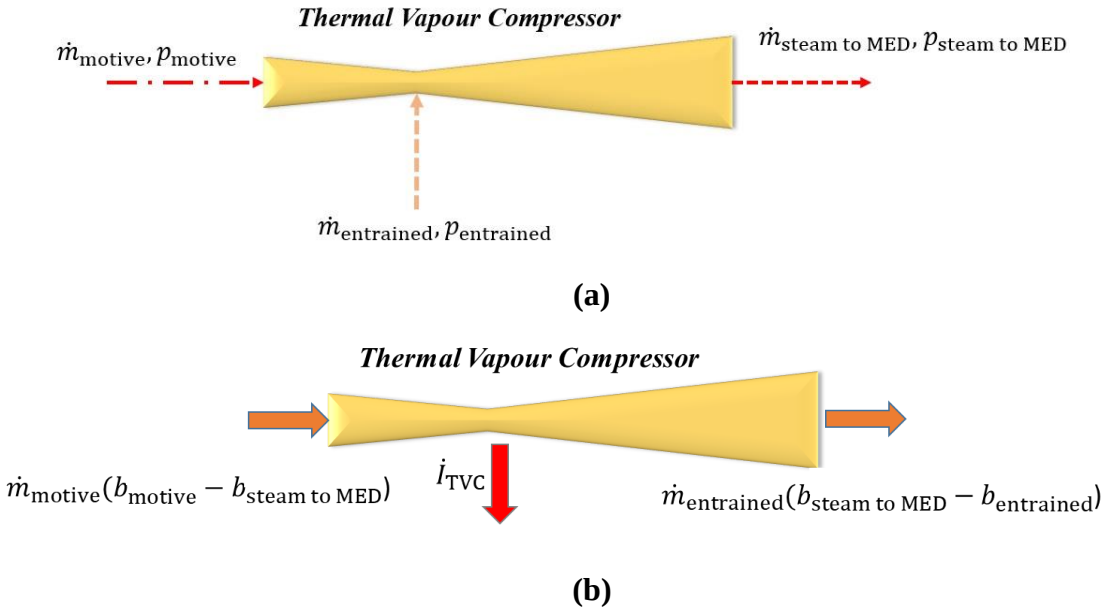

Figure 4.6 *Physical Scheme* ***(a)*** *and Exergy model* ***(b)*** *for Thermal Vapor Compressor*

4.8.2.2 Feedwater preheating

As shown in Figure 4.7, in a generic feed preheater the thermal exergy of feedwater is increased (together with its temperature) from $\dot{B}^{th}_{feed,in}$ to $\dot{B}^{th}_{feed,out}$ by recovering the thermal exergy released by condensing a fraction of the distillate produced within the coupled effect, i.e. $\dot{B}^{th}_{D,\,j\ to\ ph}$. By means of the exergy balance presented in Equation (4.9), it is possible to quantify the amount of exergy destroyed mainly due to the heat transfer across finite temperature difference between the two streams. The exergy efficiency of preheater can be calculated by the simple expression provided in Equation (4.10).

$$\dot{B}^{th}_{feed,out} - \dot{B}^{th}_{feed,\mathrm{int}} + \dot{I}_{ph} = \dot{B}^{th}_{D,\,j\ to\ ph} \tag{4.9}$$

$$\eta_{ex,ph} = \frac{\dot{B}^{th}_{feed,out} - \dot{B}^{th}_{feed,\mathrm{int}}}{\dot{B}^{th}_{D,\,j\ to\ ph}} \tag{4.10}$$

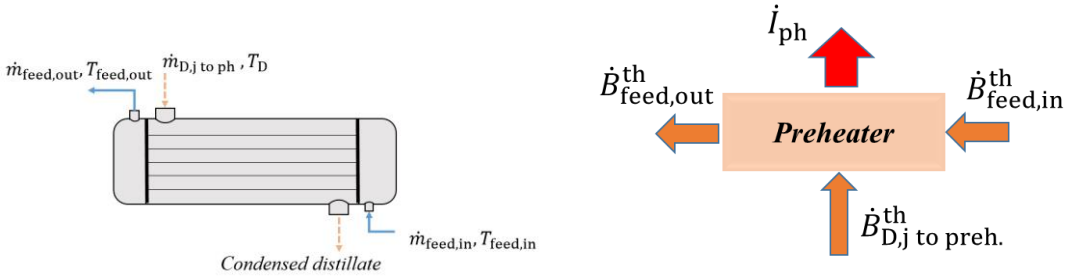

(a) **(b)**

Figure 4.7 *Physical Scheme* ***(a)*** *and Exergy model* ***(b)*** *for a generic feed preheater*

4.8.2.3 Distillate generation within 1st effect

A schematic representation of the exergy flows entering and exiting the 1st effect is given in Figure 4.8. Exergy balance for this effect is expressed by Equation (4.11), whereas exergy efficiency may be calculated based on Equation (4.12).

As intuitive from a rapid analysis of the figure, exergy flows entering the 1st effect are related to the following contributions: (i) the thermal exergy rate $\left(\dot{B}_{steam\ to\ MED} - \dot{B}_{cond\ to\ boiler}\right)$ released by the supplied steam flow (exiting the thermal vapor compressor) which condensates tube-side of the falling film evaporator, (ii) the thermal exergy of feedwater, indicated as $\dot{B}^{th}_{feed,1}$.

Some additional consideration is needed for the thermal exergy of the distillate produced in the 1st effect, i.e. $\dot{B}^{th}_{D,1}$. According to the definition of exergy efficiency given, for the examined effect, in Equation (4.12), the thermal exergy content of the distillate is intended as a sort of "non-extracted" (i.e. non-consumed) fraction of the thermal exergy supplied to the effect, that will be used in successive effects to generate further distillate. This interpretation clarifies the presence of $\dot{B}^{th}_{D,1}$ as a subtractive term at the denominator of exergy efficiency formula, rather than as a positive term at the numerator (where only the useful exergy product of the effect, i.e. the chemical exergy of distillate $\dot{B}^{ch}_{D,1}$, is included).

$$\dot{B}^{th}_{feed,1} + \left(\dot{B}_{steam\ to\ MED} - \dot{B}_{cond\ to\ boiler}\right) - \left(\dot{B}^{th}_{D,1} + \dot{B}^{ch}_{D,1} + \dot{B}^{th}_{B,1} + \dot{B}^{ch}_{B,1}\right) = \dot{I}_{eff,1} \qquad (4.11)$$

$$\eta_{ex,eff\,1} = \frac{\dot{B}^{ch}_{D,1}}{\dot{B}^{th}_{feed,1} + \left(\dot{B}_{steam\ to\ MED} - \dot{B}_{cond\ to\ boiler}\right) - \dot{B}^{th}_{D,1}} \qquad (4.12)$$

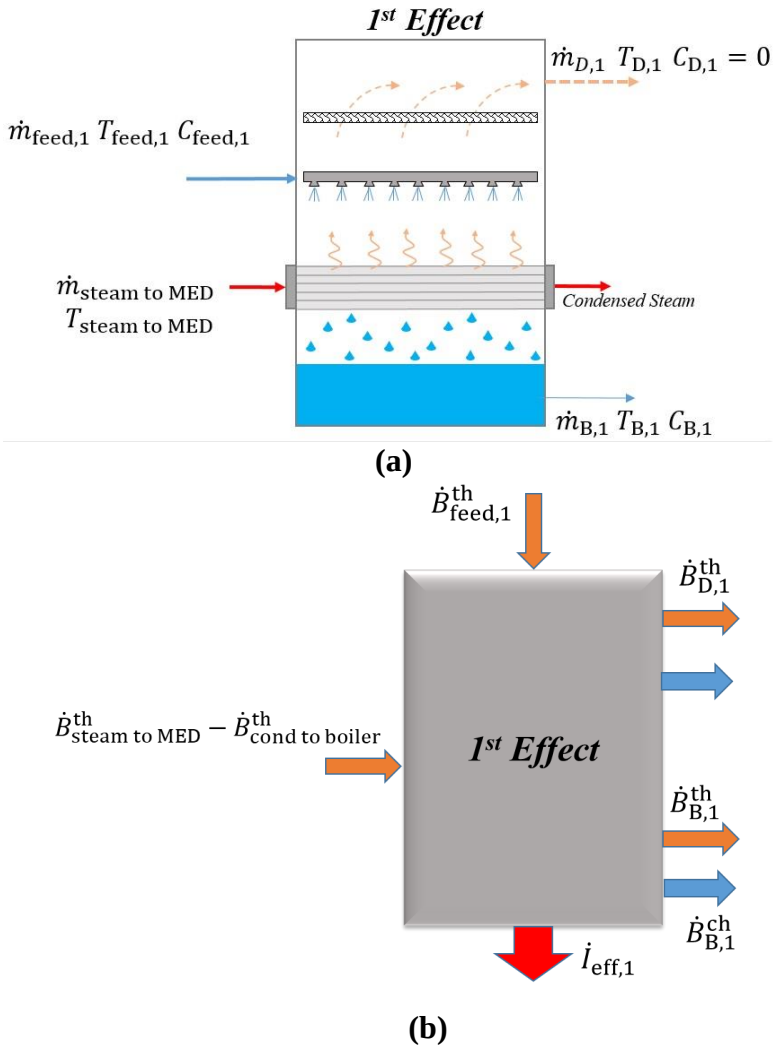

Figure 4.8 *Physical Scheme* ***(a)*** *and Exergy model* ***(b)*** *for the 1st effect*

4.8.2.4 Distillate generation within the generic "j-th" effect

As regards a generic "j-th" effect, for j =2 to N, a simple scheme of exergy flows entering and exiting the effect is presented in Figure 4.9. Also, the exergy balance and the analytical expression of exergy efficiency are provided in Equations (4.13) and (4.14), respectively. For a generic effect, the supplied exergy is constituted by

the following contributions: (i) the thermal exergy of feedwater $\dot{B}^{th}_{feed,j}$ (due to the parallel-feed configuration of the examined plant), (ii) the thermal exergy $\dot{B}^{th}_{D,\ (j\text{-}i)\ to\ j}$ of the distillate produced at the "(j-1)-th" effect (excluding the fraction eventually used for feedwater preheating), and (iii) variation of thermal exergy of the brine flow, indicated as $\left(\dot{B}^{th}_{B,\ (j-1)} - \dot{B}^{th}_{B,j}\right)$.

Exergy product of the "j-th" effect is represented by the chemical exergy of distillate, i.e. $\dot{B}^{ch}_{D,j}$. As already explained for the 1st effect, also for the generic "j-th" effect the thermal exergy of distillate, i.e. $\dot{B}^{th}_{D,j}$, is not considered a useful product but as a "non -extracted" fraction of the exergy input.

$$\dot{B}^{th}_{feed,j} + \dot{B}^{th}_{D,\ (j\text{-}i)\ to\ j} + \dot{B}^{th}_{B,\ (j\text{-}i)} - \left(\dot{B}^{th}_{D,j} + \dot{B}^{ch}_{D,j} + \dot{B}^{th}_{B,j} + \dot{B}^{ch}_{B,j}\right) = \dot{I}_{eff,j} \tag{4.13}$$

$$\eta_{ex,\ eff\ j} = \frac{\dot{B}^{ch}_{D,j}}{\dot{B}^{th}_{feed,j} + \dot{B}^{th}_{D,\ (j\text{-}i)\ to\ j} - \dot{B}^{th}_{D,j} + \left(\dot{B}^{th}_{B,\ (j\text{-}i)} - \dot{B}^{th}_{B,j}\right)} \tag{4.14}$$

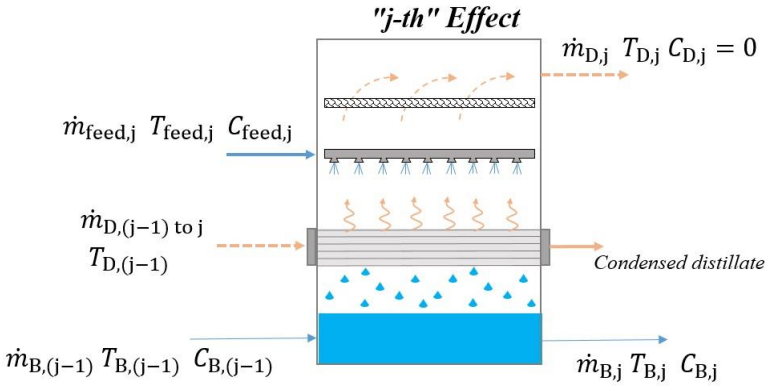

(a)

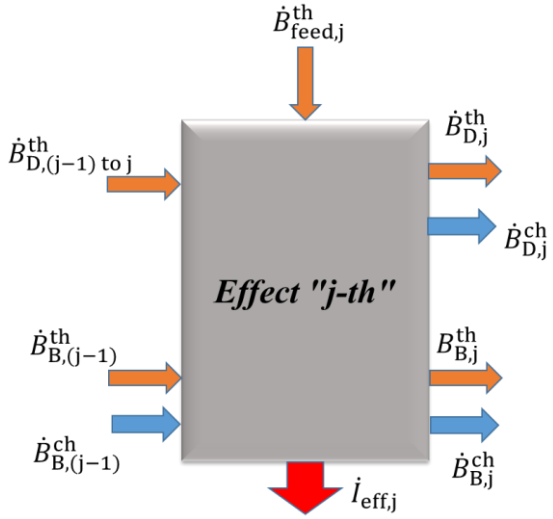

(b)

Figure 4.9 *Physical Scheme* ***(a)*** *and Exergy model* ***(b)*** *for the "j-th" effect*

4.8.3 Exergy Analysis for subprocesses of the reference MED-TVC

Once defined the general formulation of exergy balances and exergy efficiencies for each of the main subprocesses occurring in a MED unit, a detailed exergy analysis is carried out for the reference MED-TVC, based on its actual operating data shown in Table 4.2.

Thermal Vapor Compression of entrained steam

According to Equation (4.15) the exergy performance of thermal vapor compression is equal to 15.64%.

$$\eta_{ex,TVC} = \frac{\dot{m}_{entrained} \cdot (b_{steam\ to\ MED} - b_{entrained})}{\dot{m}_{motive} \cdot (b_{motive} - b_{steam\ to\ MED})} = \frac{709.6}{4537} \cong 0.156 \qquad (4.15)$$

This poor performance highlights that a high exergy destruction rate occurs within this component. Two aspects can be here remarked:

- Despite the low exergy efficiency, the inclusion of the TVC is beneficial in terms of overall exergy performance of the plant, compared to the hypothesis of directly producing by methane boilers the whole amount of low-grade steam supplied to the 1st effect. In fact, the conversion of chemical exergy of methane into thermal exergy of the supplied steam would achieve an even lower exergy efficiency, due to the low temperature of the required steam;
- Although seemingly located upstream the whole energy conversion chain in the MED-TVC system, the very low efficiency of the thermal vapor compressor does not represent an upper bound for the efficiency of the whole plant, since its lay-out is not "strictly sequential", due to the presence of exergy recirculating flows (such as the entrained steam). However, the plant achieves an overall exergy efficiency much lower than the TVC alone, due to the additional exergy destructions occurring along the evaporation processes in each effect.

Feedwater preheating

Exergy performance for each preheater was assessed on the basis of Equation (4.10). Results are shown in Figure 4.10. As can be seen, the down condenser and the preheater 5 achieve a lower exergy efficiency than preheaters 1, 2, 3 and 4. Exergy destruction in the feed preheating process is related to heat transfer across a finite temperature difference between a fraction of the produced distillate which condenses shell-side and the feedwater being heated up tube-side. In the specific case, by analyzing the temperature profile for each preheater, a greater temperature difference is observed for preheaters 5 and down condenser with respect to the others, thus being justified the lower values of their exergy performance. It can be observed that

in most of the preheaters quite high exergy efficiencies are achieved, due to the "tightly" designed temperature profiles between the exchanging fluids.

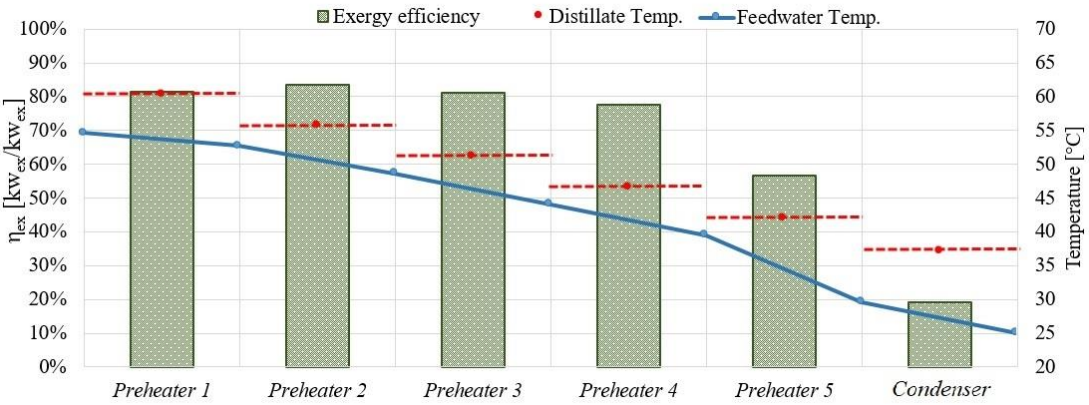

Figure 4.10 *Exergy Efficiency and Temperature profile for feedwater preheaters*

Exergy Analysis Results at whole effect level

Exergy flows related with brine, distillate and feedwater streams for each effect are shown in Table 4.3, also providing the values of specific exergy. It is worth noting that:

- specific chemical exergy of brine $b_{B,j}^{ch}$ decreases when passing from the first to the last effect: this trend is related to the reduction in brine concentration, i.e. $C_{brine,}$ as observed from the values provided in Table 4.3. In a PF-MED configuration, as the one examined in details in the present chapter, pure water is not separated from brine exiting the previous effect as occurs in a FF-MED configuration. As a consequence, no increase in salt concentration of the brine is observed when passing from one effect to the next one. Conversely, chemical exergy flowrate of the brine $\dot{B}_{B,j}^{ch}$ increases from the 1st to the last effect, due to the gradual increase in the mass flowrate of brine that

overcomes the influence of the aforementioned slightly decrease in the specific chemical exergy.

- specific thermal exergy of the brine, $b_{B,j}^{th}$, decreases when passing from the 1st to the last effect, due to the decrease of brine temperature. When combined with the gradual increase in the brine mass flow rate, the above trend leads to a non-monotone behavior of the thermal exergy of brine flow, which initially increases and, after a maximum value at effects no. 6 and 7, gradually decreases in the successive effects.
- a constant value is obtained for specific chemical exergy of distillate $b_{D,j}^{ch}$, due to the assumption of a salts-free distillate in all the effects. In terms of exergy flow, a decrease of the chemical exergy of distillate $\dot{B}_{D,j}^{ch}$ is observed passing from the 1st to the last effect, due to the reduction in the amount of distillate generated at lower temperatures.

In Figure 4.11, values of exergy efficiency for each effect are shown, calculated based on Equations. (4.12) and (4.14). As can be seen, the 2nd law-based efficiency ranges between 16% and 22 %, indicating that only a small fraction of the thermal exergy used to evaporate feedwater within each effect is converted into chemical exergy of the distillate product.

Table 4.3 *Exergy analysis results for the examined case*

	Brine				***Distillate***				***Feed***	
Effect	$b^{th}_{B,j}$ (Jex/g)	$\dot{B}^{th}_{B,j}$ (kWex)	$b^{ch}_{B,j}$ (Jex/g)	$\dot{B}^{ch}_{B,j}$ (kWex)	$b^{th}_{D,j}$ (Jex/g)	$\dot{B}^{th}_{D,j}$ (kWex)	$b^{ch}_{D,j}$ (Jex/g)	$\dot{B}^{ch}_{D,j}$ (kWex)	$b^{th}_{F,j}$ (Jex/g)	$\dot{B}^{th}_{F,j}$ (kWex)
1	9.12	147.7	9.01	7.786	266.6	2666.0	51.48	28.60	5.924	155.2
2	8.65	282.1	8.79	15.29	257.5	2523.8	51.48	28.03	5.924	155.2
3	7.72	378.2	8.72	22.79	242.5	2376.2	51.48	28.03	5.290	138.6
4	6.83	446.3	8.72	30.38	227.8	2065.7	51.48	28.31	5.290	138.6
5	5.92	488.1	8.29	36.46	212.4	1932.4	51.48	26.02	3.777	98.95
6	5.15	510.5	8.15	43.15	197.3	1603.7	51.48	26.88	3.777	98.95
7	4.35	510.2	7.66	47.97	181.4	1487.3	51.48	23.45	2.482	65.02
8	3.65	492.5	7.39	53.23	165.2	1141.7	51.48	24.59	2.482	65.02
9	2.98	459.1	6.86	56.41	148.8	1071.2	51.48	20.59	1.449	37.97
10	2.41	414.6	6.61	60.84	132.1	687.8	51.48	22.02	1.449	37.97
11	1.84	355.4	5.98	61.66	115.2	656.6	51.48	16.30	0.147	3.85
12	1.35	287.8	5.62	63.93	95.8	95.8	51.48	18.02	0.147	3.85

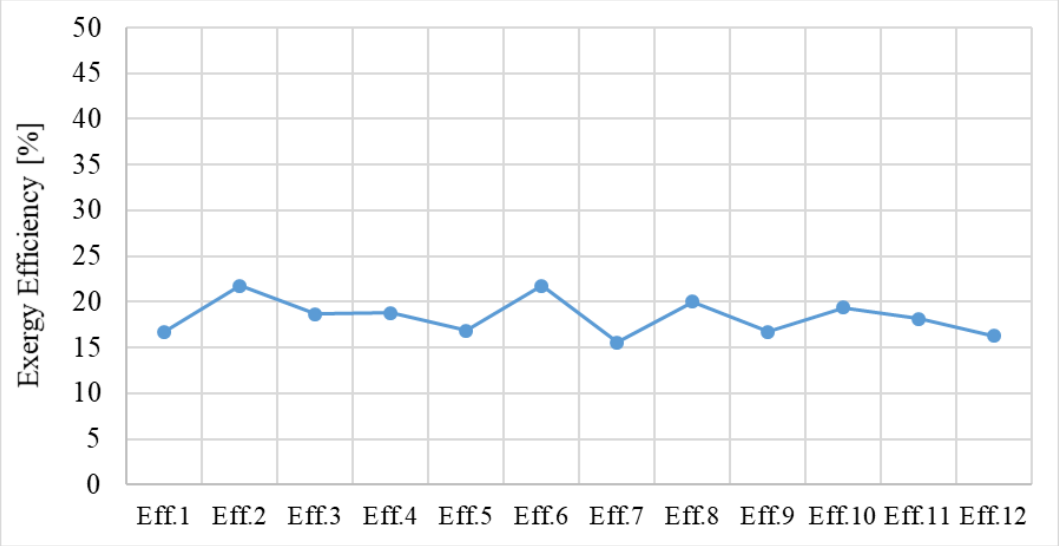

Figure 4.11 *Exergy Efficiency for each effect*

4.9 On the main outcomes of Exergy Analysis

In this paragraph, some brief interpretations of the results of exergy analysis are proposed. Based on the results of exergy analysis carried out at subprocesses level, two main criticisms may be identified in the proposed lay-out:

- The largest contribution to exergy destruction is related with the thermal vapor compressor. Consuming high-pressure motive steam to produce the

low-pressure steam supplied to the 1st effect is intrinsically inefficient, also operating with a well design steam jet ejector. In order to overcome this inherent limit of the plant, rethinking of the heat supply strategy would be absolutely needed, designing the system to be driven by low pressure steam produced exploiting heat cascades from a power cycle or a higher temperature industrial process. This need would be even more evident if the boundary of the analyzed system were extended to comprise the additional exergy destructions occurring in the methane boilers.

- The conversion, taking place in the evaporators, of thermal exergy released by condensing vapors into chemical exergy of the distillate is rather inefficient. Possible improvements based on designing the evaporators to operate with a lower temperature difference are limited by both thermodynamic constraints (i.e. related to the Boiling Point Elevation, which consumes part of the driving force available for heat transfer) and cost considerations.

4.10 Exergy Cost Accounting of the reference MED-TVC

Exergy analysis provides insights on location and magnitude of the thermodynamic losses occurring within an energy conversion system. By this tool, however, it is not possible to assess the contribution of each material or energy flow to the total exergy consumption of external resources. In this sense, the use of rigorous and systematic cost accounting techniques provides much more comprehensive results, since it reflects not only the intrinsic exergy efficiency at component or subprocess level, but it also considers the functional interactions among components which depend on the peculiar design of plant lay-out. A same component, in fact, even achieving a same exergy efficiency, may contribute differently to the consumption of external resources if located in different position along the "energy conversion chain"

One of the most reliable and comprehensive thermoeconomic approaches for the analysis of complex energy conversion systems is the well-known "*Theory of Exergetic Cost*" [4.54].

The Exergetic Cost of a material stream or energy flow represents the amount of external exergy consumed by an energy conversion system to obtain it according to a well specified process and sequence of components. Exergetic Costs are calculated based on a rigorous accounting of all the exergy destructions involved along the plant to obtain the examined stream or energy flow. Obviously, the more inefficient the energy conversion process that generates the stream, the higher the amount of irreversibility "charged" on it and, consequently, its Exergetic Cost (per unit of exergy). By means of this method, insights on the cost formation process are obtained and a clear view of the subprocesses (or the components or the specific inefficiencies) mostly contributing to increase the energy consumption of the system may be derived.

The resulting model essentially consists of the following set of equations:

- *Exergy Cost Conservation* (one for each subprocess) that, according to the conservative nature of costs, imposes that the cost of all the exergy resources entering a component equals the cost of the flows exiting the same component [4.54];
- *Auxiliary equations*, formulated based on a number of different principles (exergy extraction, multiple outputs, external assessment) and included whenever in a plant component we have several products (with unknown exergoeconomic costs), thus being insufficient the use of one single "cost balance" equation [4.54].
- *Allocation of Residues*: such flows are not allocated on the component where the exergy is uselessly discarded, but assigned as an additional input cost to the upstream components where the residue has been generated [4.55].

For the examined MED-TVC plant, the exergy cost equations are presented below in details for each sub-process. With regard to the adopted symbolism, the unit exergy cost of the "i-th" component product, indicated as k_i^* expresses the amount of the external exergy consumed by the plant for producing a unit of exergy of the product itself (being thus measured in kW_{ex}/kW_{ex}).

- ✓ *Exergy Cost Balance for the Thermal Vapor Compressor*

$$k^*_{motive}\dot{B}_{motive} + k^*_{entrained}\dot{B}_{entrained} = k^*_{steam\ to\ MED}\dot{B}_{steam\ to\ MED} \tag{4.16}$$

Auxiliary Equations for TVC:

$$k^*_{\mathrm{th,D,12}} = k^*_{\mathrm{entrained}} \tag{4.17}$$

The auxiliary equation for the TVC imposes that the thermal exergy cost of entrained vapors is equal to the exergy unit cost of distillate produced in the 12th effect. An external assessment is required for the unit exergy cost of motive steam, since the boundary of the analyzed system does not comprise the methane boiler used to produce steam. As a reasonable assumption, considering an exergy efficiency of the boiler equal to 0.45, $k^*_{th\ motive}$ results equal to 2.22 $kW_{ex}/kW_{ex.}$

- *Exergy Cost Balance for the 1st effect*

$$k^*_{steam\ to\ MED}\left(\dot{B}_{steam\ to\ MED} - \dot{B}_{cond\ to\ boiler}\right) + k^*_{th,\ feed\_1}\dot{B}^{th}_{feed\_1} + \frac{1}{12}k^*_{th,B,12}\dot{B}^{th}_{B,12} = k^*_{ch,D,1}\dot{B}^{ch}_{D,1} + k^*_{th,D\_1}\dot{B}^{th}_{D,1} + k^*_{ch,B,1}\dot{B}^{ch}_{B,1} + k^*_{th,B,1}\dot{B}^{th}_{B,1} \tag{4.18}$$

- Auxiliary Equations for the 1st effect

$$k^*_{ch,B,1} = 0 \qquad k^*_{ch,D,1} = k^*_{th,D,1} \qquad k^*_{th,B,1} = k^*_{th,D,1} \tag{4.19 a, b, c}$$

Exergy balance for the 1st preheater is given in Equation (4.18). Referring to Figures. 4.8.b, all the exergy costs of input flows are summed up and imposed equal to the total cost of the exiting exergy flows.

As can be from Eqution (4.18), thermal exergy of the brine exiting the 12th effect is considered as a residue flow and its exergetic cost, i.e. $k^{*}_{th,B,12}\dot{B}^{th}_{B,12}$, is uniformly re-allocated as an additional input cost to all the upstream effects, following the previously mentioned approach proposed in [4.55] for the allocation of residues.

In Equations (4.19 a), (4.19 b) and (4.19 c) auxiliary equations for the first effect are expressed. In particular:

- Equation (4.19 a) imposes that specific cost of chemical brine is null. This condition is coherent with the assumption not to consider the chemical exergy of the brine as a useful product of each effect (being finally rejected back to sea).
- Equations (4.19 b) and (4.19 c) impose a same unit exergetic cost for the thermal and chemical exergy of the distillate and the thermal exergy of the brine. The rational of this assumption lies in the fact that, at the proposed plant disaggregation level (with the "effect" modelled as a unique elementary component), it is not possible to distinguish between the subprocesses occurring within the effect and leading to produce these exergy flows. Then, having these exergy outputs a same "productive history", they are charged with a same amount of "exergy destruction provoked per unit exergy" and consequently assigned a same unit cost.

- *Exergy Cost Balance for "j-th" effect*

$$k^{*}_{th,feed\,j}\dot{B}^{th}_{feed,j} + k^{*}_{th,D,j-1}\dot{B}^{th}_{D,\,(j\text{-}1)\,to\,next} + k^{*}_{ch,B,j-1}\dot{B}^{ch}_{B,j-1} + k^{*}_{th,B,j-1}\dot{B}^{th}_{B,j-1} + \frac{1}{12}k^{*}_{th,B,12}\dot{B}^{th}_{B,12} = k^{*}_{ch,D,j}\dot{B}^{ch}_{D,j} + k^{*}_{th,D,j}\dot{B}^{th}_{D,j} + k^{*}_{ch,B,j}\dot{B}^{ch}_{B,j} + k^{*}_{th,B,j}\dot{B}^{th}_{B,j} \quad (4.20)$$

- Auxiliary Equations for the "j-th" effect

$$k^*_{ch,B,j} = 0 \qquad k^*_{ch,D,j} = k^*_{th,D,j} \qquad k^*_{th,B,j} = k^*_{th,D,j} \qquad \text{(4.21 a, b, c)}$$

✓ *Exergy Cost Balance for the generic preheater*

$$k^*_{th,\,feed\ in}\dot{B}^{th}_{feed\ in} + k^*_{th,D\,j}\dot{B}^{th}_{D\ to\ preheater} = k^*_{th,\,feed\ out}\dot{B}^{th}_{feed\ out} \qquad (4.22)$$

Referring to Figure 4.7, Equation (4.22) expresses the cost balance for the generic preheater.

The set of equations presented above constitutes a balanced system of linear equations that can be easily solved by software.

4.10.1 Results of Exergy Cost Accounting for the examined plant

Once defined the exergy cost accounting model for MED-TVC process, it was applied to the examined case and solved by means of *Engineering Equation Solver* [4.56]. In Table 4.4 specific costs of thermal exergy of the motive steam, entrained vapor and compressed vapor supplied to the first effect of the MED section are shown. As concerns the specific cost of thermal exergy of the motive steam, the external assessment $k^*_{motive} = 2.22$ kW_{ex} / kW_{ex} was used in this analysis. This condition states that motive steam is produced by a boiler whose exergy performance is equal to 0.45 (in particular $k^*_{\mathbf{motive}} = \dfrac{1}{\eta_{ex,boiler}} = \dfrac{1}{0.45} = 2.22$)

From the exergy cost balance of TVC, the specific cost of thermal exergy exiting from TVC and supplied to the first effect, i.e. $k^*_{steam\ to\ MED}$, results equal to 15.84 kW_{ex}/kW_{ex}. This value indicates that the unit exergy of steam supplied to 1st

effect implies the consumption of nearly 15.84 kW_{ex} of external exergy resources. This value is nearly seven times higher than the exergy cost of motive steam, due to the extremely low exergy efficiency and the high exergy destruction by irreversibility generated during thermal vapor compression of the entrained steam.

Table 4.4 *Specific exergy cost for TVC unit*

$\dot{B}_{motive}$	(kW_{ex})	6348
k^*_{motive}	(kW_{ex}/kW_{ex})	2.22
$\dot{B}_{entrained}$	(kW_{ex})	354.3
$k^*_{\text{entrained}}$	(kW_{ex}/kW_{ex})	88.73
$\dot{B}_{steam\ to\ MED}$	(kW_{ex})	2875
$k^*_{\text{steam to MED}}$	(kW_{ex}/kW_{ex})	15.84

The values obtained for the specific exergetic cost and the exergetic cost flow for each effect are presented in Table 4.5.

The unit cost $k^*_{ch,D}$ of the chemical exergy of distillate sharply increases, from 20.05 kW_{ex}/kW_{ex} to 88.73 kW_{ex}/kW_{ex}, when passing from the first to the last effect. Analogous results are observed for the specific cost of thermal exergy of distillate and brine. In spite of the parallel configuration adopted to feed salty water to the different effects, the sequential exploitation (along the effects from 1 to 12) of the thermal exergy of compressed steam (supplied to drive the 1st effect) and the high irreversibility occurring in each effect when converting thermal exergy into chemical exergy of the distillate induce a gradual increase of the unit exegetic cost of thermal exergy. Then, in cumulative terms, a unit of chemical exergy of the distillate produce in the 12th effect is "charged" with a higher amount of exergy destruction, compared to the distillate produced in the 1st effect, thus justifying the trend observed in the specific exergetic cost.

The specific cost of the thermal exergy of the feed, i.e. k^*_{feed}, dramatically increases along the feed pre-heating line, passing from 69.66 kW_{ex}/kW_{ex} (in the 1st and 2nd effects) to 461.26 $kW_{ex}/kW_{ex,}$ (in the 11st and 12nd effect). As previously explained, the thermal exergy of a small fraction of distillate is consumed as exergy source along the feedwater preheating process. Since $k^*_{th,D,j}$ values steeply increase when moving forward along the MED plant (from the 1st to the 12th effect), the preheater 5 (see plant scheme in Fig. 4.4) consumes a much more "precious" or costly exergy input to preheat the feedwater. Then, an increase in the specific cost of thermal exergy of the preheated feed is well explained, being also augmented by the lower exergy efficiencies achieved by the last preheaters (see Fig. 4.10). It is worth noting, in fact, that the steep increase of specific cost of thermal exergy from 134.91 kW_{ex}/kW_{ex} to 461.26 kW_{ex}/kW_{ex}, observed when passing from the 10th to the 11st effect, is caused by the extremely low exergy efficiency of the down condenser.

Table 4.5 *Specific Exergy Cost and Exergy Cost profiles along the MED plant*

	Brine		***Distillate***				***Feed***	
Effect	$k^*_{th,B,j}$	$k^*_{th,B,j}\dot{B}^{th}_{B,j}$	$k^*_{th,D,j}$	$k^*_{th,D,j}\dot{B}^{th}_{D,j}$	$k^*_{ch,D,j}$	$k^*_{ch,D,j}\dot{B}^{ch}_{D,j}$	k^*_{feed}	$k^*_{feed}\dot{B}^{th}_{feed}$
	$\left(\frac{kW_{ex}}{kW_{ex}}\right)$	(kW_{ex})	$\left(\frac{kW_{ex}}{kW_{ex}}\right)$	(kW_{ex})	$\left(\frac{kW_{ex}}{kW_{ex}}\right)$	(kW_{ex})	$\left(\frac{kW_{ex}}{kW_{ex}}\right)$	(kW_{ex})
1	20.05	2960.2	20.05	53446.6	20.05	573.3	69.66	10810.7
2	23.92	6746.7	23.92	60363.0	23.92	670.3	69.66	10810.7
3	28.34	10718.2	28.34	67336.4	28.34	794.2	74.49	10323.5
4	32.84	14657.4	32.84	74083.1	32.84	92.8	74.49	10323.5
5	37.78	18439.5	37.78	72999.7	37.78	983.1	88.57	8763.8
6	42.32	21602.9	42.32	78495.0	42.32	1137.6	88.57	8763.8
7	48.16	24573.1	48.16	71634.1	48.16	1129.5	107.54	6992.7
8	53.63	26414.3	53.63	76189.2	53.63	1318.9	107.54	6992.7
9	60.16	27623,1	60.16	64445.8	60.16	1238.8	134.91	5122.5
10	67.09	27818.0	67.09	68249.6	67.09	1477.4	134.91	5122.5
11	75.79	26936.9	75.79	49763.5	75.79	1235.4	461.26	1776.9
12	88.73	25538.7	88.73	53532.3	88.73	1598.7	461.26	1776.9

4.11 Outcomes of this analysis

In this chapter, exergy analysis and exergy cost accounting have been proposed for the in-depth interpretation of thermodynamic behavior of Multiple Effect Distillation processes. Exergy analysis has allowed for assessing in which processes the highest exergy destruction occurs. Exergy Cost accounting has provided with a comprehensive view of the cost formation process. A twelve effects MED parallel feed coupled with thermal vapor compression has been selected as case study. The low exergy efficiency of the whole MED process suggests that high exergy destruction occurs when converting thermal exergy of motive steam into chemical exergy of freshwater.

In order to provide a clear interpretation of the reasons for the low exergy efficiency of the MED system, a conveniently high disaggregation level has been adopted, by analyzing separately the thermal vapor compression, feedwater preheating and distillate generation. As concerns thermal vapor compression, the use of high-pressure steam to produce low pressure steam supplied to MED process resulted to be among the main responsible subprocesses for the poor plant performance. This result testifies the great convenience in supplying such low temperature processes, like the examined MED plant, by means of cogenerated heat recovered from power plants or waste heat cascaded from other industrial processes. Also, the conversion of thermal exergy into chemical exergy which takes place in the effects resulted quite inefficient, mainly due to the finite temperature difference between the heat exchanging fluid, which is in its turn limited by thermodynamic and cost constraints.

By means of exergy cost accounting, the cost formation process of the distillate could be clearly depicted. A substantial increase in specific cost of freshwater product has been observed from the first to the last effects, as a consequence of the irreversibility being cumulated along the quasi-sequential production process.

The applicative example has confirmed the potential of exergy and thermoeconomic analysis to provide with a comprehensive understanding of plant behavior, allowing the plant designer to identify the possible margins for improvement. Also, it is widely recognized in literature that the proposed methodologies can be conveniently used during plant operation, to allow for rational pricing of the product (especially in case of "dual purpose configurations).

References

[4.1] World Health Organization Report: *"Progress on sanitation ad drinking water"*, Available at: http://www.who.int/en/.

[4.2] Desaldata, www.DesalData.com.

[4.3] A. N. Mabrouk, H. E.S. Fath Technoeconomic study of a novel integrated thermal MSF–MED desalination technology, *Desalination*, Vol. 371, pp 115-125, 2015.

[4.4] M W Shahzad, M. Burhan, L. Ang, K. Choon Ng, Energy-water-environment nexus underpinning future desalination sustainability, *Desalination*, Vol. 413, pp.52-64, 2017.

[4.5] N. Ghaffour, T. Missimer, G.L. Amy Technical review and evaluation of the economics of water desalination: Current and future challenges for better water supply sustainability, *Desalination*, Vol. 309, pp. 197-207, 2013.

[4.6] G Micale, L Rizzuti, A Cipollina, *Seawater desalination conventional and renewable energy processes*, Springer, 2009.

[4.7] SIDEM MED reference list. Available at: www.sidem-desalination.com

[4.8] IDE Desalination Plant Reference List. Available at: http://www.ide-tech.com/wp-content/uploads/2016/06/E5643-107-24-stationery_web.pdf

[4.9] A. Al-Karaghouli, L.L. Kazmerski. Energy consumption and water production cost of conventional and renewable-energy-powered desalination processes. *Renew Sustain Energy Rev*, Vol. 24, pp. 343–356, 2013.

[4.10] Raphael Semiat, Energy issues in desalination processes. *Environ. Sci. Technol.*, Vol 42, pp. 8193–8201, 2008.

[4.11] H.T. El-Dessouky, H.M. Ettouney, *Fundamentals of Salt Water Desalination*, 1st Edition Elsevier Science, 2002.

[4.12] Al-Shammiri M, Safar M. Multi-effect distillation plants: state of the art. *Desalination*, Vol. 126, pp. 45–99.

[4.13] P. Palenzuela, D. Alarcón, G. Zaragoza, *Concentrating, Solar Power and Desalination Plants: Engineering and Economics of Coupling Multi-Effect Distillation and Solar Plants*, Springer International Publishing, 2015.

[4.14] G. Kronenberg, F. Lokiec. Low-temperature distillation processes in single- and dual-purpose plants, *Desalination*, Vol 136, pp. 189-197, 2001.

[4.15] L. Wu, Y. Hu, C. Gao, Optimum design of cogeneration for power and desalination to satisfy the demand of water and power, *Desalination*, Vol. 324, pp. 111–117, 2013.

[4.16] R.G. Raluy, L. Serra, J. Uche, A. Valero Life-cycle assessment of desalination technologies integrated with energy production systems *Desalination*, Vol. 167, pp. 445–458, 2004.

[4.17] 2011/877/EU: commission Implementing Decision of 19 December 2011 establishing harmonised efficiency reference values for separate production of electricity and heat in application of Directive 2004/8/EC of the European Parliament and of the Council and repealing Commission Decision 2007/74/EC Official J Eur Union, 343 (2011), pp. 91–96 23.12.2011

[4.18] A. Tamburini, A. Cipollina, G. Micale, A. Piacentino CHP (combined heat and power) retrofit for a large MED-TVC (multiple effect distillation along with thermal vapour compression) desalination plant: high efficiency assessment for different

design options under the current legislative EU framework, *Energy*, Vol. 115, pp. 1548–1559, 2016.
[4.19] E. Cardona, A. Piacentino Optimal design of cogeneration plants for seawater desalination Volume 166, 15 August 2004, Pages 411-426
[4.20] Osman A. Hamed. Overview of hybrid desalination systems-current status and future prospects. Desalination, Vol. 186, pp. 207-214, 2005.
[4.21] T. Rensonnet, J. Uche, L. Serra Simulation and thermoeconomic analysis of different configurations of gas turbine (GT)-based dual-purpose power and desalination plants (DPPDP) and hybrid plants (HP), *Energy*, Vol. 32, pp. 1012-1023, 2007.
[4.22] S. Lattemann, T. Höpner, Environmental impact and impact assessment of seawater desalination, *Desalination*, Vol. 220, pp-1-15, 2008.
[4.23] C. Sommariva, H. Hogg, K. Callister Environmental impact of seawater desalination: Relations between improvement in efficiency and environmental impact, *Desalination*, Vol. 167, pp. 439–444, 2007.
[4.24] Dawoud M, Al Mulla M. Environmental impacts of seawater desalination: Arabian Gulf case study. *International Journal of Environment and Sustainability*, Vol. 1, pp. 22-37, 2012.
[4.25] IC Karagiannis, PG Soldatos Water desalination cost literature: review and assessment *Desalination*, Vol. 233, pp. 448-456, 2008.
[4.26] D. Sambrailo, J. Ivic and A. Krstulovic, Economic evaluation of the first desalination plant in Croatia, *Desalination*, Vol. 170, pp. 339–344, 2005.
[4.27] A Ophir, F Lokiec, Advanced MED process for most economical sea water desalination *Desalination*, Vol. 182, pp. 187–198, 2005.
[4.28] K.V. Reddy, N. Ghaffour, Overview of the cost of desalinated water and costing methodologies, *Desalination*, Vol.205, pp.340-353, 2007.
[4.29] M. Al-Sahali, H. Ettouney, Developments in thermal desalination processes: Design, energy, and costing aspects *Desalination*, Vol. 214, pp. 227–240, 2007.
[4.30] J. Andrianne, F. Alardin, Thermal and membrane processes economics: selection for seawater desalination, *Desalination*, Vol. 153, pp. 305-311, 2002.
[4.31] E. Tzen and R. Morris, Renewable energy sources for desalination, *Solar Energy*, Vol. 75 pp. 375–379, 2003
[4.32] O Al Hawaj, MA Darwish A solar pond assisted multi-effect desalting system *Desalination*, Vol 99, pp. 119–135, 1994.
[4.33] AM. El-Nashar, M. Samad, The solar desalination plant in Abu Dhabi: 13 years of performance and operation history. *Renewable Energy*, Vol. pp. 263–274, 2014.
[4.34] Moser, M. Trieb, F. Fichter, T. Potential of concentrating solar power plants for the combined production of water and electricity in MENA countries, *Journal of Sustainable Development of Energy Water and Environment Systems*, Vol. 1, pp. 122-140, 2013
[4.35] C. Li, Y. Goswami', E. Stefanakos Solar assisted sea water desalination: A review *Renewable and Sustainable Energy Reviews* Vol. 19, pp. 136–163, 2013
[4.36] A. Al-Karaghouli, D. Renne, L.L. Kazmerski Solar and wind opportunities for water desalination in the Arab Regions, *Renew Sustain Energy Rev*, 13 (2009), pp. 2397–240
[4.37] E. Barbier, Geothermal energy technology and current status: an overview. *Renewable and Sustainable Energy Reviews* Vol. 6, pp. 3-65, 2002.

[4.38] A. Ophir. Desalination plant using low grade geothermal heat. *Desalination* Vol. 40, pp. 125-132, 1982.
[4.39] K. Karytsas, The Kimolos Geothermal Desalination Project. In: Proceedings of the International Workshop on Possibilities of Geothermal Energy Development in the Aegean Islands Region, Milos Island, Greece, pp. 206–219
[4.40] Nafey, A.S.; Fath, H.E.S.; Mabrouk, A.A. Thermo-economic investigation of multi effect evaporation (MEE) and hybrid multi effect evaporation—Multi stage flash (MEE-MSF) systems. Desalination 2006, 201, 241–2542
[4.41] Alasfour, F.N.; Darwish, M.A.; Amer, A.B. Thermal analysis of ME—TVC+ MEE desalination systems. Desalination 2005, 174, 39–614.
[4.42] Choi, H.S.; Lee, T.J.; Kim, Y.G.; Song, S.L. Performance improvement of multiple-effect distiller with thermal vapor compression system by exergy analysis. Desalination 2005, 182, 239–249.
[4.43] Samaké, O.; Galanis, N.; Sorin, M. Thermodynamic study of multi-effect thermal vapour-compression desalination systems. Energy 2014, 72, 69–79.
[4.44] García-Rodríguez, L.; Gómez-Camacho, C. Exergy analysis of the SOL-14 plant (Plataforma Solar de Almeria, Spain). Desalination 2001, 137, 251–2585
[4.45] H. Sayyaadi, A. Saffari Thermoeconomic optimization of multi effect distillation desalination systems Appl. Energy, 87 (2010), pp. 1122-1133
[4.46] M.H. Khoshgoftar Manesh, H. Ghalami, M. Amidpour, M.H. Hamedi Optimal coupling of site utility steam network with MED-RO desalination through total site analysis and exergoeconomic optimization Desalination, 316 (2013), pp. 42-52
[4.47] Piacentino, A. Application of advanced thermodynamics, thermoeconomics and exergy costing to a Multiple Effect Distillation plant: In-depth analysis of cost formation process. Desalination 2015, 371, 88–103
[4.48] Cipollina, G. Micale, L. Rizzuti A critical assessment of desalination operations in Sicily, *Desalination*, Vol. 182, pp.1-12, 2005.
[4.49] A. Cipollina, M. Agnello, A. Piacentino, A. Tamburini, B. Ortega, P. Palenzuela, D. Alarcon, G. Micale A dynamic model for MED-TVC transient operation; Desalination pp. 234-257, 2017
[4.50] Temstet C., Canton G., Laborie J. and Durante A. A large high-performance MED plant in Sicily. *Desalination*; Vol.105, pp 109-114, 1996.
[4.51] T. J. (Tadeusz J. Kotas, *The exergy method of thermal plant analysis*. Butterworths, 1985.
[4.52] Cipollina, A. Micale, G. Sustainable Energy from Salinity Gradients, Woodhead Publishing, 2016.
[4.53] Hassan, A. S. Darwish A.M. Performance of thermal vapour compression. Desalination, Vol. 335 pp 41-46, 2014.
[4.54] Lozano, M.A., Valero, A. Theory of the exergetic cost, Vol 18, *Energy* pp. 939-960, 1993.
[4.55] C. Torres, A. Valero, V. Rangel, and A. Zaleta, "On the cost formation process of the residues," *Energy*, vol. 33, no. 2, pp. 144–152, 2008
[4.56] Klein S.A. *et al.*, Engineering equation solver V9.810. Middleton, WI: Solar Energy Laboratory, F-Chart Software, 2010.

Chapter 5

Exergy Analysis and Thermoeconomic Cost Accounting for a Combined Heat and Power steam cycle integrated with Multi-Effect Desalination-Thermal Vapor Compression plant

In this chapter exergy analysis and thermoeconomic cost accounting for a Combined Heat and Power steam cycle integrated with Multi-Effect Desalination-Thermal Vapor Compression plant is presented

In the first part of this chapter, a brief overview on dual-purpose plants which include Multi-Effect Desalination (MED) process is provided. Also, a literature review on Thermoeconomics for these systems is carried out.

Starting from a retrofit scheme proposed in literature for the investigated MED system, a thermoeconomic model is built. The goal is to show the capabilities of thermoeconomic cost accounting to provide: (i) a detailed picture of the cost formation process of freshwater and electricity produced in the system and (ii) a rational criterion to allocate sustained costs on both products. In the last part of this chapter, a Reverse Electrodialysis unit is integrated, in order to exploit the chemical exergy of the brine exiting the MED process. In this scenario, exergy costs for each product are evaluated.

5.1 On "Dual Purpose" and "Hybrid Plant" configuration for MED process

As already shown in Chapter 4, one of the main barriers to the spread of Multi-Effect desalination systems lies in their high-energy consumption per m^3 of

freshwater product [5.1]. Nevertheless, one of their advantage is the possibility to be fueled by low temperature heat [5.1]-[5.3]. This feature allows for the exploitation of low-grade heat available from industrial processes (which would be otherwise wasted if not used) [5.4], from power plants [5.5], or by using renewable thermal energy sources [5.6]]-[5.[5.9]. For this reason, current researches have been paying growing attention to the design of dual-purpose systems for simultaneous production of electricity and fresh water. Freshwater production from a cogeneration system allows for a decrease in specific cost and in environmental burdens of freshwater production. For instance, according to [5.10], typical cost value for MED process operated in cogeneration mode is 0.5 US$/m^3, against the 1.25 US$/m^3 obtained from a stand- alone MED process. Further economic benefits may be achieved in those contexts where cogeneration is supported by national directives as in the case of European Union Directive [5.5]. To this regard, Piacentino et al. [5.5] proposed a condensing cycle with steam extraction as an efficient CHP retrofit solution for an existing Multiple Effect Distillation with Thermal Vapor Compression (MED-TVC); the cited paper proposed a sensitivity analysis of design and operation parameters, in order to assess whether or not the produced electricity was eligible for the "high efficiency cogeneration" assessment, according to the current legislative framework.

As concerns the achievable environmental benefits, Valero et al. [5.11] carried out a Life cycle assessment for MED process in order to assess environmental impacts of this technology. In particular, by comparing results for a stand-alone configuration with respect to a cogeneration operating mode, it was shown that CO_2 emission reduces respectively by 61% when coupling MED process with a natural gas fueled Combined cycle (CC), and by 55% when considering a coal fueled CC.

A viable solution is provided by thermal desalination processes with fossil-fuel or nuclear power plants coupled with MED process [5.12].

The technical feasibility of small-medium scale integrated schemes including cogeneration and thermal desalination units has been analyzed in a recent paper by

Salimi et al. [5.13], where thermodynamic modeling and economic assessment for a reciprocate engine coupled to a multiple effect desalination unit were presented.

An increasing interest for coupling MED processes with Concentrating Solar Power (CSP) technologies has been shown during these years. However, this is only limited to a small capacity of the system. For instance, in [5.8] the attractiveness of Concentrating Solar Power schemes integrated with thermal or mechanical desalination systems was investigated, in terms of levelized water cost and for possible application in Middle East and North Africa countries. An analysis of the potential for highly integrated solar energy systems to supply the requests from isolated communities is presented in [5.14] and [5.15]. An interesting analysis of technological and economic aspects of Multi-effect Distillation process integrated with CSP can be found in [5.7] . Also, geothermal energy represents a possible source to drive water desalination units, as testified by the comprehensive review of technologies presented in [5.9].

One of the main drawbacks of cogeneration system for electricity and freshwater is the simultaneous water and electricity generation [5.16] which does not allow for plant flexibility during plant operation in those contexts where seasonal water and power demands are extremely variable and not perfectively matched. In this situation, the system is not run at its maximum efficiency values, thus not achieving profitable energy saving. A way to address this problem is the use of "*hybrid systems"* [5.17]. Hybrid desalination systems combine thermal and membrane processes. The main advantages of these systems are: (i) the reduction in specific energy consumption, (ii) the flexibility in operation in the case of highly variable water and electricity demand, (iii) the cost saving due to the reduction in post-treatment of freshwater, and (iv) the possibility to use a unique low intake/out fall construction. In other words, by means of a "*hybrid plant configuration*" full load operation for the overall plant is maintained in those periods when power demand decreases significantly. The profitability of hybrid system as CC+MED+RO with

respect to a stand-alone RO plant is highly sensitive with fuel market prices [5.18]. Clearly, in GCC, where fossil fuels are extensively subsided, profitability of a hybrid plant with respect to stand alone RO is still assured [5.18].

One of the largest hybrid desalination plant in the world is "*Fujairah 2*" located in the United Arab Emirates [5.18]. The capacity plant is equal to 596,500 m^3/day. It combines Multiple Effect Distillation process with Reverse Osmosis, whose capacity is respectively equal to 450,000 m^3/day and 136,500 m^3/day. By means of this configuration, the power plant runs at its maximum capacity all year long.

5.1.1 Applications of Thermoeconomics in the analysis of dual-purpose plants

Most of the works available in literature focusing on the application of *Thermoeconomics* in dual purpose power plants integrated with desalination units has been oriented to the optimization of these systems. For instance, in Uche et al. in [5.19] carried out a thermoeconomic optimization of the design of dual-purpose power plant, composed by a steam power plant coupled with a MSF desalination unit. The minimization of total cost has been achieved by local optimization of each subprocess, thanks to the thermoeconomic isolation principle. A reduction in the computing resources and a simplification of the mathematical problem were achieved. In [5.20], thermoeconomic optimization of a hybrid pressurized water reactor (PWR) power plant coupled with a multi effect distillation desalination system with thermo-vapor compressor (MED-TVC) was carried out. In Ortega-Delgado et al. [5.22], an exergoeconomic cost accounting was carried out for comparing thermal (MED) and membrane (RO) desalination processes integrated with CSP. The analysis allowed for selecting a plant configuration with the lowest levelized cost for the freshwater and the electricity produced. In [5.23] two different combined solar cycles with different configurations of Multi-Effect distillation (MED) processes are considered. In the first configuration, the solar energy is directly utilized from the solar collector field via evaporator heat exchanger to the

first effect of the MED process. In this case, only potable water is produced. In the second case, the exhausted energy from the organic Rankine cycle (ORC) turbine is used in the first effect of the MED process and both electric power and desalted water are produced. The exergoeconomic analysis allowed for evaluating unit cost variation according to different design alternatives. Another interesting paper concerning exergoeconomic analysis of alternative solar-driven polygeneration systems can be found in [5.24]. A thermoeconomic assessment of an innovative dual-purpose system composed by transcritical CO_2 refrigeration cycle coupled with a MED system was carried out [5.25]. The analysis provided insights into the effect of exergy destruction and capital investments at each component sublevel.

5.2 Description of retrofit steam cycle for the investigated MED-TVC process

The thermoeconomic analysis carried out in this chapter refers to the same CHP-MED-TVC plant presented in [5.5]. Here, the potential of thermoeconomic cost accounting is investigated as an instrument to provide with a rational criterion to allocate costs of the consumed resources, either in the form of natural gas and capital investment, on the produced freshwater and electricity.

As concern the MED-TVC process, it is the same described in Chapter 4. It is worth reminding here, that it is an existing plant located in Trapani (Sicily), constructed and started-up in 1995. The plant is composed by four identical MED-TVC units with a specific capacity of 9000 m^3/day each, for a total plant capacity of 36000 m^3/day. The MED-TVC units are of the parallel-feed type and are constituted by twelve effects each Temstet C., Canton G., Laborie J. and Durante A. A large high-performance MED plant in Sicily. *Desalination*; Vol.105, pp 109-114, 1996.[5.26]-[5.27].

The retrofit scheme proposed consists of a topping CHP steam cycle with condensation and steam extraction. The scheme is illustrated in Figure 5.1, where all the material flows are identified and consecutively numbered to allow for a clear

formulation of the thermodynamic and thermoeconomic models of the plant. Steam is assumed to be produced in a conventional natural gas-fueled boiler (consisting of different sections, namely economizer, vaporizer, superheater and reheater); furthermore, three stage steam turbines are considered and respectively indicated as High Pressure, Intermediate Pressure and Low Pressure (i.e. HP, IP and LP). Surplus heat is discarded via a water-cooled condenser; in order to increase the efficiency of the cycle, a number of pre-heaters is included, and in particular:

a. 1 closed-type feedwater heater with drains pumped forward;
b. 5 closed-type feedwater heaters with drains cascaded backward;
c. 1 direct-contact feedwater heater, which also serves as a deaerator.

In order to allow for a more comprehensive assessment of plant efficiency, 5 different steam extraction pressures will be alternatively considered, respectively equal to p_A=4890 kPa, p_B=2800 kPa, p_C=1480 kPa, p_D=700 kPa and p_E=290 kPa and corresponding to the five extraction points indicated as A, B, C, D and E in Figure 5.1.

Also, the number of MED units simultaneously operating will be imposed to range between 1 and 4, in order to account for possible scheduled or unscheduled maintenance and eventual unexpected reductions in the freshwater demand. It is worthwhile observing that the retrofitted plant layout exploits the methane-fueled boilers as backup units, to supply motive steam for the desalination unit in case of temporary unavailability of steam extraction from the turbines, or in peak hours when the high price of electricity might suggest to maximize the power production and operate the CHP plant in “power production only” mode.

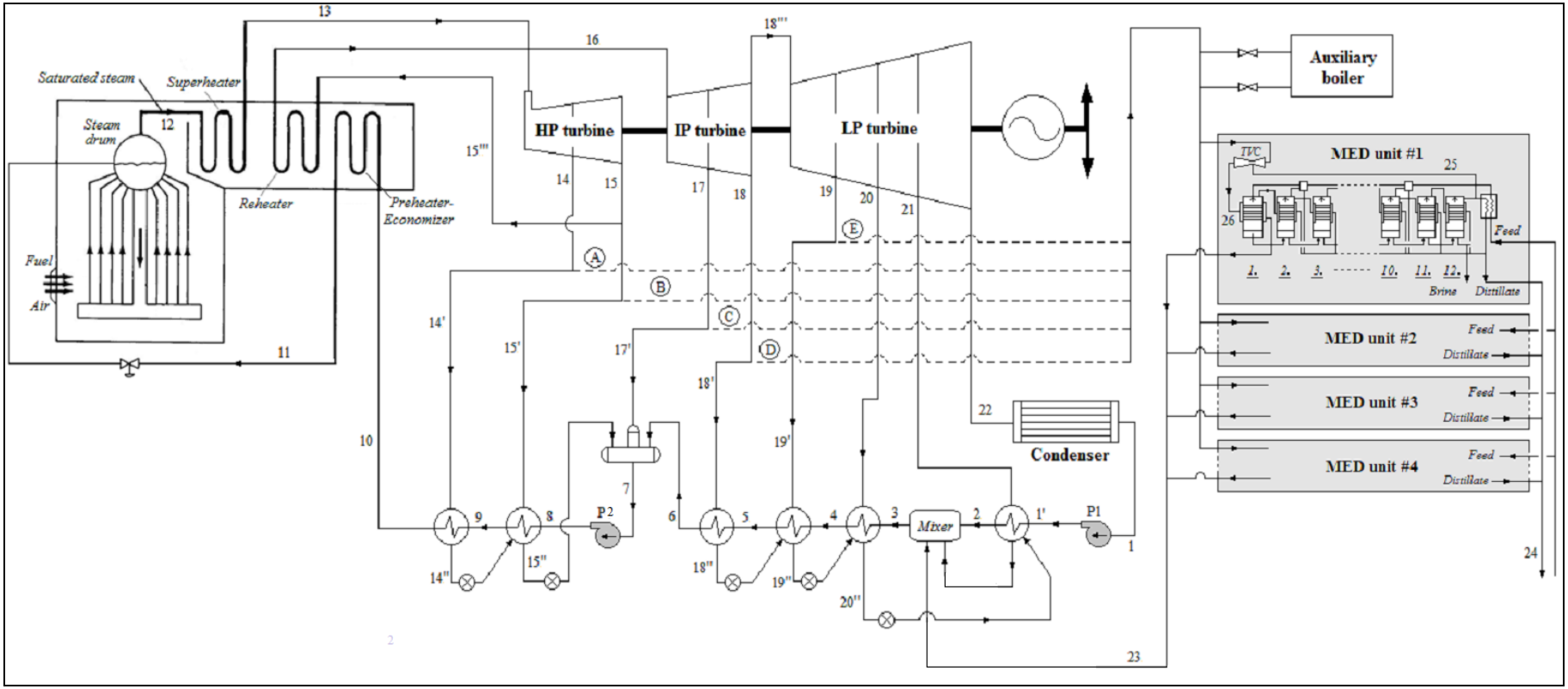

Figure 5.1 *Physical layout of CHP-MED-TVC plant [5.5]*

The main thermodynamic parameters of the power cycle are presented in Table 5.1 and Table 5.2. Some design values as Terminal Temperature Difference (TTD) of preheaters, steam extraction pressure for preheating section were selected according to the common practices in thermal power plant design, as suggested in [5.28].

Table 5.1. *Main features of Steam Power Plant*

Parameter		
Superheating Temperature		450°C
Reheating Temperature		450°C
Efficiency of steam generator		0.94
Isentropic efficiency of HP turbine, η^{HP}		0.90
Isentropic efficiency of IP turbine, η^{IP}		0.86
Isentropic efficiency of LP turbine, η^{LP}		0.84
Isentropic efficiency of pumps, η^{pumps}		0.85
Terminal Temperature	$TTD_{\text{preheater 1}}$	3°C
Difference of preheaters, *TTD*	$TTD_{\text{preheater 2}}$	3°C
	$TTD_{\text{preheater 3}}$	0°C
(i.e. "saturation	$TTD_{\text{preheater 4}}$	-1°C
temperature	$TTD_{\text{preheater 5}}$	1°C
of bled steam – exit	$TTD_{\text{preheater 6}}$	-2°C
water temperature")	$TTD_{\text{preheater 7}}$	-3°C
Net electric power production, $\dot{W}_{net}$		90 MW

An accurate thermodynamic model of the "CHP+MED-TVC" system was developed and implemented in Engineering Equation Solver software [5.29]. For the sake of brevity, the model is not presented here into details; it essentially consists of energy and mass conservation equations applied to each component by using EES built-in thermo-physical properties functions. The model includes a semi-empirical polynomial correlation representing the behavior of the steam-jet ejectors that drive the MED units.

Furthermore, as will be shown below, additional equations concerning the off-design operation mode of some components were also implemented in this model.

As concerns the effects of non-ideality, pressure drops along the pipes and in the steam generator are neglected, while irreversible expansion of the working fluid is taken into account by the isentropic efficiencies. Although this approach implies some deviations from the actual behavior of real-world plants, accounting only for the internal irreversibilities along the expansion process seems sufficient and coherent with the methodological scopes of the present analysis, which is essentially aimed at developing a reasonable structure of the cost formation process. Also, being the model based on a simplified modelling of a steam cycle, validation was not necessary (nor could it have been performed against experimental data, since the steam plant only represents a theoretical retrofit scheme, the real installation currently including only the MED units supplied by steam boilers). However, the technical soundness of the model is sufficient since the values obtained for the thermodynamic properties and plant performance are absolutely coherent to the typical values which can be found in literature and practice.

In Table 5.2 the thermodynamic parameters of the working fluid in each state are shown, for the particular operating condition with null steam extraction, i.e. with the plant operated in "power production only" mode. At full load operation, the steam cycle achieves a 90 MW_e net power production.

Table 5.2 *Thermodynamic properties of material streams in case of null motive steam extraction for the MED units*

Flow	p_i [kPa]	T_i [°C]	h_i [kJ/kg]	s_i [kJ/kg-K]	$\dot{m}_i$ [kg/s]
1	56.0	34.9	146.2	0.503	34.45
2	1476.0	56.5	237.9	0.786	34.45
3	1476.0	59.1	248.5	0.818	73.07
4	1476.0	86.7	364.4	1.154	73.07
5	1476.0	120.0	504.6	1.526	73.07
6	1476.0	166.0	702.4	2.002	73.07
7	1476.0	196.6	836.9	2.298	90.00
8	8000.0	197.7	844.7	2.299	90.00
9	8000.0	232.1	1001.0	2.618	90.00
10	8000.0	265.5	1161.0	2.926	90.00
11	8000.0	295.0	1317.0	3.207	90.00
12	8000.0	295.0	2758.0	5.743	90.00
13	8000.0	450.0	3272.0	6.555	90.00
14	4890.0	378.4	3144.0	6.577	7.24
14'	4890.0	262.5	1147.0	2.907	7.24
15	2800.0	305.7	3013.0	6.603	82.75
15'	2800.0	230.0	990.3	2.610	13.62
16	2800.0	450.0	3347.0	7.118	76.38
17	1480.0	364.3	3179.0	7.158	3.30
18	700.0	275.8	3008.0	7.205	31.04
18"	700.0	165.0	697.2	1.992	6.26
18"'	700.0	275.8	3008.0	7.205	42.03
19	290.0	190.0	2845.0	7.456	3.85
19'	290.0	120.0	503.5	1.527	10.11
20	101.9	104.3	2688.0	7.560	3.10
20'	101.9	89.7	375.9	1.190	13.22
21	28.1	59.5	2529.0	7.679	0.62
22	5.6	34.9	2391.0	7.789	34.45

As stated above, the analysis will be performed, for five different steam extraction pressures, assuming the number of MED-TVC units to be supplied with extracted steam to range between 1 and 4. When the number of operating MED units varies, the mass flow rate of steam to be extracted also varies proportionally, and the operating condition of the steam turbines consequently changes. Of course, the pressure profiles are also influenced by the steam extraction pressure. The adopted thermodynamic model accounts for such off-design operating conditions by calculating all the intermediate pressures and all the modified isentropic efficiencies, based on the following equations derived from application of nozzle analogy [5.30]:

$$\frac{\dot{m}}{(\dot{m})_{\mathrm{d}}} = \frac{p_u^t}{(p_u^t)_{\mathrm{d}}} \sqrt{\frac{1-\left(\frac{p_k}{p_u^t}\right)^2}{1-\left(\frac{(p_k)_d}{(p_u^t)_d}\right)^2}} \tag{5.1}$$

$$\frac{\eta_{\mathrm{is}}}{(\eta_{\mathrm{is}})_{\mathrm{d}}} = 1-\alpha\left[\frac{\frac{(p_k)_d}{(p_u^t)_d}}{\frac{p_k}{p_u^t}}-1\right]^2 \tag{5.2}$$

In Equations (5.1) and (5.2) p_k and p_u indicate respectively the pressure downstream and upstream the steam extraction section; the subscript "*d"* refers to design case, while the superscript "t" refers to total pressure. The coefficient α is a constant that depends on the number of stages and the design of each specific turbine; in the present study, this coefficient has been assigned respectively the value 0.10 for the high-pressure turbine and 0.14 for the intermediate and low-pressure turbines [5.30].

In Table 5.3 the off-design pressure variations (for any given design extraction pressure between p_{A} and p_{E}, each one indicated as "Case A"-"Case E" in the column headers in the table) are reported, when all the four units are supplied. It is worthwhile observing that the bold black values in the grey-highlighted cells refer to

the pressure levels that do not experience any variation with respect to the values in the first column ("Design" case, intended as plant operating condition in "power only mode"), being situated above the steam extraction level as evident in Figure 5.1.

***Table 5.3**. Off-design pressure for any design extraction pressure when all MED units are supplied*

	"Design" Case	*Case "A"*	*Case "B"*	*Case "C"*	*Case "D"*	*Case "E"*
p_{13} (kPa)	8000.0	**8000.0**	**8000.0**	**8000.0**	**8000.0**	**8000.0**
p_{14} (kPa)	4886.0	**4886.0**	**4886.0**	**4886.0**	**4886.0**	**4886.0**
p_{15} (kPa)	2798.0	1882.0	**2798.0**	**2798.0**	**2798.0**	**2798.0**
p_{17} (kPa)	1476.0	1147.0	1124.0	**1476.0**	**1476.0**	**1476.0**
p_{18} (kPa)	701.0	450.8	439.8	435.3	**701.0**	**701.0**
p_{19} (kPa)	291.0	183.1	178.0	175.8	171.0	**291.0**
p_{20} (kPa)	101.7	63.5	61.7	60.9	59.3	56.9
p_{21} (kPa)	28.0	18.6	17.9	17.7	17.3	16.7

Also, based on the aforementioned semiempiric model for the steam jet ejector [5.31], it was possible to calculate the amount of steam to be extracted to supply any number of MED units, as a function of the steam extraction pressure. The results are shown in Table 5.4.

***Table 5.4**. Motive steam flowrate supplied to MED-TVC units*

	Steam Flowrate to MED-TVC units (kg/s)			
	N_{units}=1	N_{units}=2	N_{units}=3	N_{units}=4
Steam Extraction in A	5.70	11.40	17.10	22.80
Steam Extraction in B	5.82	11.65	17.47	23.30
Steam Extraction in C	5.98	11.97	17.95	23.94
Steam Extraction in D	6.20	12.39	18.59	24.78
Steam Extraction in E	6.52	13.05	19.75	26.09

A very interesting result that can be obtained by solving the thermodynamic model consists in the evaluation of the penalties, in terms of lower power production, related with the CHP operation of the plant, i.e. with the steam extraction to supply

the MED-TVC units. Obviously, such penalties may be expected almost proportional to the number of MED units to be supplied and also dependent upon the steam extraction pressure assumed. In fact, when the steam extraction pressure increases (passing from the extraction point "E" toward the extraction point "A"), a larger fraction of the steam mass flow rate does not expand in low pressure stages, seriously reducing the power generation capacity. This effect may be expected to be much smoother when steam is extracted at a lower pressure.

The results are shown in Figure 5.2. As expected, the highest penalties in terms of power production are observed, for any number of MED units to be supplied, when steam is extracted at higher pressure. In particular, when all the 4 MED-TVC units are operating, the power production decreases only by 23 MW_e when steam is extracted at the lowest pressure (point "E"), while the production decreases by almost 36 MW_e when steam is extracted at the highest pressure (point "A").

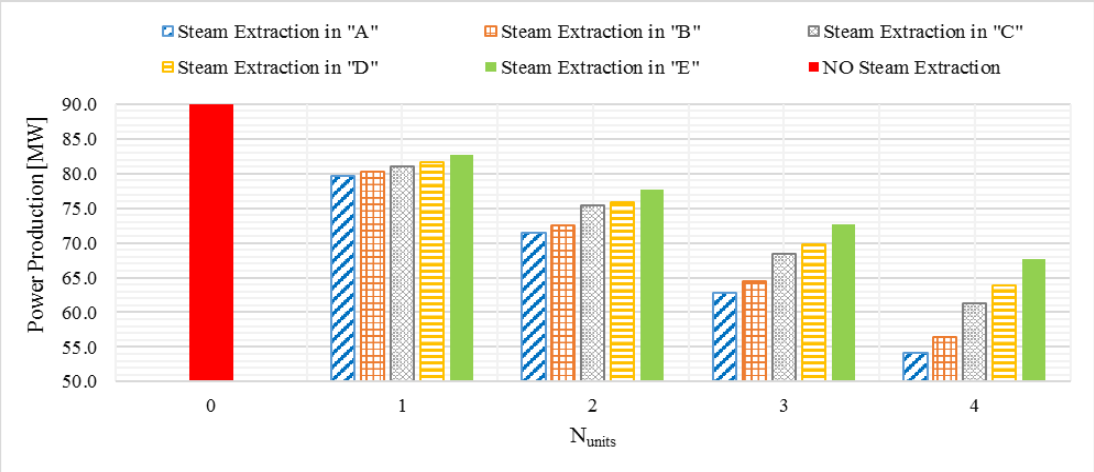

Figure 5.2. *Power Production for any design extraction pressure and number of MED units supplied*

5.3 Exergy analysis

A preliminary exergy analysis is carried out in order to calculate the exergy flow associated with all the fluid streams. In thermoeconomic modelling, it is useful and common to decompose the exergy flows into their physical and chemical fractions, in

order to allow for a more accurate definition of the productive scope of each component [5.32]. Physical exergy is related with the difference in pressure and temperature between the examined material stream and the reference state, while chemical exergy is related with the difference in chemical potentials of the constituent species of the stream; a detailed description of this topic can be found in [5.33].

Considering that in a steam cycle the working fluid does not undergo any change in its chemical composition, only physical component of exergy was considered. Once indicated as "*b*" the specific exergy of a material stream (kJ_{ex}/kg), and referring to the reference state by the subscript "0", the specific physical exergy can be calculated as follows:

$$b_{ph} = (h - h_0) - T_0 \cdot (s - s_0) \tag{5.3}$$

For the MED-TVC units, conversely, a significant variation in the chemical composition of water is observed during the evaporation process occurring in each effect, since the water passes from the incoming seawater condition to the state of the output flows, i.e. freshwater and concentrated brine. Then, in this case the chemical exergy has to be considered.

In order to calculate the chemical exergy content of distillate and brine, the approach proposed in [5.34] was used; here only some brief explanatory notes are given, being the reader invited to examine the reference work [5.34] for further details. The adopted approach adopts an "ideal solution" model to describe each material flow entering and exiting the desalination unit; as observed in [5.35], this assumption is correct only when feedwater salt concentration is lower than 70000 ppm and for recovery ratios (i.e. the ratios between the flowrates of distillate product and incoming seawater) lower than 0.7; in the examined case both these conditions are well satisfied considering that the feedwater salt concentration is equal to 38000 ppm (average value for the Mediterranean sea) and the recovery ratio is approximately 0.29 [5.26]. Chemical exergy of brine and distillate were calculated

based on the *minimum theoretical work of separation* required in any reversible desalination process; the chemical exergy flow of the freshwater and brine are respectively equal to:

$$\dot{B}_{\text{freshwater}} = \dot{N}_{\text{fresh}} \cdot \varphi \cdot R_{\text{u}} \cdot T_0 \cdot x_{\text{s,feed}}^{\text{no.diss}} \cdot \frac{x_{\text{s,brine}}^{\text{no.diss}}}{x_{\text{s,brine}}^{\text{no.diss}} - x_{\text{s,feed}}^{\text{no.diss}}} ln\left(\frac{x_{\text{s,brine}}^{\text{no.diss}}}{x_{\text{s,feed}}^{\text{no.diss}}}\right) \tag{5.4}$$

$$\dot{B}_{\text{brine}} = \dot{N}_{\text{fresh}} \cdot \varphi \cdot R_{\text{u}} \cdot T_0 \; x_{\text{s,feed}}^{\text{no.diss}} \left(\cdot \frac{x_{\text{s,brine}}^{\text{no.diss}}}{x_{\text{s,brine}}^{\text{no.diss}} - x_{\text{s,feed}}^{\text{no.diss}}} ln\left(\frac{x_{\text{s,brine}}^{\text{no.diss}}}{x_{\text{s,feed}}^{\text{no.diss}}}\right) - \cdot 1 \right) \tag{5.5}$$

In Equations (5.4) and (5.5), φ represents the dissociation factor of salts (equal to 2 for sodium chloride), R_{u} is the universal constant of gases, x_{s} is the molar fraction of the dissolved salts and F_{resh} is the molar flowrate of product freshwater

The reference state adopted for exergy calculations was seawater composition (particularly, 38000 ppm) at T_0=288,15 K and p_0=101.325 kPa. All the required expressions for exergy analysis were implemented in the EES model.

5.4 Thermoeconomic modeling of the examined dual-purpose plant

In Figure 5.3 the productive structure of the examined plant is shown. In Figure 5.4 a zoomed representation of the productive structure for the desalination unit and its thermal vapor compressor is also provided. As can be seen from both figures, the productive structure is much more complex than the physical lay-out since it includes not only the physical units, but also a number of fictitious/virtual elements, named nodes (represented by diamond-shaped symbols and associated with either branchings or junctions), which distribute (collect) exergy flows toward (from) different components, not involving any physical energy conversion process.

In the figures, all the exergy flows (represented by thin continuous black lines) are numbered according to the notation adopted in Figure 5.1 and Table 5.2. In Figures 5.3 and 5.4 the costs associated with capital investment are represented by red arrows, while the costs associated with the “residue” flows are represented by green dotted arrows.

The productive structure of the steam power plant adopted is not characterized by a simple sequential arrangement of the main components, due to its intrinsically cyclic operation and to the presence of preheaters. Nevertheless, keeping in mind the thermodynamic evolution of the working fluid in the Hirn cycle, it can be stated that a first increase of its exergy content is provided by the preheating systems, pumps and boiler (particularly in the economizer, vaporizer and superheater sections), while a second contribution is given by the reheater section of steam generator.

For the examined case, Mixer and Feedwater Heater 1 were considered as unique component in order to simplify the model.

The only dissipative component is the steam condenser: the residue here generated is the exergy flow released during steam condensation and dissipated to the cooling water. According to [5.36], this flow was assigned to the different plant components proportionally to their contribution to the increase of exergy content of the working fluid.

A brief explanation is here given for a single component, in order to accompany the reader towards an easier interpretation of the scheme, i.e. the Boiler (including its economizer, vaporizer and superheater sections). This component "consumes" different types of resources, that represent its fuels: (i) the exergy of the fuel input, $\dot{B}_{\mathrm{Fuel}}$, which is associated with a cost that depends on the unit cost of fuel, (ii) the capital investment $\dot{Z}_{\mathrm{Eco-Vap-SH}}$, expressed in (€/s) or (€/h), (iii) the residue $\psi_{\mathrm{eco-vap-SH}}\dot{P}_{\mathrm{CND}}$ that represent a fraction of the exergy lost by the working fluid at the condenser ($\dot{P}_{\mathrm{CND}}$) which is allocated, as an additional cost, to the boiler that has contributed to generate it. Conversely, the useful output is represented by the increase in the physical exergy of the working fluid, $\dot{B}_{13}-\dot{B}_{10}$.

As regards the level of disaggregation adopted for the desalination units, the MED section and the Thermal Vapor Compressor were treated as separate components (see

Fig. 5.4), in order to assess the different incidence of these units on the cost formation process of freshwater.

The exergetic model adopted for the thermal vapor compressor has a particular conceptual interest for expert thermoeconomic analysts. The TVC basically consists of an entrainment and a successive compression of the low-pressure steam (usually called entrained flow) operated by means of a relatively high-pressure steam (motive steam); the reader is invited to refer to [5.31] for further details on the operation principle of this device. As evident in Fig. 5.4, being "$\dot{B}_{MED}$-$\dot{B}_{23}$" the total exergy input to the TVC-MED unit, only a fraction of this flow is used by the thermal vapor compressor to increase the exergy of the entrained steam during its compression, while the remaining part virtually bypasses this component and is consumed directly by the MED section. In particular, once indicated with b_{26} the specific exergy of the steam exiting the TVC (corresponding to the inlet condition at the 1st effect of MED) and with b_{25} the specific exergy of the steam exiting the 12th effect and entrained by the TVC, it follows that [5.28]:

- the fraction of the inlet exergy flow which constitutes the thermal vapor compressor fuel is $\dot{m}_{MED} \cdot (b_{19} - b_{26})$;
- the fuel of the TVC is used to the increase the exergy content of the entrained steam from b_{25} up to b_{26}; hence the quantity $\dot{m}_{25}(b_{26} - b_{25})$ constitutes its product.

A black box model was adopted for the MED unit, since a higher level of disaggregation is not needed to achieve the desired results. The productive structure of the MED section indicates that it is fueled by the thermal exergy supplied by the steam flowrate and by some electricity driven from the generator and used to drive auxiliary components (i.e. pumps). Only freshwater is considered, at this step, as a useful product, since the concentrated brine is initially assumed to be disposed back to the sea, wasting all its exergy content. In this case, the exergy content of the brine was not considered a residue flow, because as shown in [5.32] the components which contribute to its formation process are the twelve MED effects and, according to the

adopted disaggregation level, the residue flow would be allocated entirely on the same MED with no influence on the unit cost of freshwater.

In Figure 5.4, the exergy flow "$\dot{B}_{MED}$-$\dot{B}_{23}$" fueling the MED units is derived from both the nodes Σ_1 and Σ_2: this representation should not lead to misleading conclusions: in fact, it indicates that the MED fuel is derived from node Σ_1 whenever the motive steam is assumed to be extracted at point "A" or "B" in Fig. 5.1, thus indicating that the reheater does not contribute directly to the formation process of the consumed steam. Conversely, for any other steam extraction pressure (points "C", "D" and "E" in Figure 5.1) the exergy flow consumed in the MED unit is assumed to be derived from node Σ_2.

In Table 5.5 the fuel, product and residue flows are presented; in the last column, the specific exergy consumption k_i is also shown: this quantity is defined as the exergy consumed by the "i-th" component in order to obtain a unit of its product:

$$k_i = \frac{F_i}{P_i} \tag{5.6}$$

Obviously, the specific exergy consumption is the inverse of exergetic efficiency, i.e. $\eta_{ex,i} = \frac{1}{k_i}$. Here, using k_i instead of $\eta_{ex,i}$ was preferred, following the commonly adopted symbolism in thermoeconomic analysis. High values of k_i are clearly achieved by the devices with a poor exergetic efficiency, which are characterized by high exergy destruction rates. In Table 5.5 the fuels, products and residues are shown for the specific case "E" (i.e. with steam extraction in "E"): it may be observed that the highest value of k_i, i.e. 11.11 $kW_{ex}/kW_{ex,}$ is obtained for the MED unit, testifying that very high irreversibility occurs during the thermal separation process.

In the power section the steam generator achieves, as usual, the highest k_i value due to both the irreversibility occurring in the heat transfer process between hot combustion gases and working fluid and the high discharge temperature of exhaust gases. No specific exergy consumption is defined for the condenser, due to the

difficulties in identifying its "product" (it is a dissipative component that lacks a useful product measurable in exergy units).

***Table 5.5**. Thermoeconomic model results for the case of steam extraction in "E"*

Component	F (kW_{ex})	P (kW_{ex})	R (kW_{ex})	k_i (kW_{ex}/kW_{ex})
Steam Generator (Eco-Vap-SH)	199755	95862	826	2.084
Steam Generator (RH)	29477	14146	179	2.084
Steam Turbine (HP)	23558	22384	0	1.052
Steam Turbine (IP)	27089	25079	0	1.080
Steam Turbine (LP)	33362	25425	0	1.312
Feed Water Heater 1 (FWH_1)	949	820	7	1.157
Feed Water Heater 2 (FWH_2)	1580	1191	10	1.327
Feed Water Heater 3 (FWH_3)	4602	3786	33	1.216
Feed Water Heater 4 (FWH_4)	3693	3352	29	1.102
Feed Water Heater 5 (FWH_5)	6962	6581	57	1.058
Feed Water Heater 6 (FWH_6)	6078	5746	50	1.058
Feed Water Heater 7 (FWH_7)	6804	6481	56	1.050
Pump 1 (P_1)	58	49	0	1.163
Pump 2 (P_2)	695	683	6	1.017
Generator	72888	71362	0	1.020
Condenser (CND)	4910	1253	0	--
Thermal Vapor Compressor	9700	2665	0	3.640
MED	15076	1356	0	11.115

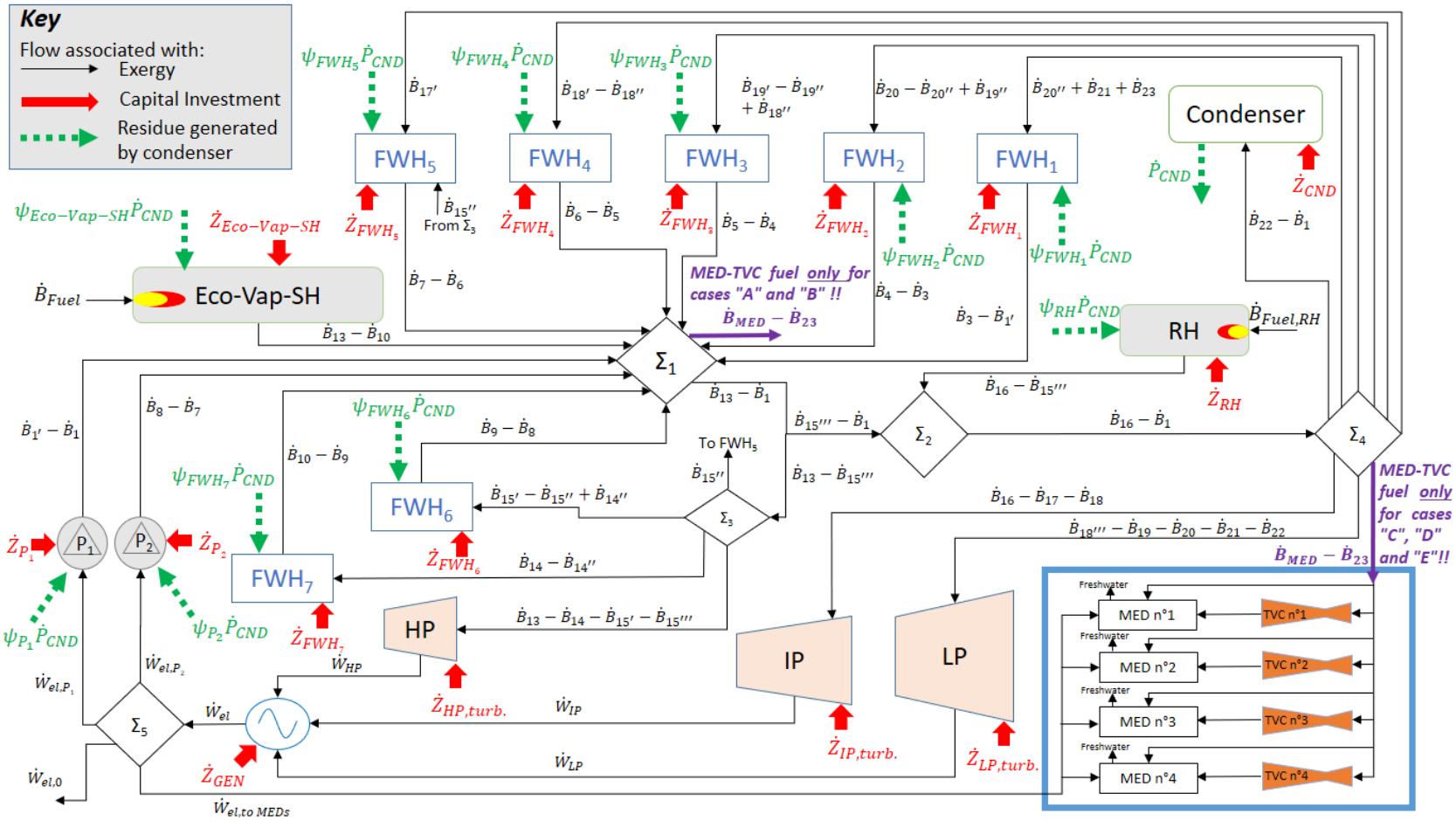

Figure 5.3 *Productive Structure of CHP-MED-TVC plant*

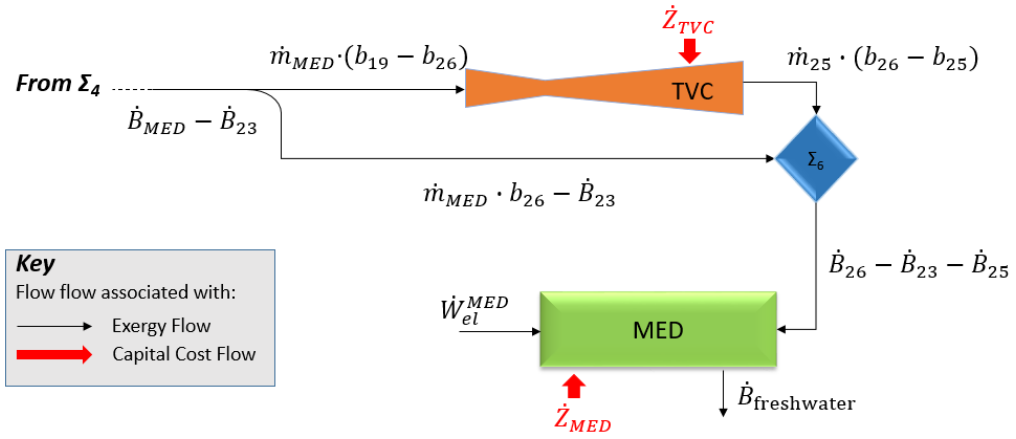

Figure 5.4 *Productive Structure of the MED-TVC desalination unit for the case of steam extraction in "E"*

It is worthwhile examining how the exergetic efficiency of the "MED-TVC" section varies with the pressure of the supplied steam; as shown in Figure 5.5, the efficiency of the unit always maintains lower than 10%, indicating that in all the examined cases a very relevant exergy destruction occurs in this component. In particular, the exergy efficiency decreases when increasing the steam extraction pressure, passing from 7.1% for steam extraction in "E" down to 4.8% when steam is extracted at the highest pressure in "A".

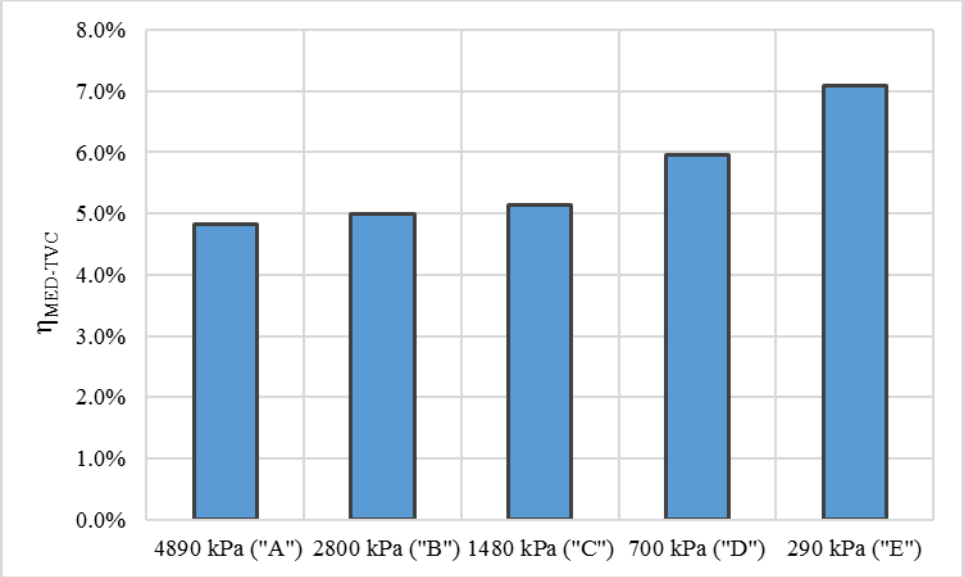

***Figure 5.5**. Exergy efficiency of the "MED-TVC" section for different steam extraction pressures*

5.5 Overall exergy efficiency of the dual purpose plant

Looking at the whole plant as a black box, the exergy of the natural gas supplied to the boiler represents the unique exergy input, while the exergy content of freshwater and the net produced electricity constitute the plant products. The exergy content of natural gas was approximated by its low heating value (thus neglecting the required correction factor [5.33], which slightly depends on the gas composition and ranges between 1.03 and 1.05). The exergy efficiency at a whole plant-level is calculated as follows:

$$\eta_{ex}^{\text{CHP-MED-TVC}}(\%) = \frac{\dot{B}_{\text{freshwater}} + \dot{W}_{\text{el,net}}}{\dot{B}_{\text{NaturalGas}}} \cdot 100 \qquad (5.7)$$

In Figure 5.6 the trend of the exergy efficiency is presented for all examined cases.

It may be observed that when the steam extraction pressure decreases, i.e. gradually passing from the point "A" to the point "E", for any number of MED units supplied the exergy efficiency of the whole plant increases. Two factors justify the observed trend:

1 at a lower extraction pressure a higher specific work is obviously obtained, since the extracted mass of steam has undergone a more intense expansion process before being supplied to the MED-TVC units;

2 at a lower extraction pressure the exergy efficiency of the MED-TVC unit also increases, as shown in Figure 5.5, due to the lower exergy destruction rete involved in freshwater production.

When the number of operating MED units decreases, the overall exergy efficiency increases; this trend is justified by the fact that the thermal desalination unit is the section of the plant with the lowest exergy efficiency. In fact, previous studies have revealed that the thermal separation of a seawater by distillation processes implies high exergy destructions, due to the very low chemical exergy content of freshwater product [5.5]. When the numbers of operating MED-TVC units decreases, the motive steam supplied to drive these units decreases almost proportionally, and a large fraction of the total exergy destruction is consequently avoided, allowing at meantime to increase the electricity production rate.

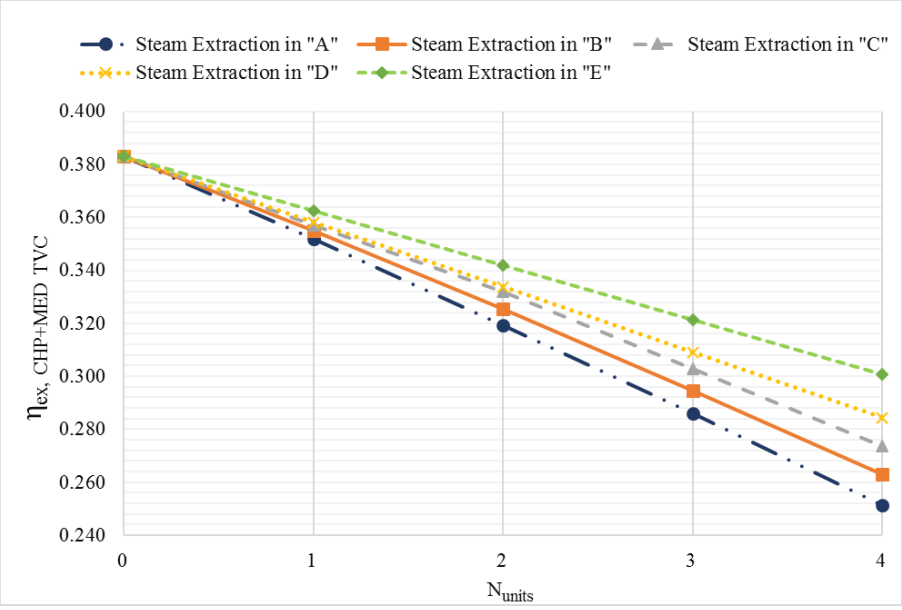

***Figure 5.6**. Overall exergy efficiency at whole plant-level, for different steam extraction pressures and number of operating MED units*

5.6 Insights into the Economic Model of the case study

In order to perform the thermoeconomic cost accounting, data on the purchase cost of plant components and equipment are also necessary. For the examined plant, appropriate cost figures derived from literature were used; in particular the cost figures were derived: for steam generators from [5.19], for turbines, condenser, pumps and preheaters from Ref. [5.37] and, finally, for the MED units from Ref. [5.38]. All these formulas were eventually updated to account for the variable value of currencies.

When referring to a steady-state thermoeconomic model, capital cost flows Ż (€/h) are required; as along the last few years the MED-TVC sections have been observed to operate quite discontinuously (for a number of reasons related with scheduled and unscheduled maintenance), calculating hourly capital cost flow becomes more difficult than if the plant was operated at constant load. For components with irregular operation profiles, a possible criterion to calculate the capital cost flows Ż was provided in [5.39], where the purchasing cost flow of the "j-th" component in a generic "i-th" hour was obtained on the basis of the amount of product produced in the examined hour, according to the following equation:

$$\dot{Z}_j = Z_j \cdot CRF \frac{\dot{P}_{j,i}}{\sum_{i=1}^{8760.} P_{j,i}} \tag{5.8}$$

where

$$CRF = \frac{(1+\iota)^n \cdot \iota}{(1+\iota)^n - 1} \tag{5.9}$$

In Equation (5.8), *CRF* is the Capital Recovery Factor of the investment to be calculated by Equation (5.9), where "ι" represents the interest rate and "n" is the plant technical or economic life; once assumed, for the examined case, an interest rate equal to 5% and a 30 years plant life cycle, a *CRF*=0.065 was obtained. This means that the

annuity corresponding to the capital investment for each component is calculated as 6.5% of its initial cost.

In Equation (5.8) $\dot{P}_{ji}$ indicates the product of the "j-th" component during the "i-th" examined hour, according to the supposed operation schedule; finally, the summation of $\dot{P}_{ji}$ over the year indicates the annual productivity of the "j-th" unit.

Based on historical data, the following annual operation schedule was assumed for the MED-TVC units, which is justified by the typical trends of scheduled and unscheduled maintenance activities and by possible control of the freshwater production capacity aimed at facing the highly irregular demand on a seasonal basis:

- 1000 h/y with only one MED-TVC unit in four operating;
- 2000 h/y with two MED-TVC units in four operating;
- 2000 h/y with three MED-TVC units in four operating;
- for 4760 h/y with all the four units operating.

5.7 Results of thermoeconomic cost accounting

The thermoeconomic cost accounting was applied on the basis of the proposed productive structure. The thermoeconomic model, not described here in details for the sake of brevity, essentially consists of cost balances (1 equation per component) and auxiliary equations formulated, for all the components with more than 1 output flow, on the basis of well-established rules presented in the Chapter 1.

In Table 5.6, for each component the thermoeconomic cost flows (i.e. capital investment $\dot{Z}$, cost of fuels $\dot{C}_F$ and residues $\dot{C}_R$ and cost of products $\dot{C}_P$), the unit thermoeconomic cost of products c_P (calculated dividing the cost of products $\dot{C}_P$ by the product measured in exergy units) and the capital and residue exergoeconomic factors are shown.

The thermoeconomic unit cost of a product, here indicated as c_P (€/kWh), represents the monetary expense in terms of external fuels and equipment purchase in order to produce a unit exergy of the examined product; the capital and residue exergoeconomic factors, f_z and f_R, respectively represent, the contribution of the capital

investment and residue costs on the total production cost of each component, calculated as follows:

$$f_Z = \frac{\dot{C}_Z}{\dot{C}_P} \tag{5.10}$$

$$f_R = \frac{\dot{C}_R}{\dot{C}_P} \tag{5.11}$$

Looking at Table 5.6, from the values of exergoeconomic factors f_z it emerges that the capital investment and residue costs account for less than 6% of the total production cost for almost all the plant components; then, the thermoeconomic unit costs of the products are mainly influenced by specific exergy consumption and by the thermodynamic irreversibility occurring in each component. Only for the MED units the capital cost has a higher influence on the total cost (i.e. 18.8%), but even here the fuel cost still represents the main fraction.

The MED unit is characterized by the highest unit exergoeconomic cost: in fact, its poor exergetic performance (i.e. its very high value of "k_{MED}") is responsible for such a relevant increase in the unit cost of desalted water.

It is worthwhile noticing the enormous difference between the thermoeconomic unit costs of desalted water and electricity, respectively equal to 1.313 €/kWh$_{ex}$ and 0.078 €/kWh$_{ex}$, which is a consequence of the two different cost formation processes within the examined plant.

The above analysis represents a rigorous procedure based on exergy costing, i.e. on the allocation of the costs proportionally to the exergy content of the product streams, thus keeping into account the whole productive chain involved in the generation of each material stream; other alternatives for cost allocations have been proven in literature to lead, eventually, to misleading conclusions. In our case, the total hourly cost at whole plant level in case of steam extraction in "E", when all the MED units are supplied, is 7051.24 €/h, while the exergy contents of products are respectively equal to 67609 kWh$_{ex}$ for electric power and 1356 kWh$_{ex}$ for freshwater. If a same cost per unit exergy was assumed for both these products (renouncing to analyze the

productive chain), a 6912.60 €/h cost would have been allocated on the electric output and only a 138.64 €/h cost on the produced freshwater. Conversely, the rigorous thermoeconomic cost accounting led us to allocate a 5563.29 €/h on the produced electric output and 1780.50 €/h on freshwater.

Table 5.6 *Thermoeconomic cost accounting results in case of steam extraction in "E"*

	$\dot{Z}$ (€/h)	$\dot{C}_F$ (€/h)	$\dot{C}_R$ (€/h)	$\dot{C}_P$ (€/h)	c_P (€/kWh$_{ex}$)	f_Z (%)	f_R (%)
Steam Gen. (Eco-Vap-SH)	141.06	5453.98	213.58	5808.63	0.0606	2.4%	3.7%
Steam Gen. (RH)	19.24	804.82	46.27	870.32	0.0615	2.2%	5.3%
HP Turbine	57.72	1499.46	0	1557.18	0.0696	3.7%	0%
IP Turbine	73.97	1715.98	0	1789.95	0.0714	4.1%	0%
LP Turbine	76.99	2113.36	0	2190.36	0.0861	3.5%	0%
FWH_1	5.62	60.08	1.83	67.53	0.0824	8.3%	2.7%
FWH_2	4.60	100.11	2.65	107.36	0.0901	4.3%	2.5%
FWH_3	5.57	291.53	8.44	305.54	0.0807	1.8%	2.8%
FWH_4	4.80	233.96	7.49	246.22	0.0735	1.9%	3.0%
FWH_5	11.70	442.01	14.66	468.37	0.0712	2.5%	3.1%
FWH_6	7.50	386.86	12.80	407.16	0.0709	1.8%	3.1%
FWH_7	8.28	433.07	14.44	455.79	0.0703	1.8%	3.2%
Pump 1	0.17	4.50	0.11	4.78	0.0962	3.5%	2.3%
Pump 2	0.62	54.17	1.52	56.31	0.0825	1.1%	2.7%
Generator	25.81	5537.48	0	5563.29	0.0780	0.5%	0%
Condenser	12.75	311.02	0	--	--	--	--
TVC	1.63	614.45	0	616.09	0.2312	0.3%	0%
MED	334.42	1446.09	0	1780.50	1.3127	18.8%	0%

5.8 Cost sensitivity to the steam extraction pressure and to the number of desalination units supplied

In this section a sensitivity analysis is carried out in order to evaluate the variations in the product costs when the extraction pressure of motive steam supplied to MED units is changed; the proposed analysis allows to identify the optimal values of the steam extraction pressure in order to minimize the unit cost of both products. Another important parameter included in the analysis, to account for the different operating conditions of the plant throughout the year, is represented by the number of MED units operated and supplied with "cogenerated" motive steam.

In Figures 5.7 (a) and (b), the freshwater and electricity costs are respectively shown. It may be observed that:

- for any given steam extraction pressure, the freshwater unit cost increases with the number of MED-TVC units supplied. As previously observed, when a larger amount of freshwater is produced, a higher mass flow rate of steam is extracted along the fluid expansion line and subtracted to the power production process; due to the poor exergetic efficiency of the desalination units (see Figure 5.5), the total exergy destruction dramatically increases with the numbers of MED units supplied. Starting from this consideration, it follows that when a higher number of MED units are activated, a larger fraction of the exergy content of the natural gas fueling the plant is devoted to freshwater production, rather than to the production of electricity. As regards the unit cost of electricity, since steam flowrate through low-pressure turbine stages (below the extraction pressure) decreases when the steam extraction increases to drive a higher number of MED units, according to Equation (5.1) the turbine isoentropic efficiencies also decrease, and their exergetic efficiency too, as a consequence; this poorer performance of the steam turbines implies that a greater exergy destruction occurs when producing 1 kWh_{ex} of electricity, so that the unit cost of electric power slightly increases with the number of MED units simultaneously operating.

- When the steam extraction pressure decreases (i.e. from point A to point E), the freshwater unit cost decreases: lower pressure of steam extraction leads to lower exergy destruction in desalination unit, due to the improvement of MED-TVC exergetic performance, as shown in Fig. 5.5: it follows that since less exergy destruction occurs, the decrease in freshwater cost is justified. The discontinuity of cost values observed for case “C” depends on the modification of the productive structure adopted when steam extraction occurs before or after steam reheater (i.e. case “A” and “B” or case “C”, “D” and “E”): in fact, as shown in Fig. 5.7 (a), freshwater cost slightly increases, respectively to case “A” or “B”. It is important to note that for case A and B, according to the productive

structure adopted (the reader should refer to Fig. 5.3), exergy destruction occurring in the reheater does not influence freshwater cost; conversely, for other cases the reheater has to be included in the productive process of freshwater. However, as can be seen from the values shown in figure, freshwater unit cost is not heavily sensitive to the irreversibility occurring within the reheater. As regards the sensitivity of the unit cost of electricity to extraction pressure, lower unit costs are obtained at low extraction pressures due to the better exergetic performance of turbines when their steam mass flowrate approaches its design value.

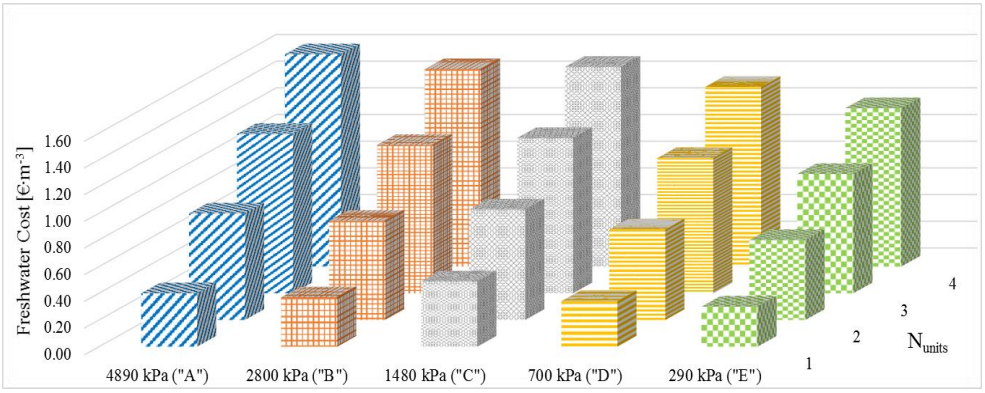

a.

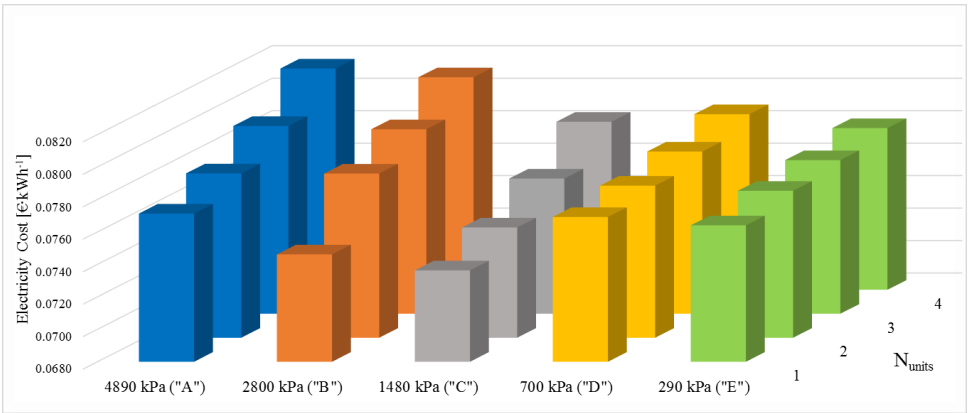

(b)

Figure 5.7 *Trend observed, for different steam extraction pressures and number of operating MED units, in terms of:* ***(a)*** *Freshwater cost,* ***(b)****. Electricity cost*

5.9 Improved lay-out based on exergy recovery from the concentrated brine by a Reverse Electrodialysis Unit

In the previous analysis, the brine released from the 12th (last) effect of each MED unit was not considered a useful product, since it was assumed to be disposed back to the sea. In this section the potential feasibility of exploiting its exergy content to produce further amounts of electricity is investigated. Such an energy conversion process may be performed using a Salinity Gradient Power (SGP) unit [5.40] In particular, in this section the use of Reverse ElectroDialysis unit (RED)

The use of a highly-concentrated brine and a low concentrated solution (like freshwater or pretreated urban wastewater [5.35]) enhances RED power output due to the high chemical potential difference between these solutions. However, for a desalination system freshwater (which would represent an excellent dilute solution) cannot be used to this scope, since it represents the useful product of the plant; furthermore, due to the large quantity of brine produced in the process, the wastewater eventually needed for the operation of a RED unit highly exceeds its reasonable availability. For this reason, below in this study the hypothesis to improve the plant layout presented in Fig. 5.1 is made by including a RED unit which uses seawater (obviously free available in any desired quantity) as dilute solution.

The technical features of the prototype supposed to be installed are similar to the ones reported in [5.41] and not repeated here for the sake of brevity; the output parameters and the performance of this unit were predicted by making use of the model described in [5.42]. A 3643 m^3/h of brine flowrate and an equal seawater flowrate were considered; taking into account that 75% of the gross electricity production is consumed by the auxiliary pumps of the unit (i.e. pumps), a net power production of 32.5 kW_{ex} resulted.

As concerns the inclusion of the RED unit in the productive structure, the functional relation between the MED and the RED unit can be represented as shown in Figure 5.8.

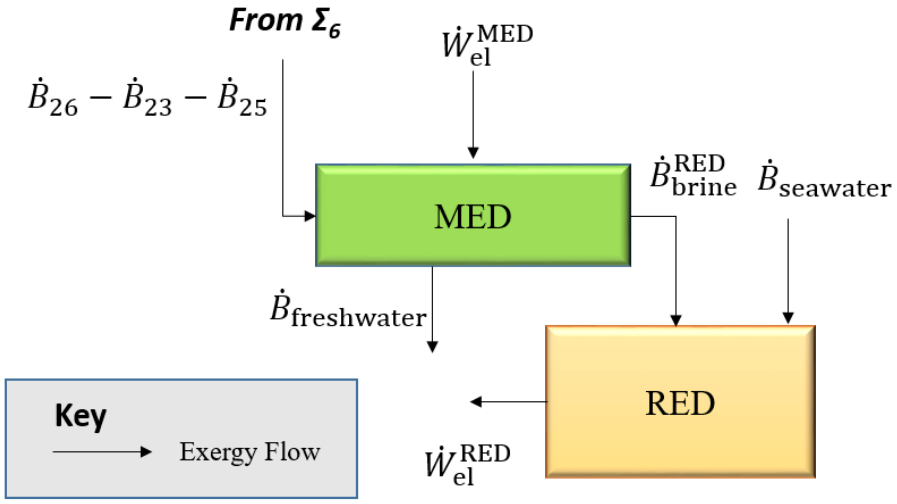

Figure 5.8 *Productive Structure of MED/RED unit*

As evident in the figure, only a fraction of the exergy content of the brine (indicated as $\dot{B}_{brine}^{RED}$) is used as a fuel for the RED unit, inside the concentrated compartment; in particular, this exergy flow is represented by the variation in the brine exergy content when it dilutes from its original concentration X_{high_in}=1 mol/l to its outlet concentration X_{high_out}=0.89 mol/l. The electric output of the unit represents its useful product. As regards the seawater entering the RED unit, since its chemical composition was assumed as dead state for exergy calculation, it has a null exergy content; furthermore, as can be seen in Fig. 5.8, the exergy of the seawater exiting the unit (at a concentration slightly higher than the dead state value) was not considered because this flow is disposed back to the sea. Then, the exergy efficiency of this unit was calculated as follows:

$$\eta_{ex}^{RED} = \frac{\dot{W}_{el,net}^{RED}}{\dot{B}_{brine}^{RED}} \tag{5.12}$$

Being the RED technology for salinity gradient power production at a prototypal development stage, no reliable cost figures are available. Then, the thermoeconomic

cost accounting for this additional unit was limited to consider only the exergy-related costs, thus neglecting the contribution related to the capital investment cost.

Then, a full comparison between the exergoeconomic costs ($\dot{C}$, in €/kWh$_{ex}$) achieved in the two scenarios, the first coincident with the plant scheme in Fig. 5.1 and not including the RED unit, the second including this additional unit for brine exergy recovery, is not feasible. Hence, the comparison was made on a different basis, i.e. in terms of exergetic unit cost k_i^* (kW$_{ex}$/kW$_{ex}$). This exergetic cost of a material stream is defined as the quantity of input exergy to the plant consumed (along the examined energy conversion process) to produce a unit exergy of the examined stream [5.43] . Then, it only provides information on the consumption of resources measurable in exergy units, losing any information about the contribution of capital investment costs and avoiding the use of monetary units.

As can be seen in Table 5.7, the two scenarios (without and with the RED unit) were analysed to allow for an easy comparison. It should be observed that for the second scenario, with inclusion of the RED unit, only cost data related to the MED and the RED unit are presented; in fact, only the desalination plant directly interacts with the RED unit, thus remaining the results for the steam cycle unchanged with respect to those obtained in the first scenario (and then not duplicated in the Table for the sake of brevity).

Looking at Table 5.7, when passing from the first to the second scenario the freshwater exergetic unit cost decreases from 37.40 down to 30.17 kW$_{ex}$/kW$_{ex}$: in fact, considering that the total MED cost production does not vary since the freshwater production is assumed not to vary between the first and the second scenario, this cost is no longer allocated only on the freshwater (as occurred in the first scenario), but also on the exergy fraction of the brine used as a fuel to drive the RED unit. Furthermore, the methodology suggests very different unit costs for the freshwater and the electricity produced by the steam cycle and by the RED unit, which resulted respectively equal to 30.17 kW$_{ex}$/kW$_{ex}$, 2.60 kW$_{ex}$/kW$_{ex}$ and 301.77 kW$_{ex}$/kW$_{ex}$.

The extremely high unit cost obtained for the product of the RED unit is a consequence of its very low exergy efficiency (i.e. η_{ex}^{RED} =10%) and the high unit

exergetic cost of its "fuel" (i.e. 30.17 kW_{ex}/kW_{ex}): as concerns this latter aspect, in fact, it must be observed that this device is fuelled by an exergy flow (i.e. part of the chemical exergy of the concentrated brine) which is approximately at the end of the "energy conversion chain" and is consequently assigned a high unit exergetic cost, since it cumulates the effects of the exergy destructions occurring along its whole "productive history" (i.e. not only in the power plant section, but also in the MED-TVC unit where high exergy destruction occurs).

Table 5.7 *Results of exergetic cost accounting of the two examined scenarios*

First Scenario					
	k_F^* (kW_{ex}/kW_{ex})	k_P^* (kW_{ex}/kW_{ex})		k_F^* (kW_{ex}/kW_{ex})	k_P^* (kW_{ex}/kW_{ex})
Steam Gen. (SH)	1.00	2.16	FWH_1	2.24	2.72
Steam Gen. (RH)	1.00	2.20	FWH_2	2.24	2.92
HP Turbine	2.25	2.37	FWH_3	2.24	2.71
IP Turbine	2.24	2.41	FWH_4	2.24	2.63
LP Turbine	2.24	2.87	FWH_5	2.25	2.45
Pump 1	2.60	3.16	FWH_6	2.25	2.46
Pump 2	2.60	3.25	FWH_7	2.25	2.44
CND	2.24	2.24	TVC	2.24	8.16
Generator	2.55	2.60	MED	3.37	37.40
Second Scenario					
	k_i (kW_{ex}/kW_{ex})	F (kW_{ex})	k_F^* (kW_{ex}/kW_{ex})	P (kW_{ex})	k_P^* (kW_{ex}/kW_{ex})
MED	8.97	15075	3.37	1680	30.17
RED	10.00	325	30.17	32.5	301.77

5.10 Outcomes of this analysis

In this chapter, a thermoeconomic cost accounting of a CHP-MED-TVC plant has been performed. This method has provided a rational basis for the allocation of costs on freshwater and electrical power.

The analysis has been carried out by considering two distinct scenarios, which differ for the rejection or the recovery of the chemical exergy content of the concentrated brine. In the first case, the brine is disposed back to the sea and its exergy is entirely

wasted; the methodology has pointed out that in such conditions the thermoeconomic unit cost of freshwater is significantly higher compared to the electricity cost, due to the higher exergy destruction involved in the production process of the former output. These two values differ approximately by one order of magnitude, being this result justified by the exergy efficiency of the MED-TVC which resulted lower than 10%. Furthermore, the sensitivity analysis has shown that the unit cost of freshwater is quite sensitive to the steam extraction pressure, suggesting a low pressure of motive steam as an optimal criterion for plant design.

As concerns the second scenario, the possibility to use the chemical exergy content of brine in order to drive a Reverse Electrodialysis unit has been considered. Due to the prototypal nature of this technology, only exergetic cost accounting has been performed. The productive structure has been modified and an opportune exergy efficiency for the RED unit has been defined. The results showed that the exergetic cost of freshwater slightly decreases, compared to the first scenario, due to the increase in the total "MED product"; in this case, in fact, a portion of the brine exergy content represents an additional useful product of the desalination unit. Furthermore, the methodology has highlighted that the exergetic cost of the electricity produced in the RED unit is extremely high, due to its low exergetic efficiency and the high unit cost of the resource/fuel it consumes.

References

[5.1] Cipollina, A. Micale, G. Rizzuti L. Seawater Desalination: Conventional and Renewable Energy Processes, Springer, 2009.

[5.2] Raphael Semiat, Energy issues in desalination processes. *Environ. Sci. Technol*., Vol 42, pp. 8193–8201, 2008.

[5.3] H.T. El-Dessouky, H.M. Ettouney, *Fundamentals of Salt Water Desalination*, 1st Edition Elsevier Science, 2002.

[5.4] T. Q. Nguyen, J. D. Slawnwhite, and K. G. Boulama, "Power generation from residual industrial heat," *Energy Convers. Manag.*, vol. 51, no. 11, pp. 2220–2229, 2010.

[5.5] Tamburini, A. Cipollina, A. Micale, G. Piacentino, A. CHP (combined heat and power) retrofit for a large MED-TVC (multiple effect distillation along with thermal vapor compression) desalination plant: high efficiency assessment for different design options under the current legislative EU framework, *Energy*, Vol. 115, pp. 1548–155, 2016

[5.6] Kalogirou, S. Seawater Desalination Using Renewable Energy Sources, Prog. *Energy Combust. Sci*., Vol. 31, pp. 242–281, 2005.

[5.7] Palenzuela, D. Alarcón, G. Zaragoza, *Concentrating, Solar Power and Desalination Plants: Engineering and Economics of Coupling Multi-Effect Distillation and Solar Plants*, Springer International Publishing, 2015.

[5.8] Moser, M. Trieb, F. Fichter, T. Potential of concentrating solar power plants for the combined production of water and electricity in MENA countries, *Journal of Sustainable Development of Energy Water and Environment Systems,* Vol. 1, pp. 122-140, 2013.

[5.9] Gude, V.G. Geothermal source potential for water desalination - current status and future perspective, *Renew. Sust. Energy. Rev.*, Vol. 57, pp. 1038-1065, 2016.

[5.10] G. Kronenberg, F. Lokiec. Low-temperature distillation processes in single- and dual-purpose plants, *Desalination*, Vol 136, pp. 189-197, 2001.

[5.11] R.G. Raluy, L. Serra, J. Uche, A. Valero Life-cycle assessment of desalination technologies integrated with energy production systems *Desalination*, Vol. 167, pp. 445–458, 2004.

[5.12] Nisan, S. Benzarti, N. A comprehensive economic evaluation of integrated desalination systems using fossil fuelled and nuclear energies and including their environmental costs Desalination, Vol. 229, pp. 125-146, 2008.

[5.13] Salimi, M., Amidpour M. Modeling, simulation, parametric study and economic assessment of reciprocating internal combustion engine integrated with multi-effect desalination unit. *Energy Conversion and Management*, Vol. 138, pp. 299-311, 2017.

[5.14] F. Calise, M. D. d'Accadia, A. Macaluso, A. Piacentino, and L. Vanoli, "Exergetic and exergoeconomic analysis of a novel hybrid solar–geothermal polygeneration system producing energy and water," *Energy Convers. Manag.*, vol. 115, pp. 200–220, May 2016.

[5.15] F. Calise, M. Dentice d'Accadia, and A. Piacentino, "Exergetic and exergoeconomic analysis of a renewable polygeneration system and viability study for small isolated communities," *Energy*, vol. 92, pp. 290–307, Dec. 2015

[5.16] E. Cardona, A. Piacentino Optimal design of cogeneration plants for seawater desalination Volume 166, 15 August 2004, Pages 411-426

[5.17] Osman A. Hamed. Overview of hybrid desalination systems-current status and future prospects. Desalination, Vol. 186, pp. 207-214, 2005.

[5.18] T. Rensonnet, J. Uche, L. Serra Simulation and thermoeconomic analysis of different configurations of gas turbine (GT)-based dual-purpose power and desalination plants (DPPDP) and hybrid plants (HP), *Energy*, Vol. 32, pp. 1012-1023, 2007.
[5.19] IDE Desalination Plant Reference List. Available at: http://www.ide-tech.com/wp-content/uploads/2016/06/E5643-107-24-stationery_web.pdf
[5.20] Uche, J. Serra, L. Valero, A. Thermoeconomic optimization of a dual-purpose power and desalination plant, *Desalination*, Volume 136, pp 147-158, 2001.
[5.21] Ansari, K., Sayyaadi, H. Amidpour, M. Thermoeconomic optimization of a hybrid pressurized water reactor (PWR) power plant coupled to a multi effect distillation desalination system with thermo-vapor compressor (MED–TVC). *Energy*, Vol. 35, pp 1981-1996, 2010.
[5.22] B. Ortega-Delgado, L. García-Rodríguez, D.-C. Alarcón-Padilla, Thermoeconomic comparison of integrating seawater desalination processes in a concentrating solar power plant of 5 MWe, Desalination. 392 (2016) 102–117.
[5.23] M.A. Sharaf, A.S. Nafey, L. García-Rodríguez, Exergy and thermo-economic analyses of a combined solar organic cycle with multi effect distillation (MED) desalination process, Desalination. 272 (2011) 135–147.
[5.24] R. Leiva-Illanes, R. Escobar, J.M. Cardemil, D.-C. Alarcón-Padilla, J. Uche, A. Martínez, Exergy cost assessment of CSP driven multi-generation schemes: Integrating seawater desalination, refrigeration, and process heat plants, Energy Convers. Manag. 179 (2019) 249–269.
[5.25] A. Farsi, S.M.H. Mohammadi, M. Ameri, Thermo-economic comparison of three configurations of combined supercritical CO2 refrigeration and multi-effect desalination systems, Appl. Therm. Eng. 112 (2017) 855–870.
[5.26] Temstet C., Canton G., Laborie J. and Durante A. A large high-performance MED plant in Sicily. *Desalination*; Vol.105, pp 109-114, 1996.
[5.27] Cipollina, A., Micale, G. Rizzuti, L. A critical assessment of desalination operations in Sicily. *Desalination*, Vol. 182, pp 1-12, 2005.
[5.28] El-Wakil, M. *Powerplant Technology*, McGraw-Hill, New York, 1984.
[5.29] Klein S.A. *et al.*, Engineering equation solver V9.810. Middleton, WI: Solar EnergyLaboratory, F-Chart Software, 2010.
[5.30] Catania, A.E. *Complementi di Macchine*, Levrotto, 1979 (Book, in Italian)
[5.31] Hassan, A. S. Darwish A.M. Performance of thermal vapor compression. *Desalination*, Vol. 335 pp 41-46, 2014.
[5.32] Piacentino, A., Application of advanced thermodynamics, thermoeconomics and exergy costing to a Multiple Effect Distillation plant: In-depth analysis of cost formation process, *Desalination*, Vol. 371, pp 88-103, 2014
[5.33] Tadeusz J. Kotas, *The exergy method of thermal plant analysis*. Butterworths, 1985.
[5.34] El-Sayed, Y.M. Spiegler, K.S. The energetics of desalination processes, *Desalination*, Vol. 134, pp 109-128, 2001.
[5.35] Mistry, K.H. Hunter, H.A. Lienhard, J.H., Effect of composition and non-ideal solution behavior on desalination calculation for mixed electrolyte solutions with comparison to seawater, *Desalination*, Vol. 318, pp 34–47, 2013.
[5.36] C. Torres, A. Valero, V. Rangel, and A. Zaleta, "On the cost formation process of the residues," *Energy*, vol. 33, no. 2, pp. 144–152, Feb. 2008
[5.37] Xiong, J. Zhao, H. Zhang, C. Zheng, C. Luh, P.B. Thermoeconomic operation optimization of a coal-fired power plant, *Energy*, Vol. 42, pp 486-496, 2012.

[5.38] Fiorenza,G. Sharma, V. Braccio, G. Techno-economic evaluation of a solar powered water desalination plant., *Energy Conversion and Management*, Vol.44, pp. 2217–2240, 2003.
[5.39] Piacentino A., Cardona F. On thermoeconomics of energy systems at variable load conditions: integrated optimization of plant design and operation, Energy Conversion and Management, Vol. 48, pp. 2341–2355, 2007.
[5.40] Cipollina, A. Micale, G. Sustainable Energy from Salinity Gradients, Woodhead Publishing, 2016.
[5.41] Tamburini, A. Giacalone, F. Cipollina, A. Grisafi, F. Vella, G. Micale, G. Pressure Retarded Osmosis: a membrane process for environmental sustainability, Chemical Engineering Transactions, Vol. 47, pp 355-360, 2016.
[5.42] Tedesco, M. Scalici, C. Vaccari,D. Cipollina, A. Tamburini, A. Micale, G. Performance of the first Reverse Electrodialysis pilot plant for power production from saline waters and concentrated brines, Journal of Membrane Science, Vol. 500, pp 33-45, 2016.
[5.43] Lozano, M.A., Valero, A. Theory of the exergetic cost, Vol 18, Energy pp. 939-960, 1993.

Chapter 6

Thermoeconomic Diagnosis of Air Conditioning Systems

Thermoeconomic diagnosis is a method for supporting detection of faults which provoke an increase of the energy consumption during the operation of energy systems. Only recently this diagnosis technique has been extended to air conditioning systems. Once properly refined, this method will allow for scheduling maintenance strategies, and cost-effective energy saving will be achieved.

Developments of this technique have relied only on simulation data without being evaluated using real data. For the first time, the performance of this diagnostic technique is tested by using experimental data obtained from a 17.5 kW packaged rooftop air conditioning unit (RTU) installed at Herrick Laboratories, Purdue University (United States of America). The RTU has been tested under a wide range of operating conditions and fault levels. The following faults have been experimentally investigated: (i) *evaporator fouling*, (ii) *condenser fouling* and (iii) *evaporator fouling along with condenser fouling*. The experimental results are used as input data in the latest thermoeconomic model proposed in literature in order to verify results previously obtained.

6.1 Thermoeconomic Diagnosis: objectives and historical development

Diagnosis is generally aimed at discovering anomalies which may lead to possible failure and to a decrease in the overall efficiency of the energy systems. The preventive

identification of malfunctions helps predicting failures and reduces system downtime by planning ad-hoc maintenance strategies. During the decades, *Fault Detection and Diagnosis techniques* (FDDs) have been proposed to detect faults in energy system. It is worth reminding here the *fault matrix* [6.1], the *artificial intelligence* [6.2], and *the gas path analysis* [6.3] which are currently used in industrial practice. Most of them are based on a simple comparison between the "*actual operating condition*" and the "*reference condition*" (i.e. where no anomalies occur). In particular, the *Fault Matrix* reveals the qualitative effects of the main anomalies on the thermodynamic parameters of a power system, allowing to assess the deviation of the operational indicators of the plant with respect to the reference condition. Such an approach can be adapted to specific components, by knowing in advance the consequences of all the possible malfunctions. *Artificial intelligence* relies also on the concept of anomaly effect, and once an anomaly occurs, the value of indicators such as efficiency, mass flow rate, etc. exceeds the predefined and acceptable values. Based on the known effects (variation of efficiency, mass flow rate, etc.) that each anomaly has, the analyst could identify the faulty component. Finally, *Gas path analysis* calculates indicators such as pressure ratio, rotor speed or shaft power during the operation, and compares such values with the reference operating condition.

However, the aforementioned techniques are affected by two drawbacks:

• They usually monitor a specific component of the system, or even part of it, thus not providing any comprehensive insights into interactions among system components when faults occur;

• Such methods can only provide information to predict failures if the component continues to operate anomalously. In general, not only detection of the anomaly and prediction of the failure are of interest, but also the quantification of inefficiencies in terms of additional fuel consumption is crucial for the operators, which may also lead to huge economic expenses.

As regards the latter aspect, *Thermoeconomic Diagnosis* tries to overcome this limit by providing a quantitative approach for assessing the impact of faults in the additional energy consumption. The idea to extend Thermoeconomics to the diagnosis of malfunctions in energy systems arose in 1980s at the University of Zaragoza, Spain. The first works concerning the application of this method to the diagnosis have been published by Valero et al. in [6.4]. In that paper, for the first time, Valero et al. presented the concepts of malfunctions and they analytically demonstrated the impact of faults on the additional energy consumptions provoked. The *Fuel Impact Formula* was proposed as a tool for diagnosis purposes. However, only in 1993, those concepts were fully described in the "*Theory of the exergetic cost*" which is one of the milestone papers on this method [6.5] .

The fuel impact formula is the key for understanding the added-value of this method with respect to other diagnosis technique such as the ones mentioned at the beginning of this paragraph. In fact, it links the variations of the unit exergy consumption of each plant components (which is so assumed as an indicator of a "possible" fault within the component), with the additional energy consumption of the whole system. In this way, a quantitative evaluation of the effect of each individual fault is provided. In paragraph 6.2, this formula will be thoroughly explained.

In 1999, Torres et al. [6.7] developed the *Structural Theory* for Thermoeconomic diagnosis in order to quantify the effect of malfunctioning component on the other components of the plant. To this aim, *Dysfunction* concept was defined (which quantitively assess the impact of malfunctioning component on the consumption of faults-free components) and the analytical procedure for determining this quantity was duly described. However, one of the main limits of fuel impact formula is to rely on the variation of unit exergy consumption of a component as an indicator of fault occurrence. Actually, the performance alteration of a component could be due to either the effect of anomaly which takes place in the component itself (i.e. *intrinsic malfunction*), or to the effect of other malfunctioning components (i.e. *induced*

malfunction). The latter can be also determined by the control system intervention, which acts in order to meet the set points such as pressure, temperature, generated power, etc. For this reason, carrying out diagnosis procedure by means of Thermoeconomics is not an easy task.

With this respect, in the decade 2000-2010, lot of efforts were devoted in Italy and Spain for developing methods aimed at filtering induced malfunctions. A thorough description of these approaches will be presented in the paragraph 6.3 of this chapter, so only the main contributions are mentioned here. In [6.8]-[6.12], Verda et al. have been focused on the effect the control system intervention on induced malfunction. The authors proposed a filtering technique based on the definition of a fictious condition, commonly indicated as *free condition*, where the system freely changes due to faults without being influenced by the control system. By comparing the *actual condition* with the *free one*, malfunction induced by the control system are filtered.

Another approach was developed by Lazzaretto et al. [6.13]-[6.14] who introduced the *characteristic curve* concept. Basically, the characteristic curve of a component provides an analytical relation among a thermoeconomic indicator such as unit exergy consumption or irreversibility, and a set of variables which are highly influenced by malfunctions occurring in the given component. By looking at changes in characteristic curve, it is possible to detect if an intrinsic and/or induced malfunction occurs.

In order to provide a benchmark case study for comparing the different approaches in 2001, the TADEUS Project (which is the acronyms of *Thermoeconomic Approach to the Diagnosis of Energy Utility Systems* in honor of Prof. Tadeus Kotas) started [6.15]. It consists of a combined cycle composed by two gas turbines (125 MWe each), two heat recovery steam generators, and a steam turbine (about 100 MWe). Two operating conditions were also defined, i.e. the operating condition to be analyzed and a reference condition without anomalies. A critical comparison of the previous approaches based on the TADEUS problem is provided in [6.15].

In 2012, Verda applied Thermoeconomic diagnosis on micro turbine to discover possible malfunctions when steady state and transient operating conditions occur [6.16].

In 2011, Melli et al. [6.17] combined Thermoeconomic Analysis and Artificial Intelligence for diagnosing energy systems. The approach integrated the capabilities of both methods to provide a more robust diagnosis technique. In particular, the capability of AI to detect malfunctions through the analysis of deviations registered by ad-hoc indicators was combined with the capability of Thermoeconomics to filter the mutual dependence of the efficiencies of the components.

In 2018, Keshavarzian et al. [6.18] enlarged the application of *Thermoeconomic Input-Output Analysis* (TIOA) to the diagnosis of energy systems. After duly providing basics on the method, the authors showed that: (i) the approach allowed to understand the interdependencies between the components and (ii) the method provides useful information for the system operators to define practical strategies to reduce the negative effects of malfunctions. The CGAM benchmark was selected to test the performance of the method. The authors considered a fault in the combustion chambers (CC). After quantifying induced effects among components, they showed the capability of the method to predict the effect of some control strategies.

6.2 The Fuel Impact Formula and the Malfunction/Dysfunction Analysis

Thermoeconomic approach for diagnosis of malfunctions in energy systems relies on the comparison between the exergy consumption in the "*actual operating condition"* and the "*reference or design operating condition"*. When a malfunction occurs, the additional overall fuel consumption ΔF_{T} is easily calculated by comparing the overall fuel consumption in the operating condition, indicated as $F_{\mathrm{T}}\left(\mathbf{X}\right)$ and the one in the reference or design condition, i.e. $F_{\mathrm{T}}\left(\mathbf{X}^{0}\right)$ as shown in Equation (6.1).

$$\Delta F_{\mathrm{T}} = F_{\mathrm{T}}\left(\mathbf{X}\right) - F_{\mathrm{T}}\left(\mathbf{X^{0}}\right) \tag{6.1}$$

where $\mathbf{X}$ and $\mathbf{X^0}$ represent two sets of thermodynamic variables measured and/or calculated respectively when the system operates under "design" (i.e. faults-free) and "faulty" conditions. In Thermoeconomics, this quantity is also known as *Technical Exergy Saving* [6.5].

By applying the exergy balance for each system component, it is possible to split the additional fuel consumption ΔF_{T} into the following contributions: (i) the extra irreversibility generated within each system component ΔI_{j} and (ii) the variation of the overall plant product ΔP_{T} as shown in Equation (6.2)

$$\Delta F_T = \Delta P_T + \sum_{j=1}^{N} \Delta I_j \tag{6.2}$$

Assuming that no variation in the final product occurs, i.e. $\Delta P_{\mathrm{T}} = 0$, an additional exergy consumption is equal to the additional irreversibility generated within each subprocess, i.e. $\Delta F_{\mathrm{T}} = \sum_{\mathrm{j=1}}^{\mathrm{N}} \Delta I_{\mathrm{j}}$. Unfortunately, it is not possible to rely on the variation in the irreversibility generated in each component as an indicator of faults. To clarify this concept, in Figure 6.1 (a), a simple sequential system is shown. If a fault occurs in "component 3" (Figure 6.1 (b)), all the other components placed upstream are forced to "produce" more exergy to satisfy the additional exergy consumed by the "component 3". An increase in the irreversibility generation is observed in all of them.

Also, the same increase in the irreversibility generation within two different components leads in general to different variations of the overall exergy consumption. In fact, as shown in Figure 6.1 (b) and 6.1 (c), an additional exergy destruction, equal to 20kW$_{\mathrm{e}}$, occurring first in "component 3" and then in "component 2", leads to a

different ΔF_T . As already mentioned in Chapter 1, in Thermoeconomics, this is known as the *Principle of non-equivalence of the irreversibility* [6.5].

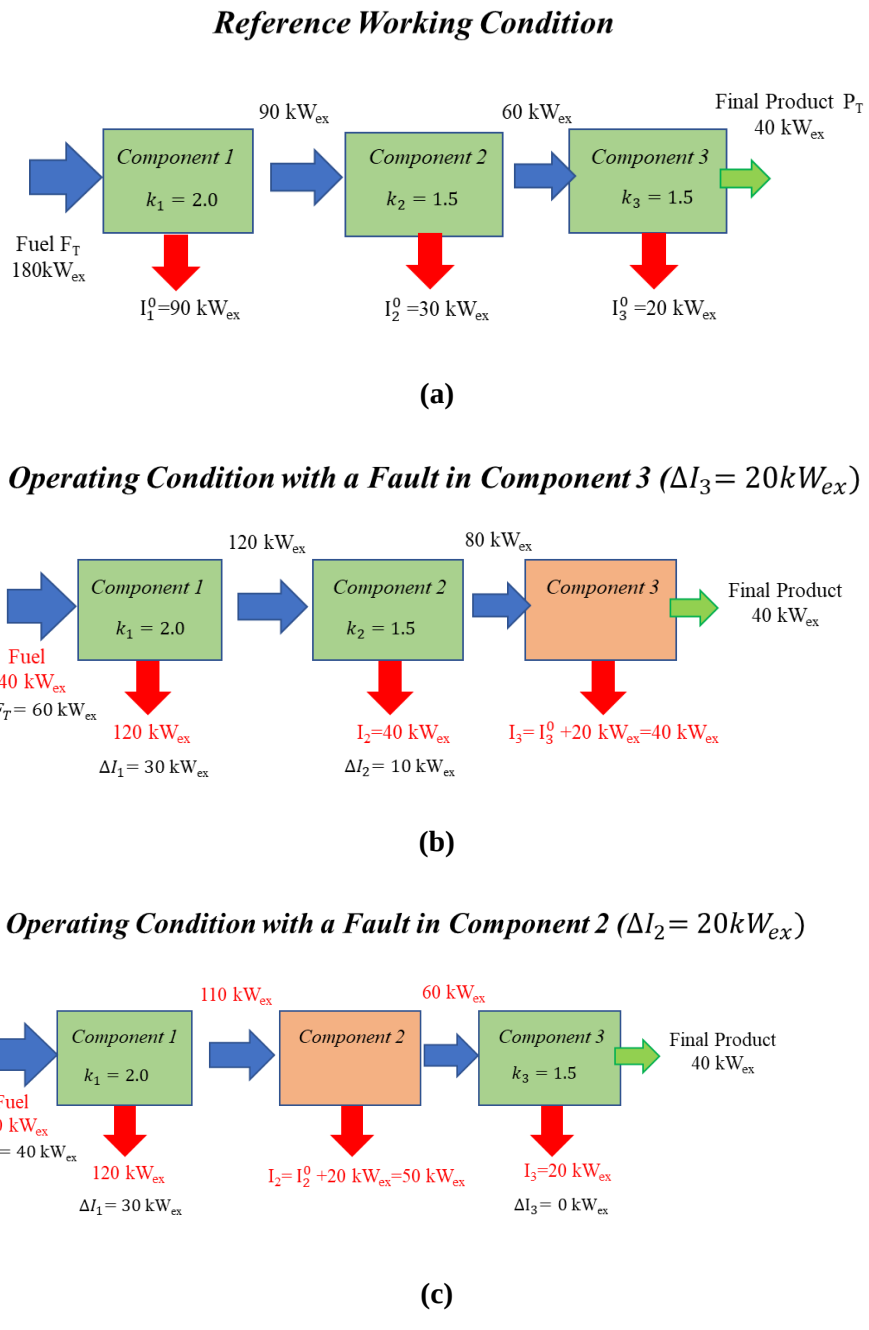

Figure 6.1 *Sequential System operating in: (a) reference condition; (b) with faults on component 3; (c) with faults on component 2*

In order to overcome the aforementioned limit, Thermoeconomics provides a useful support for fault diagnosis and detection by the *Fuel Impact Formula* and the *Malfunction/Dysfunction Analysis*.

First of all, in order to derive the Fuel Impact Formula, it is worth reminding here some concepts presented in Chapter 1. It has been mentioned that the ***PF*** representation of the thermoeconomic model is suitable for diagnosis purposes. In particular, it has been shown that the overall fuel consumption F_{T} can be expressed as a function of: (i) the vector $\boldsymbol{\kappa}_{\mathrm{e}}$, which collect the values "$\kappa_{0\mathrm{i}}$" defined as the external exergy resource consumed by the "i-th" component per unit exergy of its product, and (ii) the vector of Products **P. (**Equation (6.3))

$$F_{\mathrm{T}} = {}^{t}\boldsymbol{\kappa}_{e}\mathbf{P} \tag{6.3}$$

Be using the matrices of the technical coefficients ⟨**KR**⟩ and ⟨**KR**⟩, it has been shown that the vector of product **P** can be decomposed as shown in Equation (6.4).

$$\mathbf{P} = \mathbf{P}_{s} + \langle\mathbf{KP}\rangle\mathbf{P} + \langle\mathbf{KR}\rangle\mathbf{P} \tag{6.4}$$

When a fault occurs in the system, variations of F_{T} and **P** are observed. By differentiating Equations (6.3) and (6.4), it is easy to show that the additional exergy consumption ΔF_{T} and the variation in product $\Delta\mathbf{P}$ are equal to:

$$\Delta F_{\mathrm{T}} = \Delta\left({}^{t}\boldsymbol{\kappa}_{e}\right)\mathbf{P}^{0} + {}^{t}\boldsymbol{\kappa}_{e}\Delta\mathbf{P} \tag{6.5}$$

$$\Delta\mathbf{P} = \left|\mathbf{P}\right\rangle\left[\Delta\mathbf{P}_{\mathrm{s}} + \Delta\left(\langle\mathbf{KP}\rangle\right)\mathbf{P}^{0} + \Delta\left(\langle\mathbf{KR}\rangle\right)\mathbf{P}^{0}\right] \tag{6.6}$$

In Equations (6.5) and (6.6), $\mathbf{P}^{0}$ represents the vector of the product in the reference condition, and the matrix $\left|\mathbf{P}\right\rangle$ is equal to $\left(\mathbf{U}_{\mathrm{D}} - \langle\mathbf{KP}\rangle - \langle\mathbf{KR}\rangle\right)^{-1}$. By substituting Equations (6.6) in (6.5), and by considering that ${}^{t}\mathbf{k}_{\mathrm{p}}^{*} = {}^{t}\boldsymbol{\kappa}_{e}\left|\mathbf{P}\right\rangle$, it follows that:

$$\Delta F_{\mathrm{T}} = \Delta\left({}^{t}\boldsymbol{\kappa}_{e}\right)\mathbf{P}^{0} + {}^{t}\mathbf{k}_{\mathrm{p}}^{*}\Delta\mathbf{P}_{\mathrm{s}} + {}^{t}\mathbf{k}_{\mathrm{p}}^{*}\left[\Delta\left(\langle\mathbf{KP}\rangle\right)\mathbf{P}^{0} + \Delta\left(\langle\mathbf{KR}\rangle\right)\mathbf{P}^{0}\right] \tag{6.7}$$

Equations (6.7) can be expressed by using a scalar notation as follows:

$$\Delta F_{\mathrm{T}} = \sum_{\mathrm{i}=1}^{\mathrm{N}} \left(\sum_{\mathrm{j}=0}^{\mathrm{N}} \left[k_{\mathrm{P,j}}^{*}\left(\mathbf{X}\right) \left[\Delta\kappa_{\mathrm{ji}} + \Delta\theta_{\mathrm{ji}} \right] P_{\mathrm{i}}\left(\mathbf{X}^{0}\right) \right] + k_{\mathrm{P,i}}^{*}\left(\mathbf{X}\right) \Delta P_{\mathrm{s,i}} \right) \tag{6.8}$$

Equations (6.8) is known as the *Fuel Impact Formula*. If no variation in the overall plant production is observed, i.e. $\Delta P_{\mathrm{s,i}} = 0$, Equation (6.8) is simplified as follows:

$$\Delta F_{\mathrm{T}} = \sum_{\mathrm{i}=1}^{\mathrm{N}} \left(\sum_{\mathrm{j}=0}^{\mathrm{N}} \left[k_{\mathrm{P,j}}^{*}\left(\mathbf{X}\right) \left[\Delta\kappa_{\mathrm{ji}} + \Delta\theta_{\mathrm{ji}} \right] P_{\mathrm{i}}\left(\mathbf{X}^{0}\right) \right] \right) \tag{6.9}$$

The meaning of the fuel impact formula can be explained as follows: when the exergetic efficiency of a malfunction component decreases due to faults (which is quantified by the factor $\left(\Delta\kappa_{\mathrm{ji}} + \Delta\theta_{\mathrm{ji}}\right)$), the effect on the additional fuel consumption ΔF_{T} depends on the exergetic costs of the flows consumed by the considered component, i.e. $k_{\mathrm{P,j}}^{*}\left(\mathbf{X}\right)\left(\Delta\kappa_{\mathrm{ji}} + \Delta\theta_{\mathrm{ji}}\right) P_{\mathrm{i}}\left(\mathbf{X}^{0}\right)$. In fact, the higher the cost, the greater its impact on the additional fuel consumption. In Thermoeconomics, this quantity is named ***Malfunction Cost*** [6.6] [6.7]. In 1994, M. Reini developed the exact mathematical formalization of the Fuel Impact Formula in differential terms using both a Lagrangian and non-Lagrangian technique [6.19].

As previously shown, when a fault occurs in a component, the other system components are forced to adapt their behavior in order to supply the additional exergy consumed by the faulty one. Consequently, the amount of irreversibility generated in faults-free components varies as well. The overall increase of exergy destruction in the "i-th" component induced by the presence of faults is composed by two portions: (i) the additional local exergy destruction due to irreversibility ΔI_{i} (where $I_{\mathrm{i}}=F_{\mathrm{i}}-P_{\mathrm{i}}$) which is related to the variation of the unit exergy consumption Δk_{i} (which is equal to

$\Delta k_i = \sum_{\substack{j=1 \\ i \neq j}}^{N} \Delta \kappa_{ji}$) and (ii) the additional residue consumption ΔR_i. related to the unit residue consumption Δr_i (which is equal to $\Delta r_i = \sum_{\substack{j=1 \\ i \neq j}}^{N} \Delta \theta_{ji}$).

It is easy to show that the variation in irreversibility generation in the "i-th" component, i.e. ΔI_i, and the variation in the residue consumption, ΔR_i can be decomposed as follows:

$$\Delta I_i + \Delta R_i = \Delta\left[\left(k_i - 1\right) P_i\right] + \Delta\left(r_i P_i\right) \cong \Delta k_i P_i\left(\mathbf{X^0}\right) + \left[k_i\left(\mathbf{X}\right) - 1\right] \cdot \Delta P_i + \Delta r_i P_i\left(\mathbf{X^0}\right) + r_i\left(\mathbf{X}\right) \cdot \Delta P_i \quad (6.10)$$

In Equation (6.10), it is possible to distinguish two kinds of irreversibilities:

- ***Malfunction*** (or *endogenous irreversibility*), represented by the terms $\Delta k_i P_i\left(\mathbf{X}^0\right)$ and $\Delta r_i P_i\left(\mathbf{X^0}\right)$ which are associated with increases in unit exergy consumptions or unit generation of residues in the "i-th" component:

$$MF_i = MF_i^{(k)} + MF_i^{(r)} = \Delta k_i P_i\left(\mathbf{X^0}\right) + \Delta r_i P_i\left(\mathbf{X^0}\right) \quad (6.11)$$

- ***Dysfunction*** (or *exogenous irreversibility*), induced in the "i-th" component by the malfunction of other components that provoke a variation ΔP_i in the production rate of the "i-th" component:

$$DF_i = \sum_{i=1}^{N} DF_{ij}^{(k)} + \sum_{i=1}^{N} DF_{ij}^{(r)} = \left[k_i\left(\mathbf{X}\right) - 1\right] \cdot \Delta P_i + r_i\left(\mathbf{X}\right) \cdot \Delta P_i \quad (6.12)$$

The capability to distinguish between the additional exergy destruction in the "i-th" component provoked by faults occurring in the same component and those induced by malfunctions occurring in other components is the main added value of thermoeconomic diagnosis. To this aim, for a generic "i-th" component a malfunction cost MF_i^* [6.7] is defined:

$$MF_{\mathrm{i}}^{*} = MF_{\mathrm{i}} + \sum_{\mathrm{j=1}}^{\mathrm{N}} \left(DF_{\mathrm{ji}}^{(\mathrm{k})} + DF_{\mathrm{ji}}^{(\mathrm{r})} \right) \tag{6.13}$$

According to Equation (6.13), MF_i^* represents the additional fuel consumption provoked by faults occurring in the "i-th" component, and is calculated summing up the additional exergy destruction MF_{i} that these faults induce on the same "i-th" component (see Equation (6.11)) and the dysfunctions that these faults induce in other " j-th" components (for j=1 to N, with j≠i) [6.7].

It is easy to show that the total fuel impact equals the sum of the malfunction cost of each component as shown in Equation (6.14)

$$\Delta F_{\mathrm{T}} = \sum_{\mathrm{i=1}}^{N} MF_{\mathrm{i}}^{*} \tag{6.14}$$

It is apparent that the thermoeconomic diagnosis depends on the definition of the Fuel-Product model of the system. The expected accuracy of the results is influenced by the aggregation level of the representation adopted. Generally, two different levels are available: one is related to the number of components and the other one is related to the number of exergy flows [6.20]. More specifically, the higher the number of components, the higher the number of faults detectable. As concern the number of productive flows, the diagnosis procedure could be facilitated by separating exergy into its components (i.e. thermal, chemical and mechanical fractions). This was addressed in [6.20], where these effects on the results of the thermoeconomic diagnosis were investigated. A particularly sensitive test was carried out by simulating an anomaly in the HRSG of a combined cycle plant. It was shown that better results can be achieved when a more disaggregated level for exergy flows is adopted.

Thermoeconomic diagnosis can be classified as a *model-based* approach [6.17] since it does not require any preliminary information about the effect of the faults on thermodynamic parameters such as temperature, mass flowrate and so forth, but it

only requires the use of ad-hoc model of the system (i.e. the FPR model). This is the key difference with the fault matrix method [6.1], the gas path analysis [6.2], the AI based techniques [6.17] which are generally classified as *deductive approach*, since all rest on the preliminary knowledge of the effects provoked by all the anomalies on a set of selected parameters, generally indicated as "signature", in order to deduce possible malfunction during the operation of the systems.

6.3 Limits of Malfunction/Dysfunction analysis and overview on alternative approaches to thermoeconomic diagnosis

As previously shown, the malfunction/dysfunction approach to thermoeconomic diagnosis aims at assessing at which extent a faulty component affects the operation of other system components.

Also, the method assumes that a variation of the unit exergy consumption of a component is a sign that a possible fault may occur on it. However, there is not a biunivocal relationship between the variation of the efficiency of a component and the presence of a fault. When the variation in the unit exergy consumption in a component is not associated with faults but it is originated by the dependence of it from the operating condition, it is said that an *induced malfunction* occurs. Induced malfunction does not allow for the proper quantification of the effect of each fault (Equation (6.14)), and in order to address this issue, some approaches have been proposed. A brief description is given here follow.

One approach has been developed by Verda et al. in [6.8]-[6.12]. The authors proposed a technique for filtering malfunctions induced by the control systems and by the variation of exergy efficiency of faults-free components with the operating point. More specifically, the procedure is based on the determination of a fictious working condition named "*Free Condition*" that would have taken place if the control system did not intervene. Since this condition is fictitious as the constraints imposed by the

control system are not complied, it must be *mathematically* determined. Once removed the effect of the control system, the last step of the diagnosis technique involves the erasure of the effects induced by the dependence of unit exergy consumption from variation of the operating point. In fact, even when the free condition is determined, changes it thermodynamic parameters such as temperature, pressure and so forth, still affect the unit exergy consumption of faults-free components and further induced malfunctions occur. To take into account this contribution, a linear thermoeconomic model for each component is built.

In [6.11], Verda et al. evaluated the effect of the control system when detecting fault in a gas turbine-based cogeneration plant. The filtering approach was applied in order to filter the action of the control system and it allowed for detecting the malfunctioning component. However, the authors stressed that in order to further improve the performance of the diagnostic technique, filtering the effect of malfunctions induced by nonlinear behavior of the components (i.e. due to changes in the operating conditions) was necessary. In 2003, Verda [6.9] introduced the concept of *anamnesis* in diagnosis to refine the performance of the technique by filtering the residual induced effects. More specifically, anamnesis is the analysis of the plant case history, i.e. a series of operating condition disposed in temporal succession and referring to a sufficiently long period. In this period, it can be reasonably assumed that anomalies only increase. Thus, if the application of the diagnosis procedure to the series reveal that some of the malfunctions present an increasing trend with the time (or constant, sometime), these ones can be assumed as intrinsic malfunctions, (i.e. directly caused by the presence of anomalies). In contrast, if some other malfunctions present a decreasing or fluctuating trend with the time, these ones can be identified as induced effects.

In [6.12], Verda dealt with the accuracy level achieved in thermoeconomic diagnosis. To this regard, the author stressed how an accurate procedure can provide a lot of information but it is generally difficult to be implemented. Conversely, a simple

procedure is less accurate but much easier to be used. To this aim, three different levels of accuracy were investigated by the author: (i) comparison of the operating and reference conditions; (ii) elimination of the effects due to the intervention of the control system; (iii) elimination of the induced effects in the components. The analysis was applied to the TADEUS problem. Results showed that a simple procedure based on the direct comparison between the actual operating condition and a proper reference condition did not guarantee the correct localization of the anomalies (this is what actually is done by malfunction/disfunction analysis). Improvements in the accuracy were observed by applying the second level which filtered the induced effect by the control system intervention. In this case, the complexity of the procedure was not highly increased, but only the major anomalies were detected. In order to improve the performance of the technique, the third level was applied and effect induced by the dependence of exergy unit consumption from changes in the operating point were filtered. In this case however, the author stressed that anamnesis procedure could be more effective in improving the accuracy of the diagnostic technique.

In 2007, Verda and Borchiellini [6.21] considered the effect of errors in measurements of thermodynamic variables on the diagnosis results. The analysis considered the detection and diagnosis of an anomaly occurring in the high-pressure evaporator of a Heat Recovery Steam Generator. Results showed that the impact of the errors was not negligible, but they did not impede to locate correctly the anomaly, provided that a sufficiently large set of data were considered. Also, it was shown that *malfunction* less sensitive to the effects of errors in measurements than unit exergy consumption.

An alternative approach for addressing the intrinsic/induced malfunction problems, was proposed by Toffolo and Lazzaretto in [6.13]-[6.15]. The method relies on *characteristic curve of a component* as a tool for distinguishing intrinsic and induced malfunction in a component. In particular, a characteristic curve expresses an

analytical relationship between a thermodynamic or thermoeconomic quantity (such as mass flowrates or exergy unit consumption) and some independent variables which are mainly affected by faults occurring in the given component. When an operation anomaly occurs, the characteristic curve of the malfunctioning component changes. Conversely, all faults-free components continue to operate on their original characteristic curve (i.e. the one determined in reference state), but, in general, in a different point. In this way, by looking at the operation point location on the characteristic curve, it is possible to distinguish if the components are affected by an intrinsic or an induced malfunction.

The previous approaches have been compared in [6.15]. Results showed the capabilities of these approaches to distinguish among intrinsic and induced malfunction. However, none of them is capable to provide with information about the impact of each fault on the additional exergy consumption.

6.4 Thermoeconomic Diagnosis and other FDDs technique for air conditioning systems

Among Fault Detection and Diagnosis techniques for Heating, Ventilation and Air conditioning systems (HVAC), it is worth mentioning the *Statistical Rule Based* FDD developed by Rossi and Braun in [6.21]. The method relies on a set of thermodynamic variables, as pressures and temperatures, whose variations, indicated as "residual", is uniquely determined by a specific fault. More specifically, residuals are calculated as the difference between the measured value and an "expected value" for this set of parameters. The directional changes in the residuals (i.e. decrease or increase) are statistically compared with a set of rules, preliminary defined, in order to diagnose a fault. The approach is able to detect single faults, but it has difficulty in handling multiple faults scenario. To this aim, an alternative approach based on the "*decoupling features*" was then developed by Li and Braun in [6.22][6.23]. Differently from the

Statistical Rule Based, this approach associates only one thermodynamic variable for each fault. For instance, air flowrates were selected for detecting evaporator and condenser fouling. The technique has been proven to be promising for multiple faults scenarios, but it cannot provide any quantitative information on the impact of each fault on the additional energy consumption.

Thermoeconomic diagnosis has not been extensively applied to HVAC systems and for this reason, the method is still at a very early stage of development. In Dentice d'Accadia and De Rossi [6.26] , the method was applied for the first time to a simple vapor compression system. By means of the "fuel impact approach" the authors quantified the effect of some basic faults. In [6.27], Picallo-Perez et al. combined the capabilities of characteristic curve method with the malfunction/dysfunction approach. The proposed analysis [6.27] tried combines the main capabilities of both approaches: in fact, the first one is able to distinguish whether a malfunction is induced and/or intrinsic. Conversely, the second one provides quantitative information of the impact of each fault in additional exergy consumption. Also, in the cited paper the challenge of applying diagnoses to building thermal facilities was addressed and a dynamic representation of the thermoeconomic model of the system was included. The method was applied to a domestic hot water and heating facility by considering also the dynamic behavior of energy demands. A multiple faults scenario was simulated, and promising results were achieved. However, no air-cooling units were included in the analysis.

In Piacentino and Talamo [6.28], thermoeconomic diagnosis was applied for the first time to an air-cooled direct expansion air conditioning unit considering some faults commonly occurring in HVAC systems [6.25]. By means of "virtual experiments" carried out by the simulator IMST-Art [6.31], fault-free scenarios were first simulated and then faults were imposed by changing the most affected parameters associated with the fault under consideration. Results showed that: (i) the method is not able to deal with "system level" faults, i.e. faults not associated with any specific

component like refrigerant under- or over-charge and (ii) the "productive" model for the expansion valve erroneously leads to identify this component as faulty even when its operation has no anomalies.

An innovative thermoeconomic model was proposed in [6.29]. This model filters the malfunction induced on the expansion valve. Promising results were achieved when considering single faults scenario as condenser fouling, compressor valve leakage but the performance of the method was still unsatisfactory when handling multiple faults scenarios. Also, in [6.29] the sensitivity of the performance of the technique to the fault level was evaluated. Results showed that when passing from a light to a heavy level of the fault, the performance of the technique got worst due to non-linearity in the thermodynamic behavior of components not properly filtered by the adopted thermoeconomic model. In [6.30], the robustness of the diagnostic technique for the detection of evaporator fouling in direct-expansion air-conditioning units was investigated. Particularly, the sensitivity of the technique to the thermodynamic conditions of the air entering the evaporator coil (i.e. temperature and relative humidity) was evaluated. It was observed that the technique was very efficient in detecting the fault on the evaporator, but the quantitative performance was highly sensitive to the psychrometric conditions of the air. More specifically, the performance of the technique became unsatisfactory when the relative humidity of the inlet air increased.

6.5 On the thermoeconomic model proposed for direct expansion air conditioning system.

The productive structure presented by Piacentino and Talamo in [6.29] was used in this chapter and it is shown in Figure 6.2 In this model, refrigerant exergy flows were split into thermal fraction (indicated as ΔB_i^T) and mechanical fraction, (indicated as

ΔB_i^M), which characterize "thermal" and "mechanical" disequilibrium between the refrigerant state and the reference dead state. Exergy flow splitting allows for easier analysis of the productive function of some components: for instance, mechanical exergy (blue lines in Fig. 6.2) is produced only by the compressor and then is used by other components (i.e. evaporator, thermal expansion valve (TXV) and condenser). Two types of residue flows are shown in Figure 6.2: (i) "*conventional residue*" (red dotted lines) which refers to the refrigerant exergy dissipated by the condenser into the external cooling air when the plant works at the design condition and (ii) "*marginal residues*" (green dotted lines) related to the additional exergy destruction in the TXV (i.e. $\Delta B_3^* = \left[\Delta B_3^M(\mathbf{X}) - \Delta B_3^T(\mathbf{X})\right] - \left[\Delta B_3^M(\mathbf{X^0}) - \Delta B_3^T(\mathbf{X^0})\right]$) and in the condenser (i.e. $\Delta B_2^* = \Delta B_2^{total}(\mathbf{X}) - \Delta B_2^{total}(\mathbf{X^0})$) when faults occur. The marginal residues were introduced in order to filter the induced malfunction especially in the TXV. In the improved thermoeconomic model [6.29], when malfunction in the TXV can be reasonably excluded then all the TXV marginal exergy consumption is allocated to the compressor, the condenser and the evaporator by means of the *distribution factors* a_1, a_2, and a_4. The conceptual bases of their definition may be clarified by an example: if laboratory tests reveal that condenser fouling implies much higher additional exergy destruction at the TXV than evaporator fouling, when diagnosing a real-world unit and attempting to filter the additional exergy destruction at the valve (which works correctly and cannot be responsible of this additional exergy destruction), a larger fraction should be probabilistically attributed to the possible fouling of the condenser and only a lower fraction to the possible evaporator fouling. The factor "a_i" is the fraction of the additional exergy consumed by the expansion valve that should be allocated to the i-th component, and it is calculated as the ratio between the increased exergy consumption in the TXV observed when the fault on the i-th component is occurring and the sum of the increase in exergy destructions at the valve observed imposing simultaneously the different possible faults. For instance, a_2 indicates the

fraction of the additional exergy destruction at the valve that could be originated by condenser fouling (i.e. the component 2 in Figure 6.2) and it is calculated as shown in Equation (6.15).

$$a_2 = \frac{\left[\Delta \mathrm{B}_3^M(\mathbf{X}) - \Delta \mathrm{B}_3^T(\mathbf{X})\right]_{cond\_foul} - \left[\Delta \mathrm{B}_3^M(\mathbf{X^0}) - \Delta \mathrm{B}_3^T(\mathbf{X^0})\right]}{\sum_{\substack{K=cond\_foul \\ evap\_fouling \\ comp\_leakage}} \left[\Delta \mathrm{B}_3^M(\mathbf{X}) - \Delta \mathrm{B}_3^T(\mathbf{X})\right]_K - \left[\Delta \mathrm{B}_3^M(\mathbf{X^0}) - \Delta \mathrm{B}_3^T(\mathbf{X^0})\right]} \qquad (6.15)$$

The factors a_1 and a_4 are the fraction of $\Delta \mathrm{B}_3^*$ allocated to the compressor and the evaporator, respectively, as a consequence of valve leakage and evaporator fouling. Also, it is easy to demonstrate that the condition $a_1 + a_2 + a_4 = 1$ is satisfied. The same procedure should be followed for calculating the distribution factors c_i.

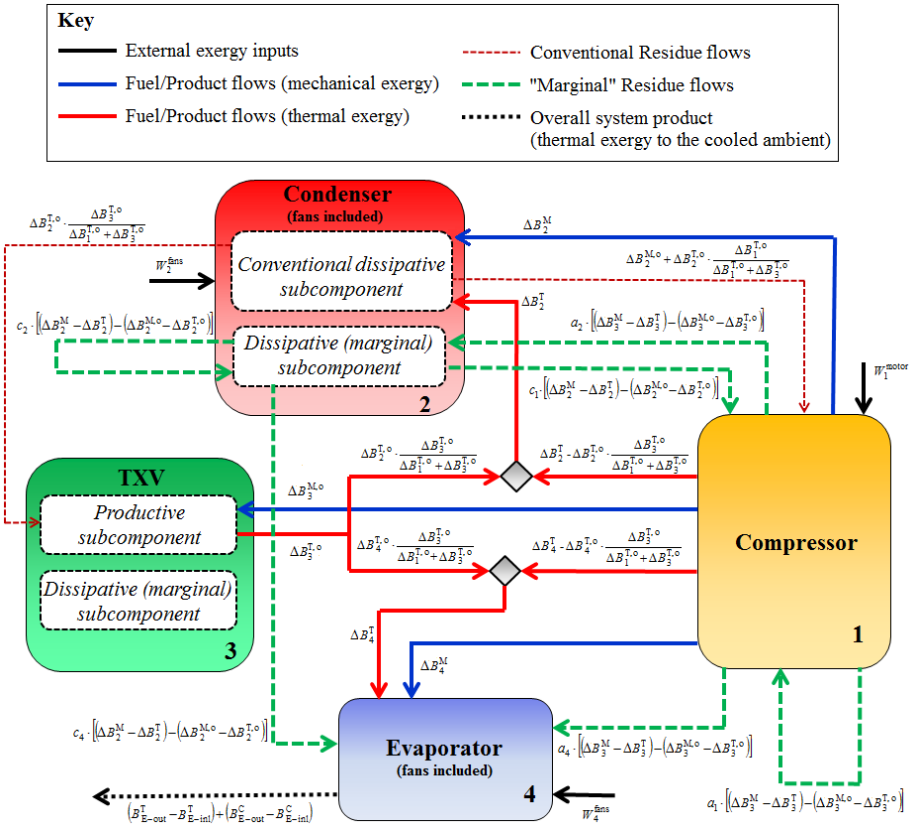

***Figure 6.2**: Thermoeconomic model for a direct expansion system proposed by Piacentino and Talamo in [6.29]*

6.6 Description of the Experimental Set-Up

A rooftop unit (RTU) was considered in this study having a rated capacity of 17.5 kW and a Seasonal Energy Efficiency Ratio (SEER) rating of 20.0. The refrigerant used is R410a. The unit can be operated in a *staged mode* or in a *variable speed mode*. Since thermoeconomic diagnosis has been developed for systems equipped with a fixed-speed compressor and fixed-speed fan, the unit was operated in "high stage mode". More specifically, in "high stage mode" both the compressor and the indoor fan run at their maximum speed, so that the RTU provides its maximum cooling capacity, conversely, in the "low stage mode" both compressor and indoor fan run at their lower speed, thus providing the minimum cooling capacity. A schematic of the test facilities is shown in Figure 6.3 (a)-(b). Two psychrometric chambers (each one equipped with its own reconditioning system) allowed to simulate the outdoor and indoor environment. A summary of the instrumentation installed on the RTU is presented in Table 6.1. A real-time controller from National Instruments was used for data acquisition and control of the RTU [6.33].

(a)

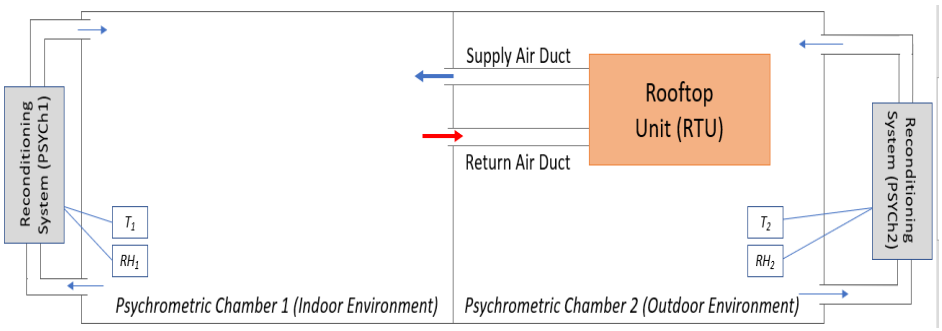

(b)

Figure 6.3: (a) *Packaged rooftop air conditioning unit installed at Herrick Laboratories[6.33]*
(b) *Schematic of the experimental facilities*

Table 6.1: *Description of RTU instrumentation [6.33]*

	Sensors Type	**Sensors Location**
Refrigerant Temperature	*T-type Thermocouples* (Accuracy ±0.5°C)	Compressor Suction Compressor Discharge Condenser Outlet TXV inlet Evaporator Inlet Evaporator Outlet
Refrigerant Pressure	*Pressure Transducers with voltage output* (Accuracy ±0.5% of the full-scale reading)	Compressor Suction Compressor Discharge Liquid line outlet
Refrigerant Mass flowrate	*Coriolis Mass flowmeter* (Accuracy ±0.5% of the full-scale reading)	On the liquid line
Dry Bulb Air Temperature	*T-type Thermocouples (*Accuracy ±0.5°C*)*	Return Air: two-by-two grid was spaced equally in a rectangular grid placed before the evaporator Supply Air: two-by-two grid spaced equally in a rectangular grid placed after the supply fan Condenser Inlet: 8 thermocouples mounted in a four-by-two grid on the face of the condenser Condenser Outlet: 4 thermocouples mounted radially on the condenser outlet

Dew Point Air Temperature	*Dew point hygrometer with chilled mirror probe* (Accuracy ±0.15°C)	Air samples were taken before the evaporator inlet and at the beginning of the supply air duct
Power Consumption	*Watt Transducers* (Accuracy of ±0.5 % of the full-scale reading)	Indoor Fan Supply Air Compressor Power Condenser Fan

6.7 Description of Testing Procedures

The following variations in boundary conditions were considered during the experimental activities: (i) temperature of the outdoor environment (here indicated as $T_{outdoor}$); more specifically, two values of $T_{outdoor}$ were investigated: 30°C, 35°C; (ii) temperature of the air entering the RTU. Particularly, the following values were examined: 24°C, 26.5°C and 29°C. For this set of temperatures, the indoor relative humidity was kept equal to 50%, (iii) for a return air temperature equal to 26.5°C, the following values of relative humidity were tested: 25%, 45% and 55% in order to isolate the effect of relative humidity on the technique performance.

The operation of the unit at each set of driving conditions was first recorded with no faults present. Then, the faults were introduced and all tests were repeated. Measurements were taken every second for all of the input and output variables. The steady state of the system was detected by comparing data of a moving averaging window of 20 minutes.

6.7.1 Faulty Scenarios: testing procedure

In order to test the performance of the technique, the following faults were experimentally investigated: (i) evaporator fouling, (ii) condenser fouling (iii) evaporator and condenser fouling. Also, two levels of faults, respectively indicated as "light" and "heavy" were tested in order to evaluate the sensitivity of the performance of the technique.

Condenser fouling was tested by placing some layers of fabric on the condenser surface as shown in Figure 6.4 (a). The number of layers was selected in order to simulate a "*light"* and a "*heav*y" fouling. Each level caused a reduction in the condenser air mass flowrate equal to 20% and 35% with respect to the fault-free scenario. Measurements of the condenser air flowrate were carried out by means of the virtual sensor proposed by Li and Braun in [6.23] which is based on an energy balance on this component. In Table 6.2, some experimental results for the heavy condenser fouling are shown. An increase in the condensing pressure and subcooling was observed. Conversely, the evaporating pressure, the refrigerant quality at the evaporator inlet and the superheat at the compressor suction were approximately constant. The power consumed by the compressor increased as a consequence of the increased pressure ratio. No changes in the consumption of indoor fan and in the cooling capacity were observed.

Evaporator fouling was tested by acting on the opening of an iris damper placed on the supply air duct of the unit as shown in Figure 6.4 (b). Different levels were selected by measuring the air pressure drop across the RTU while running the indoor fan at its maximum speed (around 1250 rpm). Considering a 150 Pa air pressure drop (about 0.6 inch of water) across the RTU for the fault-free scenario (i.e. when the damper is fully open), two levels of fouling were tested: (i) a "*light"* fault which corresponds to a 280 Pa air pressure drop (about 1.0 inch of water) and (ii) a "*heavy"* evaporator fouli*g* which corresponds to 380 Pa air pressure drop (about 1.5 inches of water). In Table 6.2, some experimental results are shown for the heavy evaporator fouling. Differently from the condenser fouling, this fault provoked a significant reduction in the RTU sensible capacity (about 26%). Also, due to reduction in the air mass flowrate across the evaporator, the exiting air was cooler and more dehumidified as shown respectively by the dry bulb temperature and dew point temperature of the supply air. Reduction in the evaporating and condensing pressure was also observed.

In the multiple fault scenario, both heavy condenser fouling and heavy evaporator fouling were tested. As shown in Table 6.2, a reduction of the RTU cooling capacity is observed due to the reduction in the air mass flowrate across the evaporator. An increase in the condensing pressure and the subcooling was observed due to the condenser fouling. Also, the compressor power increased due to increases in the pressure ratio.

(a) **(b)**

Figure 6.4: (a) *Light Condenser fouling simulated by a layer of fabric placed on the condenser surface* ***(b)*** *Iris damper used for simulating evaporator fouling equipped with a black screw for adjusting its opening.*

Table 6.2: *Experimental Results for the free-fault case and faulty scenarios ($T_{outdoor}$=35°C)*

	Return Air		***Supply Air***		***Air Mass Flowrate***
	Dry Bulb Temp.	*Dew Point Temp.*	*Dry Bulb Temp.*	*Dew Point Temp.*	
	[°C]	[°C]	[°C]	[°C]	[kg/s]
Free-Fault	26.5	14.2	15.9	11.6	1.22
Condenser Fouling	26.5	14.2	15.5	11.6	1.28
Evaporator Fouling	26.5	14.2	14.29	11.08	0.90
Multiple Faults	26.5	14.2	13.42	10.3	0.931

	Refrigerant Quality	*Suction Pressure*	*Suction Temp.*	*Suction Superheat*	*Discharge Pressure*	*Subcooling*	*Refrigerant Mass Flowrate*
	[-]	[kPa]	[°C]	[°C]	[kPa]	[°C]	[kg/s]
Free-Fault	0.20	1095.6	15.3	5.8	2827.9	9.5	0.102
Condenser Fouling	0.19	1078.1	15.4	5.7	3274.6	15.4	0.103
Evaporator Fouling	0.20	1036.1	14.33	5.88	2746.5	9.38	0.097
Multiple Faults	0.19	1016.4	13.0	5.2	3347.3	16.7	0.097

	Indoor Fan Power	*Outdoor Fan Power*	*Compressor Power*	*Sensible Capacity*	*Cooling Capacity*
	[W]	[W]	[W]	[W]	[W]
Free-Fault	1131	291	3788	15115	17035
Condenser Fouling	1140	342	4351	14837	16727
Evaporator Fouling	862	287	3700	11189	16444
Multiple Faults	890	340	4481	12810	16380

6.8 Analysis of Diagnosis Performance by using experimental data

Before implementing the diagnostic procedure, it is useful to analyze the exergy variation of refrigerant through each component for some tested conditions. In Table 6.3, variations of thermal and mechanical exergy of the refrigerant across each component (indicated as ΔB_i^T and ΔB_i^M) are shown for the following scenarios: (i) fault-free, (ii) evaporator fouling (iii) condenser fouling and (iv) condenser fouling along with evaporator fouling. Also, for each faulty scenario the marginal exergy destruction (i.e. ΔB_i^*) occurring in the TXV and the condenser are shown. It is worth noting that exergy quantity (kJ_{ex}) instead of exergy flow (generally measured in kW_{ex}) are shown. In fact, when considering evaporator fouling (similarly in evaporator fouling along with condenser fouling), a reduction in the RTU sensible capacity is observed due to reduction in the air mass flowrate across the evaporator. As a consequence, the control will act by adjusting the cycling time of the unit in order to achieve the same average

cooling in both fault-free and faulty scenarios. In order to consider this, all the exergy flows in the faulty scenario were multiplied by the "*capacity correction factor* α_{capacity}" shown in Equation (6.16), defined as the ratio of the sensible cooling rates evaluated in fault-free and faulty conditions

$$\alpha_{capacity} = \frac{\dot{Q}_{sens}^{No,\,fault}}{\dot{Q}_{sens}^{fault}} \tag{6.16}$$

When testing condenser fouling, no reduction in the sensible capacity of the unit was observed (see Table 6.2), thus the capacity correction factor was equal to one.

Looking at the results shown in Table 6.3, it can be observed that the mechanical exergy of the refrigerant consumed in the evaporator is negligible with respect to the thermal one in all the examined scenarios, i.e. $\Delta B_4^T \gg \Delta B_4^M$. Also, the mechanical exergy produced by the compressor, i.e. ΔB_1^M, is entirely used in the expansion valve to increase the thermal exergy of the refrigerant supplied to the evaporator.

An increase in the variation of mechanical exergy of the refrigerant through the compressor (i.e. ΔB_1^M) occurs when condenser fouling is imposed, as a consequence of the higher condensing pressure. Conversely, when evaporator fouling is tested, this increase is related to the prolonged on-time of the system, since no substantial variation in condensing and evaporating pressure are observed, as shown in Table 6.2.

The thermal exergy consumed in the evaporator to cool and dehumidify air is approximately constant for condenser fouling since evaporating pressure and refrigerant mass flowrate are also constant (see Table 6.2). Conversely, when considering evaporator fouling, the thermal exergy consumed in the evaporator increases due to both the decrease in the evaporating pressure and changes in the on-time of the system.

The highest value for the mechanical exergy produced by the compressor, i.e. ΔB_1^M =2.213 kW_{ex}, is observed in the multiple faults scenario, as a consequence of: (i) increase in the condensing pressure due to condenser fouling and (ii) a longer on-time of the system due to reduction in the cooling capacity. For the same reasons, the highest values for the additional exergy destruction in the TXV and the condenser are obtained in this case.

Table 6.3: *Refrigerant Exergy Results for $T_{outdoor}$=30°C, T_{ra}=26.5°C, RH_{ra}=50%*

	Faults-free		***Evaporator Fouling***			***Condenser Fouling***			***Evaporator Fouling + Condenser Fouling***		
	ΔB_i^M	ΔB_i^T	ΔB_i^M	ΔB_i^T	ΔB_i^*	ΔB_i^M	ΔB_i^T	ΔB_i^*	ΔB_i^M	ΔB_i^T	ΔB_i^*
	[kJ_{ex}]		[kJ_{ex}]			[kJ_{ex}]			[kJ_{ex}]		
1.Compressor	1.684	0.766	2.099	0.842	--	1.827	1.272	--	2.213	1.851	--
2.Condenser	-0.013	-0.806	-0.013	-0.946	0.141	-0.010	-1.231	0.451	-0.011	1.912	1.106
3.TXV	-1.671	1.413	-2.084	1.761	0.066	-1.814	1.473	0.083	2.199	1.731	0.210
4.Evaporator	-0.001	-1.360	-0.001	-1.870	--	-0.001	-1.330	--	-0.001	1.673	--

6.9 Calibrating the Thermoeconomic model for the tested unit

Before carrying out thermoeconomic diagnosis, it is necessary to calculate the distribution ratios a_i and c_i for the examined system. Since compressor valve leakage was not considered, it is possible to set a_1 and c_1 equal to zero. For this reason, the marginal exergy destruction in the condenser, i.e. ΔB_2^*, and in the TXV, i.e. ΔB_3^*, are evaluated only for the condenser and evaporator fouling. Results are shown in Table 6.3. The marginal exergy destruction in the condenser is greater when imposing condenser fouling with respect to evaporator fouling. Since the mechanical fraction of exergy used in the condenser is always negligible, this marginal exergy destruction is due to the thermal exergy. In fact, when condenser fouling is tested, more compressor power is consumed due to increase in the condensing pressure. As a consequence, a greater amount of thermal exergy has to be discharged into the cooling air. Conversely, the marginal exergy destruction in the expansion valve is comparable for both faults.

By means of the previous values, calculation of the distribution factors for the tested system was done as follows:

$$a_2 = \frac{\left[\Delta B_3^M(\mathbf{X}) - \Delta B_3^T(\mathbf{X})\right]_{cond\_foul} - \left[\Delta B_3^M(\mathbf{X^0}) - \Delta B_3^T(\mathbf{X^0})\right]}{\left[\Delta B_3^M(\mathbf{X}) - \Delta B_3^T(\mathbf{X})\right]_{cond\_foul} - \left[\Delta B_3^M(\mathbf{X^0}) - \Delta B_3^T(\mathbf{X^0})\right] + \left[\Delta B_3^M(\mathbf{X}) - \Delta B_3^T(\mathbf{X})\right]_{evap\_foul} - \left[\Delta B_3^M(\mathbf{X^0}) - \Delta B_3^T(\mathbf{X^0})\right]} = 0.557 \quad (6.17)$$

Since the condition $a_2+a_4=1$ has to be respected, it follows that $a_4 = 0.443$. By comparing the values obtained for a_2 and a_4, it follows that for a given increase in the marginal exergy of the TXV, the approach allocated it almost equally to the condenser and to the evaporator. The same procedure was followed for calculating the c_i factors, and the following values are obtained: $c_2 = 0.762$ $c_4 = 0.238$. Since c_2 is greater than c_4, it is clear that marginal exergy consumption in the condenser is mainly induced by condenser fouling rather than evaporator fouling.

6.10 Definition of the diagnosis performance indicator

The efficiency of the diagnostic procedure in properly identifying a generic "fault "j" and quantifying the additional energy consumption that it provokes can be evaluated by introducing an appropriate indicator, $\Psi^{fault\ j}$, defined as ratio between the malfunction cost (i.e. the additional energy consumption induced by the "fault j", according to the estimation provided by the diagnostic technique) and the "fuel impact" ΔF_T, *i.e.* the actual additional energy consumption induced by the "fault "j", calculated as difference between the energy consumption evaluated by the simulator in presence of "fault j" and the consumption evaluated when "fault j" is absent. For an air-conditioning system, being the energy consumption related with the electricity W needed to drive the compressor and the fans, once indicated by {Ω} a generic set of multiple simultaneous faults that include "fault j" (i.e. a fault in the component "j"), $\Psi^{fault\ j}$ is expressed as:

$$\Psi^{\text{fault j}} = \frac{MF_j^*}{\Delta F_T^{\{\text{fault j}\}}} = \frac{MF_j^*}{W^{\{\Omega\}} - W^{\{\Omega - \text{fault j}\}}} \tag{6.18}$$

If a single fault is considered, for instance evaporator fouling, then in Equation (6.18) $\{\Omega\}=\{\text{fault 4}\}$ is imposed, having been the evaporator identified as component 4. As $\Psi^{\text{fault 4}}$ represents the ratio between the "estimated additional energy consumption" and the "actual/exact additional energy consumption", we may conclude that:

- when $\Psi^{\text{fault 4}}=1$ the diagnostic procedure perfectly quantifies the additional energy consumption provoked by the fouled evaporator (i.e. by "fault 4");
- when $\Psi^{\text{fault 4}}>1$ or $\Psi^{\text{fault 4}}<1$ the diagnostic procedure respectively over- or under-estimates the additional energy consumption provoked by "fault 4".

6.11 Sensitivity analysis of diagnostic performance to outdoor and return air temperature

In Figure 6.5 and 6.6, the performance indicators $\Psi^{\text{fault,2}}$ and $\Psi^{\text{fault,4}}$ are presented for condenser fouling and evaporator fouling, for different temperatures of both the outdoor environment and the returning air to the RTU. In both cases, the relative humidity of the returning air (RH) was kept equal to 50%. Also, heavy faults were assumed in this analysis. In the figures, the fuel impact and the malfunction costs are expressed in kW_{ex}, while the performance indicators are dimensionless, according to Equation (6.18).

An ideal performance of the diagnostic technique would be represented by the following results: (i) $\Delta F_T = MF_2^*$ (i.e. the estimated additional fuel impact MF_2^* due to condenser fouling equals the total fuel impact), (ii) $MF_1^* = MF_4^* = 0$ (i.e. the estimated additional fuel impacts due to compressor leakage and evaporator fouling are null) and

(iii) $\Psi^{fault,2}$=1. Looking at the results for the condenser fouling in Figure 6.5, it is possible to observe that:

- the malfunction cost MF_2^* is always positive and greater than other malfunction costs (i.e. MF_1^* and MF_4^*) thus allowing for detection of this fault regardless of the boundary condition. From a quantitative point of view, promising results are achieved by means of the adopted thermoeconomic model, which provides a reasonable quantitative estimation of the additional consumption provoked by these faults as testified by the value of the indicator $\Psi^{fault,2}$ which has a range 0.5-1.5 for almost all cases.
- A non-null malfunction cost MF_1^* is detected for the compressor. This is due to the effect of the induced malfunction on this component which is not properly filtered by the adopted productive structure. The negative values of MF_1^* prevent the risk of erroneous detection of the compressor as a "faulty component". In fact, these negative values indicate that the compressor works "better than in fault-free conditions" (at least from an exergetic viewpoint), and this is a consequence of the increase in its isentropic efficiency when condenser fouling is imposed. In a more refined thermoeconomic model, this induced malfunction should be properly filtered and reallocated on the component which originates this. No malfunction is induced on the evaporator by condenser fouling as shown by negligible values of MF_1^*.
- The performance of the diagnostic technique is not particularly sensitive to the outdoor temperature and the temperature of the air entering the evaporator coil.

Looking at the results for the evaporator fouling in Figure 6.6, it is possible to observe that:

- For a given outdoor temperature, the performance of the diagnostic technique is influenced by the temperature of the air entering the evaporator coil. More specifically, it gets worst when increasing this temperature from 24°C to 29°C.It

is worth noting that in this case the malfunction induced on the condenser is not always negligible and the malfunction cost MF_2^* can be even higher than MF_4^*, thus not allowing for an easy and univocal detection of this fault.

- Also, for evaporator fouling a non-null malfunction cost MF_1^* is detected for the compressor. However, since MF_1^* is negative there is no risk of erroneously detecting this component as "faulty".
- The performance of the diagnostic technique is not particularly sensitive to the outdoor temperature.

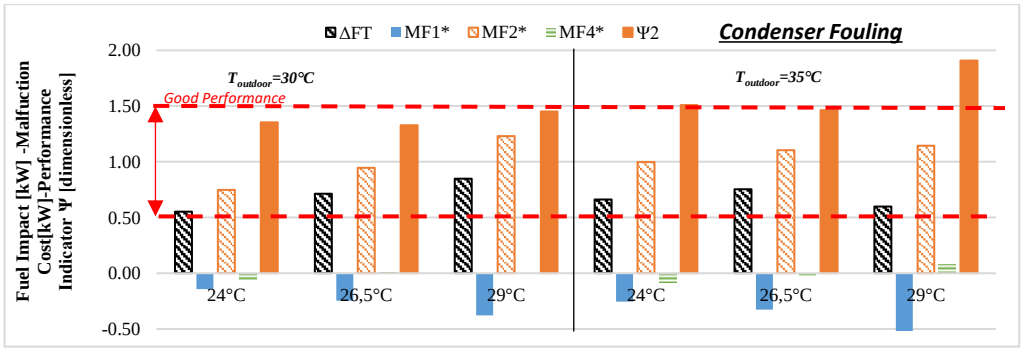

Figure 6.5: *Condenser fouling: sensitivity analysis of the technique to the outdoor temperature and to return air temperature.*

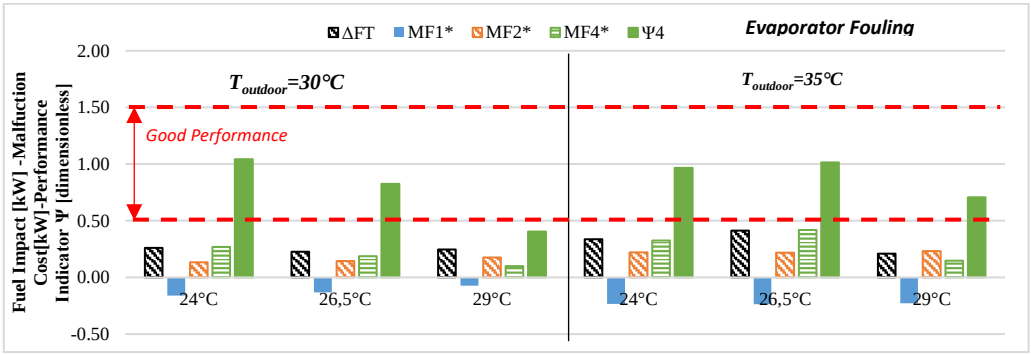

Figure 6.6: *Evaporator fouling: sensitivity analysis of the technique to the outdoor temperature and to return air temperature.*

6.12 Sensitivity analysis of the diagnostic technique to fault level and return air relative humidity

As shown in [6.29], when increasing the level of the fault, the performance of the technique gets worst due to non-linearities in the behavior of components responsible for induced malfunction in fault-free components. To consider this effect, experimental tests were carried out by considering two levels of condenser fouling and evaporator fouling, indicated as "light" and "heavy". At the same time, in order to evaluate the influence of the relative humidity on the performance of the technique, these tests were carried out considering three values of the return air relative humidity (RH), i.e. 25%, 45% and 55%. The return air temperature was kept equal to 26.5°C. Results of this analysis for the condenser and evaporator fouling are shown in Table 6.4. For condenser fouling, it is possible to observe that:

- A good performance of the technique is achieved as proved by the values of the indicator $\Psi^{fault,2}$ which always ranges between 0.5 and 1.5 regardless of the imposed level of condenser fouling. Then, it is worth noting how the performance of the diagnostic technique decreases when passing from a "*light"* to a "*heavy"* condenser fouling. This trend is verified regardless of the relative humidity of the air entering the evaporator coil.
- The performance of the technique is moderately sensitive to the relative humidity of the air entering the RTU. In particular, at higher relative humidity the condenser fouling is more readily detected as the main contributor to the additional consumption (as evident from the higher values of $\Psi^{fault,2}$)

In Table 6.4, results for evaporator fouling are also shown. It is possible to observe that:

- the performance of the diagnostic technique decreases when passing from a "*light"* to a "*heavy"* level, as can be seen by looking at the of indicator $\Psi^{fault,4}$. Also, a good performance of the technique is achieved from a quantitative point

of view as supported by the values of the indicator $\Psi^{fault,2}$ which always range between 0.5 and 1.5.

- A positive malfunction cost is detected for the condenser MF_2^*. Even though its values are lower than those assumed by evaporator malfunction cost MF_4^*, this is a weakness of the diagnostic and future developments of the technique should be aimed at filtering this induced malfunction.
- A high sensitivity of the performance of the diagnostic technique to the relative humidity of the entering air is observed. Specifically, the higher the humidity content of the air, the worst its performance. Looking at Table 6.4, it is possible to note that when the evaporator coil is dry, i.e. when the RH=25%, the quantitative performance is quite good ($\Psi^{fault,2} \approx 1$). These trends are coherent with the main results achieved in [6.30], where a great sensitivity of the technique performance with the relative humidity of inlet air at the evaporator coil was also observed.

Table 6.4 *Sensitivity analysis of the diagnostic technique to the fault level and the return air relative humidity.*

	Condenser Fouling					
	Light Fault			***Heavy Fault***		
RH	**25%**	**45%**	**55%**	**25%**	**45%**	**55%**
MF_2^*	0.102	0.653	0.760	2.167	1.278	1.150
ΔF_T	0.133	0.810	0.576	1.805	1.98	1.515
$\Psi^{fault,2}$	**0.763**	**0.807**	**1.319**	**0.659**	**0.646**	**0.760**

	Evaporator Fouling					
	Light Fault			***Heavy Fault***		
RH	**25%**	**45%**	**55%**	**25%**	**45%**	**55%**
MF_4^*	0.193	0.149	0.102	0.847	0.340	0.193
ΔF_T	0.197	0.130	0.186	0.928	0.517	0.360
$\Psi^{fault,4}$	**0.979**	**1.145**	**0.549**	**0.913**	**0.653**	**0.536**

6.13 Analysis of the technique performance in a multiple fault scenario

In this section, the analysis considers the presence of both heavy evaporator and heavy condenser fouling. In [6.29], it was shown that the performance of the technique got worst in multiple fault scenarios. The results for the examined case are presented in Table 6.5. It is possible to observe that: The technique is able to detect a combination of condenser and evaporator fouling faults as demonstrated by the positive values of the malfunction cost MF_2^* for condenser fouling and MF_4^* for evaporator fouling.

Negative values for MF_1^* are obtained, due to induced malfunction on the compressor. From a quantitative point of view, the performance is not satisfactory. The adopted thermoeconomic model is extremely sensitive to the relative humidity of inlet air, eventually leading to $\Psi^{fault,2}$ and $\Psi^{fault,4}$ values much lower or higher than 1. In particular, while in dry coil conditions the technique tends to overestimate the additional consumption provoked by evaporator fouling (see $\Psi^{fault,4}$=4.069) and underestimate the one provoked by condenser fouling (see $\Psi^{fault,2}$=0.470); the opposite occurs when a wet operating condition is examined. In both cases, the negative values are one of the main causes of this erroneous quantitative estimation, and methodological refinements are needed in order to converge toward the "ideal performance" condition where $MF_1^* = 0$ would be obtained (since no faults were imposed to the compressor).

Table 6.5: *Results for the multiple fault scenario*

	Heavy Condenser Fouling - Heavy Evaporator Fouling		
	RH=25%	**RH=45%**	**RH=55%**
MF_1^*	-0.733	-0.481	-0.729
MF_2^*	1.123	1.367	1.282
MF_4^*	0.941	1.236	1.301
ΔF_T	1.36	2.144	1.875
$\Psi^{fault,2}$	***0.470***	***0.951***	***0.965***
$\Psi^{fault,4}$	***4.069***	***1.372***	***0.488***

6.14 On the main outcomes of this analysis

For the first time, thermoeconomic diagnosis of air cooling systems has been applied by means of real data available from a packaged rooftop air conditioning unit. The analysis has aimed at verifying results obtained from previous studies in the literature based on simulation-based data.

Three faulty scenarios have been considered: evaporator fouling, condenser fouling, evaporator fouling along with condenser fouling. Results have shown that: (i) the diagnostic technique is able to detect a single fault, but its quantitative performance is satisfactory only for the condenser fouling, (ii) The performance of the technique depends upon the level of fault imposed, and specifically it decreases when the fault level increases and this trend was verified regardless of the type of tested fault, (iii) for evaporator fouling, the performance of the diagnostic technique is sensitive to the relative humidity of the air entering the evaporator coil. More specifically, when considering a dry evaporator coil very promising results were achieved. Conversely, when the latent fraction of the cooling rate increases, the quantitative performance of the diagnostic technique is less reliable and (iv) in multiple faults scenarios, the technique is capable of detecting the simultaneous presence of condenser and

evaporator fouling, but it provides a poor quantitative estimation of their impacts on the increased consumption mainly due to the induced malfunctions on the compressor, which should be filtered.

References

[6.1] Saravanamuttoo HIH, Maclsaac BD. Thermodynamic models for pipeline gas turbine diagnostics. J Eng Power 1983;105:875–84.
[6.2] Biagetti T, Sciubba E. Automatic diagnostics and prognostics of energy conversion processes via knowledge-based systems. Energy 2004;29:2553–72.
[6.3] Li YG. Performance-analysis-based gas turbine diagnostics: a review. Proc Inst Mech Eng Part A J Power Energy 2002;216:363–77.
[6.4] Valero A., Torres C. and Lozano M. A., 1990, "On Causality in Organized Energy Systems: - Part II: Symbolic Exergoeconomics; Part III: Theory of Perturbations", Proceedings of FLOWERS 90, Florence
[6.5] Lozano, M. A., Valero, A. (1993). Theory of the Exergetic Cost. Energy. Vol. 18, N. 9, pp. 939-960.
[6.6] Torres C, Valero A, Serra L, Royo J. Structural theory and thermoeconomic diagnosis: Part I. On malfunction and dysfunction analysis. Energy Conversion and Management 2002;43:1503–18.
[6.7] Valero A., Torres C., and Lerch F., 1999, "Structural Theory and Thermoeconomic Diagnosis. Part III: Intrinsic and Induced Malfunctions," Elsevier Science, Energy Conversion and Management, 40, 1627-1649.
[6.8] Verda, V., Serra, L., Valero, A. (2001). A procedure for filtering the induced effects in the thermoeconomic diagnosis of an energy system. ASME IMECE. New York.
[6.9] Verda V. An improved thermoeconomic diagnosis procedure for the detection of different malfunctions of complex energy systems. ASME; 2003. p. 209–16.
[6.10] Verda V, Serra L, Valero A. Thermoeconomic diagnosis: zooming strategy applied to highly complex energy systems. Part 1: detection and localization of anomalies. J Energy Resour Technol 2005;127:42–9.
[6.11] Verda V, Serra L, Valero A. The effects of the control system on the thermoeconomic diagnosis of a power plant. Energy 2004;29:331–59.
[6.12] V. Verda, "Accuracy level in thermoeconomic diagnosis of energy systems," *Energy*, vol. 31, no. 15, pp. 3248–3260, Dec. 2006.
[6.13] Toffolo, A., Lazzaretto, A., 2003, "A new thermoeconomic method for the location of causes of malfunctions in energy systems". ASME paper IMECE2003-42689
[6.14] Toffolo A, Lazzaretto A. On the thermoeconomic approach to the diagnosis of energy system malfunctions indicators to diagnose malfunctions: application of a new indicator for the location of causes. Int J Thermodyn 2004;7:41–9.38
[6.15] Lazzaretto A, Toffolo A, Reini M, Taccani R, Zaleta-Aguilar A, Rangel-Hernandez V, et al. Four approaches compared on the TADEUS (thermoeconomic approach to the diagnosis of energy utility systems) test case. Energy 2006;31:1586–613.
[6.16] Verda V, Baccino G. Thermoeconomic diagnosis applied to the transient operation of a microturbine. Vol. 6 Energy, Parts A B, ASME; 2012. p. 1579
[6.17] R. Melli, V. Verda, and S.-G. Vernica, "A Thermoeconomic-Artificial Intelligence Combined Approach to the Diagnosis of Energy Systems," no. 54907. pp. 247–254, 2011.
[6.18] S. Keshavarzian, M. V. Rocco, and E. Colombo, "Thermoeconomic diagnosis and malfunction decomposition: Methodology improvement of the Thermoeconomic Input-Output Analysis (TIOA)," *Energy Convers. Manag.*, vol. 157, pp. 644–655, 2018.

[6.19] Lozano M.A., Bartolomé J.L., Valero A., and Reini M., 1994, "Thermoeconomic Diagnosis of Energy Systems," Flowers 94 - Florence World Energy Research Symposium, Florence. Italy
[6.20] Verda, V., Serra, L., Valero, A. (2002b). Effects of the Productive Structure on the Results of the Thermoeconomic Diagnosis of Energy Systems. International Journal of Applied Thermodynamic. Vol. 5 (No. 3), pp. 127-137
[6.21] V. Verda and R. Borchiellini, "Exergy method for the diagnosis of energy systems using measured data," *Energy*, vol. 32, no. 4, pp. 490–498, Apr. 2007.
[6.22] Rossi, T.M.; Braun, J.E. (1997) A statistical rule-based fault detection and diagnostic method for vapor compression air conditioners, *HVAC&R Research*, Vol. 3 No. 1, pp. 19-37.
[6.23] Li, H. Braun J.E. (2007) A methodology for diagnosing multiple simultaneous faults in vapor compression air conditioners, *HVAC&R Research*, Vol. 13(2), pp. 369-395
[6.24] Li, H. Braun, J.E. (2007) Decoupling features and virtual sensors for diagnosis of faults in vapor compression air conditioners. *Int. J. Refrigeration*, Vol.30 Issue 3, pp. 546–564.
[6.25] Breuker, M.G.; Braun, J.E. (1998) Common Faults and Their Impacts for Rooftop Air Conditioners. *HVAC&R Research*, Vol. 4 No. 3, pp. 303-318
[6.26] Dentice D'Accadia, M., De Rossi, F. (1998) Thermoeconomic analysis and diagnosis of a refrigeration plant. *Energy Conversion and Management*, Vol. 39 No. 12, pp. 1223-1232.
[6.27] A. Picallo-Perez, J. M. Sala-Lizarraga, and C. Escudero-Revilla, "A comparative analysis of two thermoeconomic diagnosis methodologies in a building heating and DHW facility," *Energy Build.*, vol. 146, pp. 160–171, Jul. 2017
[6.28] Piacentino, A. and Talamo, M., (2013a) Critical analysis of conventional thermoeconomic approaches to the diagnosis of multiple faults in air conditioning units: Capabilities, drawbacks and improvement directions. A case study for an air-cooled system with 120 kW capacity, *International Journal of Refrigeration*, Vol. 36 No. 8, pp 24-44.
[6.29] Piacentino, A. and Talamo, M. (2013b) Innovative thermoeconomic diagnosis of multiple faults in air conditioning units: methodological improvements and increased reliability of results, *International Journal of Refrigeration*, Vol. 36 No. 8, pp 2343-2365.
[6.30] Piacentino, A. Catrini, P. (2016) Assessing the Robustness of Thermoeconomic Diagnosis of Fouled Evaporators: Sensitivity Analysis of Exergetic Performance of Direct Expansion Coils. *Entropy*.
[6.31] IMST-Group Instituto de Ingeniería Energética Universidad Politécnica de Valencia. (2014) Advanced Refrigeration Technologies Software IMST-ART Release 3.60 www.imstart.com.
[6.32] Torres, C. Valero, A. Rangel, V. Zaleta A. (2008) On the cost formation process of the residues, *Energy*, Vol. 33, pp 144-152.
[6.33] Patil, A. Development and Evaluation of Automated Virtual Refrigerant Charge Sensor Training Kit, Master Thesis, Purdue University, 2018

Chapter 7

Integrating Thermoeconomics and Life Cycle Assessment for the analysis of energy systems

In this chapter, an integrated approach based on *Life Cycle Assessment* and *Thermoeconomics* is proposed as a method for evaluating the "exergo-environmental profile" of energy conversion systems along their life cycle.

The procedure combines the capabilities of these two techniques to account simultaneously for aspects related to thermodynamics of energy conversion processes and to the environmental impacts along the plant life cycle, i.e. from raw material extraction to the disposal of facilities. First of all, a brief overview on exergy-based method proposed for evaluating the energo-environmental profile of energy systems is carried out. Then, after giving some insights into both methods, the capabilities of the integrated approach are illustrated by applying it to a water-cooled vapor compression chiller. A number of scenarios concerning possible design alternatives, context conditions and levels of maintenance are investigated by means of this approach.

7.1 Overview on Exergy-based environmental analysis

In the last few decades, large efforts have been devoted to develop rigorous techniques aimed at minimizing both the consumption of non-renewable energy sources and the environmental impacts of energy systems.

To this regard, through first- and second-law based approaches such as Exergy Analysis or Thermoeconomics [7.1]]-[7.[7.3], it is not possible to evaluate the consequences of different design options in terms of environmental impacts, health hazards and total consumption of natural resources. In fact, even when accounting for energy consumption, the following limits could be observed:

- both methods consider only processes occurring within the physical boundaries of the energy system, thus excluding those involved for supplying resources to this system. For instance, in the case a coal-fueled power plant, the energy consumed for the mining process, for the transportation of the fuel to the physical facility are not accounted.
- secondly, only the operative phase is considered, thus energy consumptions of processes involved for the construction and disposal of the facilities are excluded.

It is apparent that any design improvement proposed by these methods should be verified in a life-cycle perspective, since a reduction of the irreversibility within a given system may not always involve a reduction of its primary energy-resources requirements. This concept may be clarified by a simple example: when selecting the refrigerant to be used in a conventional chiller, it could be argued that the best choice is represented by the fluid that would best perform during plant operation (for instance, allowing to achieve highest values of Energy Efficiency Ratio). On the other hand, if the perspective is broadened, it is worth considering also the energy embodied in the refrigerant charge, i.e. the energy required to prepare it for industrial use, the environmental impacts burdening its production process. Its global warming potential, if the refrigerant is partially lost in air by leakage, should be considered along with the potential risks and hazards for human health. Its effects to the environment and total use of natural resources and the final disposal should be also considered.

In order to gain a thorough understanding (i.e. both environmental impacts and energy use) of the results achievable by any plant design improvement, it is advisable

to broaden the scope of these analyses by connecting them with the accounting of environmental impacts occurring along the whole productive processes and along its life cycle. Before introducing the integrated approach proposed in this chapter, a brief literature review on relevant exergy-based methods developed to this aim is proposed here follow.

7.1.1 Cumulative Exergy Consumption (CExC) and Thermoecological Cost

The concept of *Cumulative Exergy Consumption* was proposed by Szargut and Morris in 1986 [7.4]. It was developed on the basis of the Cumulative Energy Consumption (CEnC) concept proposed by Chapman in [7.5]]-[7.[7.6] some years before. In particular, CEnC analysis aims at quantifying the consumption of fuels or other energy carriers to obtain a given product by considering the productive chain leading from natural resources to the final product. However, in [7.4], Szargut and Morris stressed the following limits of CEnC analysis: (i) the CEnC does not account for the consumption of non-energetic raw materials and (ii) this indicator does not evaluate the degree of thermodynamic perfection of the production processes. To overcome these limits, the authors proposed exergy as a basis for accounting for natural resources consumption and similarly to CEnC, they introduced the *Cumulative Exergy consumption* (CExC) concept [7.4]. In particular, the CExC of a product quantifies the exergy of the natural resources consumed in all the steps of the productive chain burdening a given product. This analysis allows for identifying: (i) those steps in a process where the main losses of exergy arise and (ii) for competing processes leading to the same product (or products), it permits a selection based on a thermodynamic criterion. In this way, the cumulative primary exergy "embodied" in a product over its entire production process is evaluated. With this method, both renewable and non-renewable exergy contributions are considered, including also the exergy of water, metals, minerals and so forth. For instance, in [7.7] Morris carried out

a CexC analysis of the chlor-alkali processes.

Some years later, Szargut proposed the concept of *thermoecological cost* [7.8]. The *thermoecological cost* (TEC) was defined as 'the cumulative consumption of *non-renewable* exergy burdening a given product, which is increased by a supplementary term accounting for the necessity to abate or compensate the negative effects of harmful wastes rejection to the environment [7.9]. In this approach, the contributions to TEC due to harmful wastes are divided in two fractions, which are related to: (i) neutralized wastes, which are considered by their so-called "*exergetic abatement cost*" and (ii) substances emitted directly into the environment, which are considered by a "*compensation cost*" based on monetary indices of harmfulness accounting for the external impacts. Some papers on TEC have been published during this decade. For instance, in [7.9] Szargut et al. evaluated the thermoecological cost of products connected with a blast-furnace process. In [7.10] Stanek et al. carried out an exergy and thermoecological analysis for different chillers. In [7.11], the thermogeological optimization of solar collector used for the generation of hot water was presented. The original Szargut's formulation of TEC analysis focuses only on the operational phase of a production plant. In order to evaluate a global impact of a considered production, in [7.12] Stanek supplemented the TEC approach with data resulting from LCA.

Kostowski et al. [7.13] proposed the integration of thermoeconomic analysis with the theory of thermoecological cost. The method aims to overcome one of the limits of thermoeconomic analysis, which usually does not consider the exergy used along the supply chain of the resources in input to a given process. This approach has been applied in order to evaluate the production of electricity in the process of natural gas transmission at pressure reduction stations [7.13], and also to the analysis of trigeneration systems fueled by fossil [7.10] and renewable energy sources [7.15]. In [7.16], the thermoecological analysis of nuclear power plant was carried out. In that paper, results showed the great influence of exergy consumption along the "uranium chain" (defined as the ensemble of processes involved from uranium extraction, up to

the delivery of the fuel to the power station) on the thermoecological cost of the electricity produced. Results were also compared to the thermoecological cost of coal power plant.

7.1.2 Exergoenvironmental Analysis

Meyer et al. [7.17] proposed the *Exergoenvironmental Analysis* as a tool for allocating environmental impacts on products in energy systems. Like Thermoeconomics, this method rests on the assumption that exergy of heat/mass flows is a rational basis to allocate environmental impacts. In order to allocate impacts on the exergy flows exiting a component, "*environmental impact balances*" are set, imposing that the sum of the environmental impacts of output streams equals the sum of impacts of input streams plus the component-related impacts (which account for the construction, maintenance and disposal of the component). The environmental impacts can be estimated by a preliminary materials inventory and Life Cycle Assessment (LCA) and a successive evaluation of a "single aggregated indicator" (the Eco-indicator 99 assessment method has been extensively adopted so far). This is a key-aspect for the practical application of exergoenvironmental analysis: due to the need to allocate environmental impacts to exergy flows and easily define exergoenvironmental cost balances, the heterogeneous impacts obtained by an "exposure and effect analysis" (e.g. eutrophication, ionization radiation, carcinogenesis, etc.) must be preliminarily a*ggregated* into a single indicator. The results of an exergoenvironmental analysis and the value of ad-hoc indicators like the *exergoenvironmental factor* allow the analyst for assessing whether the environmental performance of a component is mostly affected by its thermodynamic inefficiencies or by impacts generated during its manufacturing and disposal. Morosuk et al. [7.18] performed an exergoenvironmental analysis at component level for a vapor-compression refrigeration machine with a closed compressor and identified (a) the

relative contribution of each component to the total environmental impact and (b) options for reducing the environmental impact associated with the overall system. The paper provided results in terms of single aggregated indicators: eco-indicator 95, eco-indicator 99 and cumulative exergy consumption index.

7.1.3 Exergy Life Cycle Assessment

The *Exergy Life Cycle Assessment* (ELCA) was proposed by Cornelissen in 1997 [7.19]. This method represents an extension of cumulative exergy consumption for the entire life cycle of the system. ELCA assumes the "*global exergy destruction"* as an indicator of the *environmental cost*, and it computes the use of materials and energy over the entire life cycle of a system, including operation and dismantling. However, labor and capital externalities are not included in this method.

A refinement of ELCA was proposed by Rocco et al. [7.20] which integrates the *Input-Output* analysis as an analytical framework to model the supply chain of resources for a system operating in a given national economy. The method structured a basis for comparison of similar products output by different systems operating in the same context. In [7.21], the method was applied to an existing Waste-to-Energy Plant operating in the Italian context and the non-renewable exergy embodied in the electric output was assessed.

7.1.4 Extended Exergy Analysis (EEA)

The *Extended Exergy Analysis* (EEA) has been developed by Sciubba since 1998 [7.22]. The attribute "extended" is a reminder that the resulting product cost includes materials, energy and externalities, and that the calculation is done along the whole life cycle of the system. This method tries to join the features of the previously mentioned exergy-based methods, but at the same time to account for labor and capital

externalities, since they represent primary resource flows in input to the system. More specifically, EEA uses exergy as a quantifier of the amount of resource consumed by a system. This method calculates the exergy equivalents of human labor and capital fluxes based on two postulates, thus allowing to include them (as homogeneous terms) in the evaluation of a cumulative primary exergy "embodied" in a product over its entire production process (in a life cycle perspective). EEA also provides a rigorous definition of the spatial and time domains used to calculate equivalent primary exergy of a process. Hence, EEA someway addresses one of the main criticisms raised by economists on these methods, which is related to the strict dependence of costs, in real worlds applications, on location and time. EEA has been successfully applied in different sectors, allowing to perform articulate sustainability studies even at a societal level [7.23].

7.2 Fundamentals of the integrated approach based on Thermoeconomics and Life Cycle Assessment

The previous literature overview highlights that several comprehensive approaches have attempted to integrate Life Cycle Assessment and exergoeconomic analysis. Most of these methods, however, consider the environmental dimension of the problem by highly simplified approaches, based on a preliminary assessment of environmental externalities and a successive reduction of the results by adopting for the different impacts a same metrics. Such an approach, while having benefits in terms of computational efficiency and potential to provide easy-to-interpret results (a clear optimal solution may often be identified), on the other hand provides the policy or decision maker with only a *limited set of indicators*, which may also depend upon some more or less arbitrary assumptions.

The integrated approach based on LCA and Thermoeconomics is a novel approach centered around the performance assessment of energy conversion systems, focusing

on both the thermodynamic aspects of the process and on the impacts related to the use of energy and materials. The idea behind this approach is that assessing the performance of an energy system through a single or a limited number of environmental indicators (assessed through weighting several more specific ones) may be scarcely effective. If the effect of the system design is to be evaluated, a comprehensive set of results calculated along the entire life cycle of the system could reveal very precious, allowing to detect trade-offs between contrasting effects that would remain "hidden" when using methodologies based on a single aggregate indicator. When assessing the performance of the system from a Life Cycle perspective, the different impacts in terms of toxicity, health hazards, raw materials use, etc. should be individually identifiable. Then the proposed approach, while renouncing to provide a few synthetic performance indicators, is aimed at offering to the analyst a detailed set of results about the individual energo-environmental aspects to be considered.

Though it could be argued that such a complete set of data might be difficult-to-interpret for non-expert analysts, it might conversely allow for keener insights during the optimization or the energo-environmental assessment of energy systems. The proposed approach will also allow for higher transparency and traceability of results, based on the use of a wide range of indicators that will not be aggregated.

Obviously, this approach should be implemented through an adequate compromise between computational time requirements, effectiveness of the decision support model and simplicity of use for the decision-maker.

The approach is targeted at a wide number of problems (such as optimization) where aspects related to both the primary energy consumption and the environmental impacts are to be kept simultaneously into account. In such cases, multi-objective optimization is often performed in order to identify the configuration that best fits with the desired objectives. However, the use of Pareto frontiers is of limited effectiveness

whenever the analysis is expected to account for a large number of objectives (not being limited to energy consumption and CO_2 emissions, but including different environmental impacts). In this paragraph the fundamentals of the integrated methodologies are briefly presented, clarifying the different contributions that Thermoeconomics (and in particular, the exergetic cost accounting) and LCA provide to the energy analysts.

7.2.1 Exergy Cost Theory: some complementary concepts

As shown in Chapter 1, the exergetic cost of a product is the amount of exergy consumed to obtain the give product according to a selected energy conversion system [7.24]. In particular, this cost is calculated based on a rigorous accounting of all the exergy destructions involved along the energy conversion process. The more inefficient the components that generate the stream, the higher the amount of irreversibility "charged" on it and, consequently, its exergetic cost. Since, all details about exergy cost calculation have been provided in Chapter 1, only an additional concept is here introduced.

The "unit exergetic cost" k_P^* does not discriminate whether the exergy consumption involves exploitation of renewable or non-renewable sources. Then, when analyzing an energy system, it is often useful (as already stated in literature) to account separately for the amount of non-renewable exergy resources consumed to produce the desired output. To this purpose, it is necessary to extend the boundary of the examined system, in order to include the external processes that contribute to supply exergy to the examined energy system.

Typical examples may be represented by systems, such as refrigeration plants, which consume electricity that may have been generated by a mix of technologies comprising both fossil-fueled power plants and renewable energy systems. After having identified the mix of technologies contributing to power generation in a specific

site where the plant is located, it is possible to define $\kappa_{NR,i}$ as the amount of non-renewable exergy consumed per unit of external exergy supplied (in the form of electricity) to the examined system; then, multiplying the unit exergy cost of the product $k^*_{P,i}$ of a generic "i-th component" by $\kappa_{NR,i}$ a modified unit exergetic cost is obtained, i.e. $k^*_{NR,i}$, which expresses the amount of non-renewable exergy consumed per unit product.

7.2.2 Insights into Life Cycle Assessment (LCA)

A large number of methods and indicators to quantify sustainability have been developed in the last decades; they differ in terms of shape, applications, rationale and mathematics behind the calculations. The risk is, usually, to make decisions about sustainable development without considering their effects on the broad consumption and production systems.

The quantification of the sustainability of a product/service needs to be examined throughout its whole life cycle, also including the upstream and downstream processes associated with the production (e.g. production of raw, auxiliary and operating materials) and with the disposal (e.g. waste treatment). Environmental impacts refer to all relevant extractions from the environment (e.g. ores and crude oil), as well as emissions into the same (e.g. wastes and carbon dioxide).

In this context, environmental sustainability can be quantified on a life cycle thinking-based approach by using the Life Cycle Assessment (LCA). LCA evaluates all stages of a product's life from the assumption that they are interdependent, meaning that one operation leads to the next. LCA enables the analyst to estimate the cumulative environmental impacts resulting from all stages in the product life cycle, and it is effective in both the analysis of environmental performance of a single product through a careful eco-design (by identifying the hot-spots in the life cycle of the product) or as

a metric of sustainability to perform design choices or choose between different alternatives.

The LCA methodology was developed in the last decades starting from product-oriented methods used to evaluate environmental impacts in a bigger framework oriented towards the environmental, economic, and social perspectives. At the current stage, LCA is being included into Life Cycle Sustainability Assessment (LCSA), first developed by Kloeppfer [7.25] and Finkbeiner et al. [7.26], which links the sustainability questions – including the environment, cost and social dimension – to the knowledge and research needed to address them.

LCA is based on linear equations, energy and mass balances. It is a compilation and evaluation of the inputs, outputs and the potential environmental impacts of a product or a service throughout its life cycle.

Due to its holistic, systemic and rigorous nature, environmental attributional LCA is the preferred technique when it comes to compiling and assessing information about potential environmental impacts of a product. It has been standardized in ISO 14040 [7.27] and 14044 [7.28] and it is applied by practitioners globally. The ISO 14040 series provides a technically rigorous framework for carrying out environmental LCAs.

LCA consists of four steps, briefly described in the following paragraph.

The *goal and scope*, including the system boundary and level of detail, of an LCA depends on the subject and the intended use of the study. The depth and the breadth of LCA can differ considerably depending on the goal of a particular LCA.

The *life cycle inventory analysis* (LCI phase) is the second phase of LCA. It is an inventory of input/output data with regard to the system being studied. It involves collection of the data necessary to meet the goals of the defined study

The *life cycle impact assessment* (LCIA) [7.29] is the third phase of the LCA. The purpose of LCIA is to provide additional information to help in assessing a product system's LCI results and better understand their environmental significance.

Life cycle interpretation is the final phase of the LCA procedure, in which the results of an LCI or an LCIA, or both, are summarized and discussed as a basis for conclusions, recommendations and decision-making in accordance with the goal and scope definition.

7.3 Description of the reference water-cooled chiller and basic assumptions for the combined application of Thermoeconomics and LCA

A 315-kW water-cooled vapour compression chiller is used as reference case in this chapter; the examined chiller uses R410A as refrigerant and produces chilled water at 7°C supplied to an air handling unit for air conditioning. A simplified physical scheme is shown in Figure 7.1

Due to the large cooling capacity, two independent refrigerant circuits are used to allow for an efficient capacity control during low load periods and to increase system reliability.

Brazed plate heat exchangers are used as condenser and evaporator. Details about the technical features of these components are provided in Table 7.1. The condenser discharges the heat released by the refrigerant into a cooling water flow, which increases its temperature from 30°C to 35°C. Also, the condenser is equipped with an induced-draft cooling tower, where water is cooled down by an external air flow. The cooling tower was selected based on the required capacity and the aforementioned 30-35°C temperature range. Details on this component are also provided in Table 1. Each refrigerant circuit is equipped with two scroll compressors with a 345 cm^3 displacement each and with Electronic Expansion Valves (EEV).

The cooling load profiles of the user have been calculated for a large office building in a Mediterranean area (based on aggregated consumption data) [7.30]. The annual peak of cooling load is slightly lower than 315 kW, while substantial load fluctuations were observed on a seasonal basis. Further details on the cooling load profiles are omitted, for the sake of brevity and since they are outside the methodological scopes of the study.

In order to meet a variable cooling demand, a thermostatic control for the compressor is adopted: in this case, matching between chiller capacity and cooling load is achieved by adjusting the "on" and "off" cycling time of the compressor.

Simulations were carried out by means of the plant simulator IMST-ART v. 3.40 [7.31], which adopts a finite volume discretization to solve momentum conservation and heat transfer equation for both the refrigerant and water flows. The tool allowed to simulate the dual circuit system for both evaporator and condenser. Assessments on compressor consumption and efficiency were carried out through the "*catalogue data*" option, which converts data from compressor catalogues into efficiency and consumption curves already implemented within the software. About the metering device, a 3°C superheat value at the evaporator outlet was fixed for the simulation. This condition does not differ from the actual operating mode of this system, due to the effective superheat control achieved by means of EEVs [7.32]. In Table 7.2 the main thermodynamic parameters obtained by plant simulation are shown.

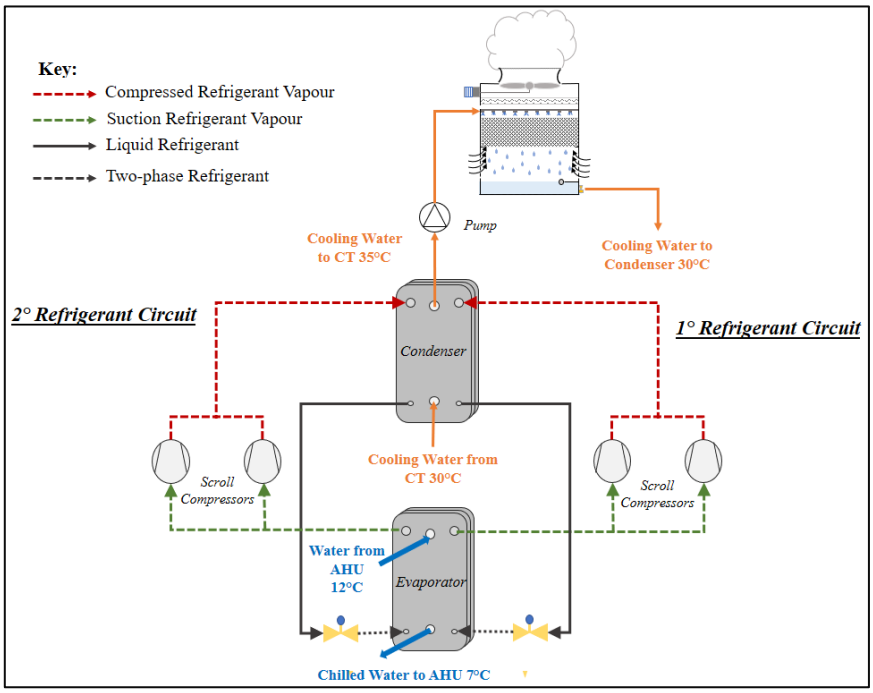

Figure 7.1 *Physical Scheme of the examined-vapor compression chiller*

Table 7.1 *Main physical data for plant equipment*

	Units	***Condenser***	***Evaporator***
Number of Plates		206	186
Inlet port size (Refrigerant Side)	mm	50	25
Outlet port size (Refrigerant Side)	mm	25	50
Inlet port size (Water Side)	mm	70	70
Outlet port size (Water Side)	mm	70	70
Channel Volume	dm^3	0.41	0.41
Heat Transfer Area	m^2	18.58	16.75
Flow Arrangement		Counter-current	Counter-current
	Units	***Cooling tower***	
Type		Induced Draft Counter-flow	
Number of Fan		2	
Fan Motor	kW	(2) 2.2	
Air Flowrate	m^3/h	11.3	
Water Flowrate	l/s	18	
Water Usage (make up water)	m^3/h	0.8	
Height	mm	2908	
Length	mm	2237	
Width	mm	1226	
Weight	kg	950	

Table 7.2 *Main Thermodynamic data for the Base Case Design*

	Units	
T_{evap}	°C	2.5
T_{cond}	°C	40.8
ΔT_{Sub}	°C	2.4
T_{disch}	°C	64.4
Refrigerant flow rate	kg/s	1.93
Cooling Capacity	kW	315
EER	W/W	4.62

7.4 On the productive structure adopted for thermoeconomic analysis of the chiller

The productive structure of the chiller, i.e. the representation depicting the functional interactions (in terms of exergy flows) between plant components, is shown in Figure 7.2. The condenser and the cooling tower were considered as a unique functional component since both these units contribute to the same objective, that is the discharge of thermal exergy to the surrounding environment. Then, these units can be considered, from a functional viewpoint, as a unique "dissipative" component.

In Figure 7.2, for the sake of clarity the physical exergy of refrigerant is split into a *thermal fraction*, indicated as ΔB_i^T (see red dashed lines), and a *mechanical fraction*, indicated as ΔB_i^P (see blue dashed lines). These exergy fractions are respectively related to "thermal" and "mechanical" disequilibrium between the refrigerant state and the reference environmental state [7.33]. By splitting exergy flows into these two fractions, a more accurate definition of the consumed resources and the productive purpose of each plant component can be provided. For instance, it may be observed that the compressor "produces" mechanical exergy (transferred to the fluid and related to the increase in refrigerant pressure) which is mostly consumed as a fuel in the EEV, where it is partially converted (with high exergy destruction) into thermal exergy of the low-quality/low-temperature refrigerant supplied to the evaporator. The residue

generated by the condenser and the cooling tower was allocated on the compressor and the EEV according to criteria provided in [7.34].

The reference state adopted for exergy calculations was T_0=303.15 K and p_0=101.325 kPa. All the thermo-physical properties of refrigerant and external fluids were calculated by built-in functions available in *Engineering Equation Solver* library [7.35].

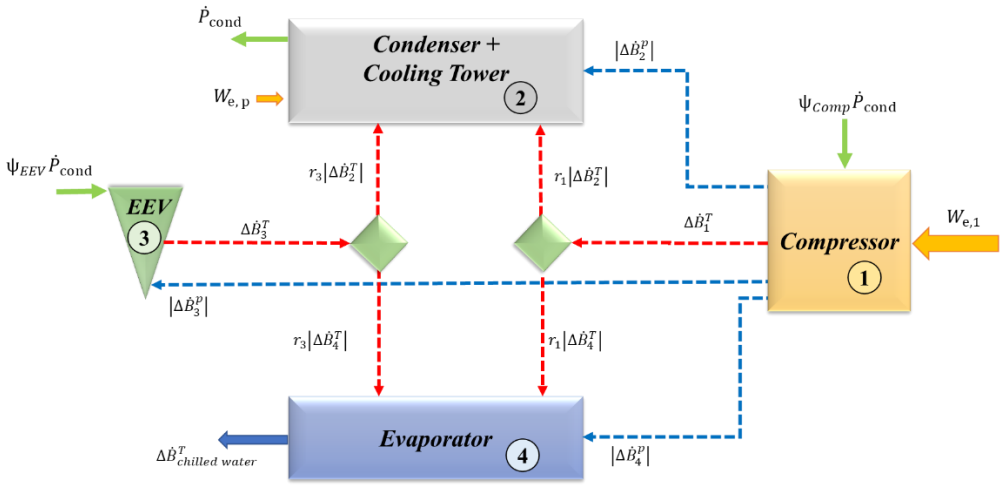

Figure 7.2 *Productive Structure of the examined-vapor compression chiller*

7.5 Life Cycle Assessment assumptions and bill of materials

For the examined case study, Life Cycle Assessment was developed in accordance to the international standards of series ISO 14040 [7.27]. The goal of LCA is to assess the energy and environmental impacts of the chiller along its life-cycle. The functional unit (FU) selected for the study is the cooling of a large office building (with a 315 kW_c demand peak) for 20 years.

The system boundaries include the following steps:

- Raw materials and energy supply;
- Transportation of raw materials;

- Transportation of systems' components from their production site to the installation site;
- Use phase;
- Maintenance and substitution of systems components.

The life cycle steps of "construction and installation" and "end of life" have not been considered due to a lack of quantitative information. The following impact categories have been used to calculate the energo-environmental performances of the FU:

- Acidification, accumulated exceedance [Mole of $H^+_{eq.}$]
- Ecotoxicity for aquatic fresh water, USEtox (recommended) [CTU_e]
- Freshwater eutrophication, EUTREND model, ReCiPe [kg P_{eq}]
- Human toxicity cancer effects, USEtox (recommended) [CTUh]
- Human toxicity non-canc. effects, USEtox (recommended) [CTUh]
- Ionising radiation, human health effect model, ReCiPe [kg $U235_{eq}$]
- IPCC global warming, excl biogenic carbon [kg $CO_{2\text{-}eq.}$]
- IPCC global warming, incl biogenic carbon [kg $CO_{2\text{-}eq.}$]
- Marine eutrophication, EUTREND model, ReCiPe [kg $N_{\text{-}eq.}$]
- Ozone depletion, WMO model, ReCiPe [kg $CFC_{\text{-}11\ eq}$]
- Particulate matter/Respiratory inorganics, RiskPoll [kg $PM2{,}5_{\text{-}eq.}$]
- Photochemical ozone formation, LOTOS-EUROS model, ReCiPe [kg $NMVOC_{eq}$]
- Resource Depletion, fossil and mineral, reserve Based, CML2002 [kg $Sb\text{-}_{eq.}$]
- Terrestrial eutrophication, accumulated exceedance [Mole of $N_{eq.}$]
- Total freshwater consumption, including rainwater, Swiss Ecoscarcity [UBP];
- Primary energy [MJ].

The characterization factors for the Primary energy calculations are based on the Cumulative Energy Demand method [7.36], which provides an estimation of the consumption of renewable (biomass, wind, solar, geothermal, water) and non-renewable (fossil, nuclear) energy sources. The environmental characterization factors are derived from the ILCD 2011 impact assessment method [7.37]-[7.38].

The indicators used here are from the ILCD/PEF recommendation from [7.39], included as part of the product environmental footprint (PEF) development. However, it is worth mentioning that the chemical-related midpoint level impact categories addressing human toxicity and ecotoxicity are accompanied by considerably larger uncertainties than the energy-conversion related midpoint level categories addressing e.g. acidification, photochemical ozone formation or global warming impacts. The data collection process involved the units reported in Table 3.1, including the individual components of each equipment and details on the mass and production site

***Table 3.1**. Bill of materials of the system investigated*

	Component	**Mass** (kg)	**Production Site**
Evaporator	Stainless steel	128.8	China
Compressor	Copper	23.9	USA
	Carbon Steel	135.2	
	Oil	6.7	
Plate heat exchanger (condenser)	Stainless steel	141.4	China
Refrigerant	R410A	18	USA
Liquid line pipes	Copper	1.96	Italy
Suction line pipes	Copper	2.7	Italy
Discharge line pipes	Copper	5.52	Italy
Cooling tower	Galvanized steel	770	Italy
	Copper	6	
	Carbon Steel	34	
	Aluminum	40	
	PVC	100	
Pumps	Copper	8.7	China
	Aluminium	49.3	
	Cast Iron	54	
Electronic expansion valve	Brass	1.5	Slovenia
Filter drier	Stainless steel	1.45	Slovenia
	Molecular sieve	1.27	

The eco-profiles of materials and energy sources are derived from [7.36]. In the present study a useful life of 20 years is estimated, with an annual electricity consumption of 62.8 MWh_e. The maintenance phase includes two annual drier filter substitutions for each refrigerant circuit.

7.6 Definition of a set of alternative scenarios to clarify the potential of the integrated TEC-LCA approach

The integrated use of Thermoeconomics and LCA attempts to provide a comprehensive view of the energo-environmental impacts of an energy system, thus representing a useful support to decision making in both the plant design and operation phases. To point out the potential of the method, a set of alternative scenarios will be analyzed, which may be classified as follows:

- Scenarios based on modified plant designs;
- Scenarios based on alternative context conditions (in terms of mix of technologies contributing to electricity generation);
- Scenarios based on different levels of accuracy of the maintenance programs (with a particular focus on the detection of refrigerant leakages).

7.6.1 Scenarios based on modified plant designs

The detailed plant design presented in the previous section is a possible set of well-balanced components able to ensure an efficient plant operation. However, each of the aforementioned design variables represents a potential parameter to be optimized in order to improve the energo-environmental performance of the system.

The scope of the analysis can be clarified by a simple example. Let us consider the size of the condenser as a variable to be optimized: a larger unit, while contributing to

reduce the condensing pressure and increase the plant efficiency (thus leading to lower energy consumptions), on the other hand it would cause a higher use of raw materials and a consequent higher amount of energy and emissions "embodied" in the materials. Obviously, whatever the objective function assumed, the optimal size will result from a trade-off between these opposite effects. Such a problem can be efficiently analyzed by the proposed integrated approach.

A number of scenarios are defined, each one implying a specific change in the design of one component compared to the base case, assumed here as a reference. For each scenario, accurate bills of materials were estimated under the following assumptions:

- *Scenario 1- Undersized condenser*: the condenser is undersized by reducing its heat transfer area by 7.5% compared to the base case. A higher condensing pressure and a decrease of chiller Energy Efficiency Ratio (EER) value may be expected. The bill of materials revealed a reduction by about 23.1% in galvanized steel use for condenser construction, compared to the base case;
- *Scenario 2 - Oversized condenser*: the condenser is oversized by increasing its heat transfer area by 7.5% compared to the base case (symmetric change to the previous scenario). A lower condensing pressure may be expected, as well as an increase in the chiller EER. In this scenario, the galvanized steel required in the construction phase is 57% higher than in the base case;
- *Scenario 3- Undersized evaporator:* the evaporator is assumed to be slightly undersized, compared to the base case. The size reduction was calculated by imposing a limited reduction in the chiller capacity (from 315 kW to 306 kW, which will result in slightly prolonged "on cycles" during cooling load peak hours). A lower evaporating pressure and a decrease in the EER are expected to be the main deviations in the system performance. In this scenario, the

galvanized steel required in the construction phase is 31% lower than in the base case.

- *Scenario 4- Undersized cooling tower:* in this case a reduced capacity of the cooling tower was assumed, expected to result in a higher condensing pressure (as a consequence of the higher temperature of cooling water) and a lower EER. The bill of materials for the undersized cooling tower showed, for the different materials, a weight reduction ranging between 20 and 40% compared to the base case, and in particular included: 590 kg of galvanized steel, 4 kg of copper, 21 kg of carbon steel, 20 kg of aluminum, 55 kg of PVC.

Accurate simulations of plant operation were performed for each alternative design by IMST-ART. Thermodynamic results are shown in Table 7.4. From a comparison with the results presented in Table 7.2 for the base case, it may be observed that any change in the design of the chiller slightly affects its capacity (with variations ranging from -2.8% to +0.9%), but it has a higher impact on the EER values (which decreased, in scenario 3, by 5.9% compared to the base case) due to the relevant changes in the refrigerant thermodynamic cycle.

Table 7.4*. Thermodynamic data for all the examined scenarios based on modified plant design*

	Units	***Undersized Condenser***	***Oversized Condenser***	***Undersized Evaporator***	***Undersized Cooling Tower***
T_{evap}	°C	2.5	2.6	1.6	2.6
T_{cond}	°C	41.3	40.3	41.3	42.0
ΔT_{Sub}	°C	1.9	1.2	5.5	2.6
T_{disch}	°C	65.3	63.7	66.3	67.2
Refrigerant Flowrate	kg/s	1.93	1.93	1.82	1.93
Cooling Capacity	kW	318	314	306	310
EER	W/W	4.59	4.64	4.44	4.35

7.6.2 Scenarios based on different mixes of technologies contributing to electricity generation

As clarified in the previous sections, the mix of sources and technologies that generates the exergy flow (electricity, in the examined case study) supplied to the plant as an "external input" highly influences the overall exergo-environmental profile of the plant and, also, the optimal trade-offs between energy consumption/environmental impacts/costs respectively tied to thermodynamic inefficiencies in plant operation and in the other stages of the life cycle. Then, it is worth discussing the contribution of the proposed approach in highlighting how these trade-offs vary when different context conditions are considered. In the case study, since the water chiller is driven by electricity, two different scenarios are considered to assess the sensitivity of results to the electricity generation mix:

- *Scenario A*: the Italian grid energy mix was assumed. More specifically, based on data available from [7.40] for 2015, the following shares to electricity generation were considered: 45% natural gas (NG, consumed in combined cycle power plants), 15% coal, 8% oil, 32% from renewable energy sources (RES).
- *Scenario B:* electricity is only supplied by renewable energy technologies (i.e. this is a so-called 100% RES penetration scenario). In particular, 100% electricity generation by means of photovoltaic technology was assumed (such an assumption is reasonable due to the fact that the office requires air-conditioning and consumes electricity only during daytime).

Due to the use of a fraction of non-renewable exergy, a non-null value of κ_{NR} can be calculated for Scenario A:

$$\kappa_{NR}^{ScenarioA} = \frac{f_{CC}\ \dot{E}_{el}}{\eta_{ex,CC}} + \frac{f_{coal}\ \dot{E}_{el}}{\eta_{ex,Coal}} + \frac{f_{oil}\ \dot{E}_{el}}{\eta_{ex,oil}} = \frac{0.45}{0.5} + \frac{0.15}{0.4} + \frac{0.08}{0.4} \approx 1.48 \qquad (7.1)$$

In Equation (7.1) the factors $f_{\substack{CC \\ plant}}$, $f_{\substack{coal \\ plant}}$ and $f_{\substack{oil \\ plant}}$ indicate the share of contribution to the electricity production respectively by natural gas fuelled combined cycles (CC), coal-fuelled and oil-fuelled steam power plant. Also, average exergetic efficiencies equal to 50% for the combined cycle technology and to 40% for steam power plants (regardless of the consumed fuel, either coal or fuel oil) [7.41] were considered. According to these values, κ_{NR} is equal to 1.48 kW_{ex}/kW_{ex}, that means that 1 kWh of "electric" exergy is responsible for an average 1.48 kWh consumption of non-renewable primary exergy.

Conversely, when referring to Scenario B, due to the absence of fossil fuel in the mix of electricity generation, no consumption of non-renewable exergy is traceable, thus a null value for κ_{NR} was assumed below in the analysis.

7.6.3 Scenarios based on different levels of accuracy of the maintenance programs

It is also worth discussing the potential of the proposed approach in highlighting the effects of maintenance and troubleshooting programs during the chiller lifetime. In particular, the effects of one of the most frequent "faults" experienced by refrigeration systems, i.e. the refrigerant charge loss, on the exergo-environmental profile of the plant is investigated. Two environmental issues are commonly related to refrigerant leakages:

- an increase in the exergy consumption caused by the degradation of the Energy Efficiency Ratio in case of refrigerant undercharge, compared to the "ideal charge" condition, if an appropriate maintenance program has not been adopted to restore refrigerant charge to its nominal value. Also, when considering a fossil fuel-based electricity generation mix, this lower EER implies an increased consumption of non-renewable exergy sources;

- an increase in the total GHG emissions [7.42], mainly due to the refrigerant dispersion into the environment and the indirect impact related to the increased electricity consumption. The former of these contributions may be prevalent, under specific operating conditions, due to the very high Global Warming Potential (GWP) of the examined refrigerant.

The analysis was carried out by comparing the exergo-environmental profiles for a system with an "ideal maintenance program", where no refrigerant leakage occurs during plant lifetime, and for a case of "poorly maintained chiller", where an average refrigerant loss equal to 540 g/year (i.e. 3% of total chiller refrigerant charge) was assumed. The former scenario is assumed to represent the reference "base case" in the following paragraph. In Table 7.5, results obtained from accurate plant simulations for the reference case and the "poorly maintained" chiller are presented.

***Table 7.5**. Thermodynamic data for the two examined maintenance scenarios*

	Units	***Ideally Maintained System***	***Poorly maintained System***
T_{evap}	°C	2.5	2.5
T_{cond}	°C	40.8	40.5
ΔT_{Sub}	°C	2.4	1.31
T_{disch}	°C	64.4	64.10
Refrigerant Flowrate	kg/s	1.93	1.93
Cooling Capacity	kW	315	313
EER	W/W	4.62	4.60

7.7 Results and discussion

Below in this section the results are presented for the "Base Case" design and the alternative scenarios previously defined. For a clearer presentation, the section is structured into subsections, each one focusing on a specific scenario.

7.7.1 Application of the Integrated approach to the "Base Case" design

In this section, the results achieved by the integrated TEC-LCA approach are presented for the *Base Case* design. The analysis has been carried out by assuming "Scenario A" as a reference for electricity generation and an "ideal maintenance". Table 7.6 shows LCA results with regards to the base case.

Table 7.6*. Life cycle impacts of Water-Cooled Chiller for the "Base Case Design" when consumed electricity is supplied by the Italian Energy generation mix*

	Units	*Values*
Acidification	Mole of $H_{+\ eq.}$	7.93E+03
Ecotoxicity for aquatic fresh water	CTUe	8.12E+04
Freshwater eutrophication	kg $P_{\ eq}$	3.99E+00
Human toxicity cancer effects	CTUh	3.29E-03
Human toxicity non-canc. effects	CTUh	3.49E-02
Ionising radiation, human health effect model	kg U235 $_{eq}$	8.79E+04
IPCC global warming, excl biogenic carbon	kg CO_{2eq}	2.95E+06
IPCC global warming, incl biogenic carbon	kg $CO_{2\ eq}$	2.93E+06
Marine eutrophication	kg $N_{\text{-Equiv.}}$	8.44E+01
Ozone depletion	kg $CFC_{\text{-11 eq}}$	1.87E-01
Particulate matter/Respiratory inorganics	kg $PM2{,}5_{\text{Equiv.}}$	2.85E+02
Photochemical ozone formation	kg NMVOC	6.00E+03
Resource Depletion, fossil and mineral	kg Sb-Equiv.	3.41E+00
Terrestrial eutrophication	Mole of $N_{\ eq.}$	2.24E+04
Total freshwater consumption	UBP	2.53E+06
Primary energy demand from renewable and non-renewable resources	MJ	4.84E+07

Figure 7.3 reports the relative share of the construction and use step on the total environmental impacts. The results identify a complex profile where some impacts are mainly due to the use phase (particulate matter emissions, primary energy, freshwater consumption, marine eutrophication, human toxicity non-cancer effects), being prevalently related to the high energy use during plant operation. Conversely, other indicators show a primary relevance of the construction step, with shares higher than 91% (e.g. ozone depletion, ionizing radiation). All other indicators exhibit an

intermediate trend, where both the above phases influence the impact, although a higher share of impacts caused by the use step can be often observed (see the 61.47% contribution of Terrestrial eutrophication and the 86% contribution in the case of Global Warming).

For the sake of completeness, when analyzing the total impacts related to the construction phase, the exergy of materials should be also accounted for. Indeed, according to Szargut [7.9] any material element (or compound) with a given composition and concentration has chemical exergy, which is defined as the minimum work needed to produce it from common substances available in the reference environment (for instance the earth's crust, seawater or atmospheric air). To this aim, in Szargut [7.98] and in Rivero [7.43] the reference environment and the reference chemical reactions for each compound were defined. In this study, the standard chemical exergy of materials was derived from the *Exergoecology Portal* [7.44], where it is calculated on the basis of the exergy balance of formation reaction:

$$b_{comp}^{ch} = \Delta G_f + \sum b_{el}^{ch} n_{el} \qquad (7.2)$$

In Equation (7.2) b_{comp}^{ch} is the chemical exergy of the material or compound, ΔG_f its formation Gibbs energy, n_{el} the number of mole of the element "el" and b_{el}^{ch} its standard chemical exergy (values tabulated in [7.8]).

Chemical exergy was calculated for some of the materials presented in Table 7.3, and in particular for steel, aluminum and copper. Based on the unit exergy per mol of materials and the mass of these elements, the following total chemical exergy of materials embodied in the system were calculated: 2.27 MWh_{ex} for steel, 0.73 MWh_{ex} for aluminum and 0.03 MWh_{ex} for copper. However, this contribution is neglected for two main reasons:

a. Considering an annual electric exergy consumption equal to 62.8 MWh_e/y and a useful life of the system of 15 years, it may be easily assessed that the exergy

embodied in materials accounts approximately for 0.4% of the exergy involved during the operational phase. Then, the exergy of materials can be excluded with negligible error;

b. As clarified in the previous sections, the proposed combined approach exploits the capability of Thermoeconomics only with the aim to analyze the plant performance during the operation phase, while standard LCA is adopted in parallel to evaluate a wide set of environmental impacts. Then, the proposed approach does not represent an Exergy Life Cycle Assessment, where the exergy of materials and the external assessment of exergy cost of inputs should have been necessarily included.

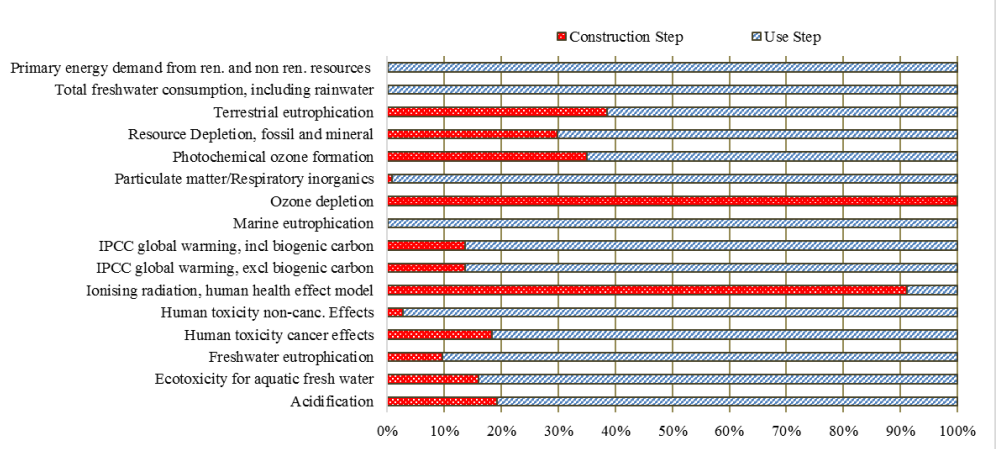

Figure 7.3 *Incidence of construction step and use period on the life cycle impacts for the "Base Case" design when assuming Scenario A for electricity generation*

Since the use phase has been proven to contribute significantly to the environmental impacts of the system, actions aimed at reducing energy consumption during chiller operation may lead to an improvement of the exergo-environmental profile of the system. By means of exergetic cost accounting an accurate and comprehensive view of the energy conversion process may be acquired, thus assessing

to which extent each subprocess contributes to the total exergy consumption of the system.

Table 7.3 shows the results of the exergetic cost accounting performed for the base case, providing, for each component, the exergy flows representing its Fuel (*F*), Product (*P*) or generated Residue (*R*). Also, the same table includes the values of the specific exergy consumption k_i (i.e. the inverse of exergy efficiency), the Exergetic unit cost k_i^* and the non-renewable specific exergy consumption $k_{NR,i}^*$. The physical significance of $k_{NR,i}^*$ can be easily explained: for a generic "i-th"component, it is calculated by multiplying the unit exergetic cost k_i^* (i.e. electricity consumed per unit of exergy product of component "i-th") by the non-renewable exergy consumption per unit of electricity, κ_{NR} (equal to 1.48 kW_{ex}/kW_{ex} in scenario A assumed for the reference case). Then, $k_{NR,i}^*$ indicates the amount of non-renewable exergy consumed per unit of exergy product of component "i-th".

The results show that the unit exergetic cost of chilled water, i.e. k_4^* in Table 7.7, is heavily affected by the exergy destruction occurring within the evaporator, EEV and compressor, in a decreasing order of contribution. In fact, according to the proposed productive structure, the energy conversion process can be considered as "quasi-sequential" (although not in a strict sense, due to the presence of minor recirculating exergy flows): (i) the compressor consumes electricity to "generate" pressure exergy, (ii) the EEV consumes pressure exergy to "produce" thermal exergy, (iii) the evaporator consumes thermal exergy to produce the desired cooling effect. Then, each of the above three components contributes to increase the unit exergetic cost along the energy conversion chain, proportionally to its specific exergy consumption k_i (which is slightly higher for the evaporator, the least efficient component).

No cost values are provided for the "condenser + cooling tower" unit due to the dissipative nature of these components. About the exergy consumption of non-

renewable exergy sources, since a high share of fossil fuel was assumed for *Scenario A*, the amount of non-renewable exergy involved to produce a unit of exergy of chilled water (i.e. $k^*_{NR,4}$ value in Table 7.7) is equal to 4.595 kW_{ex}/kW_{ex}.

***Table 7.7**. Exergy Cost Accounting Results for the "Base Case" design assuming Scenario A as reference for electricity generation*

	Fuel	*Product*	*Residue*	k_i	k_i^*	$k^*_{NR,i}$
	(kW_{ex})			(kW_{ex} / kW_{ex})		
Compressor	68.35	57.22	4.34	1.195	1.224	1.811
Condenser/ Cooling Tower	17.88	14.95	-	-	-	-
EEV	42.61	32.40	10.61	1.312	2.685	3.974
Evaporator	32.10	22.95	-	1.399	3.104	4.595

7.7.2 Sensitivity analysis of exergo-environmental profile of the chiller

In this section the sensitivity of the exergo-environmental profile is investigated, applying the integrated TEC-LCA approach to the set of alternative scenarios presented in section 7.6. The following assumption is made: each examined combination of design, electricity generation mix and maintenance program accuracy will differ from the "reference case" by a single change. Then, for example, when attempting to assess the changes induced in the exergo-environmental profile by a reduced size of the condenser (Scenario 1), all the other design variables, the electricity generation mix and the accuracy of the maintenance program will be assumed coincident with those assumed in the reference case. Such an approach allows the analyst to isolate the effects of a specific change.

7.7.2.1 Application of the integrated approach to alternative design scenarios

Based on the results from plant simulations and additional bills of materials performed for the set of "alternative design" scenarios indicated as 1-4 in the previous section, thermoeconomic cost accounting and Life Cycle Assessment were carried out.

To allow for an easier analysis of the changes induced by each modified design, in Table 7.8 the variation of the unit exergy consumption, Δk_i, and the unit exergetic cost, Δk_i^*, with respect to the base case are directly provided. A simple comparison between the Δk_4^* values (indicating the variations in the unit exergetic cost of chilled water) allows the analyst to identify the alternative scenarios that induce exergy savings (for $\Delta k_4^* < 0$) or increased exergy consumption (for $\Delta k_4^* > 0$) during plant operation compared to the base case.

As expected, only the alternative scenario "*Oversized Condenser"* achieves a reduction in the external exergy consumption, due to the lower condensing pressure resulting from the increased heat transfer area. For all the other cases, the positive Δk_4^* values indicate that an increase in exergy consumption occurs, the highest impact being observed for the scenario that assumes an "*Undersized Cooling Tower"*.

In Figure 7.4, the non-renewable exergy consumption per unit exergy of chilled water is presented for all the examined scenarios. The values are coherent with the aforementioned Δk_4^* trends, but they provide a more intuitive perception of the impact of each examined design scenario. Of course, the exergoeconomic analysis could also provide further insights, thus allowing an expert analyst to formulate keener interpretations of the trends. For instance, for the "*Undersized evaporator*" scenario, it could be observed that:

- the compressor has only negligible variations in its exergy efficiency (as clear from the -0.024 variation in the unit exergy consumption), but it increases its production cost of "pressure exergy" as an obvious consequence of the lower suction pressure;
- the expansion valve benefits of the lower evaporating pressure, thus increasing its capability to convert pressure exergy into thermal exergy and decreasing the cost of the produced thermal exergy;

– the evaporator experiences a dramatic reduction in its exergy efficiency (see the 0.130 variation in its unit exergy consumption), ultimately being the main responsible for the decreased efficiency of the whole plant.

–

***Table 7.8**. Variation of Exergy Consumption, unit exergetic cost for Alternative Design Scenarios with respect to the "Base Case Design"*

	Undersized Condenser		***Oversized Condenser***		***Undersized Evaporator***		***Undersized Cooling Tower***	
	Δk_i (kW_{ex} /kW_{ex})	Δk_i^* (kW_{ex} /kW_{ex})	Δk_i (kW_{ex} /kW_{ex})	Δk_i^* (kW_{ex} /kW_{ex})	Δk_i (kW_{ex} /kW_{ex})	Δk_i^* (kW_{ex} /kW_{ex})	Δk_i (kW_{ex} /kW_{ex})	Δk_i^* (kW_{ex} /kW_{ex})
Compressor	0.001	0.173	-0.028	0.114	-0.024	0.129	-0.021	0.194
EEV	-0.011	-0.039	0.011	-0.148	-0.033	-0.170	0.044	0.166
Evaporator	0.022	0.078	0.020	-0.030	0.130	0.134	0.013	0.198

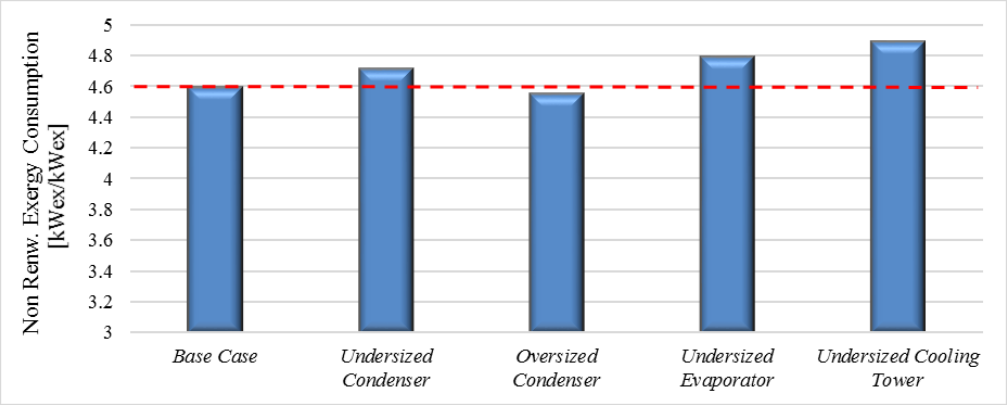

***Figure 7.4** Non-renewable exergy consumption for each alternative design scenario*

However, as previously clarified, the effects on the energy conversion efficiency induced by changes in plant design represent only one face of the medal, with the other one being related to the different impacts of the plant along its lifecycle. In fact, any

alternative design has a slightly different bill of materials and all the effects should be simultaneously accounted for, to identify possible trade-offs.

In Figure 7.5 detailed results of LCA study for the four "modified design" scenarios are shown. More specifically, by means of a radar diagram, percentage variations of each impact category with respect to the "Base Case" are shown. The presented impacts obviously include both the contributions related to the embodied energy and environmental impact of plant components and the environmental impacts related to plant operation.

The proposed diagram offers a complete picture of the exergo-environmental profile of the plant, thus allowing the analyst to objectively identify which modifications in chiller design are most promising from a lifecycle perspective.

It may be observed, for instance, that in spite of the lower amount of raw materials used in the "*Undersized Evaporator*" scenario, most of the impact indicators observe, for this scenario, a positive deviation from the base case (thus indicating an increase in the corresponding impact). This is explained by considering the degradation of plant efficiency provoked by the smaller evaporator size, which produces additional environmental impacts (due to the increased electricity consumption) that exceed the reduction in the "embodied" environmental impacts. Obviously, this result is highly influenced by the electricity generation mix (Scenario A) assumed as a reference for the base case.

On the other hand, among the examined cases the "*Oversized Condenser*" scenario is the most promising alternative from a life cycle perspective. Only for this case, slight negative percentage variations of impacts are observed with respect to the base case. This result again testifies that, based on the expected plant operation and the assumed electricity generation mix, the "use phase" impacts dominate compared to those related to the construction phase. In fact, though additional materials are required for a larger

condenser, the lower environmental burdens during plant operation offset the increase in environmental impacts of the construction phase.

It is worth noting that the above explained concept does not apply to all the cases. In fact, not only the generic change in the "amount of raw materials", but also the specific materials and the considered impact indicator should be considered. As an example, let us examine the ionizing radiation impact category: for this indicator, the "*Oversized Condenser*" is identified as the worst scenario. Conversely, improvements are observed for both the "*Undersized Evaporator*" (8% reduction compared to the base case) and "*Undersized Cooling Tower*" (2% reduction) due to the decreased use of steel and, for the latter scenario, aluminum and PVC.

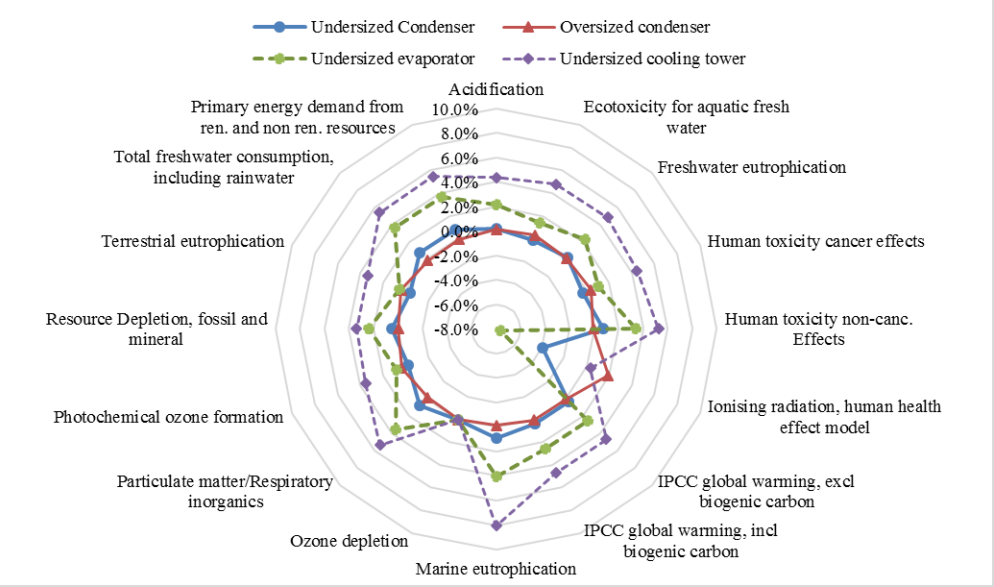

Figure 7.5 *LCA results for the alternative plant designs for Scenario A*

7.7.2.2 Exergo-environmental profile of "Base case design" for a different electricity generation mix

In this section, the influence of electricity generation mix on the exergo-environmental profile of the plant is assessed, referring to the base case design and assuming an ideal maintenance program. Before showing detailed LCA results for *Scenario B* (electricity generation by renewable sources), the incidence of each phase on the overall life cycle impacts is shown in Figure 7.6.

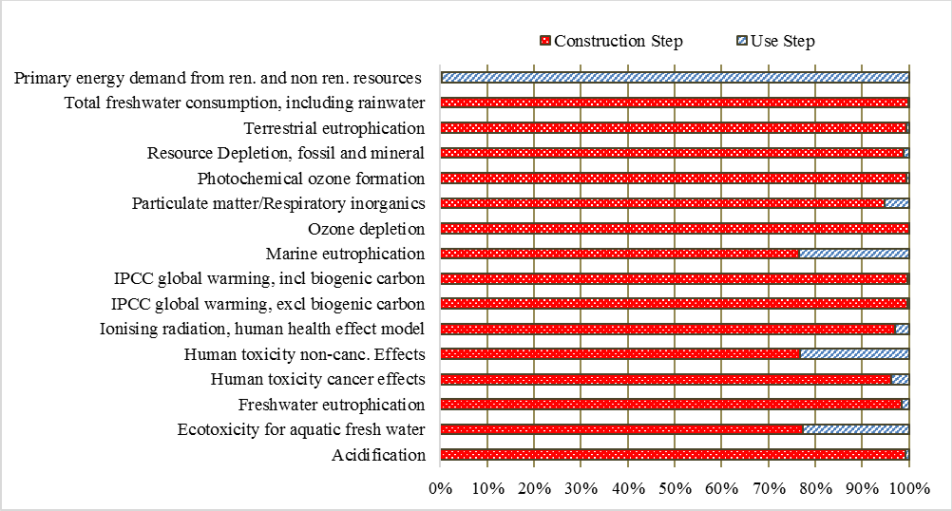

Figure 7.6. *Incidence of construction phase and use phase on the life cycle impacts for the "Base Case" design when assuming Scenario B for electricity generation*

Moving from the standard Italian generation mix (Scenario A) to a fully decarbonized one (Scenario B), the relevance of the paradigm shift hereby proposed is immediately evident: a fully decarbonized energy sector could largely reduce all the environmental impact categories. When comparing the results shown in Figures 7.3 and 7.6, it is possible to observe that when electricity is generated by RES, the construction phase impacts prevail with respect to those related to the use phase for almost all the examined indicators. In both scenarios the use phase is largely prevalent as regards the *Primary energy demand indicator* (at the representation scale the contribution of the construction phase cannot be even visualized), due to the large

capacity of the plant and its prolonged utilization throughout the space cooling season. In this case, differently from scenario A, only renewable exergy is consumed to drive the chiller, so that a null value for $k^{*}_{NR,i}$ is obtained. Table 7.9 presents detailed results for LCA analysis of the *base case* design when assuming scenario B for the electricity generation mix. In particular, the percentage variation for each impact category with respect to scenario A is presented. It may be observed that a reduction in environmental impacts occurs due to the substitution of fossil fuel with solar energy. Particularly, high benefits are traced for the indicators marine eutrophication, total freshwater consumption and particulate matter. Conversely, a negligible variation is observed for Ozone Depletion, which in the case at hand is mostly related to the construction phase of the system.

***Table 9**. Life cycle impacts of the Water-Cooled Chiller for the "Base Case Design" when consumed electricity is entirely supplied by photovoltaic system as assumed for Scenario B*

	Units	*Scenario B*	*Percentage variation with respect to Scenario A*
Acidification	Mole of $H_{+\ eq.}$	1.53E+03	-80.7%
Ecotoxicity for aquatic fresh water	CTUe	1.68E+04	-79.3%
Freshwater eutrophication	kg $P_{\ eq}$	3.94E-01	-90.1%
Human toxicity cancer effects	CTUh	6.29E-04	-80.9%
Human toxicity non-canc. effects	CTUh	1.23E-03	-96.5%
Ionising radiation, human health effect model	kg $U235_{\ eq}$	8.26E+04	-6.0%
IPCC global warming, excl biogenic carbon	kg CO_{2eq}	4.03E+05	-86.3%
IPCC global warming, incl biogenic carbon	kg $CO_{2\ eq}$	4.03E+05	-86.3%
Marine eutrophication	kg $N_{\text{-Equiv.}}$	1.16E-01	-99.9%
Ozone depletion	kg $CFC_{\text{-11 eq}}$	1.87E-01	0.0%
Particulate matter/Respiratory inorganics	kg $PM2{,}5_{\text{Equiv.}}$	2.73E+00	-99.0%
Photochemical ozone formation	kg NMVOC	2.12E+03	-64.7%
Resource Depletion, fossil and mineral	kg Sb-Equiv.	1.03E+00	-69.8%
Terrestrial eutrophication	Mole of $N_{\ eq.}$	8.67E+03	-61.3%
Total freshwater consumption	UBP	4.00E+03	-99.8%
Primary energy demand from renewable and non-renewable resources	MJ	1.75E+07	-63.9%

7.7.2.3 Effects of maintenance program on the exergo-environmental profile of the chiller

In this scenario, the exergo-environmental profile obtained for the base case assuming an "*ideal maintenance program*" (where no refrigerant leakage occurs during plant lifetime) is compared with the alternative scenario assuming a "*poorly maintained chiller*" (where a 540 g/year average refrigerant loss is considered). In order to perform the above comparison and isolate the effects of the accuracy of the maintenance program, only the base case design and Scenario A for the electricity generation mix are considered.

In Table 7.10, the results of the exergetic cost accounting are shown. As a consequence of the average refrigerant undercharge experienced by the chiller (quantified based on a two years period assumed between two consecutive troubleshooting interventions restoring the nominal charge), an increase of the unit exergetic cost of refrigerated water equal to 0.023 kW_{ex}/kW_{ex} is observed. Based on the 1.48 kW_{ex}/kW_{ex} value of κ_{NR} calculated for the scenario A, the increase in the non-renewable exergy cost $\Delta k^*_{NR,i}$ of refrigerated water is equal to 0.034 kW_{ex} per kW_{ex} of water. The increase in refrigerated water cost is related to the lower exergetic efficiency of the EEV and the Evaporator caused by the lower condensing and evaporating pressures.

Table 7.10. *Results of exergetic cost accounting for a "poor maintenance" scenario and deviations from the "ideal maintenance" reference case.*

	k_p (kW_{ex}/kW_{ex})	Δk_p (kW_{ex}/kW_{ex})	k^*_p (kW_{ex}/kW_{ex})	Δk^*_p (kW_{ex}/kW_{ex})	$k^*_{NR,i}$ (kW_{ex}/kW_{ex})	$\Delta k^*_{NR,i}$ (kW_{ex}/kW_{ex})
Compressor	1.172	-0.023	1.353	0.129	2.002	0.191
EEV	1.327	0.015	2.578	-0.108	3.815	-0.159
Evaporator	1.429	0.031	3.127	0.023	4.629	0.034

In Table 7.11, the variations in life cycle impacts from the "ideal maintenance program" scenario are shown. From the analysis a large variation in the "*Ionising radiation, human health effect model*" and "*Ozone depletion*" resulted (see values in bold in Tab. 11). These additional impacts have been mainly caused by the production phase of the additional refrigerant consumed to restore the nominal capacity of the chiller. This is justified by the null Ozone Depletion Potential of the dispersed refrigerant (R410A). Only minor increases are experienced in terms of total greenhouse emissions as a consequence of the poor system maintenance. In fact, despite the high Global Warming Potential of R410A, equal to 2090 [7.45], the total impact due to dispersion of refrigerant only amounts to 1.86E+04 kg $CO_{2eq.}$, being two orders of magnitude lower than the total IPCC global warming impact reported in Table 7.11.

Table 7.11. *Life cycle impacts of Water-Cooled Chillers in case of "ideal maintenance" and "poor maintenance with non-negligible refrigerant leakage"*

	Units	*Ideal Maintenance*	*Poor Maintenance*	*Percentage variation with respect to Ideal Maintenance*
Acidification	Mole of $H_{+\ eq.}$	7.93E+03	7.99E+03	0.74%
Ecotoxicity for aquatic fresh water	CTUe	8.12E+04	8.21E+04	1.14%
Freshwater eutrophication	kg $P_{\ eq}$	3.99E+00	4.04E+00	1.35%
Human toxicity cancer effects	CTUh	3.29E-03	3.31E-03	0.71%
Human toxicity non-canc. effects	CTUh	3.49E-02	3.51E-02	0.67%
Ionising radiation	kg $U235_{\ eq}$	8.79E+04	1.02E+05	**15.84%**
IPCC global warming, excl biogenic carbon	kg CO_{2eq}	2.95E+06	2.97E+06	0.73%
IPCC global warming, incl biogenic carbon	kg $CO_{2\ eq}$	2.93E+06	2.95E+06	0.73%
Marine eutrophication	kg $N_{\text{-Equiv.}}$	8.44E+01	8.50E+01	0,71%
Ozone depletion	kg $CFC_{\text{-11 eq}}$	1.87E-01	3.00E-01	**59.98%**
Particulate matter/Respiratory inorganics	kg $PM2{,}5_{\text{Equiv.}}$	2.85E+02	2.86E+02	0.67%
Photochemical ozone formation	kg NMVOC	6.00E+03	6.05E+03	0.79%
Resource Depletion, fossil and mineral,	kg Sb-Equiv.	3.41E+00	3.47E+00	1.98%
Terrestrial eutrophication	Mole of $N_{\ eq.}$	2.24E+04	2.26E+04	0.81%

Total freshwater consumption, including rainwater	UBP	2.53E+06	2.55E+06	0.64%
Primary energy demand from ren. and non ren. resources	MJ	4.84E+07	4.87E+07	0.64%

7.7.3 On the possibility to perform articulate sensitivity analyses with simultaneous changes in design variables and context conditions

In the previous section, in order to isolate the effects of each alternative scenario compared to the base case assumed as a reference, the possibility to account for simultaneous changes in design, context and maintenance scenarios was not investigated.

In this section, an example is proposed to illustrate the capabilities of the integrated TEC-LCA approach to provide a comprehensive view of the impact of multiple simultaneous changes. In particular, the exergo-environmental profile of the water-cooled chiller is derived below for all the alternative design scenarios (individually applied), while assuming to vary also the electricity generation mix and then referring to Scenario B. In order to avoid an excessive complexity of the analysis, an "ideal maintenance" is assumed for the system.

In Figure 7.7 the results of the LCA study are shown for each alternative design, based on the electricity generation mix of Scenario B. Results in terms of percentage variation of each impact indicator with respect to the "Base Case" are again shown by a radar map to allow for an easier comparison with the results presented in Figure 7.5 for Scenario A.

Differently than in Figure 7.5, when the context of Scenario B is assumed (see Figure 7.7) the "Undersized Evaporator" design option is easily identified as the most promising one, from a life cycle perspective. Conversely, the "Oversized Condenser" scenario, which represented the most promising alternative when referring to Scenario A (Italian electricity generation mix), now represents the option with the worst environmental profile of the chiller compared to the base case. These results may be

easily explained by considering the incidence of the construction and use phases on the overall life cycle impacts: indeed, as evident from a comparison between Figures 7.3 and 7.6, in a PV-based electricity generation scenario the construction phase accounts for the largely highest share of the life cycle impact. Then, it is reasonable that scenarios implying reduced use of materials during the system construction stage achieve the highest improvements on the environmental profile of the chiller. The improvements achieved for the alternatives "*Undersized evaporator*" and "*Undersized condenser*" mainly arise from the reduction in the amount of steel used during the construction stage.

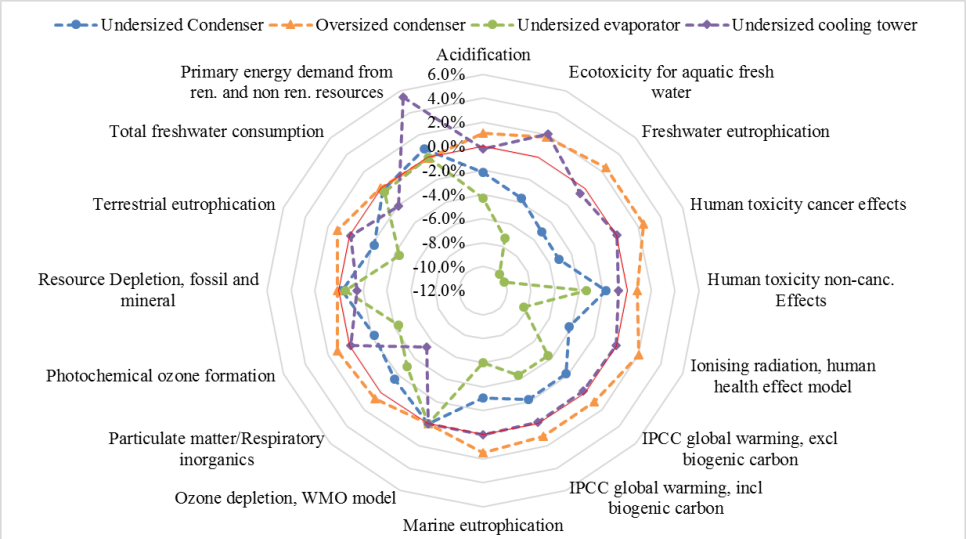

Figure 7.7 *LCA results for design alternatives when referring to Scenario B as mix of electricity generation*

Therefore, when assuming Scenario B and a null non-renewable exergy cost of electricity, the importance of the thermoeconomic analysis of the plant to derive its exergo-environmental profile and identify routes for possible improvements decreases. In fact, in this case the optimization of the exergo-environmental profile of the chiller will converge towards design solutions requiring lower consumption of materials and impacts along the construction phase. Conversely, the route toward design

optimization will not lead to a minimum value of exergy consumption in the use phase, as shown by the Δk_4^* value for the *Undersized Evaporator* case in Table 7.8.

7.8 Outcomes of this analysis

In this chapter an integrated approach for energy systems analysis which attempts to integrate the capabilities of thermoeconomic cost accounting and Life Cycle Assessment has been proposed. A water-cooled chiller has been assumed as a case study and has been examined to clarify the added value of combining these two well established methods.

The combined use of the two approaches on a same application has been revealed useful since they proved to be complimentary and achieved to a certain extent independent result. The analysis revealed that some environmental indicators are dominated by the use phase, being prevalently related to the high energy use during plant operation. Other indicators, conversely, are mainly affected by the construction step. The sensitivity analysis to some specific design variables allowed to determine trade-offs between apparently unrelated domains, e.g. in the undersized condenser scenario a decrement in exergy efficiency and very low environmental impacts were simultaneously observed. The combined TEC-LCA analysis has also revealed that using an undersized cooling tower/evaporator causes a worsening in the exergy efficiency of the system that, on a life cycle scale, is not compensated by a reduction in the embodied exergy related with the reduced amount of materials used in the production stage. Adopting a wide set of impact indicators allows the analyst to observe that the usual correlation between low exergy/energy use and low environmental impacts can be either reversed or maintained for each specific impact, if the other stages of the life cycle (besides the mere use stage) are included in the analysis. This is an important result that testifies the potential of the combined use of thermoeconomics and LCA in investigating conflating domains and modelling the

complexity behind energy systems, with the aim to avoid shifting loads from one domain to another.

The potential of the combined approach in performing sensitivity analyses has also been proven: the use of a different and fully decarbonized energy mix causes a severe reduction in the relative importance of the LCA indicators connected to the use stage. Conversely, the relative importance of the environmental impacts of construction stages increases, resulting always higher than 70%. As expected, in this scenario the only two indicators which reported no significant variations were the Primary energy use (that included the renewable contribution) and the Ozone depletion (due to the production of the refrigerants). The small variation of the Ozone depletion indicator has been further investigated by considering different maintenance scenarios. The comparison between the ideal and the "poor" maintenance has led to solid results in line with the others: the only indicators reporting significant variations was the ozone depletion (60%) and, to some extent, the Ionizing radiation (around 16%). With regard to thermoeconomic indicators, the poor maintenance scenario achieved has increased costs, mainly due to the lower exergy efficiency achieved by the EEV and the evaporator.

References

[7.1] Valero, A. Torres, C. Thermoeconomic analysis. In: Frangopoulos CA, editor. Exergy, energy system analysis and optimization, from encyclopedia of life support system (EOLSS). Oxford: EOLSS Publishers; 2004. Available at: http://www.eolss.net

[7.2] Valero, A. Thermodynamic process of cost formation. In: Frangopoulos CA, editor. Exergy, energy system analysis and optimization, from encyclopedia of life support system (EOLSS). Oxford: EOLSS Publishers; 2004. Available at: http://www.eolss.net

[7.3] Torres, C. Symbolic thermoeconomic analysis of energy systems. In: Frangopoulos CA, editor. Exergy, energy system analysis and optimization, from encyclopedia of life support system (EOLSS). Oxford: EOLSS Publishers; 2004. Available at: (hhttp://www.eolss.net).

[7.4] J. Szargut and D. R. Morris, "Cumulative exergy consumption and cumulative degree of perfection of chemical processes," *Int. J. Energy Res.*, vol. 11, no. 2, pp. 245–261.

[7.5] P. F. Chapman, G. Leach, and M. Slesser, "2. The energy cost of fuels," *Energy Policy*, vol. 2, no. 3, pp. 231–243, Sep. 1974.

[7.6] P. F. Chapman, "1. Energy costs: a review of methods," *Energy Policy*, vol. 2, no. 2, pp. 91–103, Jun. 1974

[7.7] D. R. Morris, "Exergy analysis and cumulative exergy consumption of complex chemical processes: The industrial chlor-alkali processes," *Chem. Eng. Sci.*, vol. 46, no. 2, pp. 459–465, Jan. 1991

[7.8] J. Szargut, A. Ziębik, and W. Stanek, "Depletion of the non-renewable natural exergy resources as a measure of the ecological cost," *Energy Convers. Manag.*, vol. 43, no. 9–12, pp. 1149–1163, Jun. 2002

[7.9] Szargut. Exergy Method: Technical and Ecological Applications, WITpress, 2005

[7.10] Stanek, W. Gazda, W. Exergo-ecological evaluation of adsorption chiller system, *Energy*, Vol. 76 pp 42–48, 2014

[7.11] Szargut, J. Stanek, W., Thermo-ecological optimization of a solar collector, *Energy*, Vol. 32, pp. 584-59, 2007

[7.12] Stanek, W., Czarnowska, L., Kalina, J. Application of life cycle thermo-ecological cost methodology for evaluation of biomass integrated gasification gas turbine based cogeneration. Applied Thermal Engineering, Vol. 70, pp. 1007-1107, 2014

[7.13] Kostowski, W.J. Usòn, S. Stanek, W. Bargiel, P. Thermoecological cost of electricity production in the natural gas pressure reduction process, *Energy,* Vol. 76, pp. 10-18, 2014.

[7.14] Stanek, W. Gazda, W. Kostowski W. Thermo-ecological assessment of CCHP (combined cold-heat-and-power) plant supported with renewable energy, *Energy*, Vol. 92, pp.279-289, 2015.

[7.15] Usón, S. Kostowski, W. J. Stanek, W. Gazda, W. Thermoecological cost of electricity, heat and cold generated in a trigeneration module fueled with selected fossil and renewable fuels, *Energy*, Vol. 92, pp. 308-319, 2015.

[7.16] W. Stanek, J. Szargut, Z. Kolenda, and L. Czarnowska, "Exergo-ecological and economic evaluation of a nuclear power plant within the whole life cycle," *Energy*, vol. 117, pp. 369–377, Dec. 2016.

[7.17] Meyer, L., Tsatsaronis, G., Buchgeister, J., and Schebek, L. Exergoenvironmental analysis for evaluation of the environmental impact of energy conversion systems, *Energy*, Vol. 34, pp. 75-89, 2009.

[7.18] Morosuk, T. Tsatsaronis, G. Koroneos, C. Environmental impact reduction using exergy-based methods, *Journal of Cleaner Production*, Vol. 118, pp.118-123, 2016.
[7.19] Cornelissen, R.L., Hirs, G.G., The value of the exergetic life cycle assessment besides the LCA, *Energy Convers. Manag*. Vol. 43, pp. 1417–1424, 2002.
[7.20] Rocco, M.V., Primary exergy cost of goods and services : an input-output approach, Springer, 2016.
[7.21] Rocco, M. V., Di Lucchio, A., Colombo, E., Exergy Life Cycle Assessment of electricity production from Waste-to-Energy technology: A Hybrid Input-Output approach, Appl. *Energy*. Vol. 194, pp. 832–844, 2017.
[7.22] Rocco, M.V. Colombo, E. Sciubba, E. Advances in exergy analysis: a novel assessment of the Extended Exergy Accounting method, Applied Energy, Vol. 113, pp.1405-1420, 2014.
[7.23] Dai, J., Chen, B., Sciubba, E. Extended exergy based ecological accounting for the transportation sector in China. *Renewable and Sustainable Energy Reviews*, Vol. 32, pp. 229-237, 2014.
[7.24] Lozano, M. Valero, A. Theory of the exergetic cost, Vol 18, *Energy* pp. 939-960, 1993
[7.25] Kloepffer, W. Int J Life Cycle Assess (2008) 13: 89. https://doi.org/10.1065/lca2008.02.376
[7.26] Finkbeiner, M.; Schau, E.M.; Lehmann, A.; Traverso, M. Towards Life Cycle Sustainability Assessment. *Sustainability* , Vol *2*, pp. 3309-3322. 2010
[7.27] ISO 14040, 2006. Environmental Management-Life Cycle Assessment-Principles and Framework.
[7.28] ISO 14044, 2006. Environmental Management-Life Cycle Assessment-Requirements and Guidelines
[7.29] Background Review of Existing Weighting Approaches in Life Cycle Impact Assessment (LCIA). Available at url: http://eplca.jrc.ec.europa.eu/uploads/LCIA-review-of-weighting-methods.pdf
[7.30] Piacentino A, Barbaro C. A comprehensive tool for efficient design and operation of polygeneration-based energy μgrids serving a cluster of buildings. Part II: Analysis of the applicative potential, Applied Energy, Vol. 111, pp. 1222-1238, 2013.
[7.31] IMST-Group Instituto de Ingeniería Energética Universidad Politécnica de Valencia. (2014) Advanced Refrigeration Technologies Software IMST-ART Release 3.60 www.imstart.com
[7.32] C.W. Whitman, W.M. Johnson, J. Tomczyk, E. Silberstein, Refrigeration and air conditioning technology (6th ed.) Cengage learning, Delmar 2009
[7.33] Kotas T. The exergy method of thermal plant analysis. London: Butteerworths; 1985.
[7.34] C. Torres, A. Valero, V. Rangel, and A. Zaleta, "On the cost formation process of the residues," *Energy*, vol. 33, no. 2, pp. 144–152, Feb. 2008.
[7.35] Klein S.A. et al., Engineering equation solver V9.810. Middleton, WI: Solar Energy Laboratory, F-Chart Software, 2010.
[7.36] R. Frischknecht, G. Rebitzer, The ecoinvent database system: a comprehensive web-based LCA database, J. Clean. Prod. Vol.13, pp. 1337–1343, 2005
[7.37] J.R.C. – European Commission, International Reference Life Cycle Data System (ILCD) Handbook – General Guide for the Life Cycle Assessment – Detailed Guidance, 2010
[7.38] J.R.C. – European Commission-Joint Research Centre - Institute for Environment and Sustainability: International Reference Life Cycle Data System (ilcd) handbook-

recommendations for life cycle impact assessment in the European context. first edition november 2011. publications office of the european union; 2011
[7.39] J.R.C. European Commission, Characterization factor of the ILCD recommended life cycle impact assessment methods, Database and Supporting Information, Publications Office of the European Union, February, 2012
[7.40] Terna S.p.a., "Dati statistici energia" 2015. Available at: https://www.terna.it/it-it/sistemaelettrico/statisticheeprevisioni/datistatistici.aspx
[7.41] I. Dinçer and M.A. Rosen, EXERGY : Energy, Environment and Sustainable Development. Elsevier Science, 2012.
[7.42] IPCC - Intergovernmental Panel on Climate Change- Reports Available at https://www.ipcc.ch
[7.43] Rivero, R. Garfias, M. Standard chemical exergy of elements updated, Energy, Vol.31, pp.3310-3326, 2006.
[7.44] Valero, Alicia and Valero, Antonio. The Exergy Calculator. Online tool available at the Exergoecology Portal. www.exergoecology.comwww.exergoecology.com
[7.45] A.Mota-Babiloni, J. Navarro-Esbrí, Á. Barragán-Cervera, F. Molés, B. Peris. Analysis based on EU Regulation No 517/2014 of new HFC/HFO mixtures as alternatives of high GWP refrigerants in refrigeration and HVAC systems. Int. J. Refrig, Vol. 52, pp. 21–31, 2015

Conclusion and Future Remarks

This thesis has been focused on the innovative applications of Exergy Analysis and Thermoeconomics for chemical, thermal and cooling systems. Though a great variety of case studies have been investigated, Exergy can be easily identified as the common thread.

In ***Chapter 1***, an overview on Exergy Analysis and Thermoeconomics have been presented. Strength and Limits of Exergy Analysis have been pinpointed and a brief summary of advanced exergy methods developed has been presented.

As concern Thermoeconomics, the brief historical outline has showed that this method has enlarged its application from the initial cost accounting purposes to the diagnosis of malfunction in energy systems. Symbolic Exergoeconomics have been introduced as a tool for exergy and exergoeconomic cost evaluations.

In Chapter 2 and Chapter 3, the great capability of Exergy Analysis in supporting the development of innovative energy conversion processes emerged.

*In **Chapter 2***, the exergy analysis of the innovative Reverse ElectroDialysis process has shown the capability of this method to provide with useful information concerning the design and the operation of this energy system. For instance, among all the investigated membrane properties, water permeability has been recognized to have the most detrimental effect on exergy efficiency, with exergy losses accounting for 60-80% of total exergy loss. This result is of utmost importance for membrane manufacturers, who will devote their research in reducing this effect. Also, the analysis has provided information about: (i) the effect of the flow arrangement and residence times for solution in the stack on exergy destruction and (ii) the combination of concentrate-dilute solution which allows for achieving the highest thermodynamic performance. Results of the ExA of the RED process have been preliminary for the analysis of the *RED-MED Heat Engin*e, object of ***Chapter 3***. As shown, this system aims at: (i) converting to electricity heat flow from industrial processes which would be otherwise wasted and (ii) overcoming the need of available natural salinity gradients required when operating RED process in an open-loop configuration. By means of Exergy Analysis the effects of some design and the operation parameters on the thermodynamic performance of the process have been accounted. The permselectivity of the membranes and water osmotic fluxes were revealed to be responsible for decreasing the exergy performance of the process. In addition, the influence of the MED pumping power is significant, leading to an important decrease of the global exergy efficiency. Finally, the exergy potential of the technology was assessed using high-performing membranes and higher number of MED effects, reaching global exergy efficiency of 26.5%, showing the significant potential of the RED-MED HE for the conversion of waste heat into electricity. It is apparent that efforts are still needed for the development of RED-MED HE.

After applying Exergy Analysis to these innovative energy conversion systems, Thermoeconomics has been the object of the remaining chapters.

In ***Chapter 4***, exergy cost accounting has been applied to a Multi-Effect Desalination (MED) process. In this chapter, exergy analysis and exergy cost accounting have been proposed for the in-depth interpretation of thermodynamic behavior of Multiple Effect Distillation processes. Exergy analysis has highlighted in which processes the highest exergy destruction occurs. The exergy cost accounting has provided provide a comprehensive view of the cost formation process of the freshwater produced, allowing the plant designer or manager to calculate, on a rigorous thermodynamic basis, the exergetic (or economic) amount of external resources consumed to produce each specific material stream or exergy flow.

The low exergy efficiency of the whole MED process suggests that high exergy destruction occurs when converting thermal exergy of motive steam into chemical exergy of freshwater. In order to provide a clear interpretation of the reasons for the low exergy efficiency of the MED system, a conveniently high disaggregation level has been adopted. As concerns thermal vapor compression, the use of high-pressure steam to produce low pressure steam supplied to MED process resulted to be among the main responsible subprocesses for the poor plant performance. This result testified the great convenience in supplying such low temperature processes, like the examined MED plant, by means of cogenerated heat recovered from power plants or waste heat cascaded from other industrial processes.

By means of exergy cost accounting, the cost formation process of the distillate could be clearly depicted. A substantial increase in specific cost of freshwater product has been observed from the first to the last effects, as a consequence of the irreversibility in the production process.

The applicative example confirmed the potential of exergy and thermoeconomic analysis to provide a comprehensive understanding of plant behavior, allowing the plant designer to identify the possible margins for improvements.

In ***Chapter 5,*** a thermoeconomic cost accounting of a Combined Heat and Power steam cycle integrated with Multi-Effect Desalination-Thermal Vapor Compression plant has been presented. The capability of this method to provide with a rational basis for the allocation of costs on freshwater and electrical power has been shown.

The analysis has been carried out by considering two distinct scenarios, which differ for the rejection or the recovery of the chemical exergy content of the concentrated brine. In the first case, brine is disposed back to the sea and its exergy was entirely wasted. In such conditions, the method has pointed out that the thermoeconomic unit cost of freshwater is significantly higher compared to the electricity cost, due to the higher exergy destruction involved in the production process of the former output. These two values resulted to differ approximately by one order of magnitude, being this result justified by the exergy efficiency of the MED-TVC which resulted lower than 10%. Furthermore, the sensitivity analysis has showed that the unit cost of freshwater is quite sensitive to the steam extraction pressure, and a low pressure of the motive steam was suggested as an optimal criterion for plant design. As concerns the second scenario, results have shown that the use of the chemical exergy content of brine to drive a Reverse Electrodialysis Unit allows for a reduction in the exergetic cost of freshwater produced, compared to the first scenario,

Chapter 6 has been focused on the innovative applications of Thermoeconomics to the diagnosis of faults in HVAC systems. After a brief overview on the method and its development in these decades, insights into the malfunctions/disfunction approach are given. In this thesis, thermoeconomic diagnosis of air-cooling systems has been evaluated for the first time by means of *real data* collected from a *packaged rooftop air conditioning unit* installed at the Herrick Laboratories, Purdue University. Three faulty scenarios were considered*: evaporator fouling*, *condenser fouling*, *evaporator fouling along with condenser fouling*. Results have shown that: (i) the diagnostic technique is able to detect a single fault; (ii) the performance of the technique depends

upon the level of fault imposed, and specifically it decreases when the fault level increases (iii) for evaporator fouling, the performance of the diagnostic technique is sensitive to the relative humidity of the air entering the evaporator coil (iv) in multiple faults scenarios, the technique is capable of detecting the simultaneous presence of condenser and evaporator fouling. A poor quantitative estimation of their impacts on the increased consumption mainly due to the induced malfunctions on the compressor. All these results agreed with the ones obtained from "virtual experiments" available in literature.

Future works will be focused on: (i) development of characteristic curve for each component (i.e. a mathematical model which describes the analytical dependence of the unit exergy consumption and a set of thermodynamic parameters) in order to filter induced malfunction on the compressor and (ii) detection of "system fault" as the undercharge or overcharge of the refrigerant, which is not allowed by the current thermoeconomic model.

In ***Chapter 7***, an integrated approach for energy systems analysis has been proposed with the aim to integrate the capabilities of thermoeconomic cost accounting and Life Cycle Assessment. The approach can be applied to existing plants, in order to assess the different contributions of the construction and operation steps on its total life cycle impacts. However, an even greater potential may be exploited when applying the methodology as a support tool for decision-making during the design optimization of the system: in this case the proposed approach allows for a quantitative analysis of the trade-offs between concurrent effects induced by a hypothetical change in a design variable. Also, the method allows to perform rigorous accounting of the impacts of possible alternative maintenance strategies, quantifying the effects of the performance degradation and their relative weight on the total life cycle impact. A water-cooled chiller has been assumed as a case study and examined to clarify the added value of combining these two well established methods.

The need for including a thermoeconomic analysis is clear when considering that, in most energy conversion systems having a non-renewable energy input, the impacts related to the operation phase are prevalent over those related to the construction phase. Then, the insights provided by the thermoeconomic analysis allow to identify the components and subprocesses which mostly contribute to increase the energy consumption and to identify possible routes for design improvement;

The articulate set of indicators provided by the proposed method is more difficult to exploit as a support for decision making, compared to the synthetic results achieved, in the form of a single indicator, by an exergoenvironmental cost accounting. However, it provides a larger set of information on the expected impacts of an energy system, thus increasing the awareness of the analyst on the specific effects of any design or maintenance decisions.

The variety of topic addressed in this thesis highlights the great capabilities of all exergy-based methods in the analysis of energy conversion processes. Further refinements are needed, but the most challenging thing to do is to transfer the use of these methods to the industrial field. Research must go on…

Nomenclature

A	Area (m^2)
$\dot{A}_Q$	Anergy of Heat Flow (W)
a_i	Distribution ratio on component "i" of valve's additional exergy destruction (dimensionless)
a_s	Salt Activity
a_w	Water Activity
b	Specific exergy (kJ_{ex}/kg)
$\dot{B}$	Exergy Flow (W_{ex})
B_D	Exergy Destruction (W_{ex})
$B_{D,k}^{EN}$	Endogenous exergy destruction (W_{ex})
$B_{D,k}^{EX}$	Exogenous exergy destruction (W_{ex})
$B_{D,k}^{AV}$	Avoidable Exergy Destruction (W_{ex})
$B_{D,k}^{UN}$	Unavoidable Exergy Destruction (W_{ex})
B_L	Exergy Loss (W_{ex})
$\dot{B}_Q$	Themal Exergy Flow (W_{ex})
$\dot{B}_{ji}$	Exergy flow "produced" by component "j" and "consumed" by component "i" (W_{ex})
B_i^{p}	Mechanical Fraction of Exergy Flow (W_{ex})
B_i^{T}	Thermal Fraction of Exergy Flow (W_{ex})
C_{conc}	Concentrate Molar Concentration (M)
C_{dil}	Dilute Molar Concentration (M)
c_i	Distribution ratio on component "i" of condenser's additional exergy destruction
$C_{P,i}$	Cost of the product of component "i" (€)
$C_{R,i}$	Cost of the residue allocated on component "i" (€)

$\dot{C}_{P,i}$	Cost Flow of the product of component "i" (€/h)
$\dot{C}_{R,i}$	Cost Flow of the residue allocated on component "i" (€/h)
COP	Coefficient of Performance (dimensionless)
CRF	Capital Recovery Factor (dimensionless)
ΔF_T	Fuel Impact (W_{ex})
D_{salt}	Salt permeability coefficient, m^2/s
DF_i	Dysfunction generaed in i-th component (W_{ex})
E_{cell}	Voltage generated by the cell pair (V)
E_{loss}	Ohmic loss due to internal stack resistances (W)
E_{mix}	Exergy destruction due to uncontrolled mixing phenomena (W)
E_{stack}	Voltage generated by the pile (V)
EER	Energy Efficiency Ratio (dimensionless)
f_r	Residue Exergoeconomic Factor (dimensionless)
f_z	Capital Exergoeconomic Factor (dimensionless)
F	Fuel (W_{ex})
F_T	Total fuel consumption (W_{ex})
$F_{e,i}^*$	Exergetic Cost of the external fuel (W_{ex})
F_i^*	Exergetic cost of the fuel of the "i-th" component (W_{ex})
G	Gibbs free energy (J)
h	Specific enthalpy (kJ/kg)
$\bar{h}$	Molar enthalpy (J/mol)
$\tilde{h}$	Partial Molar Enthalpy of the "i^{th}" species (kJ/kmol)
I	Electric current (A)
IEM	Ionic Exchange Membrane
$I_{r,RED}$	Exergy destruction within RED unit (W)
J	Molar Flux (mol/m^2s)
k_i	Overall unit exergy consumption of component "i" (dimensionless)
$k_{NR,i}^*$	Non-renewable Exergetic unit cost of the product of the "i-th" component (W_{ex}/W_{ex})
$k_{p,i}^*$	Exergetic unit cost of the product of the "i-th" component (W_{ex}/W_{ex})
m	Molality (mol/kg_{solv})
M_s	Salt molecular weight (mol/kg)
M_w	Water molecular weight (mol/kg)
MF	Malfunction (W_{ex})

MF^*	Malfunction cost (W_{ex})
N	Number of species in a mixture
$\dot{N}$	Molar Flowrate (mol/s)
N_{cp}	Number of cell pair
N_k	Number of discretization elements
OCV	Open Circuit Voltage (V)
p	Pressure (kPa)
P	Exergy Product (W_{ex})
P_d	Power density (W/m^2)
P_e	Electric Power (W)
P_s	Membrane Permeability to Salt (m^2/s)
P_T	Final Product (W_{ex})
P_w	Membrane Permeability to Water (m/Pa·s)
P_i^*	Exergetic cost of the product of the "i-th" component (kW_{ex})
Q	Volumetric Flowrate (m^3/s)
R_{AEM}	Anionic Membrane Resistance (Ωm^2)
R_{blamk}	Electrical resistance of the electrodic compartment (Ω)
R_{cell}	Electrical resistance of the cell pair (Ω)
R_{CEM}	Cationic membrane Resistance (Ωm^2)
R_{conc}	Electrical resistance of concentrate (Ωm^2)
R_{dil}	Electrical resistance of dilute (Ωm^2)
r_{ij}	Product junction coefficients (dimensionless)
R_{int}	Internal Stack Resistance (Ω)
R_L	Load Resistance (Ω)
R_u	Universal constant of gases (kJ/(kmol K))
s	Specific entropy (kJ/(kg K))
$\tilde{s}$	Molar Specific entropy (kJ/kmol)
$\bar{s}$	Molar entropy, J/(mol·K)
T	Temperature (°C or K)
U	Overall heat transfer coefficient, $W/(m^2K)$
v_{conc}	Concentrate Velocity (m/s)
v_{dil}	Dilute Velocity (m/s)
x_s	Salt molar fraction (dimensionless)
x_w	Water molar fraction (dimensionless)
y_{ij}	Product distribution ratio (dimensionless)
Z_i	Capital Cost of component "i" (€)

Greek symbols

α	Permselectivity
γ	Salt activity coefficient (dimensionless)
δ_m	Membrane Thickness (m)
θ_{ij}	Unit Residue Consumption (dimensionless)
η	Performance (dimensionless)
ι	Interest rate (dimensionless)
κ_{ij}	Unit exergy consumption (dimensionless)
$\kappa_{NR,i}$	non-renewable exergy consumed per unit of external exergy supplied (dimensionless)
λ	Enthalpy of Vaporization (kJ/kg)
μ_{MX}	Chemical potential of the generic solute MX
ρ	Density (kg/m^3)
ρ_{ij}	Residue Jucntion Coefficient (dimensionless)
ϕ	Osmotic Coefficient (dimensionless)
ψ_{ij}	Residue distribution factor (dimensionless)
τ_C	Dimensionless Exergetic Temperature (dimensionless)

Vectors and Matrices

‹*FP*›	Matrix of product distribution ratios (NxN)
‹*RP*›	Matrix of residue distribution ratios (NxN)
‹K*P*›	Matrix of product consumption ratios (NxN)
‹KR›	Matrix of residue consumption ratios (NxN)
$\boldsymbol{C_P}$	Vector of product cost (Nx1)
$\boldsymbol{C_e}$	Vector of external fuel cost (Nx1)
$\boldsymbol{\dot{C}_P}$	Vector of product cost flow (Nx1)
$\boldsymbol{\dot{C}_e}$	Vector of external fuel cost flow (Nx1)
$\boldsymbol{F}_e$	Vector of External Exergy Sources (Nx1)
$\mathbf{K}_D$	Matrix of unit exergy consumption (NxN)
$\mathbf{P}_s$	Vector of Final product (Nx1)
$\boldsymbol{U}_D$	Identity matrix (NxN)
$\boldsymbol{Z}$	Vector of capital cost (Nx1)
$\boldsymbol{\dot{Z}}$	Vector of capital cost flow (Nx1)

Subscripts

0	Related to reference or “dead” state
B	Related to brine
ch	Related to chemical exergy
Cond	Related to condenser
cp	Related to RED cell pairs
D	Related to distillate
in	Related to inlet
is	Related to turbine isoentropic efficiency
out	Related to outlet
ph	Related to physical exergy
s	Related to salt
sol	Related to solution
th	Related to thermal exergy
w	Related to water